Receptors based on Aryl-extended Calix[4]pyrrole Scaffolds

Yifan Li

UNIVERSITAT ROVIRA i VIRGILI

ICIQ Institute of Chemical Research of Catalonia

Receptors based on Aryl-extended Calix[4]pyrrole Scaffolds

Yifan Li

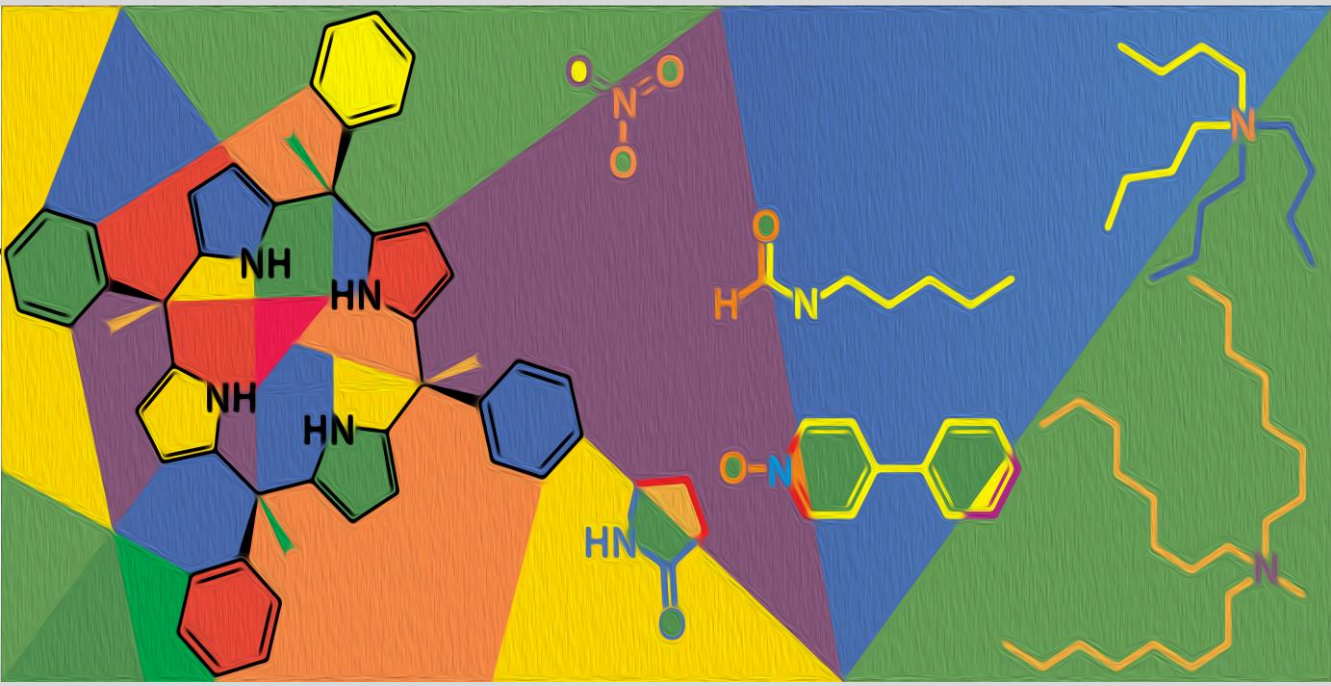

DOCTORAL THESIS
2024

DOCTORAL THESIS

Yifan Li

RECEPTORS BASED ON ARYL-EXTENDED CALIX[4]PYRROLE SCAFFOLDS

Supervised by Prof. Pablo Ballester Balaguer

UNIVERSITAT
ROVIRA i VIRGILI

Tarragona

2024

UNIVERSITAT ROVIRA I VIRGILI
Receptors based on Aryl-extended Calix[4]pyrrole Scaffolds
Yifan Li

Institut Català d'Investigació Química

Av. Països Catalans, 16
43007 Tarragona, Spain
Tel. (+34) 977 920 200
email: iciq@iciq.es

UNIVERSITAT ROVIRA i VIRGILI
Dept. de Química Analítica i Química Orgànica

Carrer de Marcel·lí Domingo, 1
43007 Tarragona, Spain
Tel. (+34) 977 55 97 69
email: sdn4@urv.cat

I STATE that the present study, entitled "Receptors based on Aryl-extended Calix[4]pyrrole Scaffolds", presented by Yifan Li for the award of the degree of Doctor, has been carried out under my supervision at the Institute of Chemical Research of Catalonia (ICIQ).

Tarragona, November 2024

Doctoral Thesis Supervisor

Prof. Pablo Ballester Balaguer

UNIVERSITAT ROVIRA I VIRGILI
Receptors based on Aryl-extended Calix[4]pyrrole Scaffolds
Yifan Li

UNIVERSITAT ROVIRA I VIRGILI
Receptors based on Aryl-extended Calix[4]pyrrole Scaffolds
Yifan Li

"Drei Verwandlungen nenne ich euch des Geistes: wie der Geist zum Kamele wird, und zum Löwen das Kamel, und zum Kinde zuletzt der Löwe" .

Also sprach Zarathustra

Nietzsche, Friedrich

UNIVERSITAT ROVIRA I VIRGILI
Receptors based on Aryl-extended Calix[4]pyrrole Scaffolds
Yifan Li

Acknowledgments

Throughout my doctoral research and the writing of this dissertation, I have received incredible support and guidance. It is bittersweet to see my Ph.D. journey coming to an end, as time always goes too fast to appreciate every moment.

First and foremost, I would like to express my deepest gratitude to my supervisor, **Prof. Pau Ballester**, for his invaluable advice, unwavering support, and patience at every stage of my doctoral journey. His profound expertise and knowledge have been instrumental in shaping my research direction and methodology. His insightful feedback helped transform my chaotic thoughts into a more scientific and logical framework.

I also deeply appreciate **Gemma Aragay**, who has always been there, ready to help. Your invaluable advice and constant encouragement over these years have been crucial in my growth, empowering me to earn the doctorate title.

A heartfelt thank you to **Qingqing Sun** and **Felipe Sierra**, whose support was vital at the beginning of my Ph.D. Without their help, I would not have adapted so smoothly to life in Tarragona.

I would also like to extend special thanks to **Naoyuki Hisano**, who has been a true inspiration and keeps motivating me to strive toward becoming an ideal scientist. The time we worked together remains one of my most cherished memories, and I am deeply grateful for the experiences you shared with me.

I am grateful to all my lab mates: **Andrea**, **Chiara**, **Evgeny**, **Eva**, **Esteban**, **Hayley**, **Jiaming**, **Kamil**, **Karen**, **Manuel**, **Mingkai**, **Pedro**, and **Siqi**, for the wonderful times we shared in the lab. My thanks also go to the visiting students: **Martina**, **Davide**, **Rossella**, and **Mario**, for bringing the Italian atmosphere into the lab.

I want to extend my deep gratitude to **Prof. Michael Schmittel**, **Indrajit Paul**, and **Amit Ghosh**, for inspiring me to be bold in my imagination.

Finally, I am profoundly grateful to my parents. Without their tremendous understanding, unwavering encouragement, and unconditional love over the past years, continuing this journey in chemistry would be impossible.

If possible, I would also like to thank **“calix[4]pyrroles”**, the family of molecules I have tried to befriend over the past four years. I cannot tell if I made it, or if it just needs more time. But in my opinion, our friendship is worth enough to write a book.

This work has been made possible thanks to the financial support from PID2020-114020GB-I00, CEX2019-000925-S, and PID2023-149233NB-I00, which are financed by MCIU/AEI /10.13039/501100011033 /FEDER, EU. CERCA Programme/Generalitat de Catalunya, AGAUR (2021 SGR 00851), and ICIQ Foundation are also acknowledged.

In memory of my grandfather,

UNIVERSITAT ROVIRA I VIRGILI
Receptors based on Aryl-extended Calix[4]pyrrole Scaffolds
Yifan Li

Table of Contents

Chapter 1: Introduction 13

1.1 Aryl-extended calix[4]pyrrole motifs 15

1.2 Calix[4]pyrrole-based anion and ion-pair receptors 17

1.3 AE-Calix[4]pyrrole-based cages: a combination of confined cavity and endo-functionalization 25

1.4 Aims of the thesis 32

1.5 Outline of the thesis 34

1.6 References and notes 36

Chapter 2: Selective binding of nitrate by a neutral bis-calix[4]pyrrole [2]rotaxane 39

2.1 Introduction 41

2.2 Results and discussions 44

2.3 Conclusions 64

2.4 Experimental section 61

2.5 References and notes 78

Chapter 3: Acid-catalyzed self-assembly of [4+2] octa-imine cages based on a tetra-amine AE-C[4]P 81

3.1 Introduction 83

3.2 Design 86

3.3 Synthesis 88

3.4 Conclusions 97

3.5 Experimental section 98

3.6 References and notes 107

Chapter 4: Binding of aliphatic diformamides by an octa-imine bis-calix[4]pyrrole cage: thermodynamic and kinetic characterization 109
4.1 Introduction 111
4.2 Results and discussions 115
4.3 Conclusions 139
4.4 Experimental section 140
4.5 References and notes 146
Chapter 5: Polar octa-imine cages as molecular containers for Huisgen 1,3-dipolar cycloaddition reactions 147
5.1 Introduction 149
5.2 Results and discussions 152
5.3 Conclusions 182
5.4 Experimental section 183
5.5 References and notes 220
Chapter 6: Self-assembly of a tetra-imine cage and its application as a molecular container for Huisgen cycloaddition reactions 221
6.1 Introduction 223
6.2 Results and discussions 225
6.3 Conclusions 257
6.4 Experimental section 258
6.5 References and notes 274
General conclusions 275
List of abbreviations 279

Chapter 1

Introduction

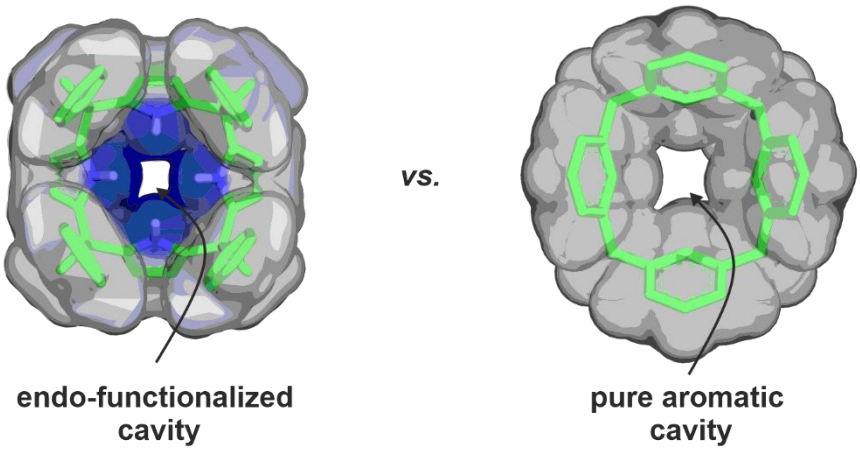

UNIVERSITAT ROVIRA I VIRGILI
Receptors based on Aryl-extended Calix[4]pyrrole Scaffolds
Yifan Li

1.1 Aryl-extended calix[4]pyrrole motifs

Calix[4]pyrroles are conformationally flexible tetrapyrrolic macrocycles, widely employed as building blocks in supramolecular architectures due to their versatile application in molecular recognition,[1] sensing,[2,3] transmembrane transport,[4,5,6,7] and the design of functional materials. [8,9,10,11]

The first synthesis of calix[4]pyrrole dates back to 1886 when von Baeyer reported the acid-catalyzed condensation of acetone and pyrrole to yield the meso-octamethyl calix[4]pyrrole **1**.[12] Structurally, calix[4]pyrroles consist of four pyrrole rings linked by sp^3-hybridized carbon atoms (meso carbons) at their α positions. The term "calixpyrrole" was coined by Sessler and co-workers in the 90s considering its structural and conformational analogy to calixarenes.[13]

The elaboration of the meso-carbons with aryl substituents (i.e. reacting aryl-alkyl-ketones with pyrrole) affords the so-called aryl-extended calix[4]pyrroles (AE-C[4]Ps). Besides their conformational isomers given by the relative orientation of the pyrrole units (e.g. cone, partial cone, 1,3-alternate), AE-C[4]Ps can exist as different configurational isomers based on the relative orientation of the meso-aryl substituents (two configurational isomers for two-wall AE-C[4]Ps (α,α and α,β) and four for four-wall AE-C[4]Ps (tetra-α, α,α,α,β, α,α,β,β and α,β,α,β, **Figure 1**)). The synthesis of AE-C[4]Ps produces reaction crudes composed of isomeric mixtures of these configurational isomers that can usually be separated using chromatographic methods.

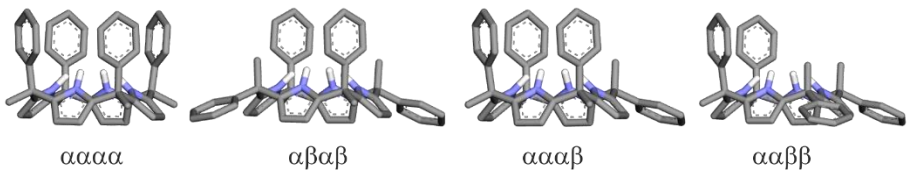

Figure 1. Configurational isomers of “four-wall” aryl-extended calix[4]pyrrole in cone conformation.

For four-wall AE-C[4]Ps, the tetra-α isomer, featuring the four aromatic panels pointing up, is typically isolated in 5-20% yield. However, specific substitutions (e.g. *m*- or *p*-hydroxyphenylmethyl ketone) or templating strategies can lead to higher yields, exceeding in special cases 35 %.[14,15] The tetra-α isomers of four-wall AE-C[4]Ps in the cone conformation display deep aromatic cavities with a polar binding

site composed of four hydrogen bond donor pyrrole NHs (**Figure 2a**). Therefore, AE-C[4]Ps can bind anions or electron-rich neutral molecules in their cavity by establishing hydrogen bond interactions. Additional non-covalent interactions, such as anion-π, CH-π, π-π, further modulate the binding properties of these receptors.[16,17]

For two-wall AE-C[4]Ps, the αα-isomer is usually produced in 5-30% yield upon cyclocondensation of a dipyrromethane and acetone.[18] In contrast to the tetra-α isomer of four-wall AE-C[4]Ps, the cone conformation of the two-wall αα-isomer presents an aromatic cleft with a polar binding site (**Figure 2b**).

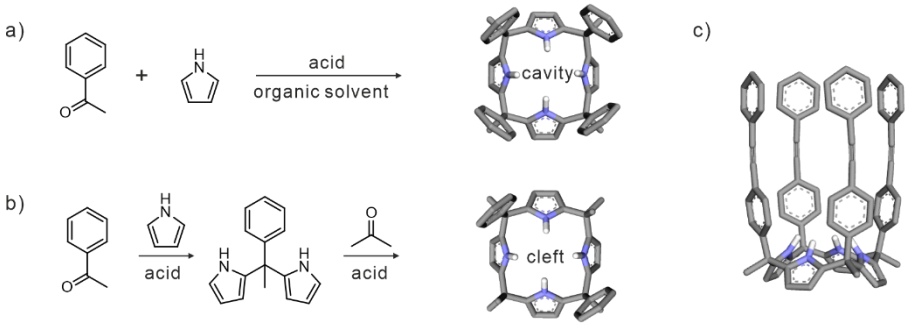

Figure 2. Synthetic schemes of (a) four-wall tetra-α and (b) two-wall αα- AE-C[4]P isomers. Top views of the EM structure of the products are shown. (c) Side view of the energy-minimized structure of SAE-C[4]P.

The aromatic cavities or clefts of AE-C[4]Ps can be further elaborated by introducing additional aromatic panels at their upper rims and producing the so-called super aryl-extended calix[4]pyrroles (SAE-C[4]Ps). "Four-wall" SAE-C[4]Ps can be prepared through a quadruple-Sonogashira coupling reaction of tetra-α tetra-iodo AE-C[4]P with aromatic panels with an ethynyl substituent, [19] resulting in a larger solvophobic/hydrophobic aromatic cavity (**Figure 2c**).

In this introduction chapter, we will describe distinguished examples of calix[4]pyrrole receptors relevant to this PhD thesis. Specifically, we will focus on anion and ion-pair receptors and endo-functionalized cages based on AE-C[4]P scaffolds.

1.2 Calix[4]pyrrole-based anion and ion-pair receptors

Over the past decade, calix[4]pyrroles (C[4]Ps) have garnered significant attention as efficient receptors for anions[13] and ion pairs.[20,21]

In non-polar solvents, C[4]Ps predominantly adopt a 1,3-alternate conformation. Upon binding of an anion or a neutral polar guest C[4]Ps undergo a conformational change from alternate to the cone conformation. In this cone conformer, the bound anion (or polar neutral guest) establishes four hydrogen bonds with the NH groups of the pyrrole rings. The counter-cations (e.g. tetra-alkylammonium) can bind the shallow and electron-rich cavity formed by the four pyrrole rings opposite to the bound anion, leading to a receptor-separated ion-pair geometry. Otherwise, cations can also be positioned near the anion, resulting in a close-contact binding mode geometry (**Figure 3**).

Solvation effects strongly influence ion-pair dissociation, anion binding, and cation recognition. Therefore, the effectiveness of calix[4]pyrroles as heteroditopic receptors is highly dependent on the type of solvent (non-polar, polar protic, or polar aprotic) and on the nature of the counter-cation. In polar solvents, the impact of the cation in the binding process is reduced due to the partial dissociation of the ion-pair and the final complex in these solvents (**Figure 3**).

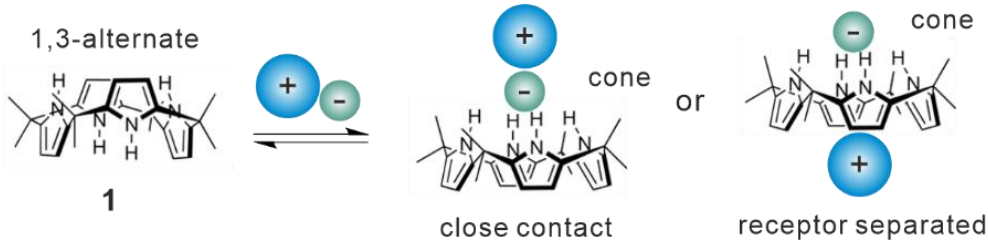

Figure 3. Conformational change experienced by octamethyl calix[4]pyrrole **1** upon ion-pair binding. Two ion-pair binding modes (close-contact and receptor-separated) are depicted.

1.2.1 AE-C[4]P receptors

As stated above, "two-wall" and "four-wall" AE-C[4]Ps bind anions by establishing four convergent hydrogen bonds. The resulting binding geometry forces the bound anion to interact (either repulsively or attractively) with the π-aromatic walls system through anion-π interactions, as shown in many X-ray crystallographic studies.

Our group investigated the strength of chloride-π interactions in solution using "four-wall" AE-C[4]Ps.[22] We used a series of AE-C[4]Ps (**2a-f**, **Figure 4a**) with different para-substituents, modifying the electronic properties of the aromatic walls. In acetonitrile solution, AE-C[4]Ps **2a-f** form 1:1 inclusion complexes with Cl^- ($Cl^-\subset$**2a-f**). In this solvent, the ion-pair precursor (tetrabutylammonium chloride, TBA·Cl) and the inclusion complex are expected to be predominantly dissociated. We determined free binding energies ΔG ranging from -3 to -7.2 kcal·mol^{-1} (K_a = 10^2-10^5 M^{-1}) using ^{1}H NMR titration and isothermal titration calorimetry (ITC) depending on the electronic nature of the meso-aryl substituent of **2**.

The $\Delta\Delta G$ calculated for the chloride-π interactions ($\Delta\Delta G_{Cl\text{-}\pi} = (\Delta G_{Cl\subset 2} - \Delta G_{Cl\subset 1})/4$) were obtained considering that the contribution of the hydrogen bond interactions was identical in all complexes and taking octamethyl calix[4]pyrrole **1** as reference for this value ($\Delta G_{Cl\subset 1}$). Moreover, this value was statistically corrected by the number of aromatic panels (i.e., 4), assuming that the anion-π interactions are additive. The $\Delta\Delta G$ values displayed a linear relationship with the para-substituent Hammet constant σ_p values. These results demonstrated that the chloride-π interactions in these complexes are mainly dominated by electrostatic effects (**Figure 4**).

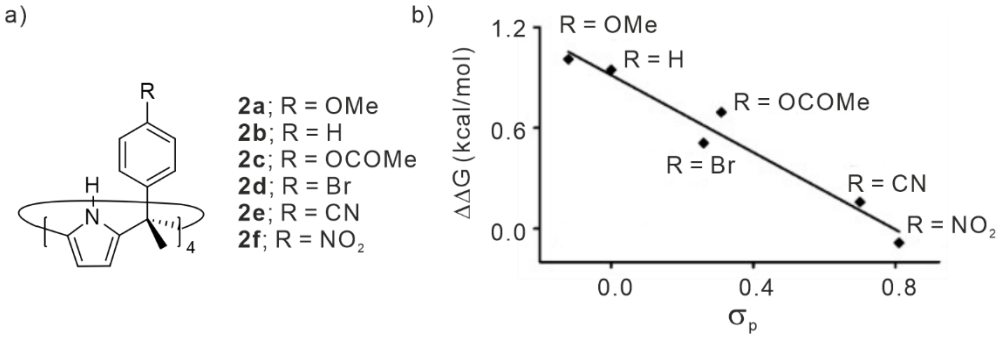

Figure 4. a) Molecular structures of "four-wall" AE-C[4]P **2a-f**. (b) $\Delta\Delta G$ values determined for the chloride-π interactions *vs* the Hammet constants of the *para*-phenyl substituents.

In a separate work, our group reported the thermodynamic characterization of halide-π interactions with a series of "two-wall" AE-C[4]Ps featuring electronically different meso-aromatic substituents. In this case, we used molecular electrostatic potentials (MEP) value at the center of the phenyl ring instead of the *p*-substituent Hammet constant to correlate the free binding energies ascribed to halide-π interactions.[23] In acetonitrile and using TBA^+ as the counter-cation for all halides (i.e. Cl^-, Br^-, I^-), anion binding with "two-wall" AE-C[4]Ps **3a-g** becomes more attractive as the MEP value at the center of the meso-aromatic units increased (i.e. more positive) (**Figure 5**). Iodide showed the most attractive anion-π interaction compared to chloride and bromide. Most likely, this is due to the larger size and higher polarizability of the anion.

NO_3^--π interactions were also studied using "two-wall" AE-C[4]Ps in acetonitrile.[24] Similarly, we described an excellent correlation between the electronic properties of the meso-aryl substituents and the free binding energy of NO_3^-⊂AE-C[4]P complexes, confirming the essential electrostatic component of NO_3^--π interactions. The trigonal planar shape of the nitrate anion allows for various binding geometries, unlike spherical halides. In the solid-state structure of NO_3^-⊂**3g** complex, two distinct binding motifs were identified: a) the nitrate was located almost perpendicular to the aromatic walls, and the TBA^+ cation was included in the shallow aromatic cavity opposite to the bound anion, providing a receptor-separated binding geometry; b) the nitrate was bound in a pseudo-parallel manner to the aromatic panels, and the cation was located close to the anion, displaying a close-contact binding geometry. Interestingly, in both geometries, the nitrate anion was hydrogen bonded to the calix[4]pyrrole core only using one oxygen atom.

The use of a polar solvent such as acetonitrile or acetone is not convenient for studying the effect of the countercation in solution. Polar non-protic solvents effectively solvate the cations. As a consequence, anions are highly dissociated from their cations and the formation of hydrogen-bonded anionic complexes with reduced ion-pairing is favored.

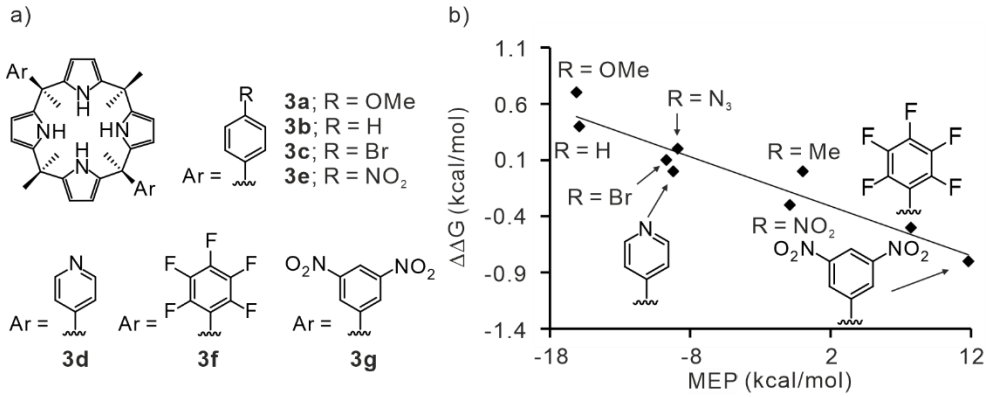

Figure 5. (a) Molecular structures of "two-wall" AE-C[4]P **3a-g** used in the evaluation of anion-π interactions. (b)Experimental *ΔΔG* values determined for the chloride-π interaction *vs* the calculated MEP values at the center of the aromatic ring.

Non-polar solvents such as chloroform and dichloromethane are typically used to study the ability of C[4]Ps to bind ion-pairs. Several works report the binding of tetraalkylammonium salts with heteroditopic calix[4]pyrrole receptors in polar and non-polar solvents.[21] Sessler and co-workers reported a strong countercation effect on the binding affinity of tetraalkylammonium chloride salts with octa-methylcalix[4]pyrrole **1** in dichloromethane. They determined K_a ranging from 10^2-10^4 M^{-1} using isothermal titration calorimetry (ITC) and ^{1}H NMR spectroscopic titrations.[25] We and others demonstrated that organic cations featuring at least one methyl substituent display larger binding affinities for C[4]P receptors. This is attributed to the superior fit of the methyl group in the shallow electron-rich cavity generated by the bound anion locking the calix[4]pyrrole in the cone conformation.[26,27]

1.2.2 Macrocyclic bis-calix[4]pyrrole receptors

In the Ballester group's journey towards the synthesis of interlocked molecules (i.e., rotaxanes, catenanes), two different bis-calix[4]pyrrole cyclic components were prepared. These macrocycles incorporate two aryl-extended calix[4]pyrrole binding sites into a rigid 3D molecular scaffold. These receptors exhibit unique binding properties, particularly for ion-pairs in nonpolar solvents, compared to the previous AE-C[4]P receptors with a single binding site. This is mainly attributed to the preorganization of the covalently connected AE-C[4]P in the cone-conformation.

Bis-calix[4]pyrrole macro-tricyclic receptor **4** was reported by our group using a template-assisted Hay coupling strategy (**Figure 7a**).[28] This rigid macrocycle, with 1,3-butadiynyl spacers, can bind two TBA·Cl or TBA·OCN ion-pairs with high cooperativity ($\alpha > 10^3$) in $CDCl_3$. [29] The complexes displayed a cascade-like arrangement of the ion-pairs, with one TBA^+ cation sandwiched between two included anions. The other countercation is bound outside in the shallow, electron-rich cup opposite to the bound anion. The high cooperativity was explained by the intimate contact ion-pair formed inside the macrocyclic cavity.

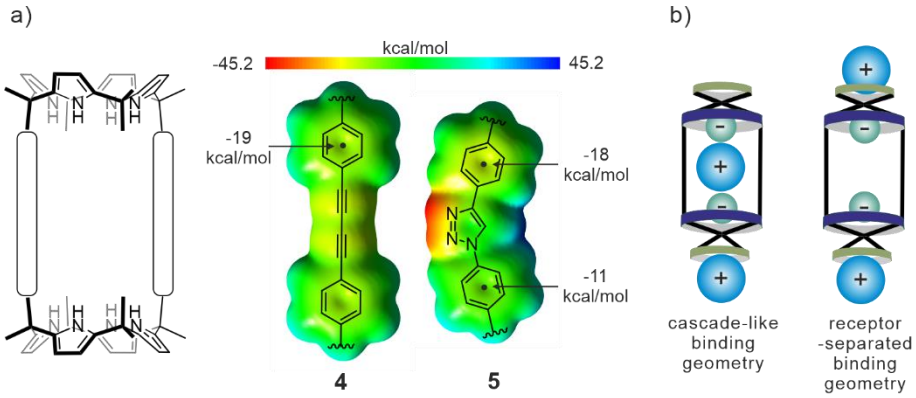

Figure 6. a) Schematic representation of the molecular structure of bis calix[4]pyrrole macrocycles **4** and **5**. The MEP and the value at the center of the aromatic ring are shown for each spacer; b) Cartoons of the two binding models found for the 2:1 ion-pair complexes of TBA·Cl/OCN and MTOA·Cl/OCN with bis-calix[4]pyrrole macrocycles **4** and **5**.

Interestingly, the use of methyltrioctylammonium ($MTOA^+$) cation rendered the binding process less cooperative and the resulting complexes showed receptor-separated binding geometries (**Figure 7b**). The $MTOA^+$ was selectively bound outside the macro-tricyclic cavity.

More recently, our group reported a similar bis-calix[4]pyrrole macrocycle, **5**, prepared via a template-assisted double copper(I)-catalyzed azide-alkyne cycloaddition (CuAAC) reaction.[30] This macrocycle featured 1,4-diphenylsubstituted 1,2,3-triazole spacers connecting the two AE-C[4]P binding sites. The size of the aromatic cleft of **5** was shorter than that of **4**. Moreover, macrocycle **5** presented two different binding sites in contrast to the two identical binding sites displayed by macrocycle **4**. Molecular modeling studies of macrocycle **5** showed two possible conformations featuring C_2 and C_{2v} symmetry, respectively. X-ray crystallography of its 2:1 chloride complexes further confirmed this structural feature, using different tetraalkylammonium salts as anion sources (**Figure 7**).

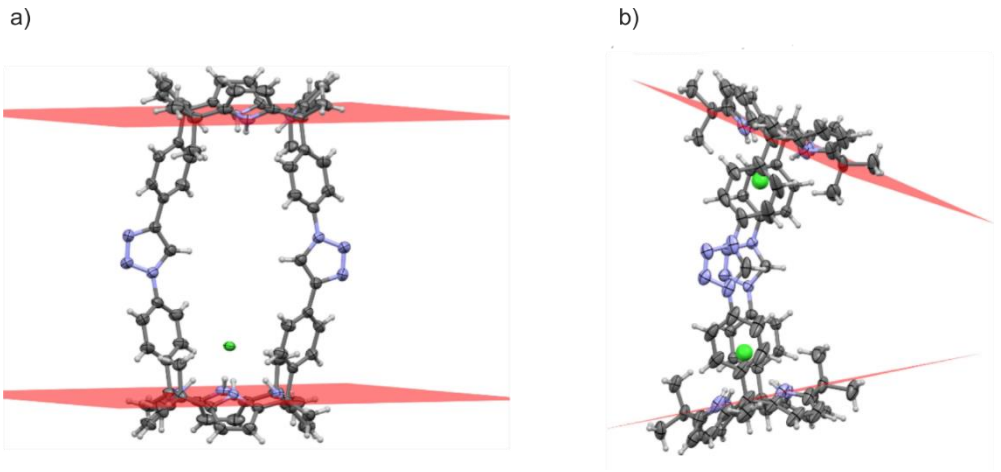

Figure 7. X-ray structures of the 1:1 complex of macrocycle **5** with MTOA·Cl (a) and 2:1 complex of macrocycle **5** with TBA·Cl (b). The structures show the two possible conformations that macrocycle **5** can adopt featuring C_2 and C_{2v} symmetry.

In close analogy to macrocycle **4**, using TBA^+ ion-pairs resulted in the formation of 2:1 complexes with receptor **5** displaying a cascade-like arrangement binding geometries. Unlike receptor **4**, we did not observe significant allosteric binding cooperativity in this case. In contrast, using $MTOA^+$ counterparts, the resulting receptor-separated 2:1 complexes showed a large negative cooperativity ($\alpha = 0.04$).

1.2.3 Mechanically interlocked receptors

The macrocycles described in the previous section were used for the design and synthesis of mechanically interlocked receptors providing unique environments for anions/ion-pairs recognition in solution.[31,32]

Building on the structure of bis-calix[4]pyrrole macrocycle **4**, our group reported the quantitative assembly of [2]pseudorotaxane-like complexes using tetrabutylammonium ion-pairs of polyatomic anions (i.e. cyanate or azide) and a ditopic linear *m*-bis-amide-pyridyl-*N*-oxide **6** axle (**Figure 8**). The binding of bidentate polyatomic anions, which were complementary in size and shape to the receptor's tridimensional binding site—where six NH hydrogen bond donors converge—led to the exclusive formation of four-particle interwoven assemblies with cyclic-component separated binding geometry.[28]

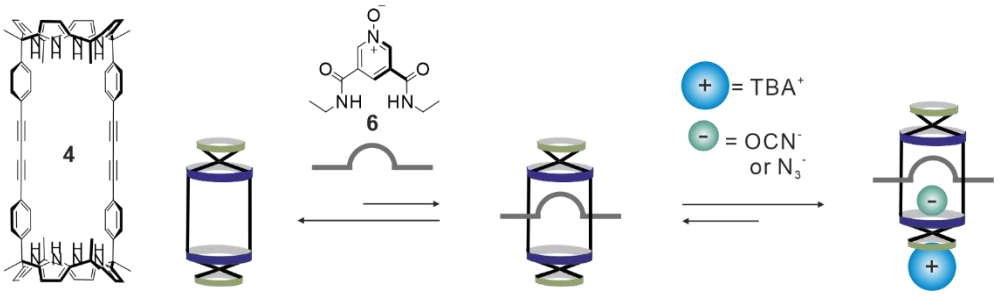

Figure 8. Two-steps quantitative self-assembly of [2]psedorotaxane like complexes.

Starting from the previous interpenetrated assembly, we prepared the corresponding [2]rotaxane **9** using an *in-situ* capping strategy via CuAAC reaction in DCM (**Figure 9**).[27] In chloroform solution, [2]rotaxane **9** formed thermodynamically and kinetically stable 1:1 ion-paired complexes with tetrabutylammonium (TBA^+) salts of both monoatomic (Cl^-) and polyatomic anions (NO_3^- and OCN^-). The binding selectivity of the [2]rotaxane in chloroform favored cyanate over chloride and nitrate anions. The change of TBA^+ cation for $MTOA^+$ in the chloride ion pair provoked an increase in the binding constants of almost three orders of magnitude. These results proved that **9** functioned as a heteroditopic receptor.

In acetone and chloroform/methanol solutions, [2]rotaxane **9** mainly acted as an anion receptor. In acetone, we determined larger binding constants for the studied anions than those previously reported in pure chloroform for the same receptor and ion-pairs.[33] Additionally, the binding selectivity displayed by rotaxane **9** in acetone was opposite to that determined in chloroform. In acetone, rotaxane **9** exhibited a

greater affinity for monoatomic chloride over polyatomic anions. These results were attributed to solvation/desolvation effects and the prevalence of the ion-dipole interactions in this solvent.

In chloroform/methanol mixtures we found that the studied anions had lower binding constants compared to those measured in pure chloroform. This was attributed to the strong competition of polar protic solvents for hydrogen bond interactions and their effectiveness in solvating anionic and cations species.

In acetone, the addition of more than one equivalent of TBA·OCN, TBA·Cl, or MTOA·Cl to a solution of rotaxane **9** led to the formation of 2:1 complexes. We proposed that in the 2:1 complex, two anions were bound to the opposite hemispheres of the bis-calix[4]pyrrole macrocycle. Additionally, the axle was displaced from the cavity, engaging in diverging hydrogen bond interactions between the amide groups and the anions. We did not observe this high stoichiometry species under the same conditions when working in chloroform/methanol mixtures.

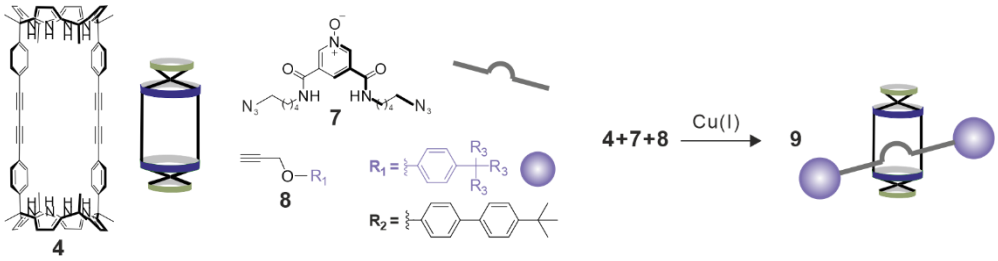

Figure 9. Cartoons and synthetic scheme for the preparation of [2]rotaxane **9** through in-situ capping strategy.

In summary, AE-C[4]Ps (**2a-f** and **3a-g**) and their tris-macrocyclic derivatives (**4** and **5**) are highly effective neutral receptors for anions and ion-pairs. Beyond these, interlocked receptor **9** forms rigid three-dimensional binding sites, where the polar groups from the interlocked components converge. The shape and size complementarity between the binding pocket of **9** and the anions mainly governed its selectivity for ion-pairs in non-polar solvents such as chloroform. However, in polar solvents solvation/desolvation effects play a crucial role in the magnitude of the binding constants of the anionic complexes.

1.3 AE-calix[4]pyrrole-based cages: a combination of confined cavity and endo-functionalization

Some synthetic molecular cages have the potential to mimic essential biological processes performed by enzymes such as molecular recognition[34] and catalysis.[35] Enzymes use polar functional groups to bind substrates and facilitate catalytic reactions. [36] Beyond these polar groups, enzyme active sites often contain hydrophobic pockets to create isolated environments for substrates, shielding them from bulk solvents and enhancing reaction efficiency.[37]

Nonspecific lipid-transfer proteins (ns-LTPs) are a class of cationic proteins found in plants, playing crucial roles in intracellular lipid shuttling during growth and reproduction. They are well-known for their capacity to bind and transport amphiphilic molecules across membranes, including phospholipids, glycolipids, and fatty acids. All ns-LTPs share a common structural motif based on eight cysteines stabilized by four disulfide bonds, and a large hydrophobic cavity in which lipids are bound. For example, wheat ns-LTP can effectively bind the fatty acid derivative prostaglandin B_2 (PGB_2) (**Figure 10**). [38] The phenol group pointing towards the hydrophobic cavity of ns-LTPs established a hydrogen bond interaction with the carboxylate group of the substrate PGB_2.

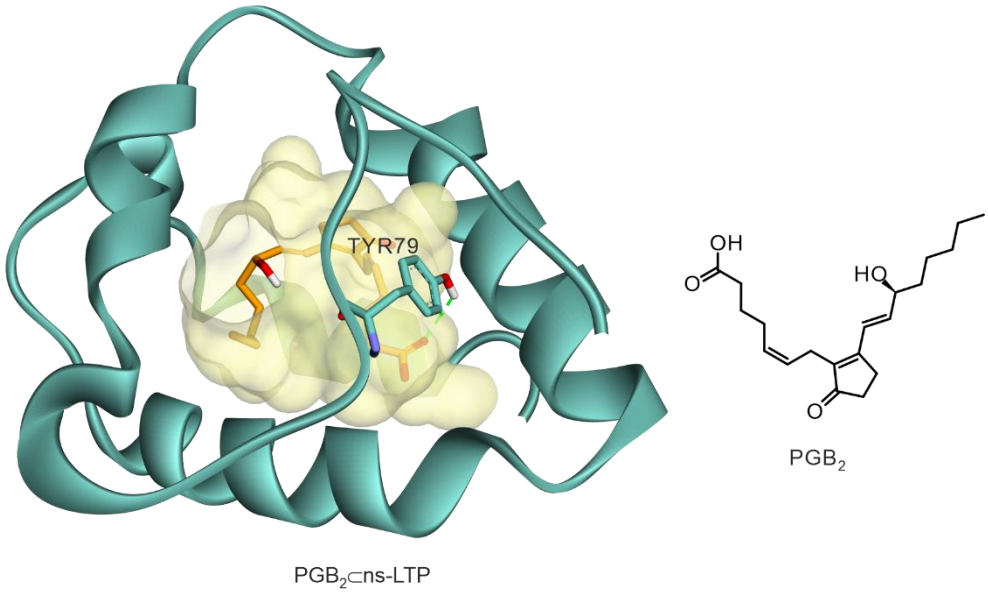

Figure 10. Left) Structure of wheat ns-LTP with bound prostaglandin B_2, adapted from pdf file reported in reference 38. The hydrophobic binding pocket is highlighted in yellow. Right) Molecular structure of PGB_2.

Synthetic molecular receptors aim to mimic the enzyme active sites by incorporating polar groups into their cavities. However, many synthetic endo-functionalized cages lack the essential hydrophobic or solvophobic cavities needed to fully isolate substrates from the surrounding solution. The absence of a defined binding pocket often limits their substrate recognition and catalysis efficiency.

In contrast, synthetic capsules and cages with confined cavities — yet lacking endo-functionalized groups — have shown advantages in stabilizing high-energy conformations[39,40,41] and reactive intermediates,[42,43,44] modulating reactivity, [45] and mediating reactions. However, they restrict their binding to non-polar guests with size and shape complementary to the cavity.

The main challenge is to develop synthetic molecular containers that integrate polar functional groups in an isolated hydrophobic microenvironment.

Among the various polar groups used in endo-functionalized synthetic cages — such as amides,[46] urea,[47] imines,[48] and triazole,[49] — pyrrole units[50] stand out as unique and particularly interesting for this PhD Thesis. In the following section, we will describe several pyrrole-based endo-functionalized cages for the binding of neutral polar molecules. We will focus our attention on AE-C[4]P-based cages combining well-defined hydrophobic cavities with inner polar groups for enhanced substrate recognition.

1.3.1 Pyrrole-based endo-functionalized cages for binding neutral polar molecules

Examples of endo-functionalized cages used for the binding of neutral polar molecules remain relatively rare. Most examples described in the literature focus on the binding of charged species (e.g. anion or cation binding). Among other reasons, this is due to the fact that electrostatic interactions between charged residues and polar groups are significantly stronger than dipole-dipole interactions that occur with neutral molecules. To date, only a few examples of pyrrole-based endo-functionalized cages have been reported for the recognition of neutral molecules.

In 2001, Beer and colleagues synthesized cryptand-like receptors **12a** and **12b** via [2+3] condensation of ethyl-triformylpyrrole **10** with ethylenediamine **11a** or butylenediamine **11b** (**Figure 11**).[51] These Schiff base-based receptors featured six converging hydrogen bond donors from pyrrole NH groups inwardly directed to the cavity. The X-ray structures of these cages showed one diamine molecule (used as linker) encapsulated in the cryptand receptor hydrogen bonded to four of the six pyrrole NHs. This result suggested the additional role of the diamine linker acting as a template in the self-assembly process. ^{1}H NMR titrations confirmed the binding of ethylenediamine **11a** and 1,2-ethanediol **13**, with receptor **12a** forming 1:1 inclusion complex with similar binding constants.

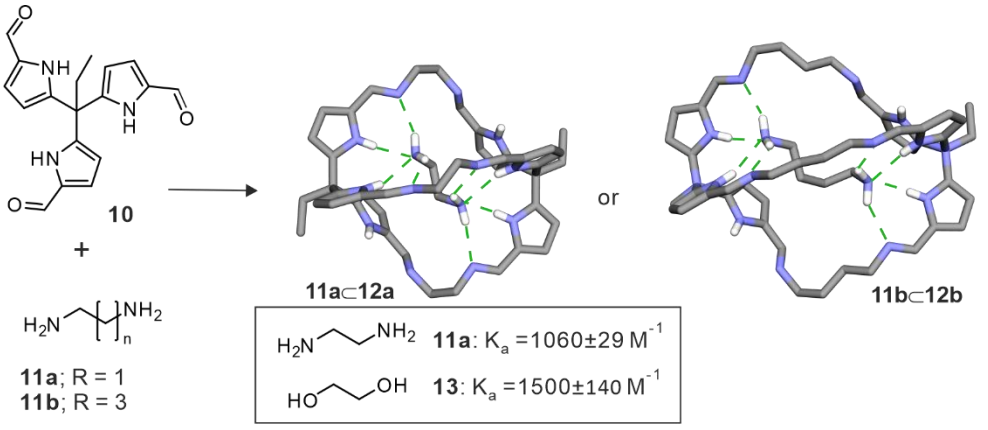

Figure 11. Synthetic scheme for preparing [2+3] hexa-imine hexa-pyrrole cryptands **12a** and **12b** for diamine recognition. Two X-ray structures (**11a⊂12a** and **11b⊂12b**) were adapted from ref. 51.

Another relevant example of a poly-pyrrolic cage used for neutral guest recognition was reported by Roelens and co-workers.[52] They investigated the binding of α- and

β-glucopyranosides using the cryptand-like cage structure **15**. The amine-based cage was obtained by reducing its parent imine counterpart **14** with $NaBH_4$ (**Figure 12**). X-ray crystallography of the amine cage **15** revealed a structure with C_{3h} symmetry, featuring a cavity with inwardly directed amine NH and pyrrole NH groups. The binding affinity of both the amine and imine cage for octyl-α-D-glucopyranoside **16a** and its β-isomer **16b** was evaluated in $CDCl_3$ solution. The polar cavity of the hexa-amine cage **15** selectively bound the β-glucopyranoside isomer **16b** over the α-counterpart **16a** in $CDCl_3$, with a binding constant of 10^4 M^{-1} for the **16b⊂15** complex. In contrast, hexa-imine cage **14**, did not show the same binding affinity for **16b**. Instead, the addition of **16b** induced the re-equilibration of dynamically covalent cage **14** to oligomeric products. Most likely the structural rigidity imposed by the imine bonds in cage **14**, hampers guest recognition. [53]

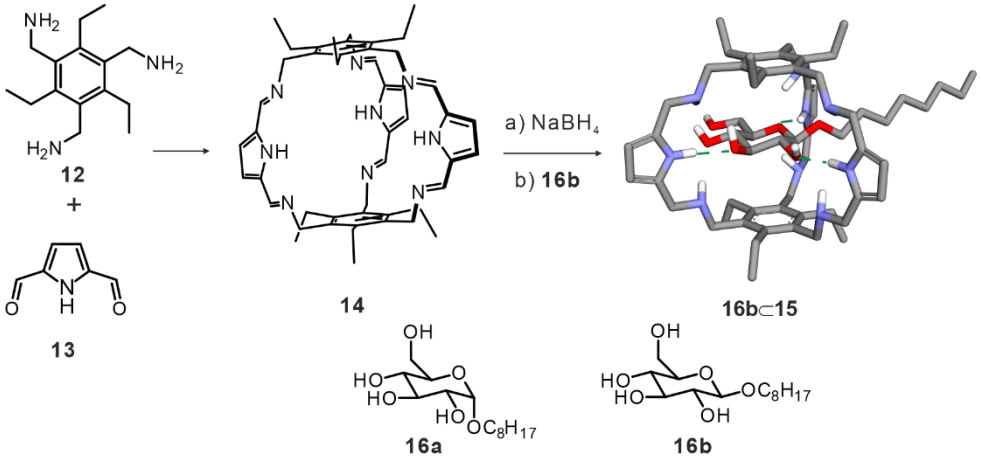

Figure 12. Synthetic scheme for the preparation of [2+3] hexa-imine tri-pyrrole cage **14** and its amine derivate **15** for β-glucopyranosides recognition studies.

These examples of pyrrole-based endo-functionalized cages **12a**, **12b**, **14**, and **15**, illustrate the challenges in isolating guests from bulk solutions for endo-functionalized cages. For both cases, Beer's and Roelens' cages, all the pyrrole units are oriented towards the cavity providing polar binding sites. This resulted in cages with large portals and poorly defined inner cavities.

1.3.2 AE-C[4]Ps-based cages for neutral guest recognition.

Our group described the first example of AE-C[4]P-based cage assembled via [2+4] imine condensation reaction of tetra-formyl aryl-extended calix[4]pyrrole **17** and 1,2-diamine linkers (**Figure 13**).[54]

4-(4-pyridinylethynyl)pyridine-*N*,*N*'-dioxide **18** was used as template**.** In chloroform and under strict stoichiometric control the bis-pyridyl-*N*-oxide ditopic guest **18** quantitatively forms 2:1 complex with AE-C[4]P **17** (**18**⊂(**17**)$_2$). The formation of this complex prevents the formation of polyimine non-capsular aggregates upon the addition of the diamine linker. Using ethylendiamine as linker produced a dissymmetric capsule obtained as a racemic mixture of M and P enantiomers. The chirality is imposed by the sense of rotation of the pairwise imine bonds. The use of enantiomerically pure (1R,2R)-(-)-1,2-diaminecyclohexane **19** as linker was expected to produce a diastereomeric mixture of M-(1R,2R) and P-(1R,2R) capsules. Notably, only one of the two diastereomers was observed in the X-ray crystal structure of the capsular construct. This result highlighted the existence of an unprecedented and efficient chirality transfer from the diamine linker to the cage assembly.

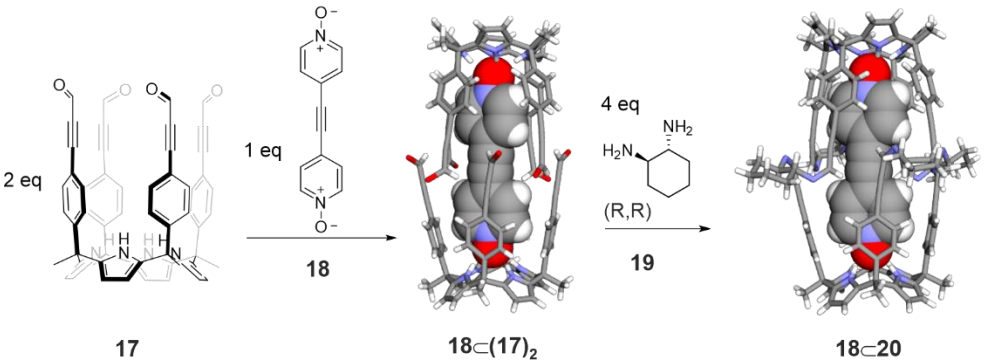

Figure 13. Synthetic scheme for the preparation of [2+4] octa-imine cage **20** assisted by ditopic guest **18**.

Metal coordination approaches have been also used to prepare calix[4]pyrrole-based cages with a well-defined polar cavity. We reported the self-assembly of a mono-metallic Pd(II)-coordination cage [**21**·Pd]$^{2+}$ in a $CDCl_3$: CD_3CN solvent mixture. The cage has two distinct polar binding sites converging to a well-defined aromatic cavity. One binding site is created by the four pyrrole NHs from the calix[4]pyrrole core unit. The other site consists of four inwardly directed α-CH protons of the pyridyl units installed at the upper rim of the SAE-C[4]P, which are coordinated to the Pd(II) center (**Figure 14a**).[55] We found that the efficient assembly of the cage

required the complementation of the hydrogen-bond needs of both opposed binding sites (e.g. two molecules of acetonitrile or suitably sized ditopic guest).

We investigated the reversible binding of mono- and di-topic planar *N*-oxide guests to cage [**21**·Pd]$^{2+}$ and their guest-exchange mechanisms. For "four-wall" AE-C[4]P and SAE-C[4]P-based unimolecular receptors we proposed that the guest exchange mechanism mainly goes through a conformational change of the calix[4]pyrrole core, from cone to alternate.

In these receptors, the rate of guest exchange is independent of the guest´s size. Nevertheless, in mono-metallic Pd(II)-cage [**21**·Pd]$^{2+}$, we proposed a "French doors" mechanism involving the rotation of the four meso-phenyl substituents, for the inclusion and exchange of planar pyridine *N*-oxide guests.

We described a change in this mechanism to accommodate sterically more demanding guests, such as quinuclidine *N*-oxide. In this particular case, a partial ligand-metal dissociation mechanism is required.[56]

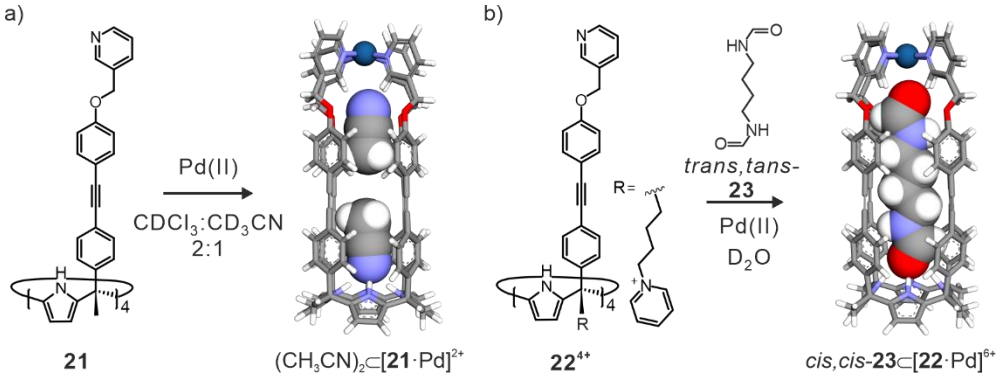

Figure 14. a) Self-assemble of mono-metallic Pd(II)-cage [**21**·Pd]$^{2+}$ in organic phase. B) Self-assembly of mono-metallic Pd(II)-cage *cis,cis*-**23⊂**[**22**·Pd]$^{6+}$ assisted by ditopic template **23** in water. In the energy minimized structure of the *cis,cis*-**23⊂**[**22**·Pd]$^{6+}$ is simplified by pruning the meso-alkyl groups into methyl groups.

The installation of four pyridinium groups at the lower rim of the previously described tetra-pyridyl SAE-C[4]P endowed the water-soluble, tetra-cationic tetra-pyridyl ligand **22**$^{4+}$.[57] The quantitative self-assembly of this coordination cage in water was facilitated by the presence of ditopic guests, such as diformamide **23** (**Figure 14b**). In solution, secondary amides are a mixture of *trans*- and *cis*-conformers. The *cis*-conformer can reach an extent of 10-20%. ^{1}H NMR spectroscopic studies revealed that cage [**22**·Pd]$^{6+}$ showed exquisite conformational

selectivity for the binding of diformamide guest *cis,cis*-**23**. While one end of the diformamide is always bound in *cis*-conformation upon inclusion in one of the calix[4]pyrrole hemispheres of the cage, the opposite end might be bound in the *cis*- or *trans*-forms depending on the length of the diformamide alkyl spacer and the best fit to the cavity's dimensions.

Recently, our group successfully self-assembled a [1+1] tetra-imine cage (**26**) from tetra-formyl AE-C[4]P **17** and tetra-aniline AE-C[4]P **24** (**Figure 15**).[58] The cage is self-assembled in the presence of bis-pyridyl-*N*,*N'*-dioxide with a ~65% yield. Moreover, we demonstrated that the bis-*N*-oxide template was not mandatory for the assembly. Tetra-imine cage **25** was assembled in pure chloroform, however, it required larger reaction times and higher temperatures and provided lower yields (~50%). However, using a 9:1 $CDCl_3$:CD_3CN solvent mixture to assemble the cage resulted in similar yields to those obtained using the bis-*N* oxide template (~65%). The acetonitrile molecules bind the calix[4]pyrrole core and pre-organize it in the cone conformation.

The self-assembly of the tetra-imine cage, including weakly bound solvent molecules promoted the study of its thermodynamic and kinetic binding properties with mono- and di-topic pyridine *N*-oxide guests. We found that the kinetics of inclusion processes were dependent on the nature of the included solvent molecules ($CDCl_3$ or CD_3CN) and the dimensions of the guests.

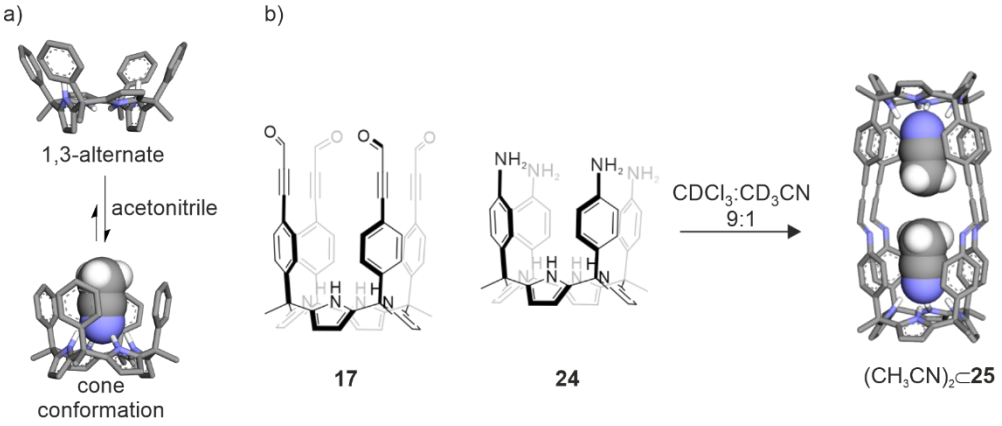

Figure 15. a) Conformational equilibrium of AE-C[4]P upon acetonitrile binding. b) [1+1] imine condensation reaction between **17** and **24** assisted by acetonitrile molecules.

1.4 Aims of the thesis

This thesis explores the design and synthesis of molecular receptors with endo-functionalized solvophobic cavities, specifically based on AE-C[4]P scaffolds. In particular, we will focus on three main topics: the synthesis and characterization of interlocked receptors, the self-assembly of polyimine cages, and the study of their applications in molecular recognition and mediation of chemical reactions.

To achieve these objectives, we pursue the following specific goals:

1) Synthesis of a neutral [2]rotaxane based on a bis(calix[4]pyrrole) macrocycle featuring binding selectivity for chloride and nitrate anions or ion-pairs.

In the introduction, we described that we previously reported a [2]rotaxane receptor based on a bis-calix[4]pyrrole macrocyclic component, and a bisamidepyridyl-*N*-oxide axle. This receptor exhibited selective binding for cyanate over nitrate and chloride in chloroform. We propose that using a structurally related interlocked structure featuring a distinct bis-calix[4]pyrrole macrocycle of reduced size we could increase its selectivity for smaller spherical or trigonal anions such as Cl^- or NO_3^-, respectively, over the larger cylindrical OCN^-. To characterize the binding properties of this new interlocked receptor we perform experiments in various solvents, including chloroform, acetone, and $CHCl_3$/MeOH mixtures, using ^{1}H NMR spectroscopy and isothermal titration calorimetry (ITC).

2) Self-Assembly of [4+2] and [1+1] Polyimine Dynamic Covalent Cages based on AE-C[4]P scaffolds.

Building on the synthesis of the previously reported [4+2] and [1+1] octa- and tetra-imine cages discussed in the introduction, we propose assembling analogous polyimine cages with larger cavities. The assembly of the previously described polyimine dynamic covalent cages was capricious. We aim to study the effect of adding catalytic amounts of Brønsted acid (e.g. acetic acid) on the reproducibility and yield of the condensation reaction for the new calix[4]pyrrole polyimine cages. We expect that the larger cavity of these new assemblies will allow the inclusion of larger guests and facilitate their application as molecular reactor vessels for the mediation of chemical reactions.

3) Evaluation of the Binding Properties of the Self-Assembled Poly-imine Cages with neutral guests.

We plan to study the binding properties of the self-assembled cage solvates with monotopic and ditopic pyridine *N*-oxides and diformamides guests, using ^{1}H NMR

spectroscopy and ITC experiments. The kinetics of guest inclusion and exchange will also be examined to gain insights into the binding/exchange mechanisms.

4) Study of Huisgen Cycloaddition Reactions Mediated by self-assembled Polyimine Cages.

We will evaluate the potential of the self-assembled polyimine cages to mediate 1,3-dipolar cycloaddition reactions. We plan to prepare azido and ethynyl-derived pyridine *N*-oxide derivatives that can simultaneously bind the cavity of the polyimine cages. We aim to investigate how the confined environment influences the reaction rate (i.e. acceleration) and regioselectivity.

1.5 Outline of the thesis

This doctoral thesis is organized into six chapters: an introduction (**Chapter 1**), five chapters including the results and discussion of the research findings (**Chapters 2–6**), and finally, a chapter dedicated to general conclusions summarizing the outcomes and significance of the work.

Chapter 1 provides an overview of the fundamental concepts relevant to the research topics explored in this thesis, particularly on the use of aryl-extended calix[4]pyrrole scaffolds in the design of molecular receptors. Key achievements from prior studies, which lay the foundation for the current work, are briefly outlined. Each of the following chapters (Chapters 2–6) is also accompanied by its own introduction, offering a more specific background related to the discussed research.

Chapter 2 describes the synthesis and characterization of a [2]rotaxane receptor incorporating a bis-calix[4]pyrrole macrocycle featuring two distinct binding sites. This chapter explores the binding affinity and selectivity of the rotaxane receptor for a series of tetraalkylammonium ion pairs. The thermodynamic properties of the binding processes are investigated using different solvents.

Chapter 3 discusses the self-assembly of [2+4] octa-imine cages formed via an eight-fold condensation reaction between two aryl-extended tetra-amino calix[4]pyrrole units and four aldehyde linkers in a 9:1 $CDCl_3$:CD_3CN solvent mixture. Acetonitrile is used as a template to pre-organize the AE-C[4]P units into the cone conformation, favoring the formation of the thermodynamically favored cages. The addition of Brønsted acids such as acetic acid, is evaluated for the quantitative assembly of the cages. The inclusion of weakly-bound acetonitrile molecules in the cages' cavity facilitates its application as molecular receptors and reaction vessels.

Chapter 4 focuses on the binding studies of a shape-persistent [4+2] octa-imine cage with various homologous diformamide guests. The host's conformational selectivity for different isomers of diformamide mixtures is examined, and the thermodynamic stability of the resulting inclusion complexes is compared. Additionally, the kinetics of guest exchange are discussed, providing insights into the dynamic behavior of the cage-guest systems.

Chapter 5 explores the binding properties of a [4+2] octa-imine cage with several p-substituted pyridine *N*-oxides and *N*-substituted 4-pyridones containing terminal ethynyl and azido groups. The octa-imine cage is used as a reaction vessel to

mediate the 1,3-dipolar cycloaddition (Huisgen cycloaddition) between azido- and ethynyl-derived pyridine *N*-oxides and 4-pyridone guests co-included within the cavity. The optimal preorganization of the reacting groups of the bound substrates is shown to enhance the reaction rate and provide regioselectivity towards the 1,4-disubstituted triazole isomer.

Finally, **Chapter 6** describes the self-assembly of a [1+1] tetra-imine cage based on two different calix[4]pyrrole units. The resulting cage features a cylindrical cavity slightly larger than the [4+2] octa-imine cages discussed in previous chapters. Similarly to **Chapter 5**, we described the potential of this endo-functionalized cavity to mediate the intramolecular Huisgen cycloaddition reaction. The influence of cavity size on reaction acceleration is also analyzed, providing further insights into the role of confined spaces in accelerating chemical transformations.

1.6 References and notes

[1] Mulugeta, E.; He, Q.; Sareen, D.; Hong, S.-J.; Oh, J. H.; Lynch, V. M.; Sessler, J. L.; Kim, S. K.; Lee, C.-H., *Chem* **2017,** *3* (6), 1008-1020.
[2] Sierra, A. F.; Hernández-Alonso, D.; Romero, M. A.; González-Delgado, J. A.; Pischel, U.; Ballester, P., *J. Am. Chem. Soc.* **2020,** *142* (9), 4276-4284.
[3] Sierra, A. F.; Aragay, G.; Peñuelas-Haro, G.; Ballester, P., *Org. Chem. Front.* **2021,** *8* (11), 2402-2412.
[4] Kim, D. S.; Sessler, J. L., *Chem. Soc. Rev.* **2015,** *44* (2), 532-546.
[5] Martínez-Crespo, L.; Sun-Wang, J. L.; Sierra, A. F.; Aragay, G.; Errasti-Murugarren, E.; Bartoccioni, P.; Palacín, M.; Ballester, P., *Chem* **2020,** *6* (11), 3054-3070.
[6] Gale, P. A., *Chem* **2020,** *6* (11), 2873-2875.
[7] Martínez-Crespo, L.; Sun-Wang, J. L.; Ferreira, P.; Mirabella, C. F. M.; Aragay, G.; Ballester, P., *Chem. Eur. J.* **2019,** *25* (18), 4775-4781.
[8] Wang, X.; Xie, L.; Lin, K.; Ma, W.; Zhao, T.; Ji, X.; Alyami, M.; Khashab, N. M.; Wang, H.; Sessler, J. L., *Angew. Chem., Int. Ed.* **2021,** *60* (13), 7188-7196.
[9] Chen, D.; Luo, D.; He, Y.; Tian, J.; Yu, Y.; Wang, H.; Sessler, J. L.; Chi, X., *J. Am. Chem. Soc.* **2022,** *144* (37), 16755-16760.
[10] Xie, L.; Zheng, Z.; Lin, Q.; Zhou, H.; Ji, X.; Sessler, J. L.; Wang, H., *Angew. Chem., Int. Ed.* **2022,** *61* (1), e202113724.
[11] Wang, H.; Jones, L. O.; Hwang, I.; Allen, M. J.; Tao, D.; Lynch, V. M.; Freeman, B. D.; Khashab, N. M.; Schatz, G. C.; Page, Z. A.; Sessler, J. L., *J. Am. Chem. Soc.* **2021,** *143* (48), 20403-20410.
[12] Baeyer, A., *Ber. Dtsch. Chem. Ges.* **1886,** *19* (2), 2184-2185.
[13] Gale, P. A.; Sessler, J. L.; Král, V.; Lynch, V., *J. Am. Chem. Soc.* **1996,** *118* (21), 5140-5141.
[14] Díaz-Moscoso, A.; Hernández-Alonso, D.; Escobar, L.; Arroyave, F. A.; Ballester, P., *Org. Lett.* **2017,** *19* (1), 226-229.
[15] Anzenbacher, P.; Jursíková, K.; Lynch, V. M.; Gale, P. A.; Sessler, J. L., *J. Am. Chem. Soc.* **1999,** *121* (47), 11020-11021.
[16] Gil-Ramírez, G.; Escudero-Adán, E. C.; Benet-Buchholz, J.; Ballester, P., *Angew. Chem., Int. Ed.* **2008,** *47* (22), 4114-4118.
[17] Aragay, G.; Hernández, D.; Verdejo, B.; Escudero-Adán, E. C.; Martínez, M.; Ballester, P., *Molecules* **2015,** *20* (9), 16672-16686.
[18] Bruno, G.; Cafeo, G.; Kohnke, F. H.; Nicolò, F., *Tetrahedron* **2007,** *63* (40), 10003-10010.
[19] Escobar, L.; Aragay, G.; Ballester, P., *Chem. Eur. J.* **2016,** *22* (38), 13682-13689.
[20] Custelcean, R.; Delmau, L. H.; Moyer, B. A.; Sessler, J. L.; Cho, W.-S.; Gross, D.; Bates, G. W.; Brooks, S. J.; Light, M. E.; Gale, P. A., *Angew. Chem., Int. Ed.* **2005,** *44* (17), 2537-2542.
[21] Gross, D. E.; Schmidtchen, F. P.; Antonius, W.; Gale, P. A.; Lynch, V. M.; Sessler, J. L., *Chem. Eur. J.* **2008,** *14* (26), 7822-7827.
[22] Gil-Ramírez, G.; Escudero-Adán, E. C.; Benet-Buchholz, J.; Ballester, P., *Angew. Chem., Int. Ed.* **2008,** *47* (22), 4114-4118.
[23] Adriaenssens, L.; Gil-Ramírez, G.; Frontera, A.; Quiñonero, D.; Escudero-Adán, E. C.; Ballester, P., *J. Am. Chem. Soc.* **2014,** *136* (8), 3208-3218.

[24] Adriaenssens, L.; Estarellas, C.; Vargas Jentzsch, A.; Martinez Belmonte, M.; Matile, S.; Ballester, P., *J. Am. Chem. Soc.* **2013,** *135* (22), 8324-8330.
[25] Sessler, J. L.; Gross, D. E.; Cho, W.-S.; Lynch, V. M.; Schmidtchen, F. P.; Bates, G. W.; Light, M. E.; Gale, P. A., *J. Am. Chem. Soc.* **2006,** *128* (37), 12281-12288.
[26] Gross, D. E.; Schmidtchen, F. P.; Antonius, W.; Gale, P. A.; Lynch, V. M.; Sessler, J. L., *Chem. Eur. J.* **2008,** *14* (26), 7822-7827.
[27] Romero, J. R.; Aragay, G.; Ballester, P., *Chem. Sci.* **2017,** *8* (1), 491-498.
[28] Valderrey, V.; Escudero-Adán, E. C.; Ballester, P., *J. Am. Chem. Soc.* **2012,** *134* (26), 10733-10736.
[29] Valderrey, V.; Escudero-Adán, E. C.; Ballester, P., *Angew. Chem., Int. Ed.* **2013,** *52* (27), 6898-6902.
[30] Molina-Muriel, R.; Aragay, G.; Escudero-Adán, E. C.; Ballester, P., *J. Org. Chem.* **2018,** *83* (21), 13507-13514.
[31] van Dongen, S. F. M.; Cantekin, S.; Elemans, J. A. A. W.; Rowan, A. E.; Nolte, R. J. M., *Chem. Soc. Rev.* **2014,** *43* (1), 99-122.
[32] Langton, M. J.; Beer, P. D., *Acc. Chem. Res.* **2014,** *47* (7), 1935-1949.
[33] Molina-Muriel, R.; Romero, J. R.; Li, Y.; Aragay, G.; Ballester, P., *Org. Biomol. Chem.* **2021,** *19* (45), 9986-9995.
[34] Dong, J.; Davis, A. P., *Angew. Chem., Int. Ed.* **2021,** *60* (15), 8035-8048.
[35] Yoshizawa, M.; Klosterman, J. K.; Fujita, M., *Angew. Chem., Int. Ed.* **2009,** *48* (19), 3418-3438.
[36] Liu, S.; Li, S.; Shen, G.; Sukumar, N.; Krezel, A. M.; Li, W., *Science* **2021,** *371* (6524), eabc5667.
[37] Wu, M.-C.; Yow Tsong, T., *J. Phys. Soc. Jpn.* **2013,** *82* (11), 114801.
[38] Tassin-Moindrot, S.; Caille, A.; Douliez, J.-P.; Marion, D.; Vovelle, F., *Eur. J. Biochem.* **2000,** *267* (4), 1117-1124.
[39] Trembleau, L.; Rebek, J., *Science* **2003,** *301* (5637), 1219-1220.
[40] Tashiro, S.; Kobayashi, M.; Fujita, M., *J. Am. Chem. Soc.* **2006,** *128* (29), 9280-9281.
[41] Tashiro, S.; Tominaga, M.; Yamaguchi, Y.; Kato, K.; Fujita, M., *Angew. Chem., Int. Ed.* **2006,** *45* (2), 241-244.
[42] Yoshizawa, M.; Kusukawa, T.; Fujita, M.; Yamaguchi, K., *J. Am. Chem. Soc.* **2000,** *122* (26), 6311-6312.
[43] Yoshizawa, M.; Kusukawa, T.; Fujita, M.; Sakamoto, S.; Yamaguchi, K., *J. Am. Chem. Soc.* **2001,** *123* (43), 10454-10459.
[44] Restorp, P.; Rebek, J., Jr., *J. Am. Chem. Soc.* **2008,** *130* (36), 11850-11851.
[45] Breiner, B.; Clegg, J. K.; Nitschke, J. R., *Chem. Sci.* **2011,** *2* (1), 51-56.
[46] Bhat, A. S.; Elbert, S. M.; Zhang, W.-S.; Rominger, F.; Dieckmann, M.; Schröder, R. R.; Mastalerz, M., *Angew. Chem., Int. Ed.* **2019,** *58* (26), 8819-8823.
[47] Jing, L.; Deplazes, E.; Clegg, J. K.; Wu, X., *Nature Chem.* **2024,** *16* (3), 335-342.
[48] Acharyya, K.; Mukherjee, P. S., *Angew. Chem., Int. Ed.* **2019,** *58* (26), 8640-8653.
[49] Liu, Y.; Zhao, W.; Chen, C.-H.; Flood, A. H., *Science* **2019,** *365* (6449), 159-161.
[50] Wang, F.; Bucher, C.; He, Q.; Jana, A.; Sessler, J. L., *Acc. Chem. Res.* **2022,** *55* (12), 1646-1658.
[51] Fox, O. D.; Rolls, T. D.; Drew, M. G. B.; Beer, P. D., *Chem. Commun.* **2001,** (17), 1632-1633.

[52] Francesconi, O.; Ienco, A.; Moneti, G.; Nativi, C.; Roelens, S., *Angew. Chem., Int. Ed.* **2006,** *45* (40), 6693-6696.
[53] Francesconi, O.; Gentili, M.; Roelens, S., *J. Org. Chem.* **2012,** *77* (17), 7548-7554.
[54] Galán, A.; Escudero-Adán, E. C.; Ballester, P., *Chem. Sci.* **2017,** *8* (11), 7746-7750.
[55] Escobar, L.; Villarón, D.; Escudero-Adán, E. C.; Ballester, P., *Chem. Commun.* **2019,** *55* (5), 604-607.
[56] Escobar, L.; Escudero-Adán, E. C.; Ballester, P., *Angew. Chem., Int. Ed.* **2019,** *58* (45), 16105-16109.
[57] Sun, Q.; Escobar, L.; de Jong, J.; Ballester, P., *Chem. Sci.* **2021,** *12* (40), 13469-13476.
[58] Mirabella, C. F. M.; Aragay, G.; Ballester, P., *Chem. Sci.* **2023,** *14* (1), 186-195.

Chapter 2

Selective binding of nitrate by a neutral bis-calix[4]pyrrole [2]rotaxane

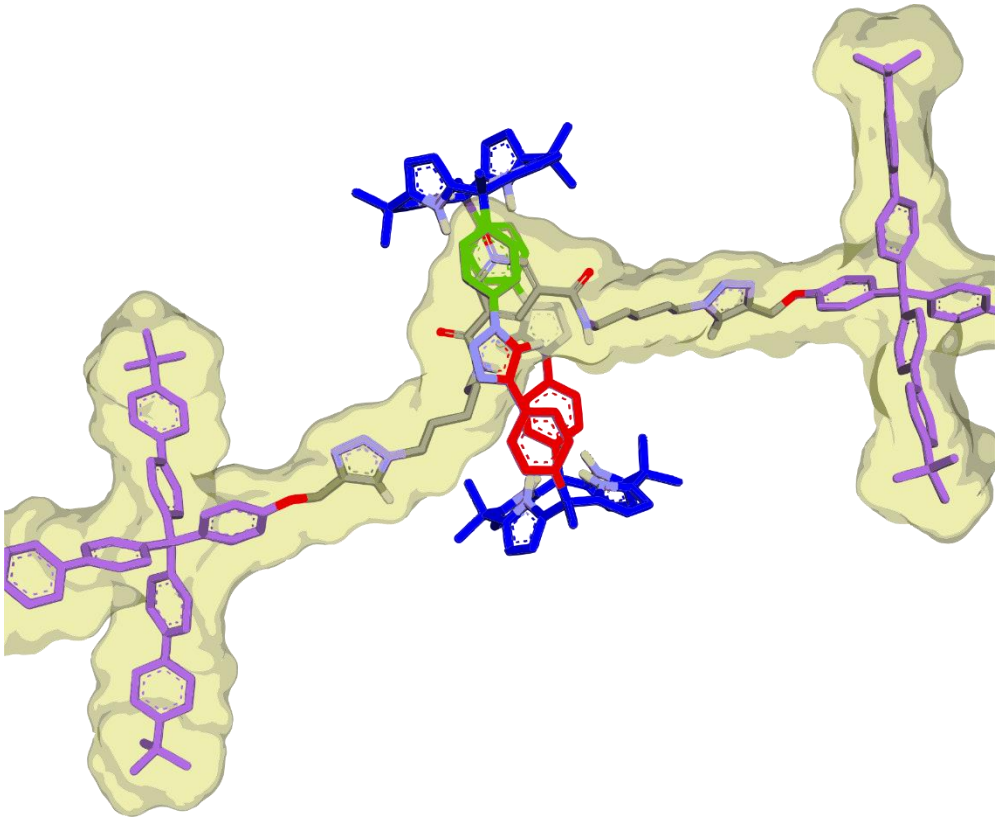

Part of this Chapter has been published in:

Y.Li, R. Molina-Muriel, G. Aragay, P. Ballester. *Org. Chem. Front.*, **2024**, *11*, 5374-5384

UNIVERSITAT ROVIRA I VIRGILI
Receptors based on Aryl-extended Calix[4]pyrrole Scaffolds
Yifan Li

2.1 Introduction

The widespread occurrence of anions in the environment and their essential role in biological processes have generated increasing interest in developing synthetic receptors capable of selectively binding to these negatively charged species.[1]

In this field, mechanically interlocked molecular hosts like rotaxanes and catenanes have demonstrated the ability to form polar cavities suitable for anion binding, offering superior binding selectivity and affinity compared to non-interlocked analogs.[2] The interlocked architecture creates three-dimensional solvophobic binding sites, where polar functional groups within the molecular structure converge and are partially shielded from solvent interactions. Some of these receptors rely solely on hydrogen or halogen bonding groups for anion binding,[3] though combining both types of bonds[4] produces a synergistic effect,[5] further stabilizing the resulting anionic complexes.

Numerous studies in the literature report that mechanically interlocked receptors often exhibit a preference for binding halides over oxo-anions.[3,6] This is likely due to the larger size, higher solvation energies, and distinct binding geometries of oxo-anions compared to halides.[7],[8] It is also notable that positively charged receptors generally show stronger anion-binding affinities than their neutral counterparts, although their selectivity is frequently diminished by direct charge–charge (Coulombic) interactions.[9]

Beer and colleagues reported a neutral indolocarbazole [2]rotaxane receptor that exhibited a preference for binding sulfate (4518 M^{-1}), acetate (2359 M^{-1}), and dihydrogen phosphate (2049 M^{-1}) over halides (142–739 M^{-1}) and nitrate (<100 M^{-1}) (**Figure 1**). All complexes displayed 1:1 binding stoichiometry in a solvent mixture of 95:5 acetone and water.[10] The observed selectivity was attributed to the relative basicity and size of the anions. Additionally, the hydrogen bonding pattern within the three-dimensional interlocked structure of the receptor's binding pocket influenced the geometric and functional complementarity between the anions and the receptor. The study also noted the formation of higher-order aggregates, specifically 2:1 complexes, during the titration of the [2]rotaxane with the tetrahedral sulfate dianion in the same solvent mixture.

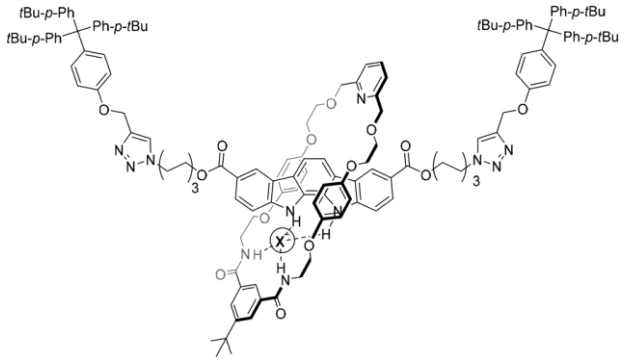

Figure 1. Anionic complex of the indolocarbazole containing [2]rotaxane described by Beer and co-workers.

No examples of neutral rotaxane receptors that exhibit binding selectivity for the environmentally significant nitrate anion have been reported in the literature. In line with this, some years ago, we described the synthesis and binding properties of the neutral [2]rotaxane **1**, which features a bis-calix[4]pyrrole cyclic component with two identical hemispheres and a 3,5-bis-amidepyridyl-*N*-oxide axle (**Figure 2**).[11] In chloroform solution, [2]rotaxane **1** functioned as a heteroditopic receptor, binding tetrabutylammonium (TBA) salts of both monoatomic (Cl^-) and polyatomic anions (NO_3^- or OCN^-). These complexes exhibited a ternary (1:1:1) ion-paired neutral nature, displaying receptor-separated binding geometry and exceptional kinetic and thermodynamic stability. In chloroform, [2]rotaxane **1** showed a preference for cyanate over chloride and nitrate anions. However, a few years later, we reported a reversal in its binding selectivity in acetone solution.[12] In this case, [2]rotaxane **1** showed stronger binding to the monoatomic chloride anion compared to polyatomic nitrate and cyanate. This change was attributed to the formation of predominantly 1:1 anionic complexes in acetone and the significance of ion–dipole interactions in their stabilization. Furthermore, in acetone, the addition of more than one equivalent of Cl^- or OCN^- to the solution of **1** led to the formation of 2:1 complexes, each containing two bound anions.

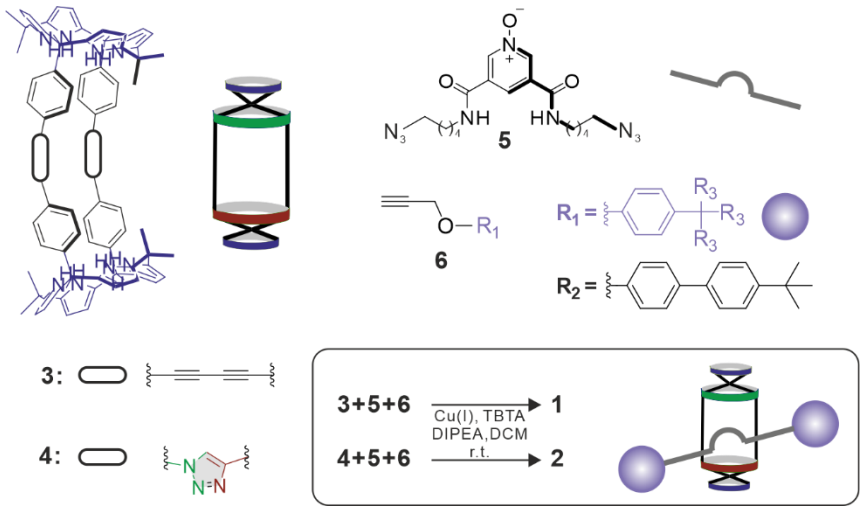

Figure 2. Line-drawing structures of the bis-calix[4]pyrrole macrocycles **3** and **4**, 3,5-bis-amidepyridyl-*N*-oxide axle **5**, and stopper **6**. The schematic representations of **5** and **6** and the cartoons for macrocycle **4** and rotaxane **2** are also indicated. In the cartoons, we use a color code to differentiate the two binding sites: the *N*-substituted hemisphere is represented with green color and the *C*-substituted counterpart in garnet color. Inset: synthetic scheme for the preparation of [2]rotaxanes **1** and **2**. The included cartoon represents rotaxane **2** featuring two chemically non-equivalent hemispheres.

Building on the previous findings, we set out to explore the potential for achieving nitrate binding selectivity with a structurally related interlocked system. For this purpose, we designed [2]rotaxane **2**, which utilizes the same 3,5-bis-amidepyridyl-*N*-oxide axle but incorporates a different macrocyclic unit. We replaced the bis(calix[4]pyrrole) macrocycle **3**, featuring 1,3-butadiynyl spacers, with the previously described bis(calix[4]pyrrole) **4**, which contains 1,4-substituted 1,2,3-triazole spacers (**Figure 2**). Macrocycle **4** has a shorter distance between its two C[4]P binding sites compared to macrocycle **3** ($d_{(Npy–Npy)}$: 14.5 Å vs. 16.2 Å). We hypothesized that reducing the size of the macrocyclic component in [2]rotaxane **2** would enhance its binding selectivity for smaller spherical or trigonal anions (e.g., Cl^- and NO_3^-) over the larger, cylindrical OCN^-.

In this chapter, we report the synthesis and characterization of the neutral [2]rotaxane **2**. We also disclose the binding properties of the new interlocked receptor **2** with tetraalkylammonium salts, both in acetone and chloroform solutions. Finally, we compare the obtained results with those previously reported for [2]rotaxane **1**.

2.2 Results and discussion

2.2.1 Synthesis

The synthesis of the molecular components for [2]rotaxane **2**—namely macrocycle **4**, the 3,5-bis-amidepyridyl-*N*-oxide axle (linear component **5**), and stopper **6**—was accomplished using previously reported procedures from the literature.[11,13]

[2]Rotaxane **2** was assembled through an "in situ" capping strategy, utilizing a copper(I)-catalyzed azide–alkyne cycloaddition reaction (CuAAC) between the pre-assembled [2]pseudorotaxane complex **5@4** and the alkyne-containing stopper **6**. After purification by column chromatography, [2]rotaxane **2** was obtained as a brownish solid with a 10% yield. The structure of [2]rotaxane **2** was fully characterized using a complete set of high-resolution analytical techniques, including 1D and 2D NMR spectroscopy and HRMS (**Figure 8-11** in experimental section).

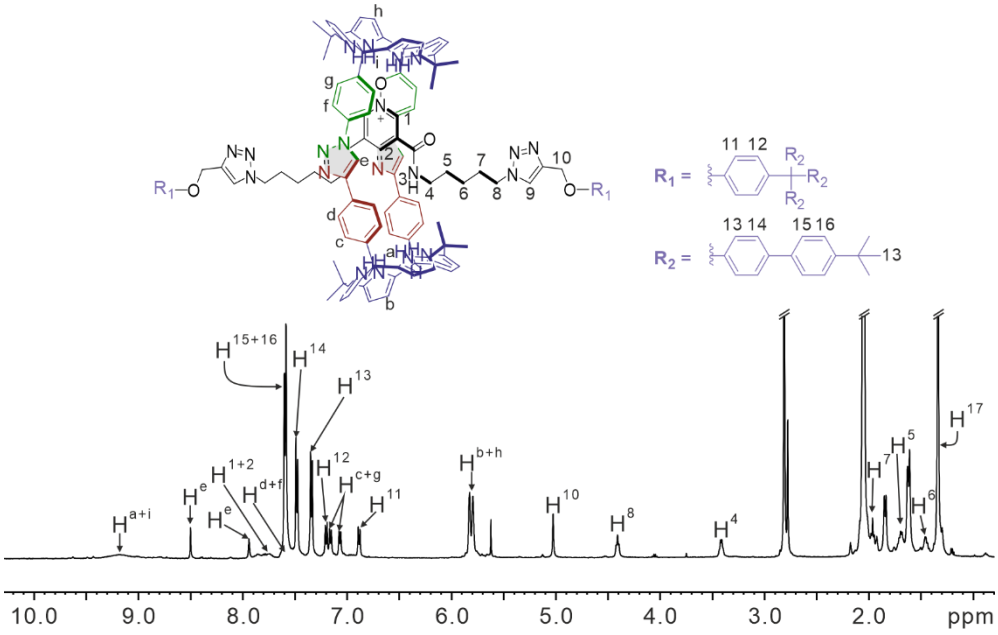

Figure 3. (Top) Molecular structure of rotaxane **2** used in this work. The C_2 symmetry conformation of the macrocycle is shown. (Bottom) ^{1}H NMR spectrum (400 MHz, 298, $(CD_3)_2CO$) of rotaxane **2** with the corresponding proton assignment.

The ^{1}H NMR spectrum of [2]rotaxane **2** in $CDCl_3$ displayed sharp, well-defined signals for most of the protons from both its molecular components (i.e., the macrocycle and axle) (**Figure 8**). Although some overlap occurred with the aromatic protons from the tris(biphenyl) stoppers on the axle, most signals could be assigned.

Notably, the signal corresponding to the pyrrole NHs (H^{a+i}) appeared as a single broad peak at δ = 9.1 ppm, a significant downfield shift compared to the two distinct signals observed for the NHs (δ = 6.8 and 6.9 ppm) in the free macrocycle **4**'s chemically different hemispheres. This downfield shift indicated that the pyrrole NHs in [2]rotaxane **2** were participating in hydrogen bonding interactions with the oxygen atom of the pyridine *N*-oxide group on the axle. Additionally, the single broad signal for the pyrrole NHs in the macrocycle's chemically non-equivalent hemispheres suggested a fast chemical exchange process on the ^{1}H NMR timescale, likely due to the pirouetting of the bound *N*-oxide group between the two binding sites of the macrocyclic component.

Notably, the ^{1}H NMR spectrum of [2]rotaxane **2** in $(CD_3)_2CO$ showed a reduction in signal overlap (**Figure 3**), with a sharp singlet at δ = 7.9 ppm assigned to the triazole proton (H^9) of the axle, confirming the covalent linkage between the 3,5-bis-amidepyridyl-*N*-oxide axle **5** and the two tris(biphenyl) stoppers **6**. Furthermore, a DOSY ^{1}H NMR experiment conducted with a 2 mM solution of [2]rotaxane 2 in $CDCl_3$ revealed that both molecular components shared the same diffusion coefficients (**Figure 10**, $D = 3.38 \pm 0.1 \times 10^{-10}$ m^2 s^{-1}), despite their size differences, confirming their involvement in the same interlocked species, [2]rotaxane **2**.

Molecular modeling studies indicated that the cyclic component of [2]rotaxane **2** can adopt two distinct conformations, exhibiting either C_s or C_2 symmetry (**Figure 12**). Previously, we observed both conformations in the X-ray structures of 2:1 chloride complexes of macrocycle **4**, formed with different tetraalkylammonium salts as anion precursors. In the C_s conformation, the angle between the two planes defined by the meso-carbon atoms of the two calix[4]pyrrole hemispheres of **4** was approximately 35.6°. In contrast, the C_2 conformation showed these two planes aligned in a parallel orientation (0°). The number of signals observed in the ^{1}H NMR spectrum of [2]rotaxane **2** corresponds to a time-averaged C_2 symmetric structure, suggesting that the cyclic component likely favors the C_2 symmetric conformation. Simultaneously, the pyridine *N*-oxide axle appears to undergo rapid chemical exchange between the two chemically distinct hemispheres. However, it cannot be excluded that both C_s and C_2 conformations of the macrocycle coexist in solution, undergoing fast exchange on the ^{1}H NMR timescale.

2.2.2 Binding studies of [2]rotaxane in Chloroform solution.

We began by investigating the interaction of [2]rotaxane **2** with tetraalkylammonium chloride salts, specifically **7a** (TBA·Cl) and **7b** (MTOA·Cl) (see **Figure 4** for structures), in chloroform solution through ^{1}H NMR titration experiments. We hypothesized that chloride binding to [2]rotaxane **2** could result in the formation of two isomeric 1:1 inclusion complexes. These two complexes would differ based on the positioning of the bound anion and the pyridine *N*-oxide group relative to the two chemically distinct hemispheres of the macrocyclic component of **2** (represented by the *N*- or *C*-substituted hemispheres, shown in green and garnet in **Figure 2–4**).

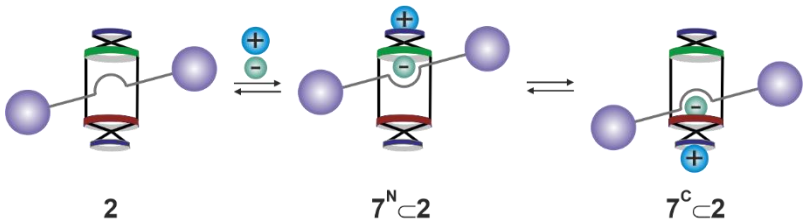

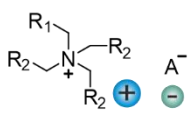

7a; A^- =Cl^-; R_1=R_2=*n*-C_3H_7
7b; A^- =Cl^-; R_1=H; R_2=*n*-C_7H_{15}
7c; A^- =NO_3^-; R_1=R_2=*n*-C_3H_7
7d; A^- =OCN^-; R_1=R_2=*n*-C_3H_7

Figure 4. Schematic cartoon of the binding equilibria of [2]rotaxane **2** with tetraalkylammonium ion-pairs **7a**–**7d** in chloroform to form the two isomeric 1 : 1 complexes.

In our previous work, we found that macrocycle **4** exhibited site selectivity when binding chloride, with the anion preferentially binding in the hemisphere containing the *N*-substituted meso-phenyl groups.[13] We aimed to determine if this selectivity was preserved in the chloride complex of [2]rotaxane **2**.

Upon adding 0.5 equiv. of TBA·Cl (**7a**) to a 2 mM solution of [2]rotaxane **2** in $CDCl_3$, two new sets of proton signals for the interlocked receptor were observed. The presence of separate signals for the free and bound receptor indicated that the binding equilibrium was slow on the ^{1}H NMR chemical shift timescale. When 1 equiv. of TBA·Cl (**7a**) was added, only the signals corresponding to the bound receptor were detected, and further additions (up to 2 equiv.) did not result in significant changes in the proton signals (**Figure 13**).

Notably, two pairs of signals of varying intensities appeared in the most downfield region of the spectrum. We attributed these to the pyrrole NHs of the bound receptor in the two possible isomeric chloride complexes (each pair consisting of H^i and H^a signals of the same intensity; **Figure 5** bottom). The pronounced and distinct downfield shifts for the pyrrole NHs in each complex suggested their involvement in hydrogen bonding interactions with two different acceptors: the chloride anion ($\Delta\delta NH_{(free\text{-}bound)}$ = −(1.4–1.5) ppm) and the oxygen atom of the *N*-oxide group ($\Delta\delta NH_{(free\text{-}bound)}$ = −(0.6–0.8) ppm). In summary, the chloride anion is bound within one calix[4]pyrrole hemisphere (either *N*- or *C*-substituted) via four hydrogen bonds from the converging pyrrole NH protons, while the *N*-oxide oxygen is hydrogen-bonded to the opposite hemisphere. The bound complex likely adopts a C_2 symmetry, with the two calix[4]pyrrole binding sites aligned in a parallel orientation (*vide infra*).

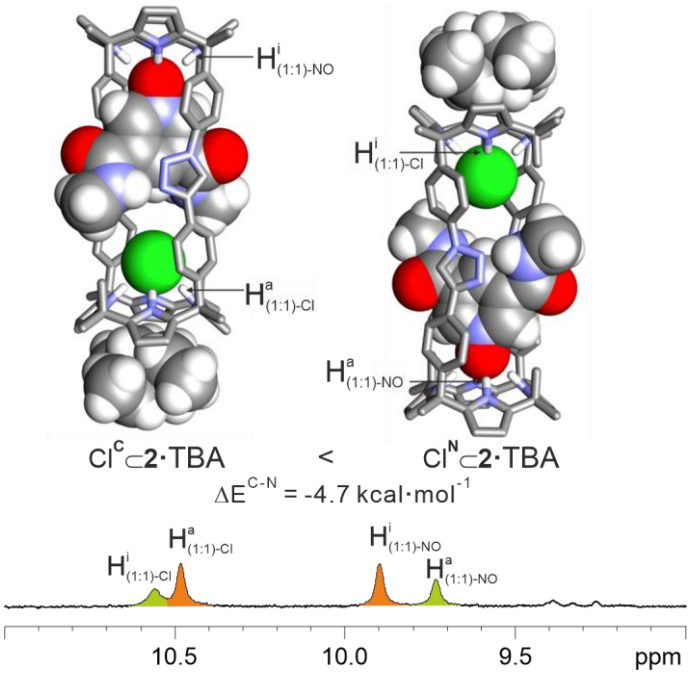

Figure 5. (Top) Energy-minimized structures (RI-BP86-D3BJ/def2-SVP) of the two geometrical isomeric complexes of $Cl^N\subset$**2**·TBA and $Cl^C\subset$**2**·TBA. The macrocycle is shown in stick representation. The chloride and the axle are displayed as CPK models. The axle alkyl chains and stoppers have been pruned to methyl to ease the calculations. The calculation assigned an energy advantage of 4.7 kcal mol^{-1} to the complex with the Cl^- in the *C*-substituted hemisphere. (Bottom) Selected downfield region of the ^1H NMR spectrum of rotaxane **2** after adding 2 equiv. of **7a**. The

tentative assignment of the proton signals of the isomeric complexes based on computational results is shown.

During the initial stage of the titration (0.5 equivalents of **7a**), we observed an upfield shift ($\Delta\delta \sim 0.5$ ppm) in the signal of the methylene protons alpha to the nitrogen atom of the tetrabutylammonium (TBA) cation compared to the free ion-paired salt. This shift suggested the involvement of the organic TBA cation in the chloride binding process with [2]rotaxane **2**. Furthermore, when more than 1 equiv. of **7a** was added, a downfield shift in the alpha-methylene protons of TBA was detected.

Previously, similar chemical shift changes and binding dynamics were observed during the titration of [2]rotaxane **1** with **7a**, supporting the formation of the ion-paired complex, Cl⊂**1**·TBA, which exhibited receptor-separated binding geometry.[11] Based on this, we propose that the interaction of **7a** with [2]rotaxane **2** also resulted in two isomeric ion-paired complexes, Cl^{N}⊂2·TBA and Cl^{C}⊂2·TBA, both featuring receptor-separated binding geometry (see **Figure 5**, top, for potential structures of the isomeric complexes). In these complexes, the TBA cation occupies a shallow, electron-rich aromatic cavity formed by the four pyrrole rings of the macrocycle in a cone conformation, positioned opposite the bound chloride. Since the addition of more than 1 equiv. of **7a** did not cause significant changes in the proton signals of bound [2]rotaxane **2**, we estimated that the apparent binding constants for the ion-paired complexes were greater than 10^4 M^{-1}.

The appearance of two distinct pairs of signals for the NHs of the two isomeric complexes indicates that they were in a chemical exchange equilibrium (pirouetting process), with slow dynamics on the ^{1}H NMR chemical shift timescale. This exchange involved the repositioning of the *N*-oxide and chloride between the two different binding sites of the cyclic component. Simultaneously, the TBA cation also switched its binding positions at the periphery of the isomeric complexes. Unlike chloride binding, the chemical exchange between free and bound TBA cations was fast on the NMR timescale.

The integration of the two pairs of pyrrole NH signals revealed a 63:37 molar ratio of the isomeric inclusion complexes, indicating minimal selectivity of the chloride for binding to either hemisphere of the macrocyclic unit in [2]rotaxane **2**. Unfortunately, the 2D NMR experiments did not provide conclusive assignments for the two pairs of pyrrole NHs to the respective complexes. To better understand the structures and relative energies of these ion-paired complexes, we performed DFT calculations using the RI[14,15,16]-BP86-D3BJ[17,18]/def2-SVP[19,20] level of theory with Turbomole v7.0 [21,22] (**Figure 5** top). The BP86 functional is known to provide

reasonable structural and energetic results,[23] and this specific level of theory represents a good balance between system size and computational reliability, which we have previously applied successfully in related systems.[24]

The calculations indicated that the isomer with the chloride ion in the *C*-substituted hemisphere of the macrocycle had a 4.7 kcal·mol^{-1} energetic advantage over the other isomeric complex. Based on this, we inferred that the more intense NH signal pair corresponded to the Cl^{C}⊂**2**·TBA isomer (**Figure 5**). Additionally, molecular electrostatic potential (MEP) calculations for a model of the *N*- and *C*-substituted meso-phenyl rings assigned more negative MEP values to the *C*-substituted meso-phenyl ring (−16.3 kcal·mol^{-1}·e^{-1}) compared to the *N*-substituted counterpart (−8.2 kcal·mol^{-1}·e^{-1}). Despite this, the energy preference for chloride binding in the *C*-substituted hemisphere, as indicated by DFT, was still observed.

Upon analyzing the energy-minimized structures, we noticed that the interactions between the axle's amide groups and the chloride were too distant ($d_{N–Cl}$ > 5.0 Å) and not ideally aligned for strong hydrogen bonding (angle N–H···Cl = 100°). We also identified bifurcated hydrogen bonds between the carbonyl oxygen atoms of the amide groups and the triazole CH ($d_{O–C}$ > 3.2 Å; angleC–H···O = 103°) and ortho-aromatic protons ($d_{O–C}$ = 3.2 Å; angle C–H···O = 118°). Furthermore, the amide NHs formed bifurcated hydrogen bonds with the nitrogen atom of the triazole ($d_{N–N}$ > 2.9 Å; angle N–H···N = 166°) and the chloride. These intra- and intermolecular interactions contributed significantly to the complexes' stability and binding geometries.

We conducted similar ^{1}H NMR titration experiments of [2]rotaxane **2** with methyltrioctylammonium chloride (MTOA·Cl, **7b**) and tetrabutylammonium salts of nitrate (TBA·NO_3, **7c**) and cyanate (TBA·OCN, **7d**) (**Figure 4**). In each case, we obtained results similar to those for TBA·Cl **7a**.

In summary, the addition of 1 equivalent of salt (CA) produced a mixture of two isomeric ion-paired complexes, A^{N}⊂**2**·C and A^{C}⊂**2**·C, in a ∼65:35 molar ratio. All complexes exhibited receptor-separated binding geometry, as indicated by the chemical shift changes of the bound organic cation, with estimated binding constants exceeding 10^4 M^{-1}.

2.2.3 ITC experiments in Chloroform

We conducted isothermal titration calorimetry (ITC) experiments to determine the precise binding constants for the 1:1 ion-paired complexes formed in chloroform solution. Gradual heat release was observed when a chloroform solution of salts (**7a**–**7d**, ~1 mM) was incrementally added to a solution of [2]rotaxane **2** (~0.1 mM) in the same solvent. The normalized integral heat data produced binding isotherms with a single inflection point at a host/guest molar ratio of 1. In all cases, the binding isotherms fit well to a 1:1 binding model, yielding stability/binding constant values in the range of 10^5–10^6 M^{-1} (**Table 1**). The binding processes were highly exothermic and driven primarily by enthalpy, with the entropy term playing a significant opposing role.

Several conclusions can be drawn from the results obtained in chloroform solution, as summarized in **Table 1**: (a) The binding affinity of rotaxane **2** for TBA·Cl (**7a**), denoted as K_{app}[Cl⊂**2**·TBA], was 16 times lower than that for MTOA·Cl (**7b**). This finding supports the idea that [2]rotaxane **2** functions as a heteroditopic receptor for ion pairs in chloroform solution. Previous reports by us and others [11,25,26] have suggested that the methyl group of the $MTOA^+$ cation better fits the shallow cavity of the initially formed anionic complex $[Cl⊂\mathbf{2}]^-$ than the bulkier butyl groups of the TBA^+ analogue. The electron-rich, shallow cavity in the $[Cl⊂\mathbf{2}]^-$ complex, defined by the pyrrole rings of the C[4]P cone conformation, is where the organic cation binds, opposite the chloride ion. This binding results in the formation of the ion-paired complex Cl⊂**2**·C. Notably, the binding affinity of **2** for TBA·NO_3 (**7c**) was over ten times higher than for TBA·Cl (**7a**) or TBA·OCN (**7d**).

Table 1. Apparent association constant values (K_{app}, M^{-1}), free energies of complexation (Δ*G*, kcal mol^{-1}) and enthalpic (kcal mol^{-1}) and entropic thermodynamic parameters (*TΔS*, kcal mol^{-1}, 298 K) for the formation of 1 : 1 complexes between [2]rotaxane **2** and the tetraalkylammonium salts **7a**–**7d** determined in chloroform solution using ITC experiments.

	$K_{app} \times 10^{-5}$ (M^{-1})[a]	ΔG	ΔH	TΔS
7a	1.8 ± 0.4	-7.2 ± 1.1	-11.1 ± 0.7	-3.9 ± 0.8
7b	29.0 ± 1.0	-8.8 ± 0.2	-10.1 ± 1.7	-1.3 ± 3.5
7c	17.9 ± 5.7	-8.5 ± 0.2	-12.5 ± 0.2	-4.0 ± 0.2
7d	3.0 ± 1.0	-7.4 ± 1.4	-9.2 ± 0.6	-1.8 ± 0.8

[a] Error values are reported as standard deviations for two ITC experiments.

2.2.4 Theoretical calculations of the binding equilibria of ion-paired complexes

We carried out DFT calculations to determine the electronic energies (ΔE) for the binding processes of TEA·Cl, TEA·NO_3, and TEA·OCN with rotaxane **2**, based on a 1:1 binding equilibrium. The electronic energy was calculated as $\Delta E = (E_{\text{ip complex}} + E_{\text{CHCl3}}) - (E_{\text{CHCl3}\subset\text{host}} + E_{\text{ip}})$. To prevent the collapse of the rotaxane structure, one implicit $CHCl_3$ molecule was placed in the cavity of rotaxane **2**. The results indicated energetic differences of $\Delta\Delta E = -7.9$ and -4.8 kcal mol^{-1} for the OCN⊂**2**·TEA complex compared to Cl⊂**2**·TEA and NO_3⊂**2**·TEA, respectively (see ESI Table S1†). However, the calculated electronic energy differences did not align with the experimentally determined free energy differences ($\Delta\Delta G$ = RT ln K_{app}[Cl/NO_3⊂**2**·TBA]/K_{app}[OCN⊂**2**·TBA] ∼ −0.3 and 1.3 kcal mol^{-1}, respectively).

It is important to note that, due to the simplicity of the 1:1 binding model used for fitting the experimental titration data, we cannot rule out the influence of different dissociation levels of the salts **7a**, **7c**, and **7d** on the apparent binding constants and free energies. The binding model does not account for salt dissociation or the stepwise formation of the final ion-paired complexes A⊂**2**·C.

2.2.5 Pairwise-competitive binding experiments of [2]rotaxane 2 in chloroform solution.

To further investigate the differences in binding affinity of rotaxane **2** for the tetrabutylammonium ion pairs **7a**, **7c**, and **7d**, as determined by ITC experiments, we performed pairwise competitive binding experiments using ^{1}H NMR. The ^{1}H NMR spectrum of a mixture of rotaxane **2** with equimolar amounts of **7a** and **7c** showed almost exclusively signals corresponding to the NO_3⊂**2**·TBA complex. Upon gradually adding **7a** (TBA·Cl) to this equimolar mixture, the signals assigned to the Cl⊂**2**·TBA complex increased, while those of the NO_3⊂**2**·TBA complex decreased. When the components **2**, **7a**, and **7c** reached a 1:3:1 molar ratio, the integral values of the distinct pyrrole NH signals, corresponding to the NO_3⊂**2**·TBA and Cl⊂**2**·TBA complexes, reflected a concentration ratio consistent with a theoretical speciation profile. This profile was generated using Hyss software,[27] the apparent association constants from the ITC experiments, and the concentrations of the free components (**2**, **7a**, and **7c**) used in the competitive binding study. The alignment of these results supports the reliability and accuracy of the ITC data analysis.

2.2.6 Theoretical calculations of the nitrate isomeric complexes

The planar, trigonal arrangement of the oxygen atoms in the nitrate anion appears to better complement the hydrogen bonding pattern of the three-dimensional binding cavity in rotaxane **2**. In contrast, the larger, cylindrical cyanate and the smaller, spherical chloride likely form less effective intermolecular interactions with receptor **2**. Energy-minimized structures of the NO_3⊂**2**·TEA complexes, computed using the RI-BP86-D3BJ/def2-SVP level of theory, revealed more favorable geometric (distance, angle) hydrogen bonding interactions between the amide groups and the oxygen atoms of nitrate compared to the chloride in Cl⊂**2**·TBA complexes (**Figure 6**).[28]

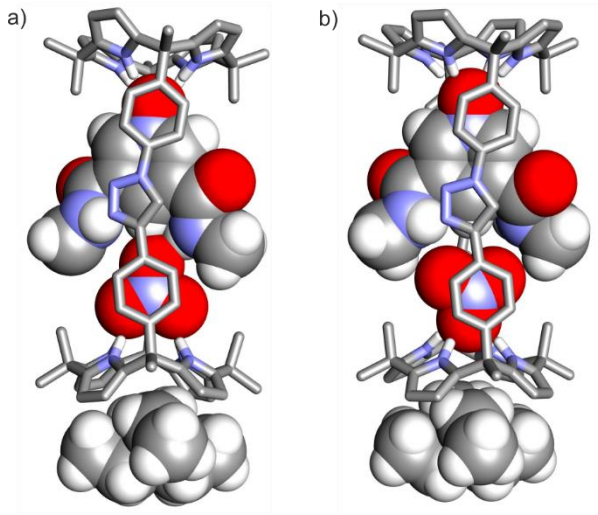

Figure 6. Energy-minimized structures (RI-BP86-D3BJ/def2-SVP) of two binding geometries of nitrate in the NO_3^C⊂**2**·TBA complex. The macrocycle is shown in stick representation. The nitrate and the axle are shown as CPK models. The axle alkyl chains and stoppers have been pruned to methyl to ease the calculations. The calculation assigned an energy advantage of 4.8 kcal mol^{-1} to the complex shown in (b) over the one shown in (a).

It is important to note that the trigonal nitrate anion can adopt two distinct binding geometries within the macrocycle cavity of rotaxane **2** (as shown in **Figure 6**). We computed these two possible binding geometries for the nitrate in the NO_3⊂**2**·TEA complex (**Figure 6a**). In the first geometry, the nitrate binds to the four pyrrole NH protons through two of its oxygen atoms, with the third oxygen forming a hydrogen bond primarily with one of the amide NH groups on the axle. In the second geometry, the nitrate interacts with the calix[4]pyrrole core via a single oxygen atom, while the two remaining oxygen atoms form hydrogen bonds with two

separate amide NH groups on the axle (**Figure 6b**). Calculations showed that the second binding geometry (**Figure 6b**) is slightly more stable, with a lower energy (ΔE = −4.8 kcal mol^{-1}). In both energy-minimized structures, the nitrate anion is positioned parallel to the aromatic walls of the macrocycle in a π-π sandwich binding geometry. The distance between the two aromatic walls of the macrocycle (d = 6.6 Å) is ideal for effective π-stacking with the bound nitrate anion.[29]

2.2.7 Study of the anion binding selectivity of [2]rotaxane **2** in acetone solution

We then investigated the binding properties of rotaxane 2 in acetone (ε = 20.7), a much more polar solvent than chloroform (ε = 4.8). In acetone, electrostatic interactions are expected to be weakened, promoting ion-pair dissociation, while strong anion binding through hydrogen bonding is maintained due to the loose solvation of the dissociated anion in this solvent.

Similar to our observations in $CDCl_3$, the gradual addition of 1 equivalent of TBA·Cl (**7a**) to a 2 mM solution of rotaxane **2** in $(CD_3)_2CO$ resulted in the appearance and subsequent increase in intensity of two new pairs of downfield-shifted signals (**Figure 7**). These signals were assigned to the pyrrole NHs of rotaxane **2** in the two isomeric anionic complexes, $[Cl^N\subset\mathbf{2}]^-$ and $[Cl^C\subset\mathbf{2}]^-$. The signals intensified as the amount of free **2** decreased, becoming prominent upon the addition of 1 equivalent of **7a**. At this point, the integral values of the two NH signal pairs indicated a 75:25 molar ratio between the two complexes.

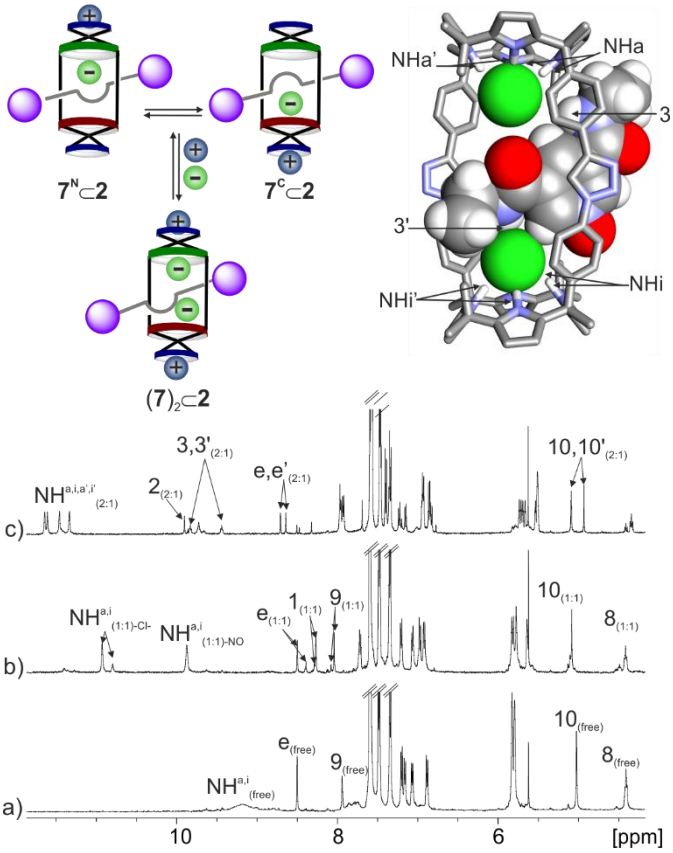

Figure 7. (Top) (Left) Schematic cartoon of the binding equilibrium between 1 : 1 and 2 : 1 complexes of [2]rotaxane **2** with **7a** and **7b** in acetone. (Right) Energy-minimized structure of the 2 : 1 complex $[Cl_2\subset\mathbf{2}]^{2-}$ with partial proton assignments. (Bottom) Selected region of the ^{1}H NMR spectra acquired during the titration of [2]rotaxane **2** (a) with incremental amounts of TBA·Cl **7a** in $(CD_3)_2CO$: 1 equiv. (b) and 3 equiv. (c) of **7a**. See **Figure 2** for the proton assignment.

In the more polar acetone solvent, the ^{1}H NMR spectrum revealed that adding more than 1 equivalent of TBA·Cl (**7a**) caused the appearance of a new set of signals for the NH protons of rotaxane **2**. Four new singlets were observed between δ = 11.6 and 11.3 ppm (**Figure 7c**), and their intensity increased with the addition of more **7a**, while the signals corresponding to the pyrrole NHs of the 1:1 isomeric complexes (δ = 10.9–9.9 ppm) diminished. This suggests an equilibrium between the 1:1 complexes and a new species, likely with a higher stoichiometry, showing slow exchange dynamics on the NMR timescale. The new species was assigned a 2:1 stoichiometry, $[Cl_2\subset\mathbf{2}]^{2-}$, in which a second chloride ion replaces the pyridine *N*-oxide unit and binds to one of the C[4]P hemispheres of the receptor's cyclic

component in the 1:1 $[Cl\subset\mathbf{2}]^-$ complex. Similar behavior was observed for the previously studied [2]rotaxane **1** when binding tetraalkylammonium chloride salts in $(CD_3)_2CO$.[11]

The binding of chloride in both C[4]P hemispheres of the macrocyclic component of **2**, along with the displacement of the axle, explains the downfield shifts in the pyrrole NH signals. After adding 3 equivalents of TBA·Cl (**7a**), only the proton signals corresponding to the 2:1 complex $[Cl_2\subset\mathbf{2}]^{2-}$ were visible in the ^{1}H NMR spectrum (**Figure 7c**). Additionally, the aromatic protons of the pyridine *N*-oxide and the amide NHs of the axle shifted downfield compared to those in the free receptor **2** and its 1:1 isomeric complexes.

In the 1:1 complexes $[Cl^N\subset\mathbf{2}]^-$ and $[Cl^C\subset\mathbf{2}]^-$, the 1,5-bis-amide-pyridine-*N*-oxide unit of the axle is hydrogen-bonded to one of the C[4]P hemispheres and positioned between its two meso-phenyl rings. The displacement of this unit from the macrocyclic cavity due to the binding of the second chloride in the $[Cl_2\subset\mathbf{2}]^{2-}$ complex likely reduces the magnetic shielding of the pyridyl and amide protons. The 2:1 complex exhibits a non-symmetric binding geometry, which is not time-averaged on the NMR timescale, resulting in the broadening and splitting of most proton signals. Specifically, the pyrrole NHs of macrocycle 2 (H^a and H^i) and the triazole CHs (H^e) appeared as four and two singlets, respectively. Additionally, the amide protons (H^3) were seen as two triplets at δ = 9.8 and 9.4 ppm (H^3 and $H^{3\prime}$), and the methylene ether groups (H^{10}) of the linear axle resonated as diastereotopic singlets.

We observed similar results in the ^{1}H NMR titration experiment of [2]rotaxane **2** with MTOA·Cl (**7b**). The key differences between the two titrations were related to the chemical shift changes in the proton signals of the two organic cations. In the case of TBA·Cl (**7a**), the proton signals of the TBA cation remained unchanged throughout the titration, indicating that the cation was not involved in the binding process. However, for the MTOA cation, its proton signals, particularly those of the methyl group, displayed chemical shift changes. This finding reinforced the idea that the methyl group of $MTOA^+$ fits better into the electron-rich aromatic cavity, opposite the bound chloride in the initially formed anionic complex $[Cl\subset\mathbf{2}]^-$, than the butyl group of TBA^+. Although these results suggest that $MTOA^+$ is involved in binding in polar $(CD_3)_2CO$ solution, its involvement was much less significant compared to that observed in chloroform solution.

We also carried out electronic structure calculations for the 2:1 dianionic complex $[Cl_2\subset\mathbf{2}]^{2-}$ at the RI-BP86-D3(BJ)/def2-SVP level of theory. The energy-minimized structure showed each chloride ion bound within the two calix[4]pyrrole

hemispheres of the macrocyclic component (**Figure 7**, top), with each chloride forming four hydrogen bonds with the pyrrole NHs and an additional bond with one of the axle's amide protons.

Furthermore, we investigated the binding properties of rotaxane **2** in $(CD_3)_2CO$ with TBA·NO_3 (**7c**) and TBA·OCN (**7d**). The addition of 1 equiv. of either salt to 2 mM solutions of rotaxane **2** resulted in two new pairs of downfield-shifted signals corresponding to the pyrrole NHs. These signals were attributed to the formation of the 1:1 isomeric anion complexes $[NO_3^{N/C}\subset\mathbf{2}]^-$ and $[OCN^{N/C}\subset\mathbf{2}]^-$, respectively. The integral values of these separate NH signal pairs indicated molar concentration ratios of 75:25 for the nitrate complex and 60:40 for the cyanate complex. Experimentally, the energy differences between the two 1:1 isomeric complexes were minimal, at 0.3 and 0.1 kcal mol^{-1}, respectively, which was consistent with computational predictions. Calculations showed a slight energetic preference (0.2–0.1 kcal mol^{-1}) for the isomers with the anion located in the *C*-substituted hemisphere, in line with results for ion-paired complexes in $CDCl_3$ solution.

The addition of more than 1 equivalent of either **7c** or **7d** to equimolar solutions of rotaxane **2** did not lead to noticeable changes in the ^{1}H NMR spectra, unlike the results seen with chloride. This suggests that, in contrast to the chloride complex, adding more than 1 equiv. of these polyatomic anions in $(CD_3)_2CO$ does not result in the formation of complexes with stoichiometries higher than 1:1. This behavior aligns with previous findings where rotaxane **1** did not form 2:1 complexes with **7c** and **7d** in $(CD_3)_2CO$.[12] Likely, the two three-dimensional cavities in rotaxane **2** are not well-suited to accommodate two polyatomic anions simultaneously.

2.2.8 ITC experiments in acetone

We conducted isothermal titration calorimetry (ITC) experiments to accurately determine the binding constants of the 1:1 complexes of rotaxane **2** in acetone solution. The titration data were fitted to theoretical 1:1 binding models. Specifically, for TBA·Cl (**7a**), we assumed that the formation of the 2:1 complex was negligible under the conditions used in the ITC experiments ([**2**] ~ 0.1 mM and [**7**] ~ 1 mM). The binding constants obtained from the ITC experiments are summarized in **Table 2** and compared with those derived from studies conducted in chloroform solution.

Table 2. Association constant values (M^{-1}) and binding selectivity for the 1 : 1 complex formed between [2]rotaxane **2** and the tetraalkylammonium salts **7a**–**d** in chloroform and acetone solutions. All binding constants were determined using ITC experiments.

1	2	3	4	5	6
salts	$CHCl_3$		$(CH_3)_2CO$		$K_{(CH3)2CO}/K_{CHCl3}$
	$K_a \times 10^{-5}$ (M^{-1})	Salt selectivity K_{TBAX}/K_{TBACl}	$K_a \times 10^{-5}$ (M^{-1})	anion selectivity K_X/K_{TBACl}	
7a	1.8 ± 0.4	1	18.5 ± 0.1	1	10.3
7b	29.0 ± 1.0	–	>100	–	>3
7c	17.9 ± 5.7	10	42.5 ± 1.5	2.5	2.3
7d	3.0 ± 1.0	1.6	6.8 ± 0.9	1.6	2.3

We reached the following conclusions by comparing the results from the anion binding selectivity studies of rotaxane **2** in the two solvents: (a) the binding/affinity constants were generally higher in acetone than in chloroform (column 6); (b) specifically for chloride, the affinity for **2** increased tenfold in acetone compared to chloroform, whereas the affinities for nitrate (**7c**) and cyanate (**7d**) only roughly doubled; (c) receptor **2** showed a selective binding preference for nitrate in both solvents (columns 3 and 5); (d) however, the selectivity of **2** for nitrate over chloride was lower in acetone (column 5) than in chloroform (column 3).

We attribute the increased binding affinities observed in acetone (column 6) to two factors: a greater degree of salt dissociation and reduced solvation of the anions. The significant increase in the binding affinity of **2** for chloride in acetone likely results from the reduced dissociation of the chloride salt in chloroform compared to that of the nitrate and cyanate. In acetone, both salts were primarily dissociated, and we evaluated the anion binding constants using theoretical models that did not account for dissociation/association equilibria.

We were pleasantly surprised by the binding selectivity of **2** for nitrate in both solvents (columns 3 and 5). This result was unexpected because chloride has a higher charge density (more negative MEP) than nitrate and cyanate (which share the same charge but have larger volumes). It is well-established that this property significantly influences the strength of electrostatic interactions, which are crucial for stabilizing the 1:1 anionic complexes under investigation. We concluded that the size, shape, and hydrogen-bonding characteristics of the three-dimensional polar cavity of **2** contributed to its remarkable selectivity for nitrate binding. Finally, we

attributed the observed decrease in selectivity for nitrate over chloride in acetone (comparing columns 3 and 5) to the reduction in competing ion-pairing equilibria and the higher MEP value of chloride. Importantly, the magnitude of the selectivity of **2** for chloride versus cyanate remains consistent across both solvents (columns 3 and 5).

2.2.9 Comparison of the binding properties of [2]rotaxane 2 with those previously described for [2]rotaxane 1

In chloroform solution, the apparent binding constant for rotaxane **2** with TBA·Cl (**7a**) was three times greater than that of its counterpart, rotaxane **1** (**Table 3**). Conversely, rotaxane **1** exhibited an apparent binding constant three times higher than rotaxane **2** when interacting with TBA·OCN (**7b**). We attributed these differences in binding affinity to the smaller dimensions of the binding site in the interlocked structure of rotaxane **2**, which favored the accommodation of the smaller, spherical chloride anion. In contrast, the larger cylindrical cyanate anion was more compatible with the anionic binding site of rotaxane **1**.

Table 3. Association constant values (M^{-1}) and binding selectivity for the 1 : 1 complexes formed between [2]rotaxane **1** and the tetraalkylammonium salts **7a**–**d** in chloroform and acetone solutions. All binding constants were determined using ITC experiments and previously disclosed in ref. 11 and 12.

salts	$CHCl_3$		$(CH_3)_2CO$	
	$K_a \times 10^{-5}$ (M^{-1})	Salt selectivity K_{TBAX}/K_{TBACl}	$K_a \times 10^{-5}$ (M^{-1})	anion selectivity K_X/K_{TBACl}
7a	0.5 ± 0.2	1	480[a]	1
7b	158 ± 16	–	700[a]	–
7c	0.4 ± 0.1	0.8	0.8 ± 0.4	0.002
7d	7.9 ± 0.2	16	30 ± 0.3	0.06

[a] Estimated value.

We observed an even more pronounced difference in the binding constants of the two rotaxanes when recognizing TBA·NO_3 (**7c**) in chloroform. The binding constant for rotaxane **2** with the nitrate salt was two orders of magnitude greater than that of rotaxane **1**. This is likely due to the planar, trigonal nitrate anion being a better fit for the size, shape, and hydrogen-bonding capabilities of the anion binding site in rotaxane **2**. However, we cannot discount the possibility that more favorable nitrate-π interactions contributed to the overall stabilization of the NO_3⊂**2**·TBA complex. In line with this, the energy-minimized structure of the NO_3⊂**2**·TBA complex revealed a shorter distance between the centers of the meso-phenyl walls surrounding the nitrate anion (d = 6.6 Å) compared to the distance in the

NO_3⊂**1**·TBA complex (d = 7.7 Å). The bis-alkynyl spacer in rotaxane **1** likely rendered its macrocyclic component conformationally less flexible than the triazole component in rotaxane **2**, which may have limited the adaptability of the interlocked binding site in rotaxane **2** for establishing efficient π–π interactions with the bound nitrate anion.

In acetone solution, rotaxane **1** exhibited a strong binding selectivity for chloride over cyanate and nitrate anions. The binding constants for rotaxane **1** with chloride and cyanate were twenty-fold and five-fold larger, respectively, compared to those observed for rotaxane **2**. These findings indicate that chloride and cyanate were better suited for the anion binding site of rotaxane **1**. In stark contrast, the binding constant for rotaxane **2** with nitrate in acetone increased fifty-fold compared to that of rotaxane **1**, surpassing the constants for both chloride and cyanate. As previously noted in chloroform studies, the planar, trigonal nitrate anion is likely a better fit for the binding site of rotaxane **2**, allowing it to maintain selectivity for nitrate even when transitioning from chloroform to acetone. In summary, rotaxane **2** demonstrated selectivity for nitrate irrespective of the solvent, whereas rotaxane **1** exhibited solvent-dependent anion selectivity.

We also recognize that the differences in anion binding selectivity between the two interlocked receptors, **1** and **2**, in acetone may be partially attributed to the distinct solvation and desolvation effects experienced by the ion pairs, the polar cavities of the free receptors, and the resulting anionic complexes. We have previously noted that solvation processes play a significant role in overall anion binding in polar solvents like acetone.

It's important to highlight that the change in solvent has a varied impact on the anion-binding properties of the two interlocked receptors. The association constant for the 1:1 complex of rotaxane **1** with chloride in acetone was estimated to be three orders of magnitude greater than in chloroform ($K_{(CH3)2CO}/K_{CHCl3}$ = 960, **Table 3**). In contrast, the solvent transition from chloroform to acetone resulted in only a one-order-of-magnitude increase in the association constant for the 1:1 complex of rotaxane **2** with chloride ($K_{(CH3)2CO}/K_{CHCl3}$ = 10.3, **Table 2**). This disparity is likely due to the different solvation and desolvation processes affecting the polar cavities of the free receptors and their corresponding anionic complexes in acetone.

2.3 Conclusions

In summary, we report the synthesis of [2]rotaxane **2**, which features a bis(calix[4]pyrrole) cyclic component with two chemically non-equivalent hemispheres and a 3,5-bis-amidepyridyl-*N*-oxide derivative axle. In chloroform, [2]rotaxane **2** forms two isomeric 1:1:1 ion-paired complexes with tetraalkylammonium salts containing monoatomic (Cl^-) and polyatomic (NO_3^-, OCN^-) anions. The anion is accommodated within one of the two calix[4]pyrrole hemispheres, where six hydrogen bond donor groups from the interlocked molecular components converge. DFT calculations indicated a lower thermodynamic advantage for the isomer with the anion bound in the *C*-substituted hemisphere. The tetraalkylammonium cation occupies the electron-rich shallow aromatic cavity created by the cone conformation of the pyrrole rings opposite the bound anion.

In acetone, receptor **2** predominantly forms anionic 1:1 complexes. For tetraalkylammonium chloride salts (TBA·Cl and MTOA·Cl), the addition of more than 1 equiv. of the salt led to the formation of 2:1 anionic complexes, with one anion bound to each hemisphere of the bis(calix[4]pyrrole) macrocyclic component.

ITC experiments showed that the binding constants for the anionic complexes formed in acetone were significantly larger (ranging from two to ten times) than those of the ion-paired analogues in chloroform. We attributed this increase to the considerable dissociation of the ion pairs in the more polar acetone solvent and the reduced solvation of the anions.

Encouragingly, [2]rotaxane **2** exhibited notable selectivity for nitrate over chloride and cyanate anions in both solvents, with the selectivity being more pronounced in chloroform. We concluded that the planar and trigonal shape of the nitrate anion allows for a better fit within the size and hydrogen bonding framework of the interlocked three-dimensional cavity, resulting in more effective interactions with the receptor compared to chloride or cyanate.

These results contrast with those previously reported for [2]rotaxane **1**, which showed a binding preference for cyanate and chloride anions over nitrate in chloroform and acetone solutions, respectively. Our findings underscore the importance of shape, size, and interaction complementarity in the three-dimensional structures provided by mechanically interlocked systems for the selective binding of anions.

2.4 Experimental section

2.4.1 General information and instruments

Starting materials and reagents were purchased from commercial suppliers and used without further purification. All reactions were performed under an argon atmosphere and protected from light unless specified. Anhydrous solvents were obtained from a solvent purification system SPS-400-6 from Innovative Technologies. All solvents were of HPLC-grade quality, commercially obtained, and used without further purification. ^{1}H NMR, ^{13}C NMR and 2D NMR spectra were recorded on a Bruker Avance 300 (300 MHz for ^{1}H NMR and 75 MHz for ^{13}C NMR), Bruker Avance 400 (400 MHz for ^{1}H NMR and 100 MHz for ^{13}C NMR), Bruker Avance 500 (500 MHz for ^{1}H NMR and 125 MHz for ^{13}C NMR) or Bruker Avance 500 with cryoprobe (500 MHz for ^{1}H NMR and 125 MHz for ^{13}C NMR). Deuterated solvents used are indicated in the characterization and chemical shifts are given in ppm.

High-resolution mass spectra (HRMS) were obtained on a Bruker HPLC-TOF using ESI as ionization mode. IR spectra were recorded on a Bruker Optics FTIR Alpha spectrometer equipped with a DTGS detector, KBr beam splitter at 4 cm^{-1} resolution using a one bounce ATR accessory with diamonds windows.

Isothermal titration calorimetry experiments were performed using a Microcal VP-ITC Microcalorimeter. HPLC grade solvents from Scharlab, SL were used. Titrations of rotaxane **2** with different alkylammonium salts in the different solvents were carried out by adding small aliquots (7-10 µL) of a solution of alkylammonium salts **7a**-**7d** into a solution of the host in the same solvent. The concentration of the guest was approximately 7-10 times more concentrated than the receptor solutions ([**2**] =10^{-4} - 10^{-3} M). The apparent association constants (K_{app}), TΔS and ΔH values for the binding processes were determined from the fit of the titration data to a 1 to 1 theoretical binding model (one set of sites model implemented in Microcal software). Error values are reported as standard deviations and accurately propagated.

2.4.2 Synthesis and characterization of rotaxane 2

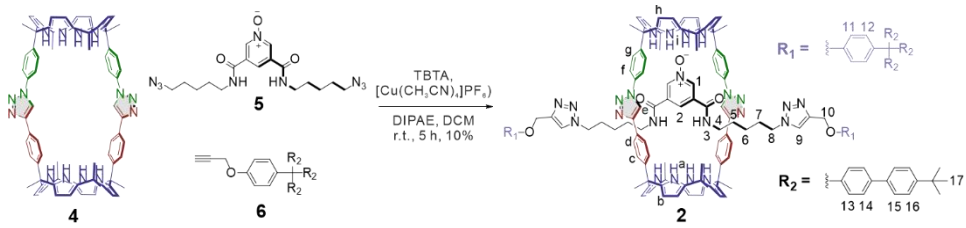

Scheme 1. Synthesis of rotaxane **2**. Reaction conditions: 1 equiv. of **4**, 2 equiv. of **5** and 4 equiv. of **6**.

Macrocycle **4**, pyridine *N*-oxide axle **5**, and stopper **6** (**Scheme 1**) were synthesized following previously reported procedures in the literature.[11,13] In a Schlenk flask, macrocycle **4** (80.0 mg, 65.0 µmol, 1 equiv.), axle **5** (52.0 mg, 130 µmol, 2 equiv.), and stopper **6** (200 mg, 260 µmol, 4 equiv.) were dissolved in 10 mL of dry and degassed DCM under the argon atmosphere. $[Cu(CH_3CN)_4]PF_6$ (12.0 mg, 32.0 µmol, 0.5 equiv.), TBTA (17.0 mg, 32.0 µmol, 0.5 equiv.), and 0.5 mL of freshly distilled diisopropylamine were added. The reaction was stirred at room temperature for 4 h. After that, 50 mL of DCM was added to the reaction crude, and the mixture was washed three times with 10 mL of water. The organic layer was dried (Na_2SO_4), filtered, and concentrated under reduced pressure to give a brown solid. The crude was purified by column chromatography on silica gel (3 g, 100:0 → 70:30 DCM:EtOAc) to afford the final product as a brown solid (20.0 mg, 6.30 µmol, 10% yield). Rf=0.4 (70:30 DCM:EtOAc).

^{1}H NMR (500 MHz, $CDCl_3$, 298 K) δ (ppm): 9.15 (br, 8H, NH), 7.98 (s, 2H), 7.53 (d, *J* = 8.5 Hz, 12H), 7.49 (d, *J* = 8.5 Hz, 12H), 7.44 (d, *J* = 8.5 Hz, 12H), 7.39 (br, 8H), 7.29 (d, *J* = 8.5 Hz, 12H), 7.20 (d, *J* = 9.0 Hz, 4H), 7.07 (br, 8H), 6.80 (d, *J* = 9.0 Hz, 4H), 5.91 (m, 16H), 5.02 (br, 4H), 4.29 (br, 4H), 3.14 (br, 4H), 1.94 (br, 4H), 1.60 (br, 4H), 1.43 (br, 4H), 1.34 (s, 54 H).

^{13}C NMR (125 MHz, $CDCl_3$, 298 K) δ(ppm): 156.1, 150.2, 145.7, 138.4, 137.6, 137.5, 132.3, 132.1, 132.0, 131.41, 128.6, 114.3, 113.4, 67.1, 63.6, 53.5, 29.7, 29.4, 25.3, 22.3, 19.8, 14.1, 13.5, 13.4.

HR-MS (ESI TOF) m/z calculated for $C_{213}H_{219}N_{23}O_5$ $[M-2H]^{2-}$ 1588.3721, found 1588.3784.

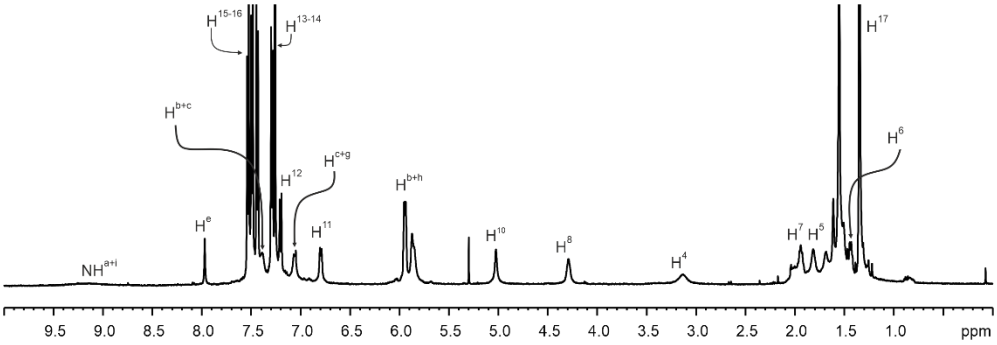

Figure 8. ^{1}H NMR spectrum (500 MHz, 298 K, $CDCl_3$) of **2**. See **Scheme 1** for the proton assignment.

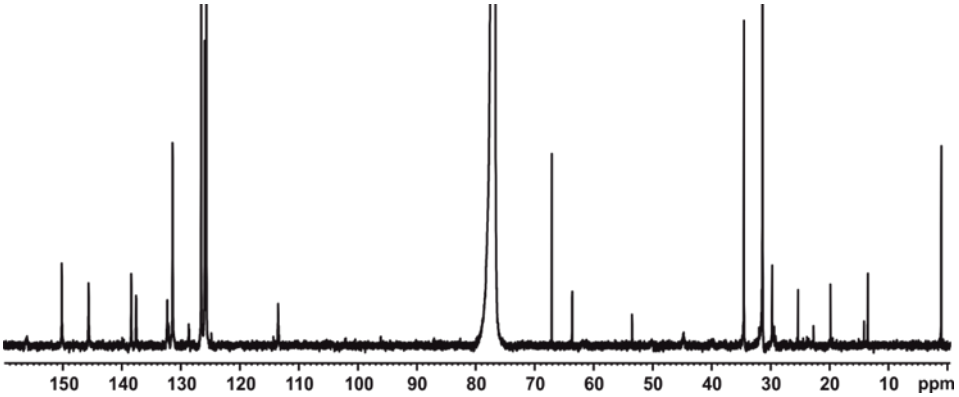

Figure 9. ^{13}C NMR spectrum (125 MHz, 298 K, $CDCl_3$) of **2**.

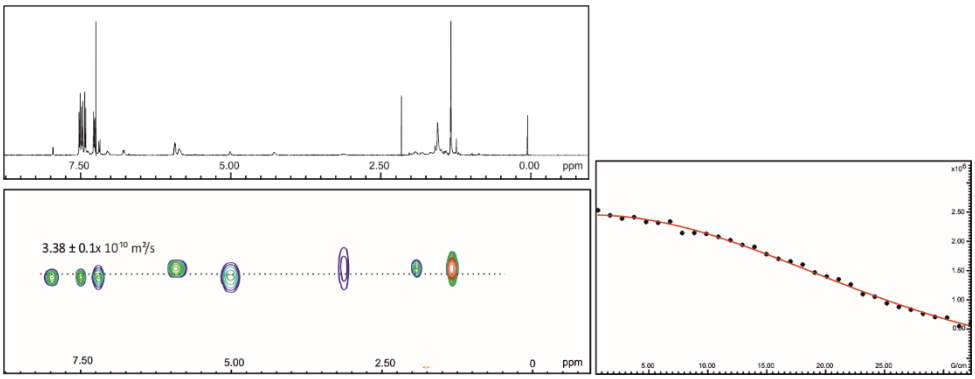

Figure 10. (left) ^{1}H pseudo 2D plot of DOSY (500 MHz, 298K, $CDCl_3$) of [2]rotaxane **2** (D20 = 0.15 s, P30 = 1 ms). (right) Fit of the decay of the signal of proton H^e to a mono-exponential function using Dynamics Center software from Bruker. Error is indicated as standard deviation.

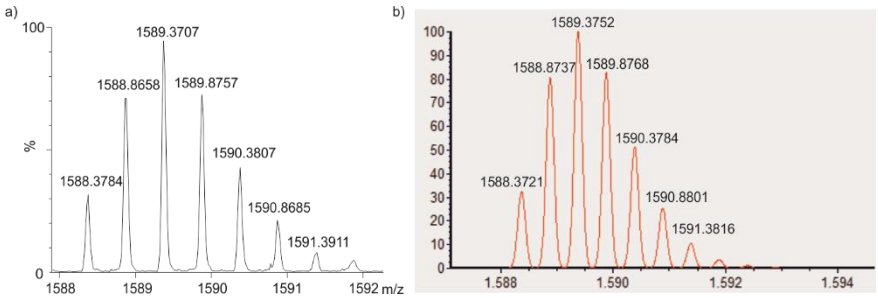

Figure 11. Experimental (a) and theoretical (b) isotopic distribution for [**2**-2H]$^{-2}$.

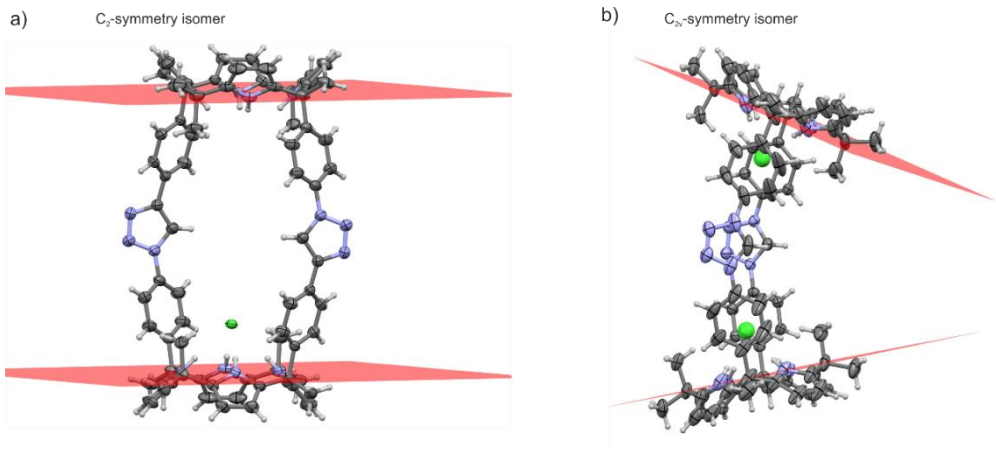

Figure 12. X-ray structures of the 1:1 complex of macrocycle **4** with MTOA·Cl **7b** (a) and 2:1 complex of macrocycle **4** with TBA·Cl **7a** (b) reported in ref. 13. The structures show the two possible conformations that macrocycle **4** can adopt featuring C_2 and C_{2v} symmetry. Macrocycle **4**, included Cl^- anions and $MTOA^+$ cation are shown as ellipsoids at 50% probability level and hydrogens as fixed-size spheres with a radius of 0.15 Å. Cations were omitted for clarity.

2.4.3 NMR experiments in $CDCl_3$

2.4.3.1 NMR titration of rotaxane with TBA·Cl **7a** in $CDCl_3$

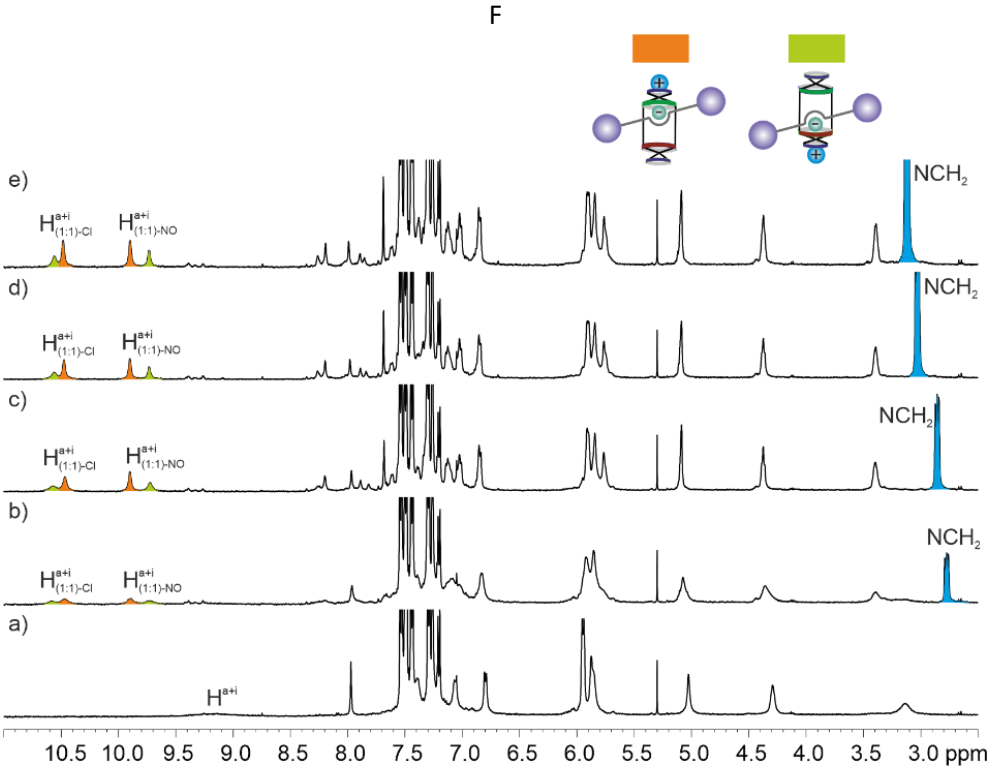

Figure 13. Selected region of the ^{1}H NMR spectra (500 MHz, 298 K, $CDCl_3$) acquired during the titration experiment of **2** (a) with incremental additions of TBA·Cl **7a**, 0.5 equiv. (b), 1 equiv. (c), 1.5 equiv. (d), and 5 equiv. (e).

2.4.3.2 NMR titration of rotaxane with MTOA·Cl **7b** in $CDCl_3$

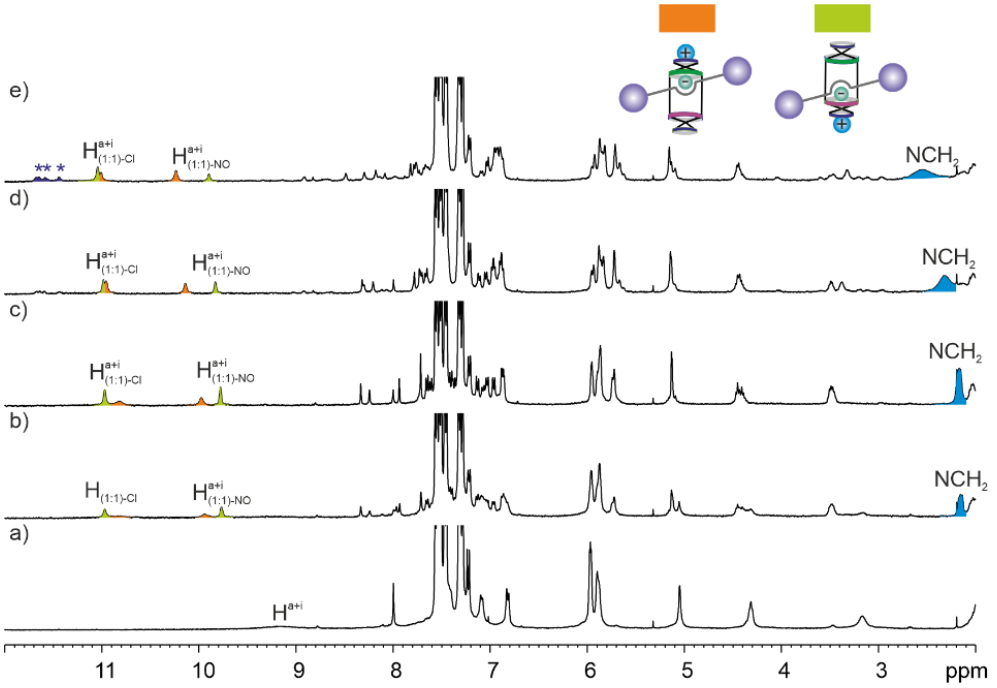

Figure 14. Selected region of the ^{1}H NMR spectra (500 MHz, 298 K, $CDCl_3$) acquired during the titration experiment of **2** (a) with incremental additions of MTOA·Cl **7b**, 0.5 equiv. (b), 1 equiv. (c) and 2 equiv. (d). * Signals related to 2:1 complex.

2.4.3.3 NMR titration of rotaxane with TBA·NO_3 **7c** in $CDCl_3$

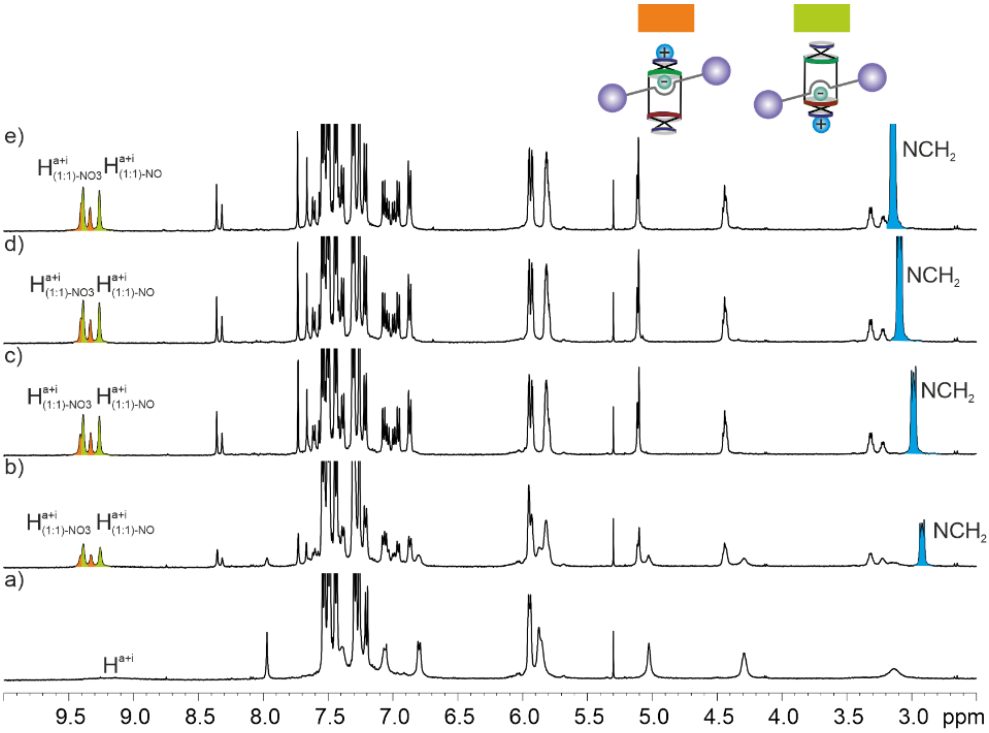

Figure 15. Selected region of the ^{1}H NMR spectra (500 MHz, 298 K, $CDCl_3$) acquired during the titration experiment of **2** (a) with incremental additions of TBA·NO_3 **7c**, 1 equiv. (b), 1.5 equiv. (c), and 2 equiv. (d).

2.4.3.4 NMR titration of rotaxane with TBA·OCN **7d** in $CDCl_3$

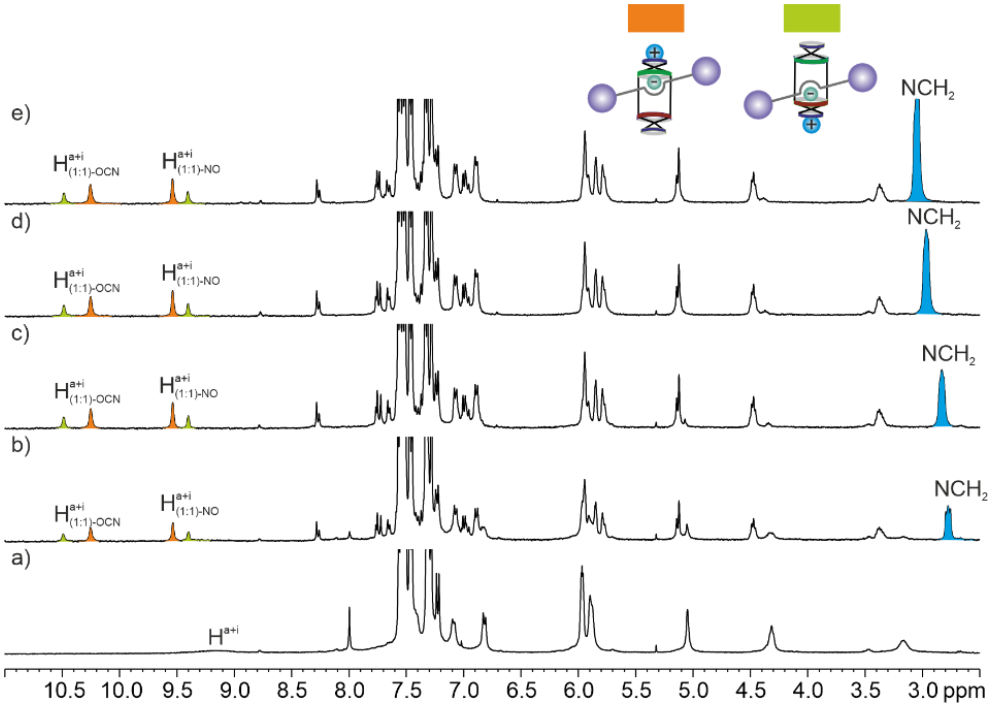

Figure 16. Selected region of the ^1H NMR spectra (500 MHz, 298 K, $CDCl_3$) acquired during the titration experiment of **2** (a) with incremental additions of TBA·OCN **7d**, 1 equiv. (b), 1.5 equiv. (c), 2 equiv. (d).

2.4.3.5 Pairwise competitive experiment in $CDCl_3$

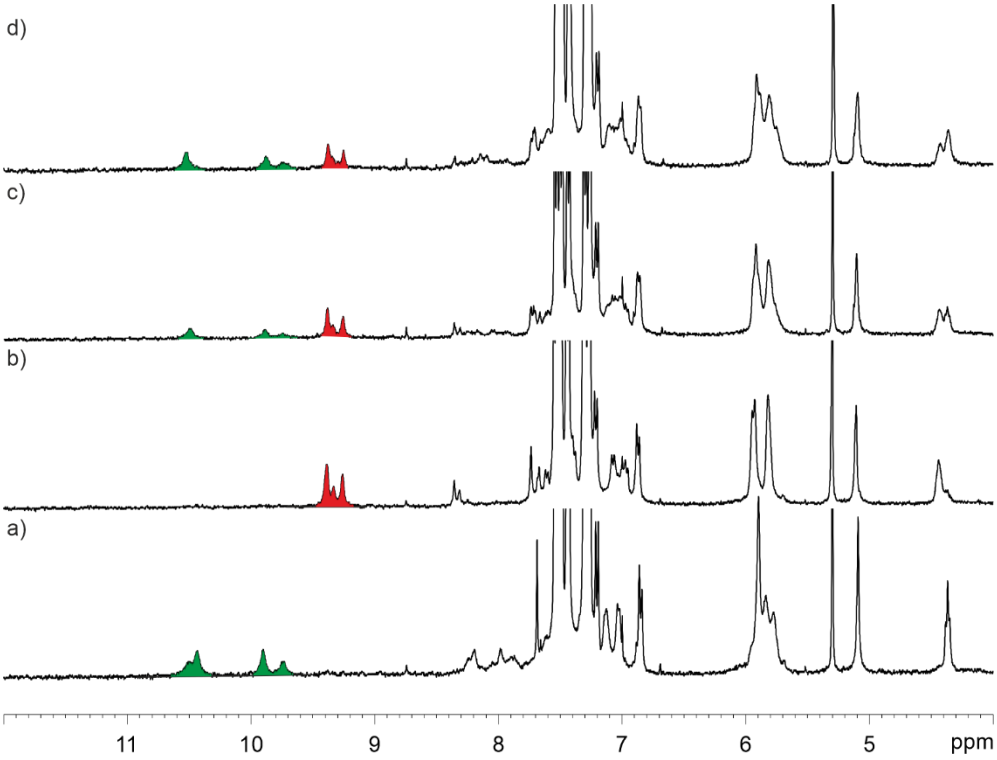

Figure 17. Selected region of the ^{1}H NMR spectra (500 MHz, 298 K, $CDCl_3$) acquired during the pairwise competitive experiment **2** with **7a** and **7c**. Rotaxane **2** with 1 equiv. of TBA·Cl **7a** (a), 1 equiv. of TBA·Cl **7a** and 1 equiv. of TBA·NO_3 **7c** (b), 1 equiv. of TBA·Cl **7a** and 3 equiv. of TBA·NO_3 **7c** (c) and 1 equiv. of TBA·Cl **7a** and 5 equiv. of TBA·NO_3 **7c** (d). Pyrrole NH signals of the **7a⊂2** and **7c⊂2** complexes are highlighted in green and red, respectively.

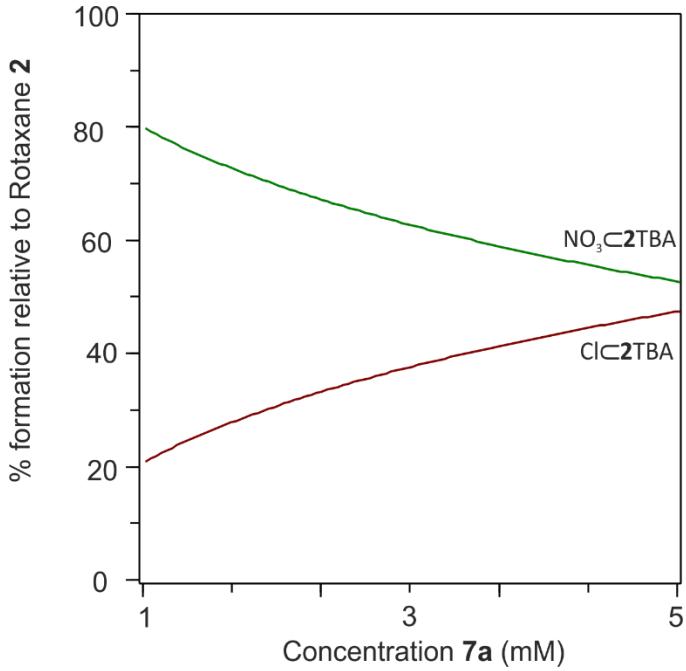

Figure 18. Speciation profile derived using the overall concentrations of the three free components (**2**, **7a** and **7c**) used in the pair-wise experiment and the values of the association constants determined from the ITC experiments. Starting point is an equimolar solution of **2**, **7a** and **7c**.

2.4.4 NMR experiments in d_6-acetone

2.4.4.1 NMR titration of rotaxane with TBA·Cl **7a** in d_6-acetone

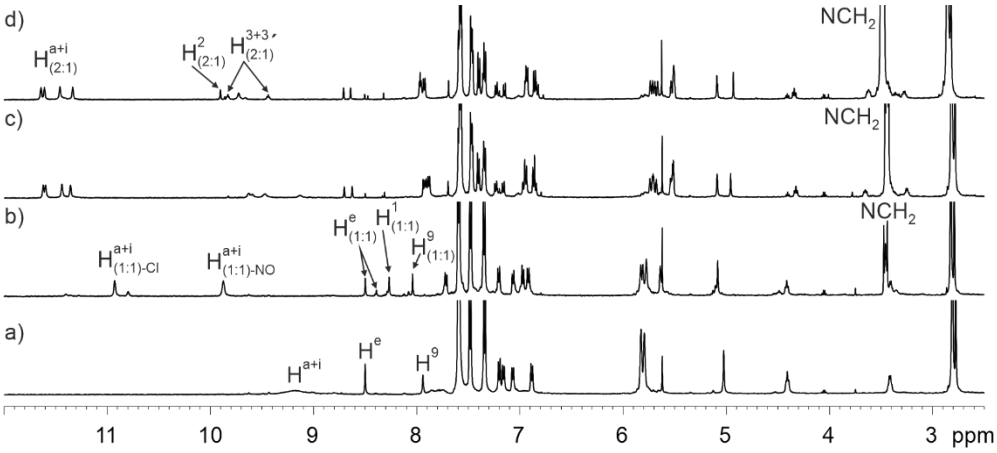

Figure 19. Selected region of the ^{1}H NMR spectra (500 MHz, 298 K, d_6-acetone) acquired during the titration experiment of **2** (a) with incremental additions of TBA·Cl **7a**, 1 equiv. (b), 2 equiv. (c), and 10 equiv. (d).

2.4.4.2 NMR titration of rotaxane with MTOA·Cl **7b** in d_6-acetone

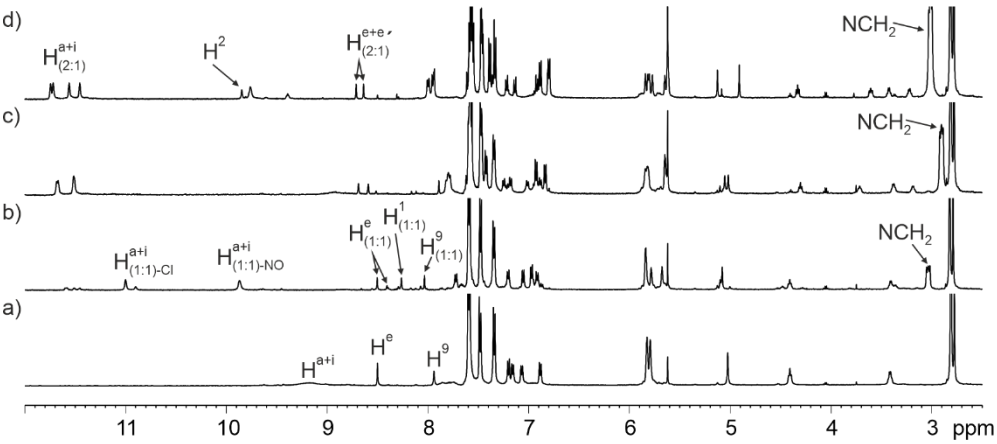

Figure 20. Selected region of the ^{1}H NMR spectra (500 MHz, 298 K, d_6-acetone) acquired during the titration experiment of **2** (a) with incremental additions of MTOA·Cl **7b**, 1 equiv. (b), 2 equiv. (c), 3 equiv. (d).

2.4.4.3 NMR titration of rotaxane with TBA·NO_3 **7c** in d_6-acetone

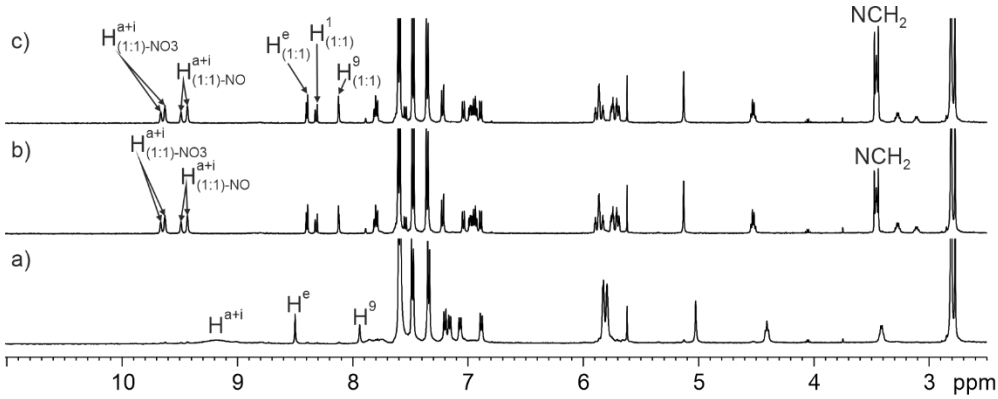

Figure 21. Selected region of the ^{1}H NMR spectra (500 MHz, 298 K, d_6-acetone) acquired during the titration experiment of **2** (a) with incremental additions of TBA·NO_3 **7c**, 1 equiv. (b), 2 equiv. (c).

2.4.4.4 NMR titration of rotaxane with TBA·OCN **7d** in d_6-acetone

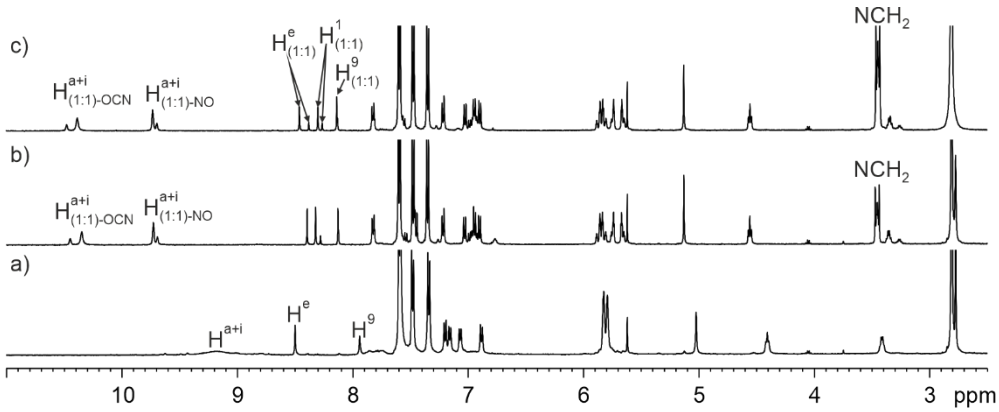

Figure 22. Selected region of the ^{1}H NMR spectra (500 MHz, 298 K, d_6-acetone) acquired during the titration experiment of **2** (a) with incremental additions of TBA·OCN **7d**, 1 equiv. (b), 2 equiv. (c).

2.4.5 ITC experiments in chloroform

2.4.5.1 ITC experiments of rotaxane with TBA·Cl **7a** in chloroform

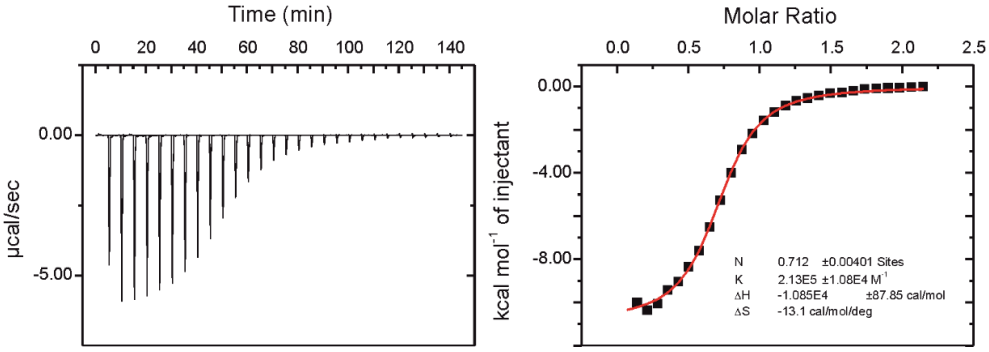

Figure 23. Left — Traces of the raw data of the titration experiment of 1.5×10^{-4} M solution of [2]rotaxane 2, with TBA·Cl solution 1.5×10^{-3} M in chloroform. Right — binding isotherms of the calorimetric titration shown on top. To determine the values of the thermodynamic variables the ITC data was fitted to a 1:1 binding model (red line).

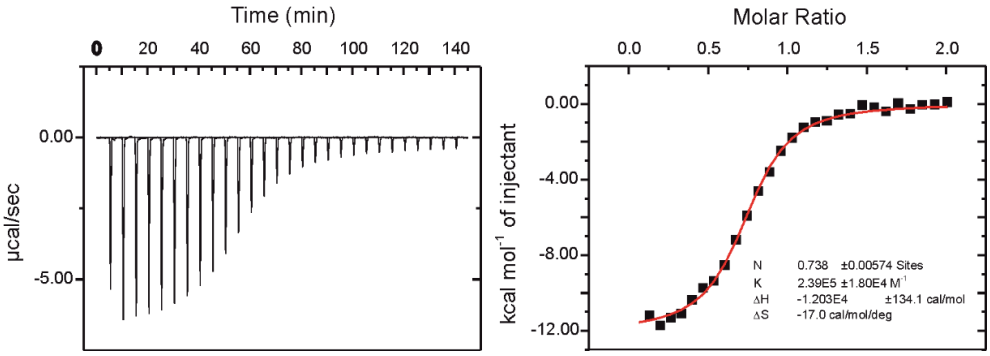

Figure 24. Left — Traces of the raw data of the titration experiment of 1.5×10^{-4} M solution of [2]rotaxane **2**, with TBA·Cl solution 1.4×10^{-3} M in chloroform. Right — binding isotherms of the calorimetric titration shown on top. To determine the values of the thermodynamic variables the ITC data was fitted to a 1:1 binding model (red line).

2.4.5.2 ITC experiments of rotaxane with MTOA·Cl **7b** in chloroform

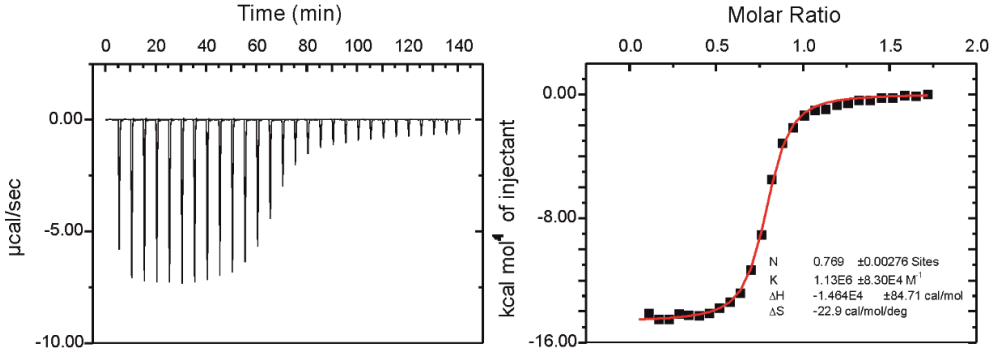

Figure 25. Left — Traces of the raw data of the titration experiment of 1.5×10^{-4} M solution of [2]rotaxane **2**, with MTOA·Cl solution 1.2×10^{-3} M in chloroform. Right — binding isotherms of the calorimetric titration shown on top. To determine the values of the thermodynamic variables the ITC data was fitted to a 1:1 binding model (red line).

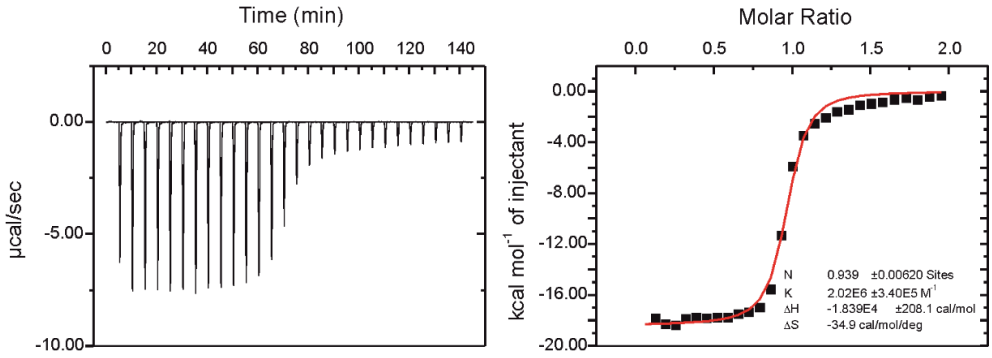

Figure 26. Left — Traces of the raw data of the titration experiment of 1.2×10^{-4} M solution of [2]rotaxane **2**, with MTOA·Cl solution 1.0×10^{-3} M in chloroform. Right — binding isotherms of the calorimetric titration shown on top. To determine the values of the thermodynamic variables the ITC data was fitted to a 1:1 binding model (red line).

2.4.5.3 ITC experiments of rotaxane with TBA·NO_3 **7c** in chloroform

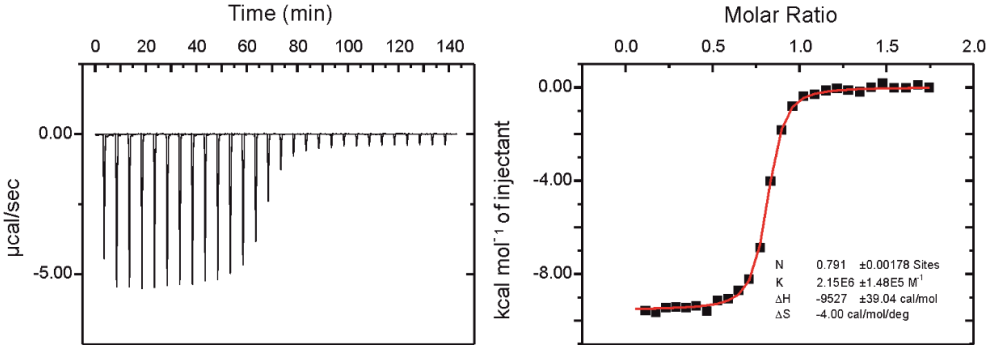

Figure 27. Left — Traces of the raw data of the titration experiment of 1.8×10^{-4} M solution of [2]rotaxane **2**, with TBA·NO_3 solution 1.4×10^{-3} M in chloroform. Right — binding isotherms of the calorimetric titration shown on top. To determine the values of the thermodynamic variables the ITC data was fitted to a 1:1 binding model (red line).

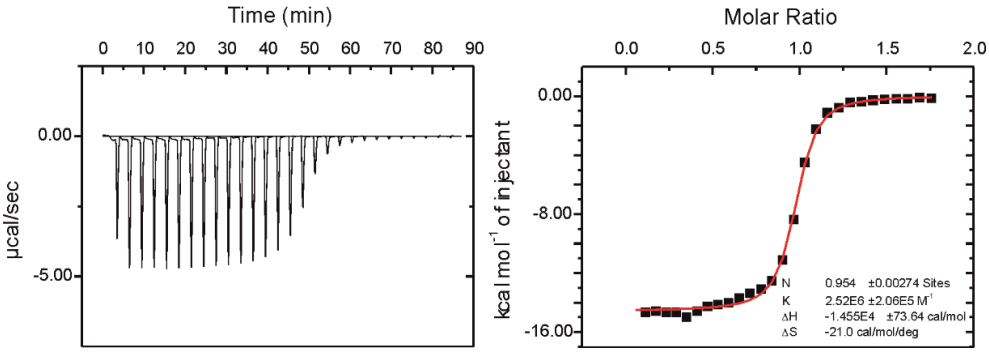

Figure 28. Left — Traces of the raw data of the titration experiment of 1.1×10^{-4} M solution of [2]rotaxane **2**, with TBA·NO_3 solution 0.9×10^{-3} M in chloroform. Right — binding isotherms of the calorimetric titration shown on top. To determine the values of the thermodynamic variables the ITC data was fitted to a 1:1 binding model (red line).

2.4.5.4 ITC experiments of rotaxane with TBA·OCN **7d** in chloroform

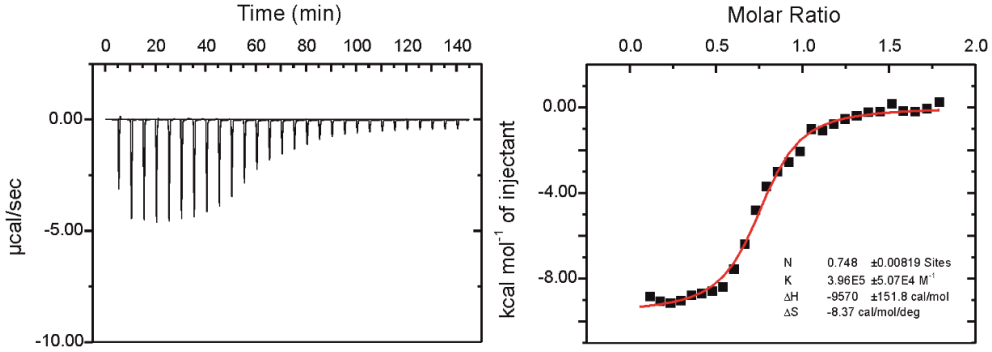

Figure 29. Left — Traces of the raw data of the titration experiment of 1.3×10^{-4} M solution of [2]rotaxane **2**, with TBA·OCN solution 1.1×10^{-3} M in chloroform. Right — binding isotherms of the calorimetric titration shown on top. To determine the values of the thermodynamic variables the ITC data was fitted to a 1:1 binding model (red line).

2.4.6 ITC experiments in acetone

2.4.6.1 ITC experiments of rotaxane with TBA·Cl **7a** in acetone

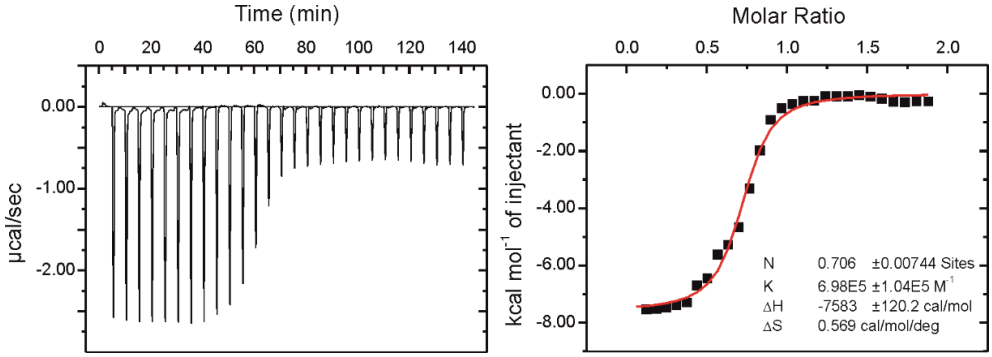

Figure 30. Left — Traces of the raw data of the titration experiment of 1.2×10^{-4} M solution of [2]rotaxane **2**, with TBA·Cl solution 1.1×10^{-3} M in acetone. Right — binding isotherms of the calorimetric titration shown on top. To determine the values of the thermodynamic variables the ITC data was fitted to a 1:1 binding model (red line).

2.4.6.2 ITC experiments of rotaxane with TBA·NO_3 **7c** in acetone

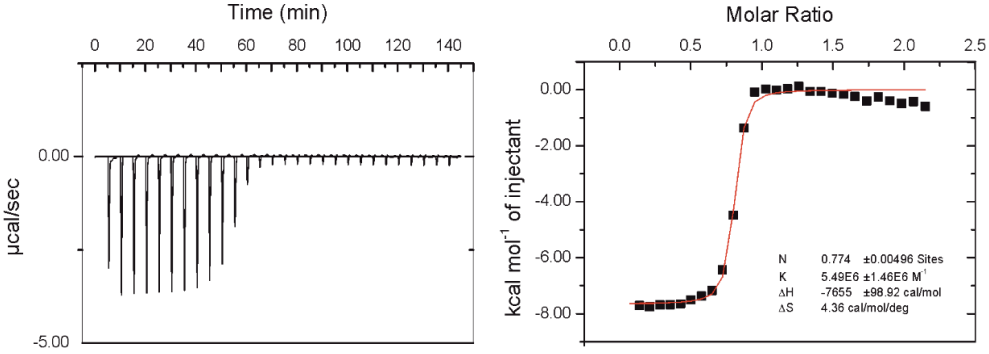

Figure 31. Left — Traces of the raw data of the titration experiment of 1.5×10^{-4} M solution of [2]rotaxane **2**, with TBA·NO_3 solution 1.2×10^{-3} M in acetone. Right — binding isotherms of the calorimetric titration shown on top. To determine the values of the thermodynamic variables the ITC data was fitted to a 1:1 binding model (red line).

2.4.6.3 ITC experiments of rotaxane with TBA·OCN **7d** in acetone

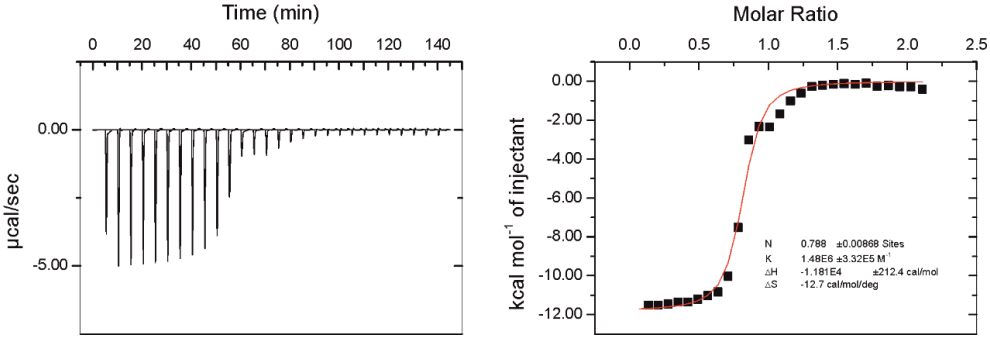

Figure 32. Left — Traces of the raw data of the titration experiment of 1.2×10^{-4} M solution of [2]rotaxane **2**, with TBA·OCN solution 1.1×10^{-3} M in acetone. Right — binding isotherms of the calorimetric titration shown on top. To determine the values of the thermodynamic variables the ITC data was fitted to a 1:1 binding model (red line).

2.5 References and notes

[1] Busschaert, N.; Caltagirone, C.; Van Rossom, W.; Gale, P. A., *Chem. Rev.* **2015,** *115* (15), 8038-8155.
[2] Wilmore, J. T.; Beer, P. D., *Adv. Mater.* **2024,** *36* (14), 2309098.
[3] Mullaney, B. R.; Thompson, A. L.; Beer, P. D., *Angew. Chem., Int. Ed.* **2014,** *53* (43), 11458-11462.
[4] Brown, A.; Mennie, K. M.; Mason, O.; White, N. G.; Beer, P. D., *Dalton Trans.* **2017,** *46* (39), 13376-13385.
[5] Plais, R.; Clavier, G.; Salpin, J.-Y.; Gaucher, A.; Prim, D., *Eur. J. Org. Chem.* **2023,** *26* (9), e202201281.
[6] Lim, J. Y. C.; Bunchuay, T.; Beer, P. D., *Chem. Eur. J.* **2017,** *23* (19), 4700-4707.
[7] Martí-Centelles, V.; Beer, P. D., *Chem. Eur. J.* **2015,** *21* (26), 9397-9404.
[8] Robinson, S. W.; Beer, P. D., *Org. Biomol. Chem.* **2017,** *15* (1), 153-159.
[9] Langton, M. J.; Duckworth, L. C.; Beer, P. D., *Chem. Commun.* **2013,** *49* (77), 8608-8610.
[10] Brown, A.; Lang, T.; Mullen, K. M.; Beer, P. D., *Org. Biomol. Chem.* **2017,** *15* (21), 4587-4594.
[11] Romero, J. R.; Aragay, G.; Ballester, P., *Chem. Sci.* **2017,** *8* (1), 491-498.
[12] Molina-Muriel, R.; Romero, J. R.; Li, Y.; Aragay, G.; Ballester, P., *Org. Biomol. Chem.* **2021,** *19* (45), 9986-9995.
[13] Molina-Muriel, R.; Aragay, G.; Escudero-Adán, E. C.; Ballester, P., *J. Org. Chem.* **2018,** *83* (21), 13507-13514.
[14] Perdew, J. P., *Phys. Rev. B* **1986,** *33* (12), 8822-8824.
[15] Eichkorn, K.; Weigend, F.; Treutler, O.; Ahlrichs, R., *Theor. Chem. Acc.* **1997,** *97* (1), 119-124.
[16] Sierka, M.; Hogekamp, A.; Ahlrichs, R., *J. Chem. Phys.* **2003,** *118* (20), 9136-9148.
[17] Grimme, S.; Ehrlich, S.; Goerigk, L., *J. Comput. Chem.* **2011,** *32* (7), 1456-1465.
[18] Grimme, S.; Antony, J.; Ehrlich, S.; Krieg, H., *J. Chem. Phys.* **2010,** *132* (15).
[19] Rappoport, D.; Furche, F., *J. Chem. Phys.* **2010,** *133* (13).
[20] Schäfer, A.; Horn, H.; Ahlrichs, R., *J. Chem. Phys.* **1992,** *97* (4), 2571-2577.
[21] TURBOMOLE V7.0 2015, a Development of University of Karlsruhe and Forschungszentrum Karlsruhe GmbH, 1989–2007, TURBOMOLE GmbH, Since 2007. Available online: https://www.turbomole.com.
[22] Ahlrichs, R.; Bär, M.; Häser, M.; Horn, H.; Kölmel, C., *Chem. Phys. Lett.* **1989,** *162* (3), 165-169.
[23] Koch, W.; Holthausen, M. C., *A chemist's guide to density functional theory*. John Wiley & Sons: 2015.
[24] Mirabella, C. F. M.; Aragay, G.; Ballester, P., *Chem. Sci.* **2023,** *14* (1), 186-195.
[25] Sessler, J. L.; Gross, D. E.; Cho, W.-S.; Lynch, V. M.; Schmidtchen, F. P.; Bates, G. W.; Light, M. E.; Gale, P. A., *J. Am. Chem. Soc.* **2006,** *128* (37), 12281-12288.
[26] Gross, D. E.; Schmidtchen, F. P.; Antonius, W.; Gale, P. A.; Lynch, V. M.; Sessler, J. L., *Chem. Eur. J.* **2008,** *14* (26), 7822-7827.
[27] https://www.hyperquad.co.uk/hyss.htm

[28] Álvarez-Moreno, M.; de Graaf, C.; López, N.; Maseras, F.; Poblet, J. M.; Bo, C., *J. Chem. Inf. Model.* **2015,** *55* (1), 95-103.
[29] Lauer, J. C.; Bhat, A. S.; Barwig, C.; Fritz, N.; Kirschbaum, T.; Rominger, F.; Mastalerz, M., *Chem. Eur. J.* **2022,** *28* (51), e202201527.

UNIVERSITAT ROVIRA I VIRGILI
Receptors based on Aryl-extended Calix[4]pyrrole Scaffolds
Yifan Li

Chapter 3

Acid-catalyzed self-assembly of [4+2] octa-imine cages based on a tetra-amine AE-C[4]P

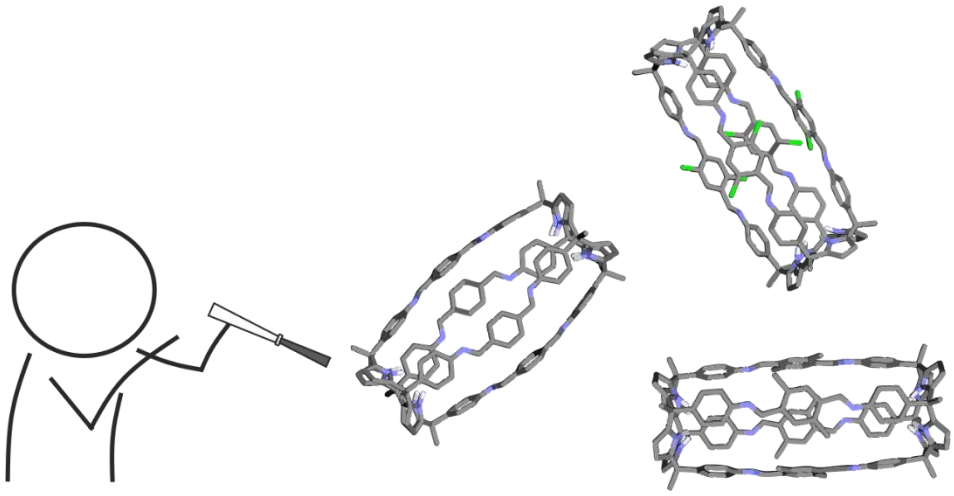

Unpublished results

UNIVERSITAT ROVIRA I VIRGILI
Receptors based on Aryl-extended Calix[4]pyrrole Scaffolds
Yifan Li

3.1 Introduction

The self-assembly of molecular cages constitutes a vibrant and timely topic of interest in supramolecular chemistry. Unlike other organic molecular containers featuring hydrophobic cavities with an open end, cages contain multiple portals connecting their "inner phase" with the bulk solution (outer phase).[1] Moreover, the size of the portals controls the in and out exchange of the guests. Guests residing in the "inner phase" feature different properties than those in the bulk solution, i.e., the surfaces of the included guest become shielded from direct solvation with molecules in the bulk solution, the local concentration of molecules in the "inner phase" is different from that in the bulk solution and the inclusion process may induce the guests to adopt high energy conformations. Taken together, the unique features provided by the nano-environment of the "inner phase" make cage containers attractive designs in many applications (i.e., molecular recognition,[2,3,4] stabilization of reactive species or intermediates,[5] mediation of chemical reactivity or even catalysis). [6,7]

The synthesis of molecular cages starts in the middle 80s via exclusively irreversible covalent bonds.[8,9] The irreversible reactions connecting the building blocks in the final cage typically results in low yields due to the lack of selectivity. The use of dynamic covalent chemistry (DCC)[10,11] for the self-assembly of organic cages takes advantage of the reversible nature of some covalent bonds. The imine linkage[12] is one of the most used reactions to self-assemble dynamic covalent cages. To the best of our knowledge, the first example of using dynamic covalent imine bonds in the self-assembly of a molecular container was reported in 1991 and produced a poly-imine *hemicarcerand* (**Figure 1a**).[13]

In analogy to the active sites of enzymes, Fischer´s lock-and-key model describes the need of complementary size and shape of a substrate (guest) for a rigid host (cage) in order to achieve high binding affinitis.[14] On top of that, molecular containers with polar interiors are better suited to mimic biological receptors (*e.g.*, proteins) compared to non-functionalized counterparts. The endo-functionalization of the containers' cavities is a must for including polar guests and the increase in binding affinity and selectivity.[15] Hydrogen bond donors, like pyrrole,[16,17] urea[18] and triazole[19], are extensively used in constructing molecular cages with polar interiors. A nice example of molecular dynamic covalent container combining both characteristics, is the hexa-imine cage described by Sessler and co-workers (**Figure 1b**). The cage was synthesized via [2+3] Schiff base condensation reaction between 1,3,5-(tris-aminomethyl)benzene derivatives and diformyldipyrrolyl linker.[20]

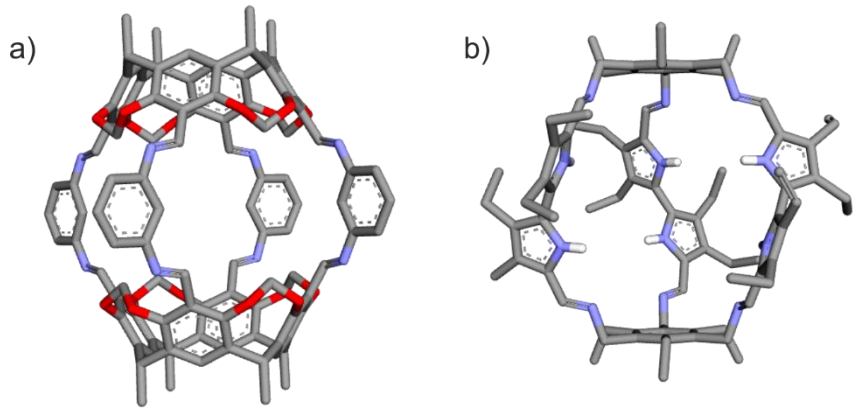

Figure 1. a) Energy minimized structure (MM3) of an [4+2] octa-imine hemicarcerand based on two tetra-carbaldehyde resoncin[4]arene units. b) X-ray structure of a [2+3] pyrrole-based hexa-imine cage (adapted from ref. 20).

The incorporation of calix[4]pyrrole scaffolds in cage architectures resulted in the preparation of molecular containers equipped with polar groups. The first example of using tetra-α-aryl-extend calix[4]pyrrole (AE-C[4]P) scaffolds in poly-imine cage synthesis was reported by our group. The octa-imine cage was prepared via [4+2] condensation reaction between two tetra-formyl AE-C[4]P and four 1,2-diamines.[21] The ditopic template (4-(4-pyridinylethynyl)pyridine-*N*,*N*´-dioxide) was necessary in the self-assembly process. The large association constant assigned to the interaction of an AE-C[4]P with a pyridyl-*N*-oxide knob ($K_a > 10^4$ M^{-1}) induced the quantitative formation of the 2:1 complex between two tetra-aldehyde AE-C[4]Ps and the bis-pyridine-*N*,*N*'-di-oxide at mM concentration. The pre-organized structure of the 2:1 complex, in which the C[4]Ps adopted the cone conformation, assisted the self-assembly of the octa-imine by favoring the formation of intramolecular imine-bonds over the intermolecular counterparts. The single-crystal X-ray diffraction structure of the inclusion complex of the cage with the template suggested that the eight imine bonds adopted a Z-configuration (**Figure 2a**). Unfortunately, the ditopic template could not be removed after the cage assembly, which limited the potential applications of the cage.

To overcome this limitation, recently, we investigated the use of solvent molecules as weakly-bound templates. Our group successfully assembled a non-symmetric [1+1] tetra-imine cage by condensing one tetra-aldehyde AE-C[4]P (1 equiv) with one tetra-amino structural analogue (1 equiv). Two acetonitrile molecules, deriving

from the chloroform:acetonitrile 9:1 solvent mixture used in the self-assembly process, acted as template. The single crystal structure of the tetra-imine cage revealed that the four imine bonds displayed an *E*-configuration. Two different-sized portals were detected in the crystal structure (Portal 1: Average 7.2 Å; Portal 2: Average 4.3 Å) (**Figure 2b**).[22]

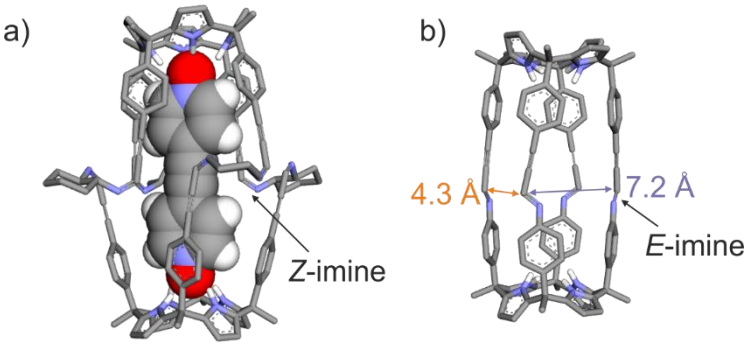

Figure 2. a) X-ray structure of [4+2] octa-imine cage including the ditopic template inside (adapted from ref. 21). b) X-ray structure of [1+1] tetra-imine cage based on two different calix[4]pyrrole hemispheres. Included guest and solvent molecules are omitted for clarity (adapted from ref. 22).

In the examples mentioned above, the formation of the inter- and intra-molecular imine bonds was fast on the human-timescale when the bis-pyridine-*N*,*N*'-di-oxide was used as template. Most likely, the traces of hydrochloric acid present in the chloroform and the intramolecular nature of most imine linkages accelerated the self-assembly. In contrast, the quantitative self-assembly of the [1+1] tetra-imine cage performed in the chloroform: acetonitrile 9:1 solvent mixture was slow on the human-timescale (hours-days). The inclusion of one acetonitrile molecule into the AE-C[4]P scaffolds preorganized them in the cone conformation but did not favor the formation of the intra-molecular imine linkages. Thus, the formation of the thermodynamically more stable product, the [1+1] cage, required longer times owing to the formation of partially reacted intermediates. Most likely, the addition of acid would have favored the reversibility of the imine bond formation allowing a faster equilibration of the mixture (Dynamic Combinatorial Library).

The substituents present in the components of the molecular containers have an influence on the cavity properties. In recent years, different substituent effects were disclosed. For example, by increasing the steric hindrance,[23] changing the electrostatic potential of the cavity,[24] and transferring protons from the "outer phase" to the "inner phase" by means of a proton wire mechanism.[25]

The present work aims to extend the use of imine bonds in the self-assembly of organic cages with sizeable and polar interiors. In this chapter, we will describe the self-assembly of a series of [2+4] octa-imine cages. The condensation reactions between two (2 equiv) tetra-amino C[4]P units and four (4 equiv) of 1,4-dicarboxyaldehyde-benzene linkers in a chloroform: acetonitrile 9:1 solvent mixture will induce the quantitative self-assembly of the octa-imine cages. We will show that acetonitrile molecules act as templates. We will also evaluate the role of adding a Lewis acid to the solvent mixture to catalyze the self-assembly of the octa-imine cages. Finally, we will briefly compare the polar cavities of the prepared octa-imine cages.

3.2 Design

Octa-imine cages **1**-**4** (Scheme 1) were designed to increase the volume of the cylindrical cavity offered by the heterodimeric tetra-imine cage recently reported by our group (**Figure 3**).[22] Although both cages possess a polar cavity with two converging endo-binding sites located at the end of their hemispheres, the self-assembly of the octa-imine container involves six molecular components, [4+2], in contrast to the two components, [1+1], present in the tetra-imine scaffold. To ease the self-assembly process of the octa-imines, we opted to use short and rigid dialdehyde aromatic linkers, i.e., 1,4-dicarboxyaldehyde-benzene derivatives. In doing so, the walls of the octa-imine cages will contain a rigid and fully conjugated aromatic system. We selected the simple 1,4-dicarboxyaldehyde-benzene **5** as linker in our initial self-assembly experiments.

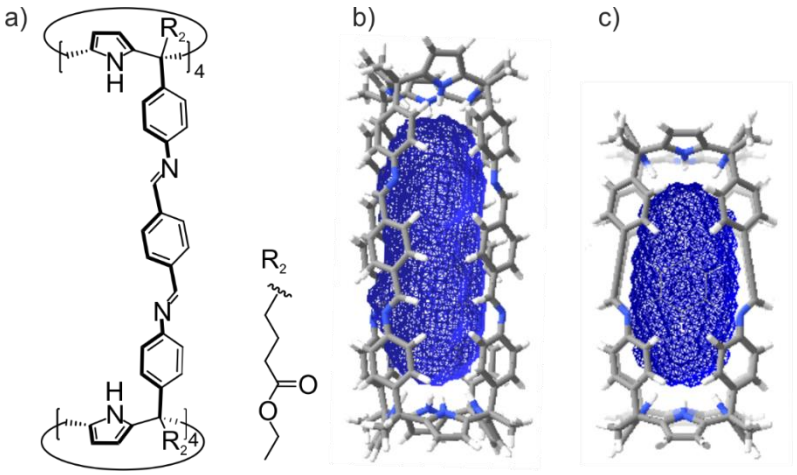

Figure 3. a) Line drawing structure of cage **1**. The energy-minimized cage **1** b) and [1+1] tetra-imine cage c). The volume of their cavity was calculated using the program Swiss PDB viewer.

Our idea was to use two additional dicarboxyaldehyde linkers, **6** and **7,** containing two *meta-meta'* chloro and methyl substituents, respectively, and study the substituent effect on the binding properties of the octa-imine cage. The substituents of the linker are expected to produce different levels of shielding to the protons of included molecules located in the middle of the inner cavity of the cage, as well as modify the overall electrostatic potential of the aromatic walls.[26]

We also selected dicarboxaldehyde linker **8** because it provided an additional feature to those commented for the previous ones. In particular, linker **8** may stabilize the rotamers of the octa-imine cage imine bonds by the formation of intramolecular hydrogen bonds (**Figure 4**). A potential advantage in using linker **8** relies on the possibility of proton transfer between the inner cavity of the cage and the bulk solution through a proton wire mechanism as described in the resorci[4]arene hexamer.[25]

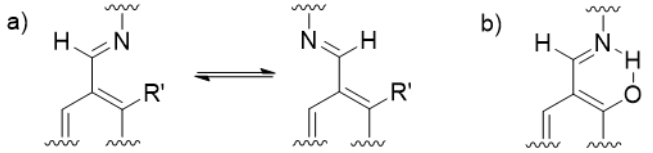

Figure 4. a) Possible rotamers of imine bonds in the octa-imine cages **1-3**. Most likely, the rotamer having the substituent in a cis-arrangement with respect to the hydrogen atom will be favored. b) The imine bonds in the octa-imine cage **4** are expected to be locked in a preferred rotamer due to the formation of an intramolecular hydrogen bonding.

In summary, compared to previous reports, the new octa-imine cages feature larger cylindrical cavities defined by rigid aromatic walls. The symmetric structure of multi-component cages allows the incorporation of different linkers. Thus, the binding properties of the cages are expected to be tuned by changing the nature of the carboxaldehyde linkers.

3.3 Synthesis

3.3.1 Acid catalyzed self-assembly of octa-imine cages

Self-Assembly of Cage **1**

In our hands, the self-assembly of the octa-imine cage **1** following the solvent-template method described in the Ph.D. thesis of Ciara Mirabella displayed reproducibility issues. In particular, the time required for achieving the quantitative self-assembly of the octa-imine cage **1** depended on the batch of deuterated chloroform employed. This result suggested that the amount of hydrochloric acid present in the $CDCl_3$ solutions influenced the reaction rate of the self-assembly process. To obtain experimental conditions leading to a reproducible self-assembly process of octa-imine **1**, we decided to investigate the effect exerted by adding Brønsted acids to the $CDCl_3$: CD_3CN 9:1 solvent mixture.

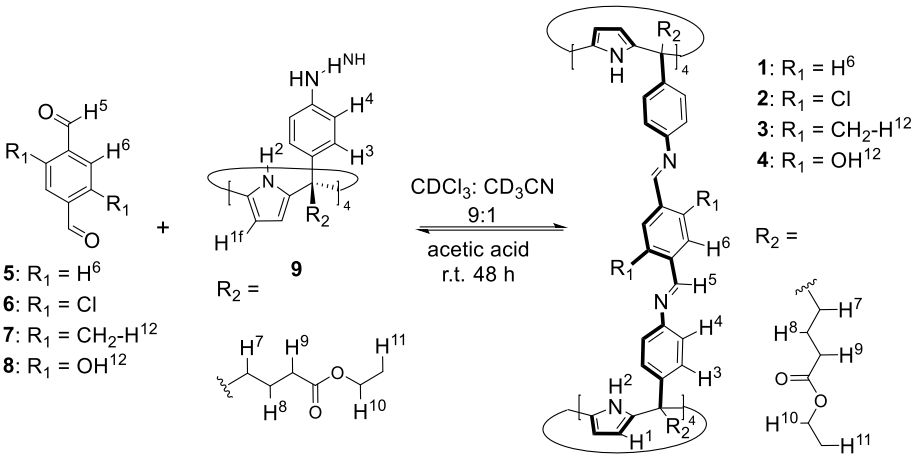

Scheme 1. Synthetic scheme of the self-assembly process for preparing calix[4]pyrrole octa-imine cages **1**-**4** from tetra-amine calix[4]pyrrole **9** and dialdehyde linkers **5**-**8.** The corresponding proton assignment is also shown.

Firstly, we monitored the self-assembly of the octa-imine cage **1** by ^{1}H NMR spectroscopy using a $CDCl_3$:CD_3CN 9:1 solvent mixture in which the putative HCl of the $CDCl_3$ was removed. To this end, we passed the $CDCl_3$ used to prepare the solvent mixture through a basic alumina column (4 mL/100 mg). The ^{1}H NMR spectrum of a solution of calix[4]pyrrole **9** (4 mM) and dialdehyde linker **5** (8.8 mM) (1:2.2 molar ratio) acquired immediately after mixing the two compounds in a freshly prepared

solvent mixture containing alumina treated $CDCl_3$, showed exclusively sharp proton signals for the two starting materials (**Figure 5**). This observation indicated a lack of formation of imine bonds. After heating the solution for 4 h at 313 K, the ^{1}H NMR spectrum revealed a decrease in the intensity of the signals assigned to **5** and **9** and the emergence of broad signals. This observation indicated the formation of oligomeric aggregates owing to the formation of imine bonds.

After heating the solution at 313 K for 3 days, the ^{1}H NMR spectrum evidenced that the proton signals of the starting materials had almost disappeared. The most significant signals were quite broad displaying at their centers chemical shift values that agreed with those of the proton atoms of the octa-imine cage **1**. We prolonged the heating at 313 K for 8 days, and the analysis of the resulting solution using ^{1}H NMR spectroscopy showed the complete disappearance of the signals of the starting material and the increase and sharpening of the set of signals attributed to cage **1**. We assumed that the remaining broadening of the signals assigned to cage **1** might be caused by the chemical exchange between oligomers and the cage being intermediate on the chemical shift timescale. Notably, the diagnostic signal of the imine protons, H^5, in cage **1** was quite sharp and centered at δ = 8.37 ppm.

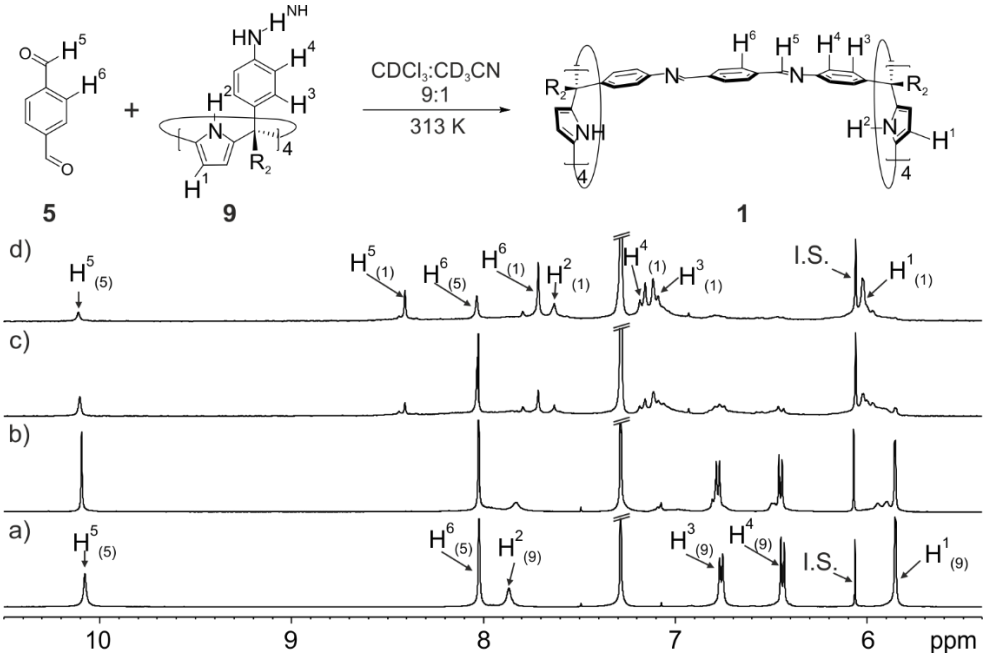

Figure 5. Selected region of the ^{1}H NMR spectra (500 MHz, alumina treated $CDCl_3$:CD_3CN 9:1 mixture) of a solution of tetra-amino calix[4]pyrrole **1** and dialdehyde linker **5** in 1:2.2 molar ratio heated at 313K for a) 0 h, b) 8 h, c) 3 days, d) 8 days. i.s. = 1,3,5-trimethyoxybenzene.

In order to prove the critical role played by acid traces in the self-assembly of the octa-imine cage **1**, we selected acetic acid and hydrochloric acid as Brønsted acid catalysts for the self-assembly process. We studied three different concentrations (0.001 mM, 0.01 mM, and 0.1 mM) of the acid catalyst (acetic acid or hydrochloric acid) in the $CDCl_3$:CD_3CN 9:1 solvent mixture. In these experiments, and to avoid additional variables, the used $CDCl_3$ was not passed through a basic alumina plug before the addition of the acid catalysts to the solvent mixture.

The results showed that after 24 hours, the self-assembly of cage **1** was not accelerated when the concentration of any of the acids was 0.01 mM or lower. However, when the concentration of the acid catalysts was 0.1 mM, the ^{1}H NMR spectrum of the solution acquired immediately after mixing the tetra-amino calix[4]pyrrole **9** and the linker **5** in a 1:2.2 molar ratio only showed broad signals (**Figure 6**). This observation indicated the immediate formation of imine bonds after mixing the components and evidenced that the self-assembly process of cage **1** is accelerated in the presence of the acids.

After 2h at room temperature, we observed the appearance of the proton signals attributed to the assembly of cage **1**. After 48 h, cage **1** was quantitively assembled based on the ratio of integral values of selected signals with those of an internal standard (1,3,5-trimethoxy-benzene).

Considering that the two acids had a similar acceleration effect on the self-assembly process of cage **1**, we selected acetic acid as the most suitable catalyst for its self-assembly. We wanted to avoid any secondary effect of a strong acid like HCl in the host-guest studies of the assembled cages. We surmised that a strong acid like HCl may protonate to a certain extent polar neutral guests (like pyridine *N*-oxide and formamide), thus affecting the accurate determination of the binding properties of the octa-imine cages.

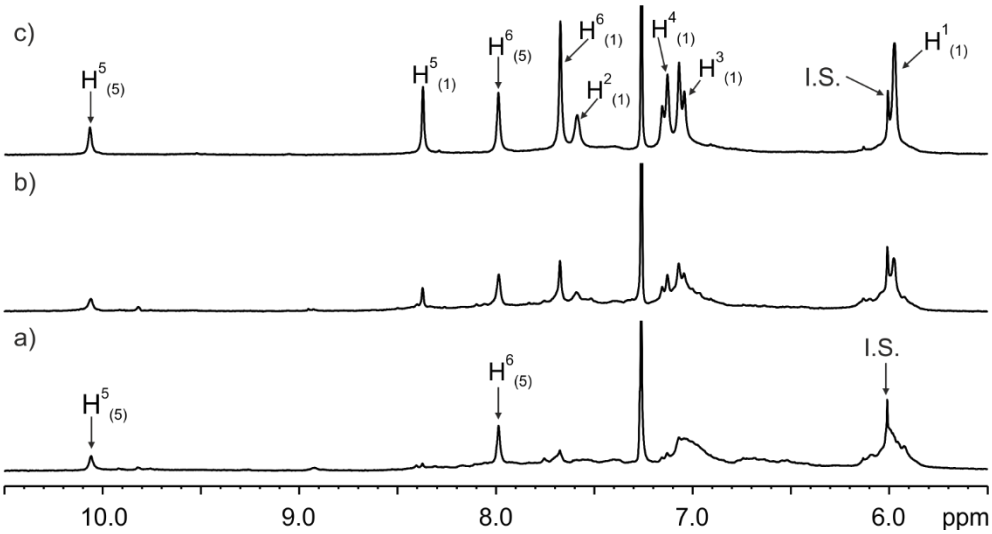

Figure 6. Selected region of the ^{1}H NMR spectra (500 MHz, at 298 K, $CDCl_3$:CD_3CN 9:1 mixture) of a solution of a mixture of tetra-amino calix[4]pyrrole **1** and dialdehyde linker **5** in 1:2.2 molar ratio also containing 0.1 mM acetic acid at 298 K a) 0 h, b) 2 h, c) 48 h. i.s. = 1,3,5-trimethyoxybenzene.

Cage **1** was characterized by a complete set of high-resolution spectra (1D and 2D NMR experiments and MS). The number of signals in the ^{1}H NMR spectrum of cage **1** agrees with an apparent D_{4h} symmetry. The pyrrole β-proton signals of the assembled cage **1** ($H^2_{(1)}$) are downfield shift compared to AE-C[4]P **9** ($H^2_{(9)}$), suggesting a conformational change of the calix[4]pyrrole scaffold. The ROESY experiment of cage **1** (**Figure 7**) showed nOE cross-peaks between the imine proton ($H^5_{(1)}$) and the protons of the *meso* aromatic panel ($H^4_{(1)}$). Notably, the aromatic proton signal of the linker, ($H^6_{(1)}$), resonated as a sharp singlet. This finding indicated that the rotation of the linker around the single bond with the imine nitrogen is fast on the chemical shift timescale (**Figure 4**).

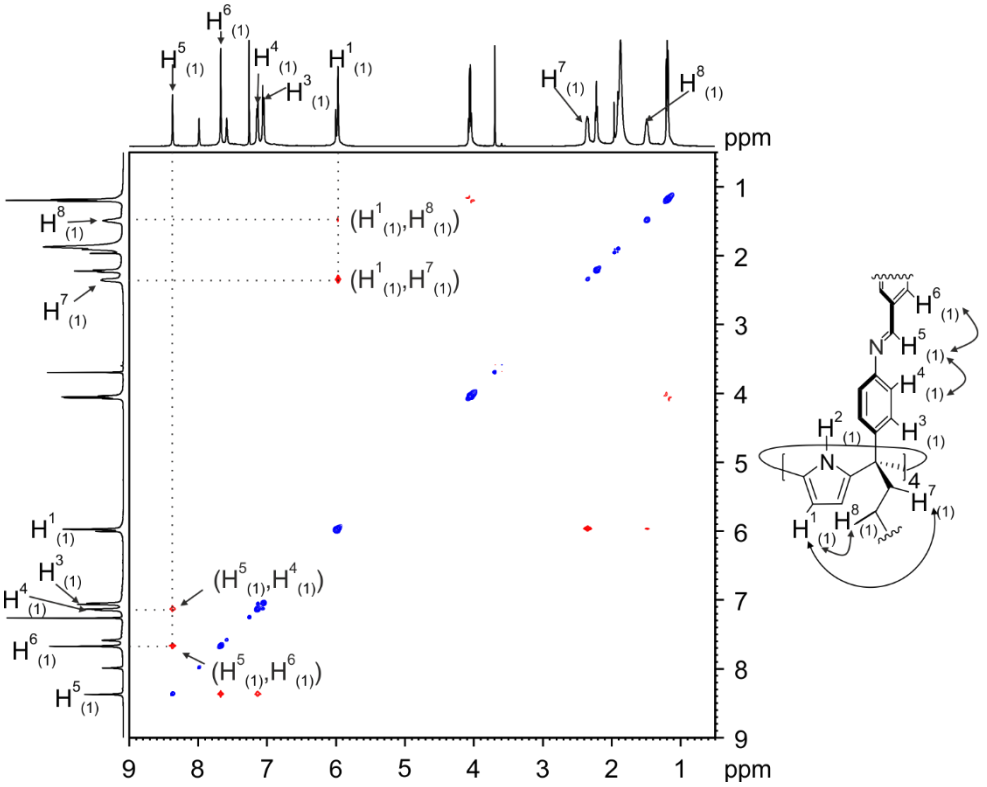

Figure 7. 2D ^{1}H ROESY NMR (500 MHz, at 298 K, $CDCl_3$:CD_3CN 9:1, d_8 = 0.3 s) spectrum of the self-assembled cage **1**. See Scheme 1 for the proton assignment.

Single crystals suitable for X-ray diffraction were obtained from the slow diffusion of *p*-xylene into a 9:1 $CDCl_3$:CD_3CN solution of the inclusion complex of cage **1** with 4,4-(buta-1,3-diyne-1,4-diyl)bis-pyridine *N*-oxide guest (**Figure 8**). Remarkably, in the solid state, cage **1** showed the eight imine bonds in *E*-configuration and directionally oriented in pairs, generating two differently sized portals of the cage (Portal 1: average dCim1···Cim2= 6.6 Å; Portal 2: average dCim1···Cim4 = 5.1 Å). The solid-state structure of the cage featured D_{2h} symmetry instead of the D_{4h} observed in the solution. This result suggested that the aromatic panels of the cage are freely rotating around its single bonds in solution.

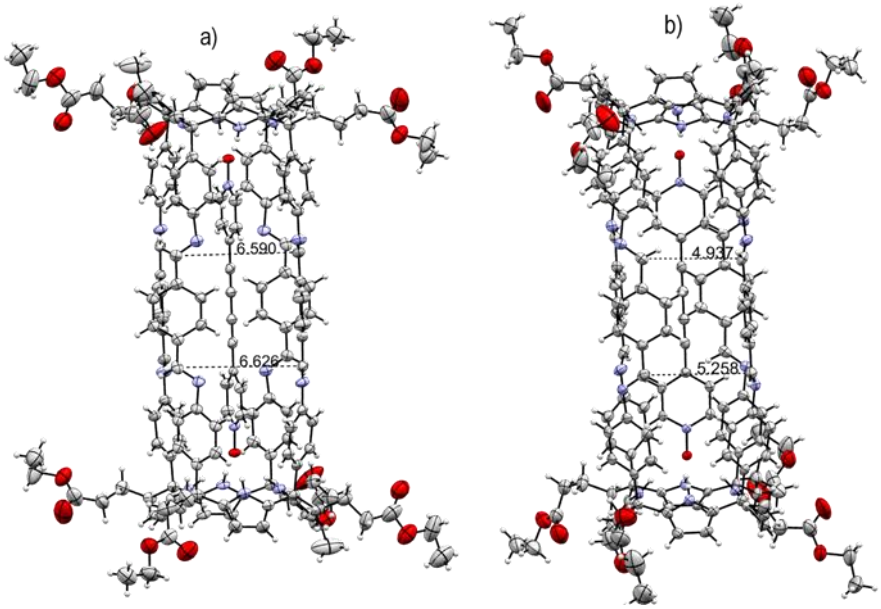

Figure 8. Two different views (a and b) of the X-ray crystal structure of the octa-imine cage **1** with 4,4-(buta-1,3-diyne-1,4-diyl)bis-pyridine *N*-oxide guest included in the cavity. Thermal ellipsoids for C, N, and O atoms are set at 50% probability. H atoms are shown as a sphere of 0.30 Å in diameter.

A ^{1}H DOSY NMR experiment assigned a diffusion coefficient of 3.10 ± 0.07 × 10^{-10} m^2/s to the protons of cage **1**. As expected, the diffusion coefficient of linker **5** was determined to be an order of magnitude larger, 1.40 ± 0.4 × 10^{-9} m^2/s.

Aiming at preparing cage **1** on a relatively large scale and removing the excess of **5** used in the solution, we assembled the cage at the same concentration mentioned above and with acetic acid as a catalyst but using a larger volume of solvent mixture. After 48 hours, the solvent mixture was removed under vacuum, and the solid residue was dissolved in dichloromethane (DCM). The precipitation of cage **1** was induced by adding 10% volume of methanol compared with DCM and slow evaporation of the solvent in a vacuum. The solid precipitate was filtered, washed with methanol and dried in a vacuum to afford pure cage **1** as a yellow solid.

3.3.2 Self-assembly of cages **7-9** featuring substituted linkers

Using an identical procedure to that described for cage **1**, separated solutions of the tetra-amino calix[4]pyrrole **9**, in a 9:1 $CDCl_3$:CD_3CN solvent mixture containing 0.1 mM acetic acid, with the di-aldehyde linkers **6-8**, respectively, in 1:2.2 molar ratios produced the quantitative self-assembly of the octa-imine cages **2-4**. The quantitative self-assembly processes of cages **2**- **4** required longer times (additional 24 h) than that of cage **1**.

Cages **2-4** were characterized by 1D and 2D ^{1}H NMR spectroscopy. The ^{1}H 2D ROESY spectra of cages **2**-**4** revealed intramolecular nOe cross-peaks between the imine proton (H^5) and the protons of *meso*-aromatic panels (H^3). However, we could not determine the preferential location of the substituents in the linkers with respect to the hydrogen atom of the imine linkages.

For cages **1-3**, the proton signals of the linker panel $H^{6f}_{(5\text{-}7)}$ moved upfield shift after the assembly of the final cage $H^6_{(1\text{-}3)}$. Contrarily, for cage **4**, the protons of the linker panel in cage $H^6_{(4)}$ appeared slightly downfield shifted compared to the same protons in the free panel $H^{6f}_{(8)}$. The large downfield shift (2.75 ppm) of the OH proton signal from $H^{12f}_{(8)}$ to $H^{12}_{(4)}$ (**Figure 9c**) suggested the formation of intramolecular hydrogen bonds between OH and imine bonds.[27]

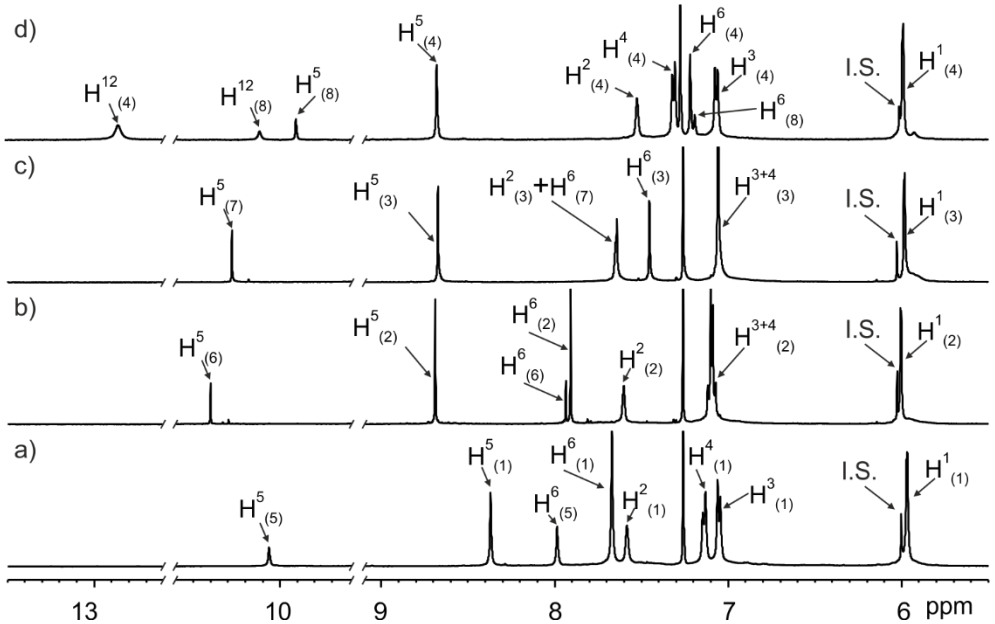

Figure 9. Selected regions of the ^{1}H NMR spectra (500 MHz, 298 K, $CDCl_3$:CD_3CN 9:1 mixture) of a 2 mM solution of (a) **1**, (b) **2**, (c) **3**, (d) **4**. i.s. = 1,3,5-trimethyoxybenzene.

3.3.3 Filling of the cages with acetonitrile molecules. The influence of the linker in the in-out exchange of acetonitrile molecules.

The size of the internal cavity of the octa-imine cages is approximately 300 $Å^3$, which fluctuates with the size of guest inside of the cavity and the conformational flexibility of the portals. The different substituents of the linkers can slightly influence the cavity volume (up to 10% of variation). The 55% packing coefficient rule[28] suggests that the inclusion of up to three molecules of acetonitrile in the internal cavities of the cages is possible.

We are aware from previous studies that the polar cavities of the C[4]P hemispheres must include one hydrogen-bonded acetonitrile molecule. There is room for another acetonitrile in the middle of the cage, sandwiched by the two molecules bound at the hemispheres. However, the central aromatic cavity of the cages can also be occupied by the substituents of their linkers. In order to demonstrate the inclusion of acetonitrile molecules in the cages, we performed gradient-enhanced nuclear overhauser effect experiments[29] (1D-GOESY) using separate solutions of the **1**-**4** cages assembled in a 9:1 $CDCl_3$:CH_3CN solvent mixture (**Figure 10**). The selective excitation of the signal of free CH_3CN (δ= 1.94 ppm) produced, in all cases, difference GOESY spectra with an additional signal of low intensity resonating *c.a.* 0.3 ppm ($\Delta\delta$ = -1.91 ppm). This upfield shifted signal was assigned to the protons of the acetonitrile molecules included in the cage, where they experienced the shielding effect of the aromatic rings shaping the internal cavity. The included acetonitrile molecules are involved in a slow chemical exchange on the chemical shift timescale with the molecules in the bulk solvent.

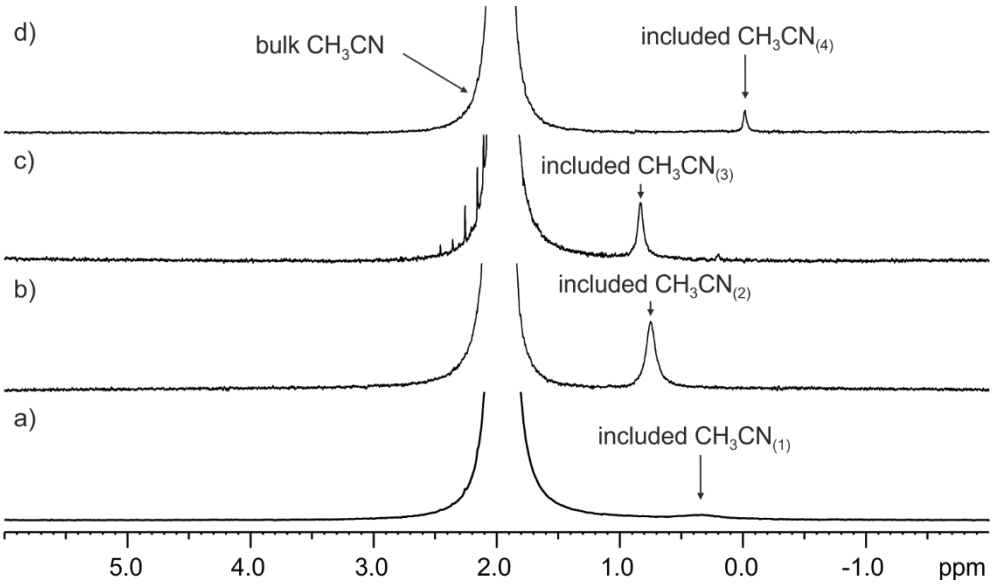

Figure 10. GOESY ^{1}H NMR experiment performed on $CDCl_3$:CH_3CN 9:1 solution of cages (a) **1**, (b) **2**, (c) **3**, (d) **4** by selective irradiation of the solvent peak (2.08 ppm). The observation of an upfield singlet in panels (a-d) indicated the inclusion of a solvent molecule.

Notably, GOESY experiments of the cages in a 9:1 $CHCl_3$:CD_3CN solvent mixture produced difference spectra displaying exclusively the irradiated free $CHCl_3$ signal of solvent (**Figure 24**). This result indicated that either chloroform is too big to be included in the cages or the solvent exchange dynamics (too fast or too slow on the chemical shift timescale) are not suitable for their characterization by GOESY experiments. The ^{1}H NMR spectra of cage **3** in the 9:1 $CDCl_3$:CH_3CN solvent mixture were used to determine an approximate integral value for the signal centered at *c.a.* 0.3 ppm. Considering all the limitations of the integration, i.e., reduced intensity of the signal and the dynamic range problem,[30] we determined an integral value accounting for 5-6 protons (**Figure 11**). This result suggested that at least two molecules of acetonitrile are included in the cages. We did not obtain experimental evidence for the inclusion of another acetonitrile molecule in the middle of the cage. It can be expected that multi CH-π and π-π interactions between the central aromatic panels induce the collapse of the middle aromatic cavity not favoring the inclusion of third acetonitrile molecule.

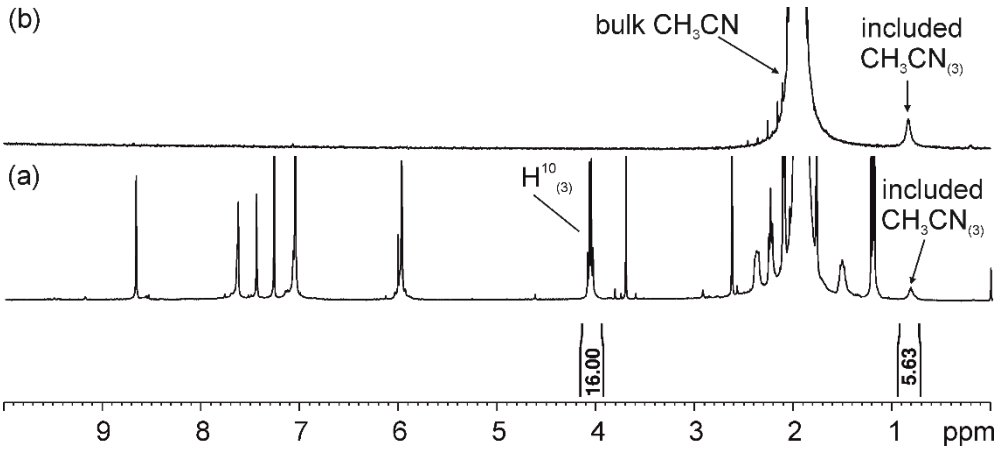

Figure 11. (a) ^{1}H NMR spectrum (500 MHz, at 298 K, $CDCl_3$: CH_3CN 9:1) of $(CH_3CN)_2\subset$**3**. (b) ^{1}H GOESY NMR of $(CH_3CN)_2\subset$**3** with excitation at 1.94 ppm (signal of the bulk solvent). See (**Scheme 1.**) for the proton assignment.

Although the chemical shift value assigned to the included acetonitrile molecules was slightly different for the four cages, their detection through GOESY experiments suggested a similar exchange barrier. The GOESY experiment of AE-C[4]P **9** in the 9:1 $CDCl_3$:CH_3CN solvent mixture did not reveal the proton singlets for the bound acetonitrile. Most likely, the chemical exchange between the free and bound acetonitrile was fast on the chemical shift timescale.[31] Taken together, we propose that the exchange of the included acetonitrile molecules in the [2+4] octa-imine cages occur through a "French doors" mechanism, which is independent of the nature of the substituents in the linkers.

3.4 Conclusions

We reported the self-assembly of [2+4] octa-imine cages (**1**-**4**) via an eight-fold condensation reaction between two units of an aryl-extended tetra amino-calix[4]pyrrole (**9**) and four units of an bis-aldehyde linker (**5-8**) in a 9:1 $CDCl_3$:CD_3CN solvent mixture. We used acetonitrile as a weakly-bound template to pre-organize the calix[4]pyrrole units in cone conformation and favor the formation of the cages as the most stable thermodynamic products. The self-assembly of the cages was accelerated by adding Brønsted acids as catalysts. The use of acetic acid at 0.01 mM concentration induced the quantitative formation of the cages after several days. We showed that at least two molecules of acetonitrile are included in cages' inner cavity. The presence of weakly bound acetonitrile molecules in the cages augurs well for their use as selective molecular receptors and unprecedented reaction vessels.

3.5 Experimental section

3.5.1 General information and instrumentation

^{1}H NMR, ^{13}C NMR and 2D NMR spectra were recorded on a Bruker Avance 400(400 MHz for ^{1}H NMR) and Bruker Avance 500 (500 MHz for ^{1}H NMR). Deuterated solvents from Eurisotop were used for the NMR studies to synthesize dynamic covalent cages. Chemical shifts are given in ppm relative to residual solvents.
Tetra-amino calix[4]pyrroles **9**[32] was synthesized by adapting previously reported procedures.

3.5.2 Synthesis and Characterization

3.5.2.1 Synthesis of imine cage **1**

Procedure A:
In an NMR tube, 0.25 mL of an 8 mM solution of tetra-amino calix[4]pyrrole **9** in $CDCl_3$: CD_3CN 9:1 mixture containing 0.01 mM acetic acid, a solution of linker **5**-**8** (17.6 mM, 0.25 mL) in the same mixture of solvents was added. The mixture was then left at room temperature for 48 hours. The mixture turned yellow color and provided cages **1**-**4** in 90% yields (according to the relative integrals of the signals of the cage and those of the i.s. in solution)

1: ^{1}H NMR (500 MHz, $CDCl_3$:CD_3CN 9:1) δ(ppm): 8.37 (s, 8H), 7.68 (s, 16H), 7.60 (br.s, 8H), 7.14 (d, *J* = 8.1 Hz, 16H), 7.06 (d, *J* = 8.1 Hz, 16H), 5.96 (s, 16H), 4.06 (q, J = 7.1 Hz, 16H), 2.39-2.31 (m, 16H), 2.21 (t, J = 7.3 Hz, 16H), 1.55-1.44 (m, 16H), 1.21 (t, J = 7.1 Hz, 24H). HR-MS (ESI TOF) m/z: $[M+2H]^{2+}$ Calculated for $C_{168}H_{170}N_{16}O_{16}$ = 1333,6485; Found 1333.6630

2: ^{1}H NMR (500 MHz, $CDCl_3$:CD_3CN 9:1) δ(ppm): 8.68 (s, 8H), 7.91 (s, 8H), 7.60 (br.s, 8H), 7.10 (d, *J* = 8.1 Hz, 16H), 7.08 (d, *J* = 8.1 Hz, 16H), 6.00 (d, *J* = 2.4 Hz, 16H), 4.07 (q, J = 7.1 Hz, 16H), 2.39-2.31 (m, 16H), 2.24 (t, J = 7.3 Hz, 16H), 1.55-1.44 (m, 16H), 1.21 (t, J = 7.1 Hz, 24H).

3: ^{1}H NMR (500 MHz, $CDCl_3$:CD_3CN 9:1) δ(ppm): 8.67 (s, 8H), 7.64 (s, 8H), 7.45 (s, 8H), 7.06 (br.s, Hz, 32H), 5.98 (d, *J* = 2.4 Hz, 16H), 4.07 (q, J = 7.1 Hz, 16H), 2.39-2.31 (m, 16H), 2.24 (t, J = 7.3 Hz, 16H),2.10 (s, 24H) 1.55-1.44 (m, 16H), 1.21 (t, J = 7.1 Hz, 24H).

4: ^{1}H NMR (500 MHz, $CDCl_3$:CD_3CN 9:1) δ(ppm): 12.89 (s, 8H), 8.69 (s, 8H), 7.548 (br.s, 8H), 7.33 (d, *J* = 8.5 Hz, 16H), 7.24 (s, 8H), 7.08 (d, *J* = 8.5 Hz, 16H), 6.01 (d, *J* = 2.7 Hz, 16H), 4.06 (q, J = 7.1 Hz, 16H), 2.39-2.31 (m, 16H), 2.21 (t, J = 7.3 Hz, 16H), 1.55-1.44 (m, 16H), 1.21 (t, J = 7.1 Hz, 24H).

Procedure B :

In a dry Schlenk tetra-amino calix[4]pyrrole **9** (18.0 mg, 16.3 µmol, 1.1 equiv.) and linker **5** (4.40 mg, 35.8 µmol, 2.2 equiv.) were dissolved in 4 ml of chloroform:acetonitrile 9:1 mixture containing 0.1 mM of acetic acid. A change in color from beige to yellow was observed. The mixture was stirred at 298 K under Ar protected from light for 48h. Afterwards, the solvent mixture was removed under vacuum. The crude cage was dissolved in 4 mL dichloromethane and 0.4 mL of methanol was added. The partial evaporation of dichloromethane in the vacuum produced the precipitation of a yellow solid which was isolated by filtration. The precipitate was washed with cold methanol to give pure cage **1** in 80% yield.

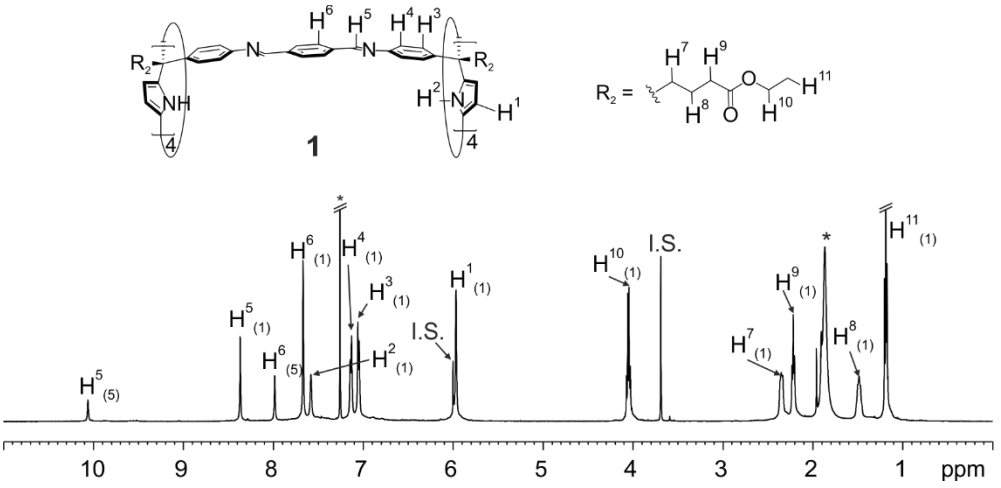

Figure 12. ^{1}H NMR spectrum (500 MHz, at 298 K, $CDCl_3$:CD_3CN 9:1) of $(CD_3CN)_2$⊂**1.**

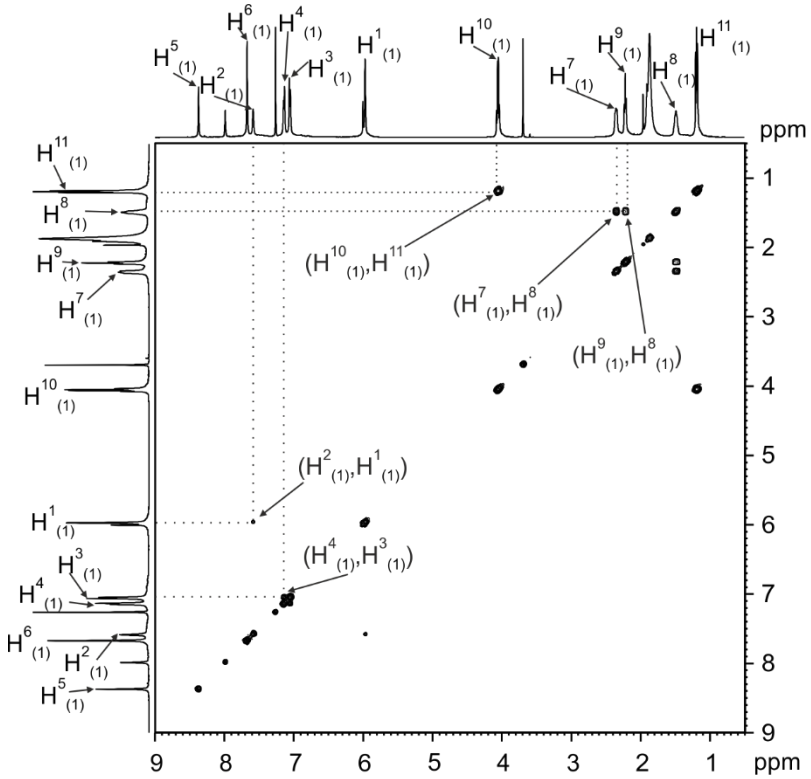

Figure 13. Selected region of ^{1}H-^{1}H COSY NMR (500 MHz, at 298 K, $CDCl_3$: CD_3CN 9:1) of a 2 mM solution of $(CD_3CN)_2\subset$**1** with an excess of bis-aldehyde linker **5**. See **Figure 12** for the proton assignments.

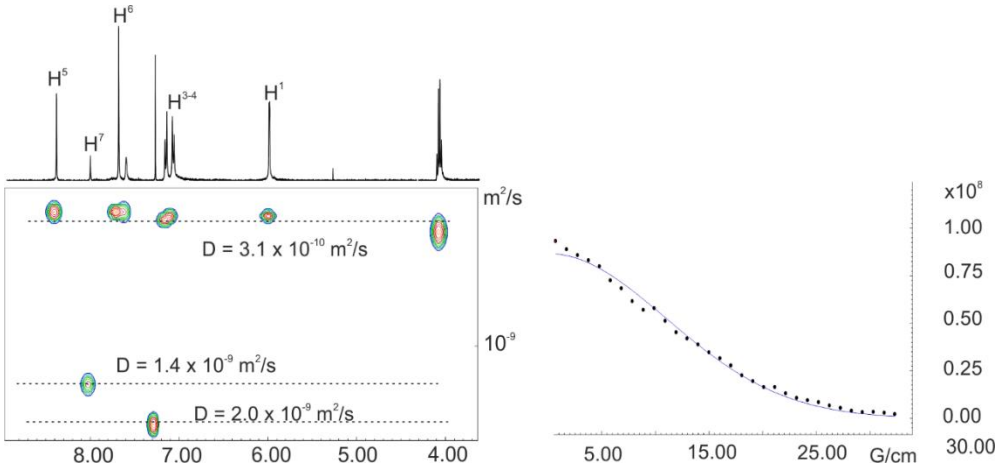

Figure 14. Left) ^{1}H pseudo-2D DOSY NMR profile of octa-imine cage **1** in a 9:1 $CDCl_3$:CD_3CN mixture at 298K and millimolar concentration. Right) Fit of the data to a monoexponential function.

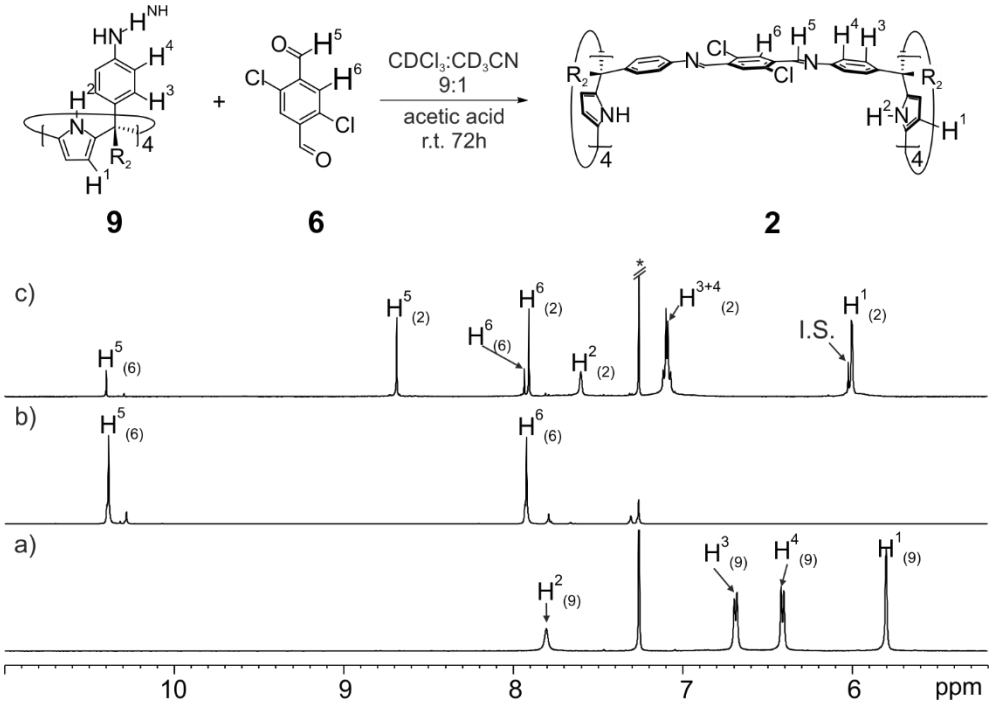

Figure 15. Selected regions of ^{1}H NMR spectra (500 MHz, at 298K, $CDCl_3$:CD_3CN 9:1 mixture) of (a) tetra-amino calix[4]pyrrole **9**, (b) di-aldehyde linker **6**, (c) 1:2 mixture of **9** and linker **6**, containing 0.1 mM acetic acid, after reaction at 298 K for 48 h to give imine cage **2**.

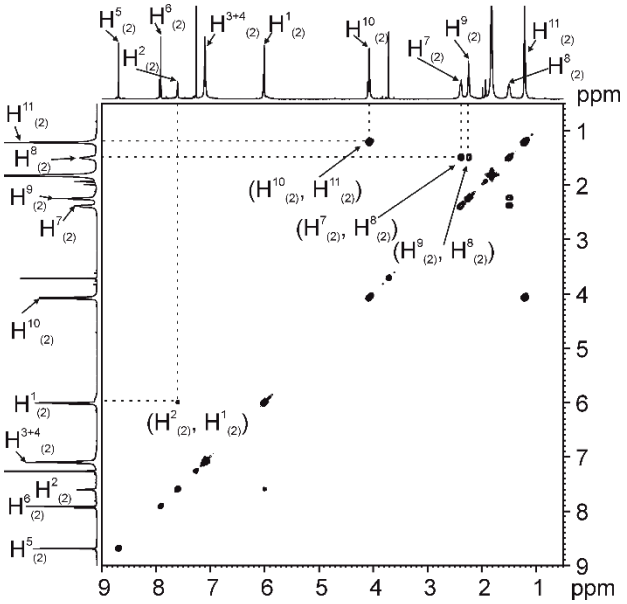

Figure 16. Selected region of ^{1}H-^{1}H COSY NMR (500 MHz, at 298 K, $CDCl_3$: CD_3CN 9:1) of a 2 mM solution of octa-imine cage solvate $(CD_3CN)_2\subset$**2** with an excess of bis-aldehyde linker **6**. See **Figure 15** for the protons assignment.

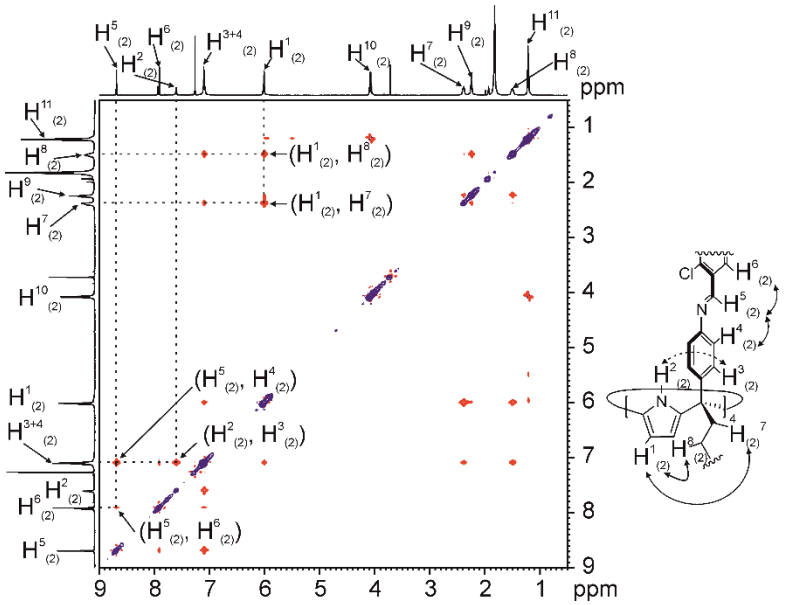

Figure 17. Selected region of ^{1}H-^{1}H ROESY NMR (500 MHz, at 298 K, $CDCl_3$: CD_3CN 9:1, d_8 = 0.30 s) of a 2 mM solution of octa-imine cage $(CD_3CN)_2\subset$**2**. See **Figure 15** for the protons assignment.

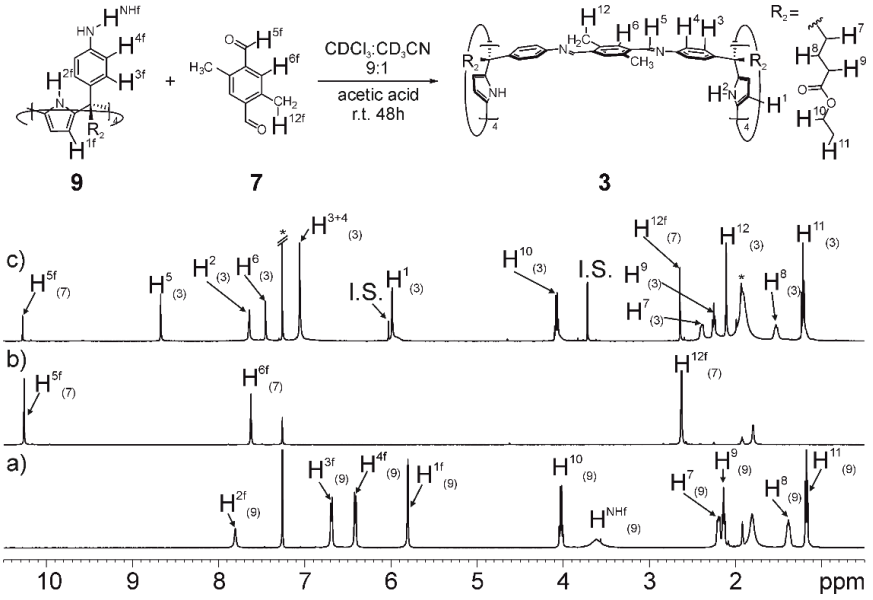

Figure 18. Selected regions of ^{1}H NMR spectra (500 MHz, at 298K, $CDCl_3$:CD_3CN 9:1 mixture) of (a) tetra-amino calix[4]pyrrole **9**, (b) di-aldehyde linker **7**, (c) 1:2 mixture of **9** and linker **7**, containing 0.1 mM acetic acid, after reaction at 298 K for 48 h to give imine cage **3**.

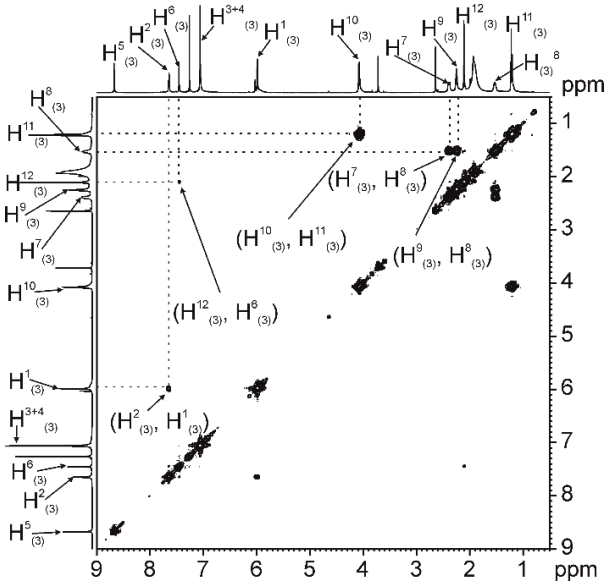

Figure 19. Selected region of ^{1}H-^{1}H COSY NMR (500 MHz, at 298 K, $CDCl_3$: CD_3CN 9:1) of a 2 mM solution of octa-imine cage solvate $(CD_3CN)_2\subset$**3** with an excess of bis-aldehyde linker **7**. See **Figure 18** for the protons assignment.

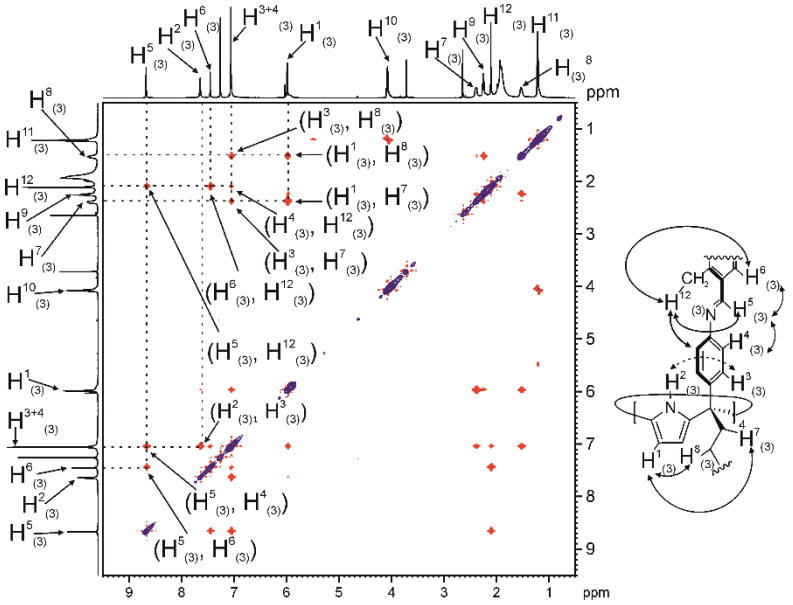

Figure 20. Selected region of ^{1}H-^{1}H ROESY NMR (500 MHz, at 298 K, $CDCl_3$: CD_3CN 9:1, d_8 = 0.30 s) of a 2 mM solution of octa-imine cage $(CD_3CN)_2\subset$**3**. See **Figure 18** for the protons assignment.

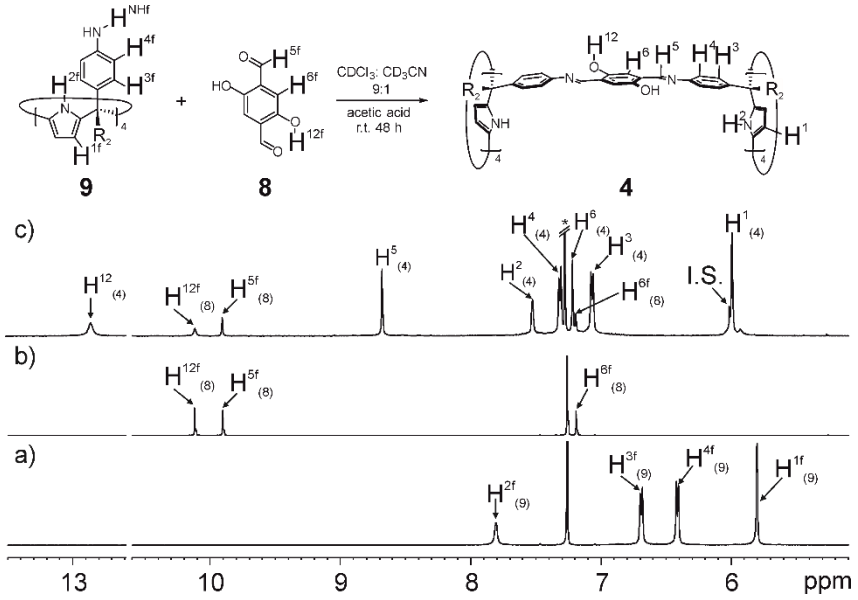

Figure 21. Selected regions of ^{1}H NMR spectra (500 MHz, at 298K, $CDCl_3$:CD_3CN 9:1 mixture) of (a) tetra-amino calix[4]pyrrole **9**, (b) di-aldehyde linker **8**, (c) 1:2 mixture of **9** and linker **8**, containing 0.1 mM acetic acid, after reaction at 298 K for 48 h to give imine cage **4**.

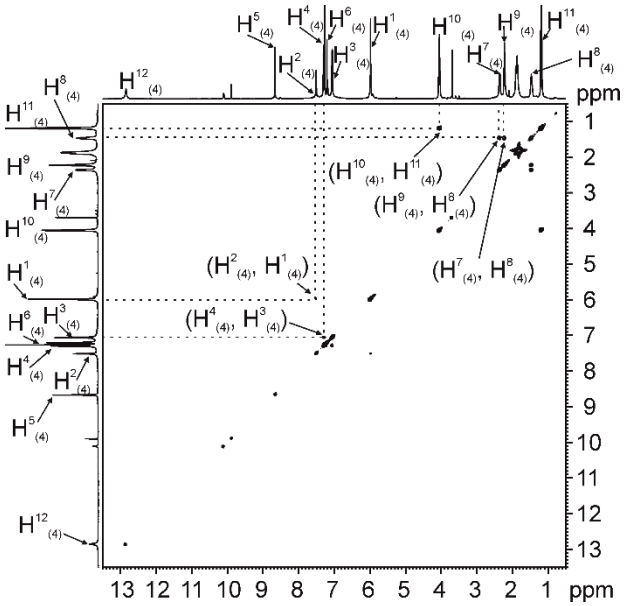

Figure 22. Selected region of ^{1}H-^{1}H COSY NMR (500 MHz, at 298 K, $CDCl_3$: CD_3CN 9:1) of a 2 mM solution of $(CD_3CN)_2\subset$**4** with an excess of bis-aldehyde linker **8**. See **Figure 21** for the protons assignment.

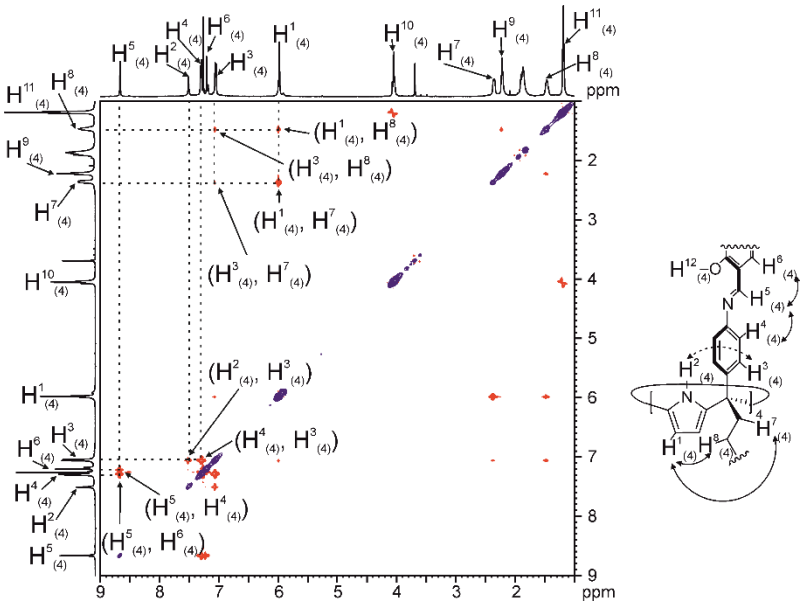

Figure 23. Selected region of ^{1}H-^{1}H ROESY NMR (500 MHz, at 298 K, $CDCl_3$: CD_3CN 9:1, d_8 = 0.30 s) of a 2 mM solution of the octa-imine cage $(CD_3CN)_2\subset$**4**. See **Figure 21** for protons assignment.

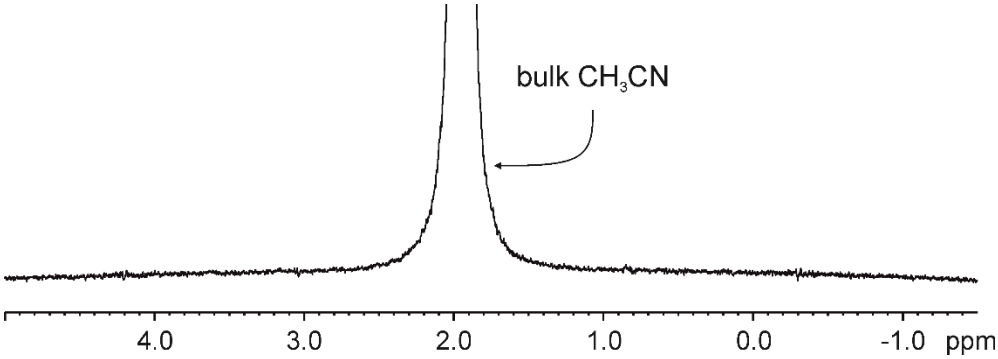

Figure 24. ^{1}H GOESY NMR (500 MHz, at 298 K, 9:1 $CDCl_3$:CH_3CN mixture) of **9** with selective excitation at 1.94 ppm (signal of the bulk solvent). The absence of exchange peaks suggests a fast exchange between the solvent molecule inside of **9** and the bulk solvent.

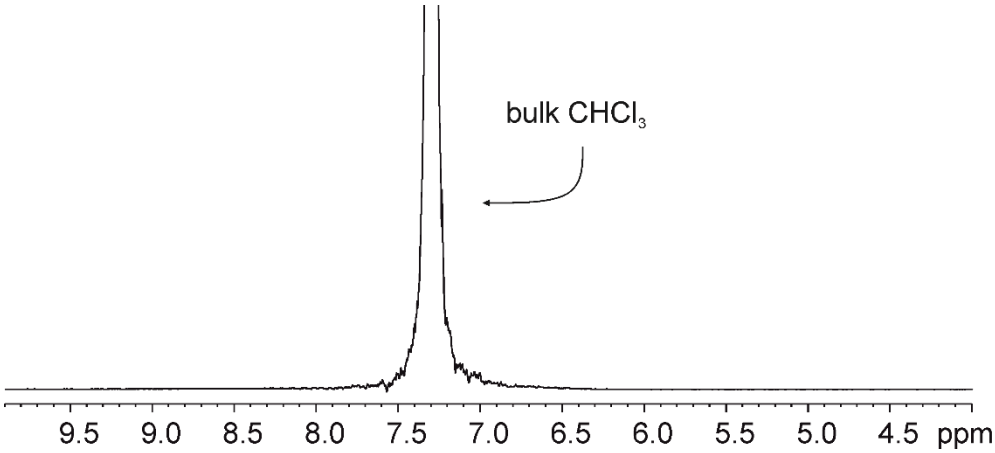

Figure 25. ^{1}H GOESY NMR (500 MHz, at 298 K, 9:1 $CHCl_3$:CD_3CN mixture) of **1** with selective excitation at 7.28 ppm (signal of the bulk solvent). The absence of exchange peaks suggests a fast exchange or no exchange between the solvent molecule inside the cage and the bulk solvent.

3.6 References and notes

[1] Hof, F.; Craig, S. L.; Nuckolls, C.; Rebek, J., Julius, *Angew. Chem., Int. Ed.* **2002,** *41* (9), 1488-1508.
[2] Tapia, L.; Alfonso, I.; Solà, J., *Org. Biomol. Chem.* **2021,** *19* (44), 9527-9540.
[3] Montà-González, G.; Sancenón, F.; Martínez-Máñez, R.; Martí-Centelles, V., *Chem. Rev.* **2022,** *122* (16), 13636-13708.
[4] Platzek, A.; Juber, S.; Yurtseven, C.; Hasegawa, S.; Schneider, L.; Drechsler, C.; Ebbert, K. E.; Rudolf, R.; Yan, Q.-Q.; Holstein, J. J.; Schäfer, L. V.; Clever, G. H., *Angew. Chem., Int. Ed.* **2022,** *61* (47), e202209305.
[5] Galan, A.; Ballester, P., *Chem. Soc. Rev.* **2016,** *45* (6), 1720-1737.
[6] Saha, R.; Mondal, B.; Mukherjee, P. S., *Chem. Rev.* **2022,** *122* (14), 12244-12307.
[7] Olivo, G.; Capocasa, G.; Del Giudice, D.; Lanzalunga, O.; Di Stefano, S., *Chem. Soc. Rev.* **2021,** *50* (13), 7681-7724.
[8] Cram, D. J.; Karbach, S.; Kim, Y. H.; Baczynskyj, L.; Kallemeyn, G. W., *J. Am. Chem. Soc.* **1985,** *107* (8), 2575-2576.
[9] Gabard, J.; Collet, A., *J. Chem. Soc., Chem. Commun.* **1981,** (21), 1137-1139.
[10] Rowan, S. J.; Cantrill, S. J.; Cousins, G. R. L.; Sanders, J. K. M.; Stoddart, J. F., *Angew. Chem., Int. Ed.* **2002,** *41* (6), 898-952.
[11] Lehn, J.-M., *Chem. Soc. Rev.* **2007,** *36* (2), 151-160.
[12] Belowich, M. E.; Stoddart, J. F., *Chem. Soc. Rev.* **2012,** *41* (6), 2003-2024.
[13] Quan, M. L. C.; Cram, D. J., *J. Am. Chem. Soc.* **1991,** *113* (7), 2754-2755.
[14] Sarkar, S.; Ballester, P.; Spektor, M.; Kataev, E. A., *Angew. Chem., Int. Ed.* **2023,** *62* (28), e202214705.
[15] Adriaenssens, L.; Ballester, P., *Chem. Soc. Rev.* **2013,** *42* (8), 3261-3277.
[16] Wang, F.; Bucher, C.; He, Q.; Jana, A.; Sessler, J. L., *Acc. Chem. Res.* **2022,** *55* (12), 1646-1658.
[17] Guchhait, T.; Pradhan, P.; Panda, L.; Sreejit K. Rao, M., *ChemistrySelect* **2022,** *7* (29), e202202671.
[18] Tromans, R. A.; Carter, T. S.; Chabanne, L.; Crump, M. P.; Li, H.; Matlock, J. V.; Orchard, M. G.; Davis, A. P., *Nature Chem.* **2019,** *11* (1), 52-56.
[19] Liu, Y.; Zhao, W.; Chen, C.-H.; Flood, A. H., *Science* **2019,** *365* (6449), 159-161.
[20] Wang, F.; Sikma, E.; Duan, Z.; Sarma, T.; Lei, C.; Zhang, Z.; Humphrey, S. M.; Sessler, J. L., *Chem. Commun.* **2019,** *55* (44), 6185-6188.
[21] Galán, A.; Escudero-Adán, E. C.; Ballester, P., *Chem. Sci.* **2017,** *8* (11), 7746-7750.
[22] Mirabella, C. F. M.; Aragay, G.; Ballester, P., *Chem. Sci.* **2023,** *14* (1), 186-195.
[23] Tang, D.; Dwyer, T.; Bukannan, H.; Blackmon, O.; Delpo, C.; Barnett, J. W.; Gibb, B. C.; Ashbaugh, H. S., *J. Phys. Chem. B* **2020,** *124* (23), 4781-4792.
[24] Wang, K.; Cai, X.; Yao, W.; Tang, D.; Kataria, R.; Ashbaugh, H. S.; Byers, L. D.; Gibb, B. C., *J. Am. Chem. Soc.* **2019,** *141* (16), 6740-6747.
[25] Li, T.-R.; Huck, F.; Piccini, G.; Tiefenbacher, K., *Nature Chem.* **2022,** *14* (9), 985-994.
[26] Asadi, A.; Ajami, D.; Rebek, J., *Chem. Sci.* **2013,** *4* (3), 1212-1215.
[27] Benke, B. P.; Kirschbaum, T.; Graf, J.; Gross, J. H.; Mastalerz, M., *Nature Chem.* **2023,** *15* (3), 413-423.

[28] Mecozzi, S.; Rebek, J., Julius, *Chem. Eur. J.* **1998,** *4* (6), 1016-1022.
[29] Stott, K.; Stonehouse, J.; Keeler, J.; Hwang, T.-L.; Shaka, A. J., *J. Am. Chem. Soc.* **1995,** *117* (14), 4199-4200.
[30] Stonehouse, J.; Adell, P.; Keeler, J.; Shaka, AJ., *J. Am. Chem. Soc.* **1994**, 116, 6037-6038.
[31] Chas, M.; Ballester, P., *Chem. Sci.* **2012,** *3* (1), 186-191.
[32] Díaz-Moscoso, A.; Hernández-Alonso, D.; Escobar, L.; Arroyave, F. A.; Ballester, P., *Org. Lett.* **2017,** *19* (1), 226-229.

Chapter 4

Binding of aliphatic diformamides by an octa-imine bis-calix[4]pyrrole cage: thermodynamic and kinetic characterization

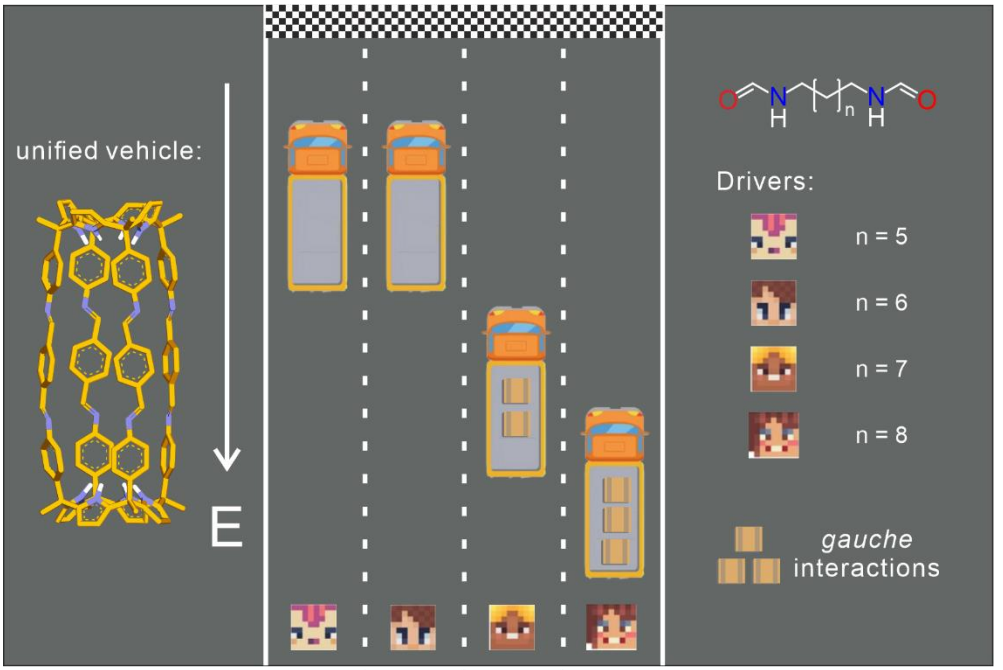

Unpublished results

UNIVERSITAT ROVIRA I VIRGILI
Receptors based on Aryl-extended Calix[4]pyrrole Scaffolds
Yifan Li

Binding of aliphatic diformamides by an octa-imine bis-calix[4]pyrrole cage: thermodynamic and kinetic characterization

4.1 Introduction

Molecular recognition[1] plays an important role in biological systems such as protein-substrate binding. The binding constants of natural receptors, like antibodies or proteins, toward target molecules lie in the range of 10^6-$10^{10}M^{-1}$. To explain how natural receptors bind specifically target molecules several models have been proposed. For example, the lock-and-key theory[2] considers the size and shape complementarity between the receptor (enzyme) and the substrate and the induced fit model[3] takes into account the flexibility of natural receptors to fit the target substrate. In both models, the guest (substrate) was simplified as a rigid structure. However, it is known that guests' flexibility also plays a critical role in molecular recognition. Those bioactive substrates like fatty acids, which feature flexible alkyl-chain-based skeletons, are commonly found in nature and cannot be neglected in molecular recognition studies.

In contrast to rigid guests, flexible guests containing alkyl chains exist in several conformations in solutions featuring comparable energies. The minimum potential energy state of an alkyl guest is shown for its fully extended conformation, in which all C_2-$C_{2'}$ dihedral angles are fixed to 180°. To adapt to the shape and size of a host cavity, guests adopt higher energy conformations which may result in additional inner strain and entropic costs. For instance, alkane guests are able to coil to adopt helical conformations with unfavorable gauche interactions (two methyl groups in closer proximity than the sum of their van der Waals radii; C_2-$C_{2'}$ dihedral angle close to 60 ° or 300°) to properly fill the host cavity (**Figure 1a**). In a confined cavity with a fixed inner volume, the high packing conformation of guests with multi-gauche interactions can be easily achieved.[4] One example is the helical conformation that alkane *n*-$C_{14}H_{30}$ adopts to properly fill the cavity of the self-assembled dimeric capsule based on tetra-imide resorcinarene cavitand (**Figure 1b**).[5] The energy-minimized structure of the helically folded guest (*n*-$C_{14}H_{30}$) containing 11 gauche interactions reduces by around 3.5 Å its length compared to the same guest in the fully extended conformation in the bulk. The unfavorable gauche interactions generated in the folding were compensated by the favorable CH-π interactions with the aromatic walls of the host. Thus, the energy cost of gauche interaction reduces from 0.9 kcal·mol^{-1} in bulk solution to 0.5-0.6 kcal·mol^{-1} in the inner cavity. The multiple gauche interactions generated in the folded guest can be identified by nOe cross-peaks between hydrogen atoms in the C_i and C_{i+4} carbons in the ^{1}H NMR spectrum.

Mecozzi and Rebek established as 55 ± 9 % the range of packing coefficient (ratio of the guest volume to the host volume) favored for the formation of inclusion

complexes in solution. For inclusion complexes containing strong intermolecular interactions between host and guest (e.g. hydrogen bonds), the PC value can go up to 70%.[6] To the best of our knowledge, the high packing inclusion complexes (PC larger than 66%) have been only reported for rigid polar guests. [7,8] Simple molecular modeling can predict somehow these values, however, in some cases might not be accurate.

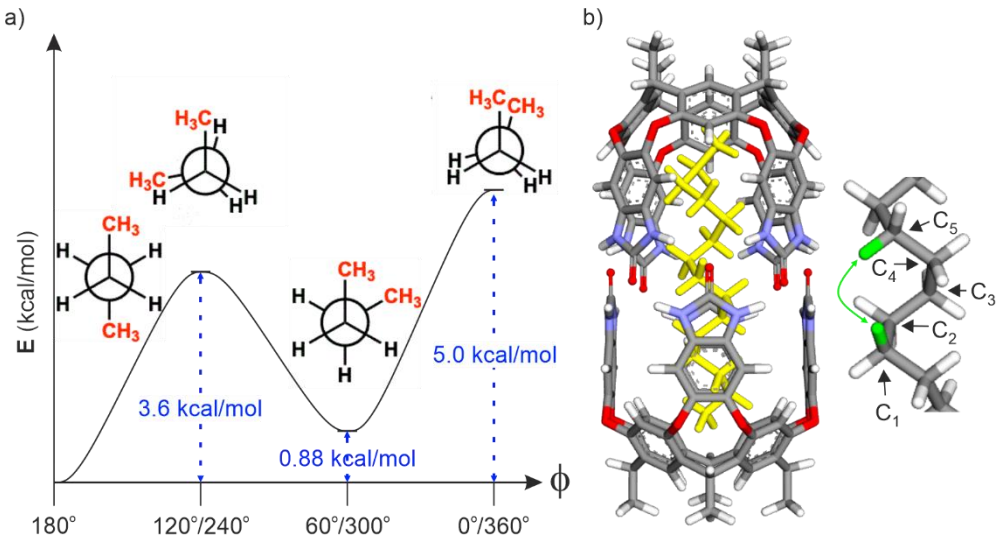

Figure 1. a) Stationary points in the energy profile for rotation around the middle C–C bond of butane. The gauche interaction ¨costs¨ around 0.9 kcal·mol^{-1}. b) Right- The front energy minimized structure (MM3) for the capsule inclusion complex adopts *n*-$C_{14}H_{30}$ in helical conformation. Left- The nOe cross-peaks between hydrogen atoms (highlighted with green) in the C_i and C_{i+4} carbons.

In 2012, we reported the use of a homologous series of *N,N,N´,N´*-tetramethy-alkyl-*N,N´*-dioxides to probe the possible level of guest induced fit in a hydrogen-bonded tetra-urea calix[4]pyrrole dimeric capsule.[9] We observed an elongation of the cavity size to accommodate the longer guests by slightly modifying the position of the urea units of the urea belt. Moreover, we observed that guest molecules folded to adapt to the limiting dimensions of the cavity. The host-guest adaption occurs as long as the favorable binding interactions compensate for the cost of the high-energy guest conformation (**Figure 2a**).

Secondary formamides are typically encountered in biology. They exist in solution as equilibrium mixtures of both *cis*- and *trans*-isomeric conformers. Dipole-dipole and steric effects around the secondary formamide bonds destabilize the *cis*-isomers (C=O and N-H are *syn*). The energy differences in alkyl formamides are large

enough that the *cis*-isomer is present in just 20%. In addition, the low energy barrier (~ 15-20 kcal·mol^{-1}) associated with the isomerization process provokes that the chemical exchange in the equilibrium is fast on the human time scale, not allowing the isolation of pure isomers, but slow on the ^{1}H NMR chemical shift time scale, producing separate signals for each one of them.

Our group demonstrated that AE-C[4]P receptors in water were capable of selectively binding the *cis*-conformer of secondary formamides with high affinity owing to its superior size and shape complementarity compared to the *trans*-isomer.[10] Recently, we described the self-assembly of a water-soluble endohedrally functionalized Pd(II) coordination cage based on super aryl-extended calix[4]pyrrole tetra-pyridyl ligand.[11] The coordination cage was assembled in the presence of aliphatic α,ω-diformamides having four and five methylene groups as spacers (**Figure 2b**). The coordination cage showed conformational selectivity for the *cis,cis*-isomer of the shorter guest (4 CH_2 units) while the longer ditopic guest (5 CH_2 units) was included preferentially as the *cis,trans*-rotamer. The X-ray structure of the latter evidenced the bending of the alkyl spacer to better adapt to the dimensions of the cavity.

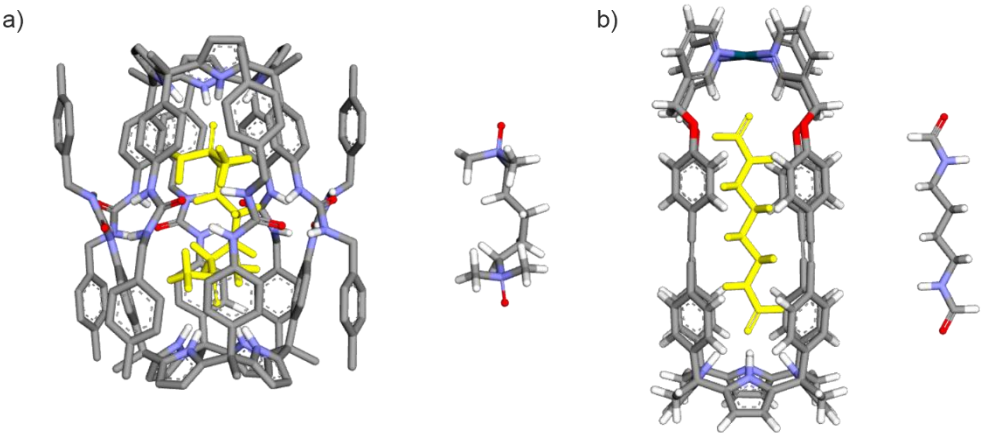

Figure 2. The energy minimized structures of a) Right-dimer capsule inclusion complex based on tetra-urea calix[4]pyrrole. Left- The *N,N,N´,N´*-tetrametheylalkyl-*N,N´*-dioxide guest inside of the capsule. b) Right- The coordination cage inclusion complex based on supra-aryl extended calix[4]pyrrole. Left- The formamide guest inside of the cage.

The cavity displayed in the dimeric tetra-urea bis-calix[4]pyrrole capsule previously described (**Figure 2a**) can elongate or widen adapting to the guest included. On the other hand, the coordination cage (**Figure 2b**) has a shape-persistent cavity.

Calix[4]pyrrole hemisphere is able to establish four hydrogen bond interactions with the formamide end in the *cis*-conformation. However, the four inwardly directed α-H protons of the pyridyl groups coordinated to Pd(II) offer weaker hydrogen bonds to the opposite formamide end. We considered that the shape persistent octa-imine cage **1** described in **Chapter 3**, featuring two identical endohedrally functionalized hemispheres, could be interesting for studying the inclusion and cavity-adaptability of diformamide guests with different lengths.

In the present chapter, we report the binding studies of the shape-persistent octa-imine cage **1** with a series of homologous diformamide guests in a mixture of organic solvents. We studied the conformational selectivity shown by the host for the diformamide isomeric mixtures of the different guests. We also compare the thermodynamic stability of the inclusion complexes and evaluate the kinetics of the guest exchange process.

4.2 Results and discussion

4.2.1 Synthesis

Octa-imine cage **1** was prepared following the procedure described in **Chapter 3**.

We synthesized a homologous series of diformamides (**2**-**7**) as potential guests, differing in the number of methylene units separating the two terminal amides. Diformamides were obtained using literature reported procedures that involve the condensation of the corresponding commercially available diamines with ethyl formate (**Scheme 1**).[12]

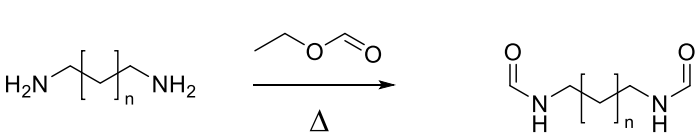

2: n = 4
3: n = 5
4: n = 6
5: n = 7
6: n = 8
7: n = 9

Scheme 1. Synthetic scheme of diformamides **2**-**7**.

The ^{1}H NMR spectra of diformamides **2**-**7** (in a $CDCl_3$: CD_3CN 9:1 solvent mixture) showed analogous chemical shifts for the formyl protons of the *cis* and *trans*-rotamers than those observed for the mono-formamides counterparts (**Figure 3**).[13] The formyl proton in the terminal *trans*-rotamer (H^{a}_{trans}) of the diformamides appeared as a singlet at δ = 8.06 ppm. In contrast, the formyl proton of the *cis*-rotamer end (H^{a}_{cis}) resonated as a doublet centered at δ =7.96 ppm, displaying a coupling constant of $^{3}J_{H\text{-}H}$ = 12 Hz. The larger coupling constant of the *cis*-rotamer agrees with the 180° dihedral torsion angle between formyl and amide vicinal protons.[14] Diformamides exist in solution as a mixture of three isomers with respect to the conformation adopted by the two terminal amides showing separate signals in the ^{1}H NMR spectrum: the most abundant *trans,trans*- (76%), the *cis,trans*- (19%) and the least abundant *cis,cis*- (5%).

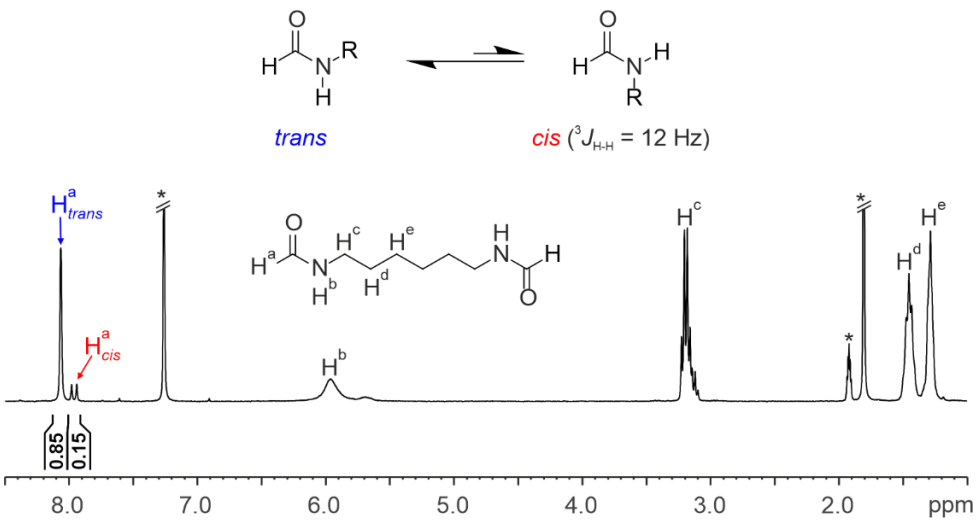

Figure 3. ^{1}H NMR spectrum (500 MHz, 298 K, $CDCl_3$: CD_3CN 9:1) of **2**. The formyl proton signals of the secondary formamides end in *cis*- and *trans*-conformations, showing slightly different chemical shifts and coupling constants.

4.2.2 Study of the inclusion of diformamide **2** (6 × CH_2) in the octa-imine cage **1**: complex **2⊂1**

We used ^{1}H NMR spectroscopy to probe the binding of diformamide **2** (six methylene units separating the formamide ends) with the octa-imine cage **1**. The ^{1}H NMR spectrum of a solution of octa-imine cage **1** (2 mM in $CDCl_3$: CD_3CN 9:1) is depicted in **Figure 4a**. To this solution, we added an equimolar amount of diformamide **2**. The ^{1}H NMR spectrum of the resulting mixture (**Figure 4b**) showed the appearance of a new set of broad signals. The free diformamide **2** and cage **1** signals were still visible in the ^{1}H NMR spectrum. The incremental addition of diformamide **2** provoked an increase in the intensity of this new set of signals at the expense of those of the free species. We attributed the new set of signals to the formation of the **2⊂1** complex. The observation of separate signals for the free and bound species in the ^{1}H NMR spectrum indicates they were in slow exchange on the ^{1}H NMR chemical shift timescale.

After the addition of 5.0 equiv. of **2** to a solution of **1** (**Figure 4c**), the set of signals corresponding to the free cage **1** was no longer detected in the ^{1}H NMR spectrum. The remaining proton signals mainly corresponded to the free diformamide **2** and the **2⊂1** complex, which agrees with a D_{4h} symmetry. In addition, the binding equilibrium featured slow exchange dynamics not only on the ^{1}H NMR chemical shift timescale but also in the EXSY time scale indicated by the lack of cross-peaks between the proton signals of free and bound diformamide **2** (t_{mix} = 0.3 s). We

assigned an energy barrier larger than 20 kcal·mol^{-1} for the chemical exchange process, supporting that the **2⊂1** inclusion complex was kinetically highly stable.[15]

The pyrrole NH proton signals of the inclusion complex ($H^1_{(cc\text{-}2\subset1)}$) did not show a significant shift compared to the free cage **1** ($H^1_{(1)}$) which most likely displayed acetonitrile molecules inside the cavity. This suggests that guest **2** is too short to establish a simultaneous ditopic interaction with the two endohedrally functionalized binding hemispheres of cage **1**. We propose that the included guest is shuttling from one hemisphere to the other and shows an average set of signals in the ^{1}H NMR spectrum of the bound species. This would explain the signal broadening and the small changes in the chemical shift of the pyrrole NH protons compared to the free counterpart.

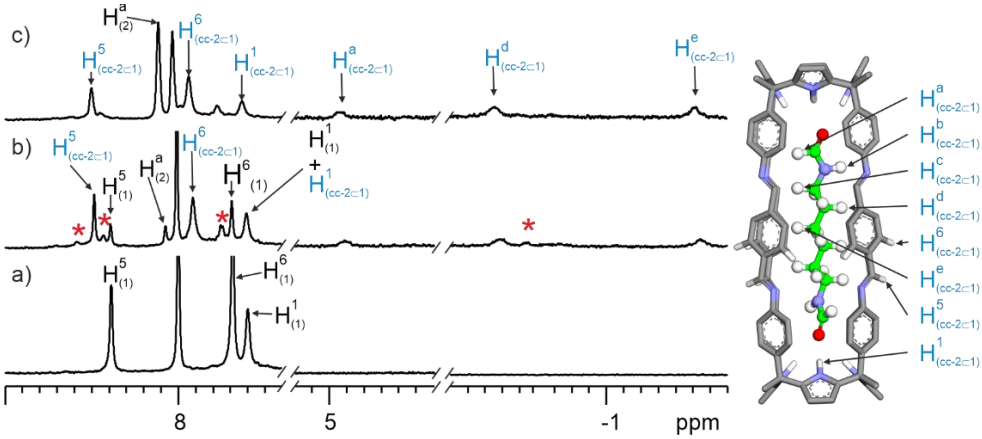

Figure 4. (Left panel) Selected regions of the ^{1}H NMR spectra (500 MHz, 298 K, $CDCl_3$: CD_3CN 9:1) of (a) octa-imine cage **1**, (b) 1:1 mixture of octa-imine cage **1** and guest **2**. (c) 1:6 mixture of octa-imine cage **1** and guest **2**. (Right panel) Energy minimized (MM3) structure of the *cis,cis*-**2⊂1** inclusion complex with the corresponding proton assignment. *The trace amount of inclusion complex, which may correspond to *cis,trans*-**2⊂1** inclusion complex. In the proton assignment, the superscripts indicate the proton and the subscripts indicate the species (free ligands (**1-7**) or inclusion complexes (**2-7⊂1**); "cc" and "ct" are used to indicate the guest *cis,cis* or cis,trans-conformation, respectively).

The 2D spectra derived from ^{1}H NOESY experiments showed intramolecular, close-contact cross-peaks (nOe peaks) between the formyl protons ($H^a_{(cc\text{-}2\subset1)}$) of the bound diformamide **2** and those of methylene group alpha- to the carbonyl (α-CH_2, $H^c_{(cc\text{-}2\subset1)}$). This result indicated that at least one of the ends of the included guest was in the *cis*- conformation. We observed nOe cross-peaks between the protons at the C_i

and C_{i+2} carbon atoms all along the aliphatic chain of bound **2** (**Figure 5**). This result together with the observed D_{4h} symmetry of the complex indicated the selective inclusion of the *cis,cis*-**2** rotamer in the cavity of **1**. Most likely, *cis,trans*-**2**⊂**1** complex is also present in solution but to a reduced extent (**Figure 4b**).

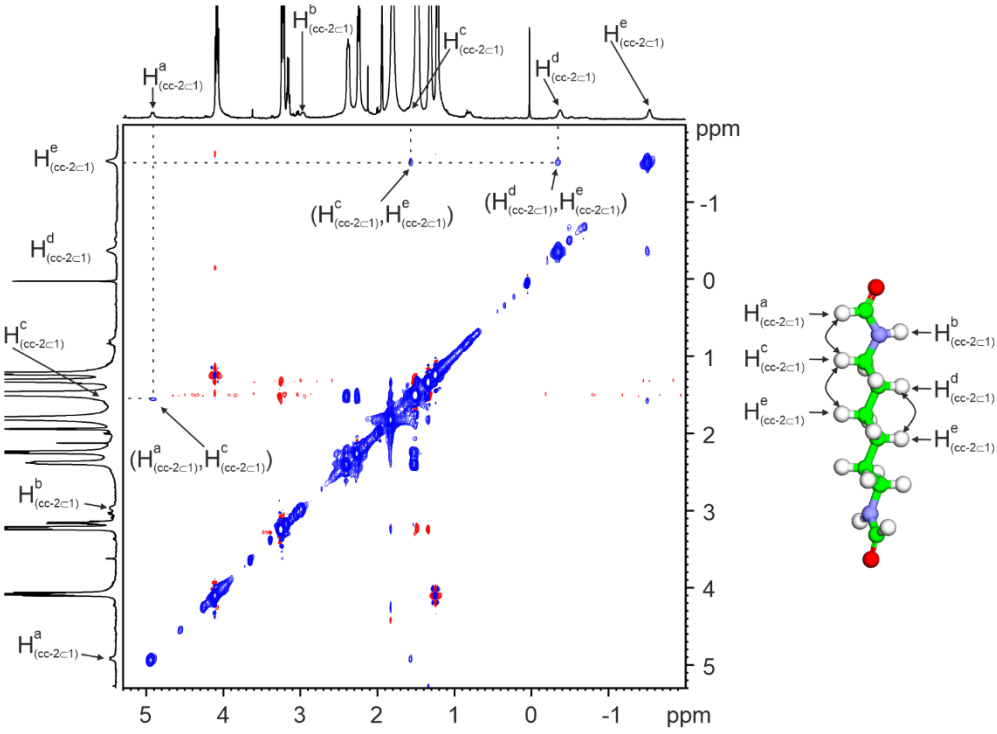

Figure 5. ^{1}H NOESY NMR (500 MHz, at 298 K, $CDCl_3$:CD_3CN 9:1 mixture) spectrum of inclusion complex *cis,cis*-**2**⊂**1**. Intramolecular close-contacts are indicated in the energy-minimized structure (MM3) of the bound *cis,cis*-**2**.

Molecular modeling studies supported the previous hypothesis. The energy minimized structures (MM3) of *cis,cis*-**2**⊂**1** (**Figure 5**) and *cis,trans*-**2**⊂**1** complex showed that the length of bound **2** in fully extended conformation is too short to reach both endohedral binding sites of cage **1**. The distance between nitrogen atoms of diagonally oriented pyrrole groups of opposite hemispheres in cage **1** is 20 Å and the distance between terminal formyl oxygen atoms of the fully extended *cis,cis*-**2** is 13.6 Å. Considering a typical hydrogen bonding distance of 3.0 Å, the length of fully extended *cis,cis*-**2**, and two hydrogen bonds is not enough to fill the gap between the two binding sites (0.4 Å). Considering the length of fully extended *cis,trans*-**2** (d(O···O), 12.7 Å), the gap between two binding sites is relatively larger (1.3 Å), which disfavored the guest shuttling between two hemispheres.

4.2.3 Study of the inclusion of diformamide **3** (7 × CH_2) in the octa-imine cage **1**: complex **3⊂1**

To a solution of self-assembled cage **1** (2 mM in $CDCl_3$: CD_3CN 9:1), we added an equimolar amount of diformamide **3** (seven methylene units separating the formamide ends). The ^{1}H NMR spectrum of the resulting mixture displayed a unique set of well-defined proton signals not coinciding with those of the free counterparts that were assigned to the bound species. The formyl protons of bound **3** were significantly upfield shifted ($H^a_{(cc\text{-}3\subset1)}$, $\Delta\delta$ = 3.54 ppm) compared to the free counterpart. This result supported the fact that the complexation process was fast on the human timescale (a few seconds). The ^{1}H NMR spectrum of the **3⊂1** complex agreed with a D_{4h} symmetry (**Figure 6b**). The addition of more than 1 equiv. of the diformamide **3** did not produce noticeable changes to the proton signals assigned to the bound species. However, we observed the emergence of the proton signals of the free diformamide **3**. Taken together, these observations supported the quantitative formation of the **3⊂1** inclusion complex, for which we estimated a binding constant larger than 10^4 M^{-1}.

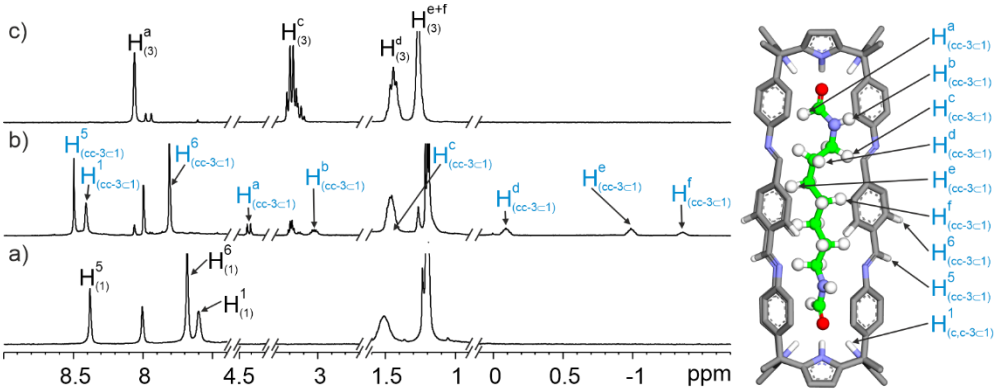

Figure 6. (Left panel) Selected regions of the ^{1}H NMR spectra (500 MHz, 298 K, $CDCl_3$: CD_3CN 9:1) of (a) octa-imine cage **1**, (b) 1:1 mixture of octa-imine cage **1** and guest **3**. (c) guest **3**. (Right panel) Energy minimized (MM3) structure of the **3⊂1** inclusion complex.

The 2D spectra derived from ^{1}H NOESY (**Figure 7**) experiments showed intramolecular, close-contact cross-peaks (nOe peaks) between the formyl protons ($H^a_{(cc\text{-}3\subset1)}$) of the bound diformamide **3** and those of methylene group *alpha*- to the carbonyl (α-CH_2, $H^c_{(cc\text{-}3\subset1)}$). This result together with the observed D_{4h} symmetry of the complex indicated the selective inclusion of the *cis,cis*-**3** rotamer in the cavity of

1. This result is also in agreement with the observation of the $H^{a}_{(cc\text{-}3\subset1)}$ protons resonating as doublets: the CH-NH $^{3}J_{H\text{-}H}$ coupling constant for formamides is larger in the *cis*-conformation resulting in the formyl proton appearing as a doublet (**Figure 3**). Considering the concentration of *cis,cis*-**3** (5% *cis,cis*-**3** in 2 mM of total **3** = 0.10 mM), we estimated a binding constant larger than 10^{5} M^{-1}.

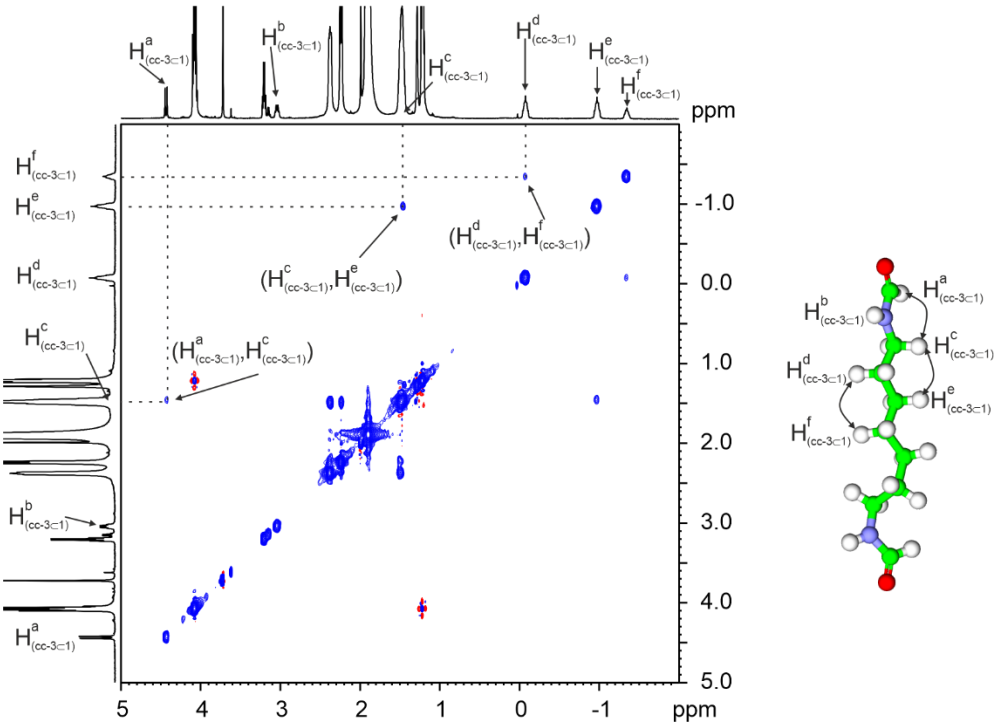

Figure 7. ^{1}H NOESY NMR (500 MHz, at 298 K, $CDCl_3$:CD_3CN 9:1 mixture) spectrum of inclusion complex *cis,cis*-**3⊂1**. Intramolecular close-contacts are indicated in the energy-minimized structure (MM3) of the bound *cis,cis*-**3**.

The complexation-induced shifts experienced by the proton signals of included *cis,cis*-**3** cannot be directly related to their depth in the aromatic cavity (**Table 1**). The proton signals of the included guests near to the phenyl spacers ($H^{e}_{(cc\text{-}3\subset1)}$ and $H^{f}_{(cc\text{-}3\subset1)}$, proved by ^{1}H ROESY) showed larger upfield shifts compared to the protons close to the imine bonds ($H^{c}_{(cc\text{-}3\subset1)}$ and $H^{d}_{(cc\text{-}3\subset1)}$).

Table 1. Experimental chemical shifts of free (δ_{free}) and bound (δ_{bound}) guest **3** and complexation-induced shifts ($\Delta\delta$).

Signal	δ_{free} (ppm)	Signal	δ_{bound} (ppm)	$\Delta\delta_{bound-free}$ (ppm)
$H^a_{(cc-3)}$	7.96	$H^a_{(cc-3\subset1)}$	4.45	-3.51
$H^b_{(cc-3)}$	5.69	$H^b_{(cc-3\subset1)}$	1.42	-4.27
$H^c_{(cc-3)}$	3.13	$H^c_{(cc-3\subset1)}$	3.05	-0.08
$H^d_{(cc-3)}$	1.45	$H^d_{(cc-3\subset1)}$	-0.06	-1.51
$H^e_{(cc-3)}$	1.28	$H^e_{(cc-3\subset1)}$	-0.95	-2.23
$H^f_{(cc-3)}$	1.28	$H^f_{(cc-3\subset1)}$	-1.32	-2.60

In the ^{1}H NOESY spectrum of the *cis,cis*-**3**⊂**1** complex, we observed nOe cross-peaks between the protons at the C_i and C_{i+2} carbon atoms all along the aliphatic chain of bound **3** (**Figure 7**). This indicated that *cis,cis*-**3** also adopted an extended conformation when bound inside cage **1**. Molecular modeling studies (MM3) supported that the length of bound **3,** in almost fully extended *cis,cis*-conformation, is ideal for establishing a ditopic hydrogen-bonding interaction between their terminal carboxyl oxygen atoms and the distal pyrrole NHs of the two C[4]P hemispheres of the cage. In fact, the distance between the two terminal oxygen atoms in the fully extended *cis,cis*-conformation of free **3** is only 0.3 Å larger than the same distance in the bound guest. We suggest that small changes in the alternated dihedral angles of the alkyl carbon chain is enough to achieve the length difference and preferred to the energy-cost of gauche interactions of a folded conformation. The width of the cage's cavity adapts to that of the included guest by establishing additional CH-π interactions and overcoming the energy cost assumed by its non-perfect alternate conformation.

4.2.4 Study of the inclusion of diformamide **4** (8 × CH_2) in the octa-imine cage **1**: complex **4⊂1**.

To a solution of self-assembled cage **1** (2 mM in $CDCl_3$: CD_3CN 9:1), we added an equimolar amount of diformamide **4** (eight methylene units separating the formamide ends). We monitored the formation of the inclusion complex using ^1H NMR spectroscopy. Immediately after the addition of **4** (~5 min), we observed the appearance of two separate and downfield shifted signals ($\Delta\delta$ = 1.15, 1.00 ppm) for the NH protons of the bound cage **1** (**Figure 8b**). This observation suggested that the formed complex featured C_{4v} symmetry instead of the expected D_{4h} symmetry produced by the inclusion of the C_2 symmetric guest **4**. With time, we detected that a broad signal resonating close to the more downfield shifted NH proton of the initially formed complex increased in intensity at the expense of those of the latter.

After 24 h at room temperature, the ^1H NMR spectrum of the mixture revealed the complete disappearance of the two NH signals assigned to the initially formed complex and the presence of the growing and downfield shifted broad singlet at 8.73 ppm (**Figure 8c**). We assigned this signal to the NH protons of a thermodynamically more stable inclusion complex of the octa-imine **1** and diformamide **4** displaying D_{4h} symmetry. The ratio of the integral values of selected protons of the host and the guest in the formed **4⊂1** complexes assigned a 1:1 stoichiometry in both cases. The more intense signals in the spectrum corresponded to the free **4**. Taken together, these observations suggested the formation of two different 1:1 inclusion complexes between **1** and **4** experiencing binding dynamics that are slow on the chemical shift timescale. Based on the symmetry properties of the formed complexes, we considered that the kinetically formed complex corresponded to the inclusion of the *cis,trans-conformer* of diformamide **4** in the octa-imine cage **1**. In turn, the thermodynamically more stable complex was assigned to the inclusion of the *cis,cis-conformer* of **4**.

The exclusive observation of the *cis,cis*-**4⊂1** complex in solution after 24h assigned an energy difference between two inclusion complexes (*trans,cis*-**4⊂1** and *cis,cis*-**4⊂1**) larger than 2.7 kcal·mol^{-1}. Considering a binding constant of cage **1** towards *trans,cis*-**4⊂1** larger than 10^5 M^{-1}, we estimated a binding constant of cage **1** with *cis,cis*-**4⊂1** larger than 10^7 M^{-1}.

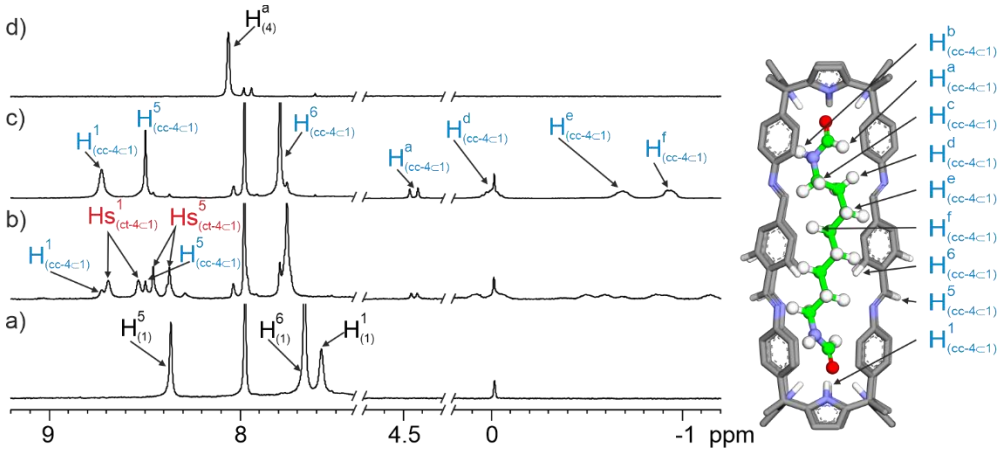

Figure 8. Selected region of the ^{1}H NMR spectra (400 MHz, at 298 K, $CDCl_3$:CD_3CN 9:1) of a) 2 mM of cage **1**, b) immediately after addition of **4** (2 mM), c) 24 hours after addition of **4** (2 mM), d) guest **4**.

The 2D ^{1}H NOESY spectrum of the most thermodynamically stable inclusion complex, *cis,cis*-**4**⊂**1** (**Figure 9**), displayed the expected intramolecular nOe cross-peaks between the signal of the formyl protons ($H^{a}_{(cc\text{-}4\subset1)}$) and that of the α-$CH_2$($H^{c}_{(cc\text{-}4\subset1)}$). The difference in chemical shifts observed for the NHs in the *cis,cis*-**4**⊂**1,** and *cis,trans*-**4**⊂**1** complexes was related to small changes in the hydrogen bond distances. Remarkably, the 2D NOESY experiment of the *cis,cis*-4⊂**1** complex produced high-intensity nOe cross-peaks between hydrogen atoms in adjacent carbons (C_i and C_{i+1}), suggesting a significant folding of the alkyl chain for the bound guest. Molecular modeling studies also supported this finding (**Figure 9**). Most likely, the alkyl chain of bound *cis,cis*-**4** rapidly exchanges between multiple conformations with regions in alternated conformation and folded sections featuring gauche interactions.

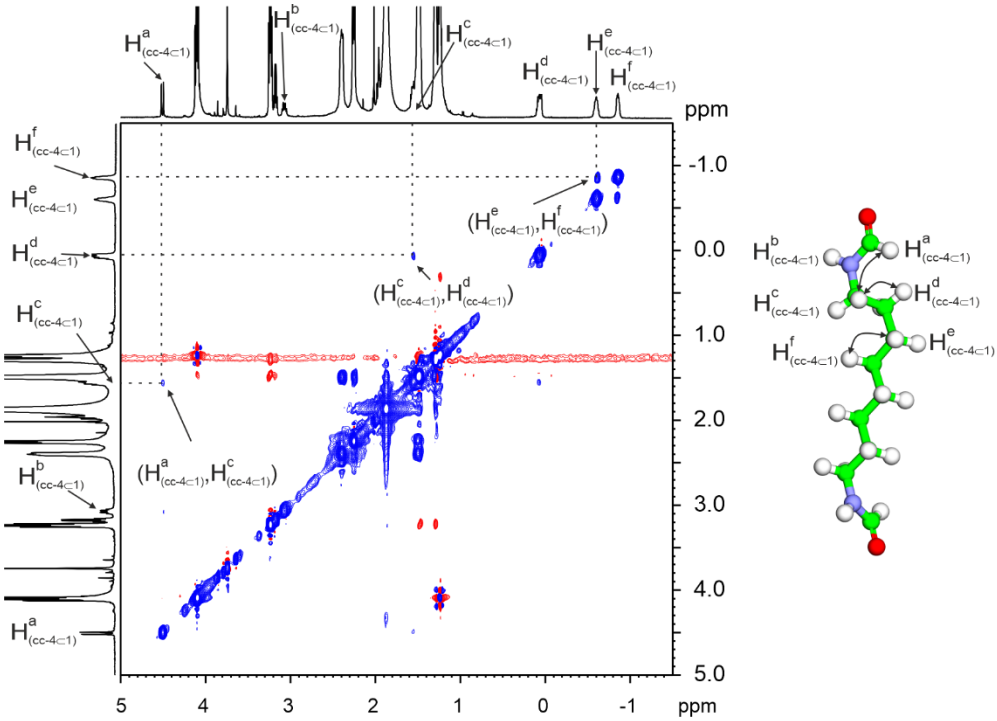

Figure 9. ^{1}H NOESY NMR (500 MHz, at 298 K, $CDCl_3$:CD_3CN 9:1 mixture) spectrum of inclusion complex *cis,cis*-**4⊂1**. Intramolecular close-contacts are indicated in the energy-minimized structure (MM3) of the bound *cis,cis*-**4**.

The distance between terminal oxygen atoms of **4** in fully extended *cis,cis*-conformation is 1.3 Å longer than that measured in the inclusion complex *cis,cis*-**4⊂1**. Based on Rebek´s study for including alkanes in capsules, each gauche interaction reduced the alkane length to around 0.35 Å when folded in a helical conformation.[5] Thus, a reduction of 1.3 Å accounted for 4 gauche interactions. The lack of nOe cross-peaks between hydrogen atoms in the C_i and C_{i+4} carbons of the guest's alkyl chain in the *cis,cis*-**4⊂1** also supported a non-helical folding, as previously mentioned. Molecular modeling studies suggested at least 3 gauche interactions in the non-helical folded alkyl chain of the diformamide **4** (**Figure 9**).

4.2.5 Studies of the inclusion of **5** (9 × CH_2) in **1**: kinetic and thermodynamic characterization of the **5⊂1** complex.

We monitored the formation of the **5⊂1** complex using kinetic ^{1}H NMR spectroscopy and an equimolar amount of the diformamide **5** (nine methylene units separating the formamide ends). We observed a similar behavior to that described in the previous section for the shorter diformamide **4**. The main difference was that after 24 h, the equilibrium between the two isomeric complexes featuring C_{4v} and D_{4h} symmetries reached a 35:65 ratio, *cis,trans*-**5⊂1**: *cis,cis*-**5⊂1**, respectively (**Figure 10**). The expected diagnostic signals for the two isomeric complexes were also observed in the ^{1}H NMR spectrum of the mixture. For example, the set of signals showing C_{4v} symmetry showed two separate signals for the formyl protons with different multiplicities (a doublet at 4.27 ppm and a singlet at 4.53 ppm) in agreement with the included *cis,trans*-**5** formamide (**Figure 11**). As in the previous case, the most thermodynamically stable complex was the *cis,cis*-**5⊂1**. The thermodynamic equilibrium of the two inclusion complexes with a ratio of 65:35 indicated that their energies are comparable ($\Delta\Delta G$ = 0.36 kcal·mol^{-1}).

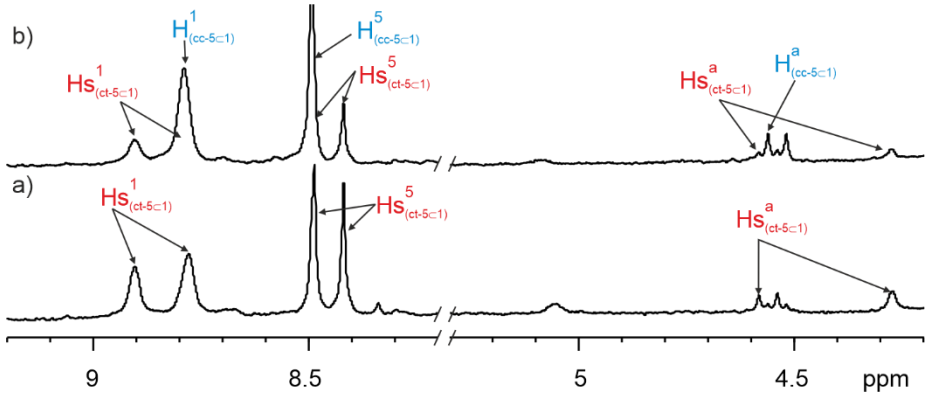

Figure 10. Selected region of the ^{1}H NMR spectra (300 MHz, at 298 K, $CDCl_3$:CD_3CN 9:1) of a) 2 mM of cage **1** immediately after the addition of **5** (2 mM), b) 24 hours after the addition of **5** (2 mM).

The distance between terminal oxygen atoms of **5** in its fully extended *cis,cis*-conformation is 2.4 Å longer than that in the inclusion complex *cis,cis*-**5⊂1**. In short, the bound cis,cis-**5** isomer must fold in order to adapt to the cavity size of **1**. Most likely, the folding of the alkyl chain does not induce a single conformation and the bound *cis,cis*-**5** is fast exchanging between multiple folded conformations. The bound *cis,cis*-**5** and *cis,trans*-**5** displayed similar lengths between terminal oxygen

atoms, most likely due to the rigid cavity of cage **1**. The distance between terminal oxygen atoms of **5** in its fully extended *cis,trans*-conformation is 1.7 Å longer than that in the inclusion complex. This shorter difference in the length variation for *cis,trans*-**5** between bound and fully-extended state compared to the cis,cis-counterpart might require less number of gauche interactions in the guest inclusion process. This might be the reason why for guest **5** the relative kinetic stability of the inclusion complexes is different from the corresponding thermodynamic stability.

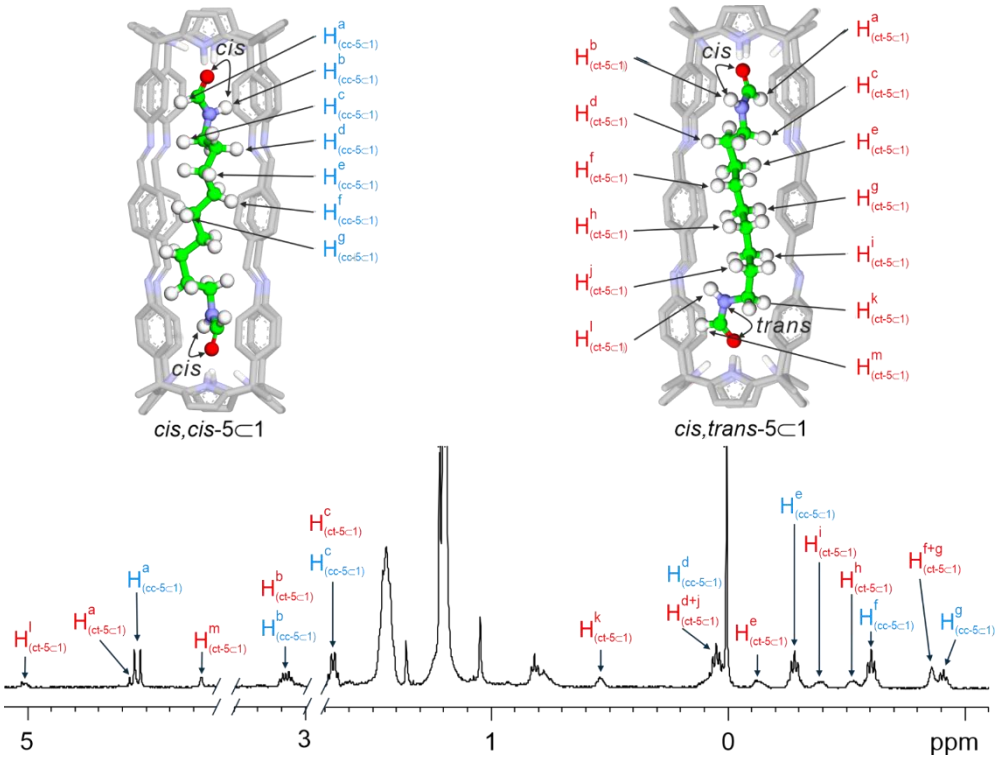

Figure 11. (Top) Energy minimized (MM3) structures of a) *cis,cis*-**5⊂1** and b) *trans,cis*-**5⊂1** inclusion complexes. The folded conformations adopted by the included diformamides *trans,cis*- and *cis,cis*- inside the cavity are better visualized by the stick representations of the bound guests shown next to the complexes. (Bottom) Selected region of the ^{1}H NMR spectrum (500 MHz, 298 K, $CDCl_3$: CD_3CN 9:1) of a 1:1 mixture of octa-imine cage **1** and guest **5** after 24 h.

4.2.6 Study of the inclusion of diformamide **6** (10 × CH_2) in octa-imine **1**: formation of the **6⊂1** complex

Similar to the experiments discussed above, we added an equimolar amount of diformamide **6** (ten methylene units separating the formamide ends) to a solution of the octa-imine cage **1** (2 mM in $CDCl_3$: CD_3CN 9:1). The ^1H NMR spectrum of the solution acquired immediately after the addition (5 min) displayed a single set of well-defined proton signals for both the host and the guest in agreement with a D_{4h} symmetry and diagnostic of the quantitative formation of the *cis,cis*-**6⊂1** inclusion complex (**Figure 12b**). The addition of more than 1 equiv. of **6** did not produce noticeable changes except for the emergence of the proton signals of the free guest. The 2D EXSY experiment (t_{mix} = 0.3 s) of the resulting mixture did not show any cross peaks due to chemical exchange between the free and bound guest indicating that the dynamics of the inclusion process were also slow on this timescale.

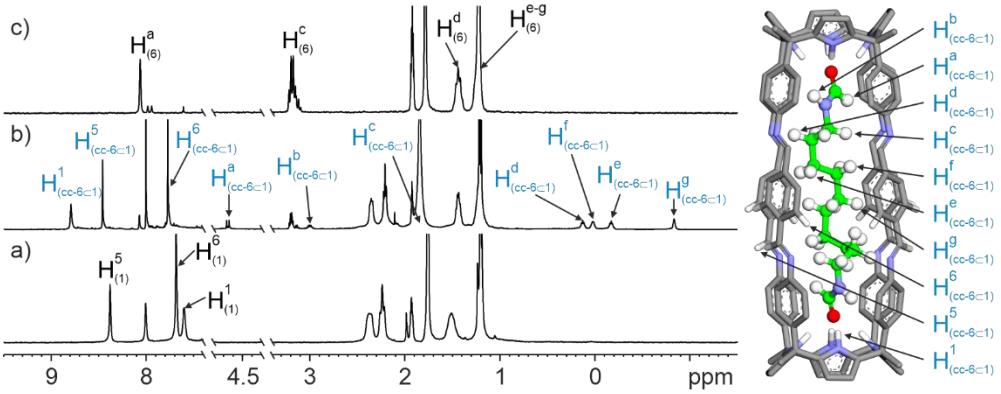

Figure 12. (Left) Selected region of the ^1H NMR spectrum (500 MHz, 298 K, $CDCl_3$: CD_3CN 9:1) of (a) octa-imine cage **1**, (b) 1:1 mixture of octa-imine cage **1,** guest **6**. (c) guest **6**. (Right) Energy minimized (MM3) structure of *cis,cis*-**6⊂1.**

The 2D ^1H NOESY experiments displayed the expected intramolecular nOe cross peak between the terminal formyl protons and the α-CH_2 methylene that was indicative of the selective inclusion of the *cis,cis*-isomer of **6** in the cavity of **1**. The upfield shift experienced by the $H^f_{(cc\text{-}6\subset1)}$ proton ($\Delta\delta$ = 1.25, ppm) 5 carbons away from the formamide end was smaller than that of $H^e_{(cc\text{-}6\subset1)}$ ($\Delta\delta$ = 1.44 ppm) placed in an extra further away carbon (**Table 2**, and **Figure 12**). In an extended conformation of the alkyl chain, protons $H^e_{(cc\text{-}6\subset1)}$ would be located closer to the center of the cage, experiencing a larger shielding owing to the magnetic anisotropy

of the phenyl spacers (vide supra). This observation suggested that the *cis,cis*-**6** isomer must suffer a significant folding in order to fit in the cavity of cage **1**.

Table 2. Experimental chemical shifts of free (δ_{free}) and bound (δ_{bound}) guest **6** and complexation-induced shifts ($\Delta\delta$).

Signal	δ_{free} (ppm)	Signal	δ_{bound} (ppm)	$\Delta\delta$ (ppm)
$H^{a}_{(cc\text{-}6)}$	7.96	$H^{a}_{(cc\text{-}6\subset1)}$	4.66	-3.30
$H^{b}_{(cc\text{-}6)}$	5.69	$H^{b}_{(cc\text{-}6\subset1)}$	3.01	-2.68
$H^{c}_{(cc\text{-}6)}$	3.13	$H^{c}_{(cc\text{-}6\subset1)}$	1.82	-1.31
$H^{d}_{(cc\text{-}6)}$	1.45	$H^{d}_{(cc\text{-}6\subset1)}$	0.14	-1.31
$H^{e}_{(cc\text{-}6)}$	1.28	$H^{e}_{(cc\text{-}6\subset1)}$	-0.16	-1.44
$H^{f}_{(cc\text{-}6)}$	1.28	$H^{f}_{(cc\text{-}6\subset1)}$	0.035	-1.25
$H^{g}_{(cc\text{-}6)}$	1.28	$H^{g}_{(cc\text{-}6\subset1)}$	-0.824	-2.10

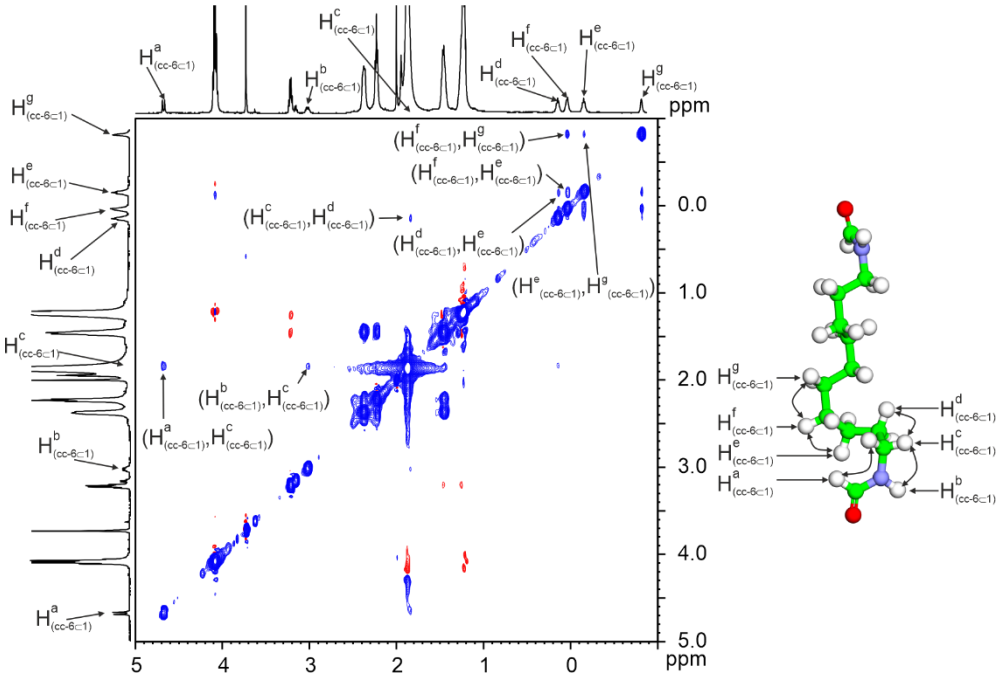

Figure 13. ^{1}H NOESY NMR (500 MHz, at 298 K, $CDCl_3$:CD_3CN 9:1 mixture) spectrum of inclusion complex *cis,cis*-**6⊂1**. Intramolecular close-contacts are indicated in the energy-minimized structure (MM3) of the bound **6**.

The 2D ^{1}H NOESY experiment of the complex showed nOe cross-peaks between most of the hydrogen atoms in adjacent carbons, except for $H^{d}_{(cc\text{-}6\subset1)}$-$H^{e}_{(cc\text{-}6\subset1)}$ (**Figure 13**). This observation supported the presence of many gauche interactions in the

folded *cis,cis*-**6** included in **1**. The molecular modeling of the *cis,cis*-**6⊂1** complex also revealed multiple gauche interactions in the folded alkyl chain of the guest. The distance between terminal oxygen atoms of *cis,cis*-**6** in fully extended conformation is 3.9 Å longer than the one measured in the MM3 energy-minimized structure of inclusion complex *cis,cis*-**6⊂1**. This difference required an extensive folding of the bound *cis,cis*-**6** as indicated above. The PC value calculated for the *cis,cis*-**6⊂1** complex is larger than 55%.

Alkanes folded in helical conformations to fit in Rebek´s dimeric capsule (vide supra).[5] The width of the cylindrical cavity of Rebek's dimer was suitable for the guest to fit with this type of folding. However, in the case of cage **1**, the width of the cavity might be too small to fit the folded alkyl chains of the included guests in a helical conformation. The absence of the characteristic nOe cross-peaks between the hydrogen atoms of the C_i and C_{i+4} carbons of the chain supported that the folding of the bound *cis,cis*-**6** did not adopt a helical conformation.

4.2.7 Studies of the inclusion of diformamide **7** (11 × CH_2) in octa-imine **1**

We added an equimolar amount of **7** (eleven methylene units separating the formamide ends) to a solution of cage **1** (2 mM in $CDCl_3$: CD_3CN 9:1). The ^1H NMR spectrum of the solution mixture showed the appearance of a new set of signals. The signals of free diformamide **7** and cage **1** were still visible in the ^1H NMR spectrum. We attributed the new set of signals to the formation of the **7⊂1** complex (**Figure 14b**). The intensity of imine proton signals of free cage $H^5_{(1)}$ and inclusion complex $H^5_{(\mathbf{7\subset 1})}$ are close to 1:1. When 2 equiv. of **7** was added (**Figure 14c**), the remaining proton signals mainly corresponded to the inclusion complex, which agree with a D_{4h} symmetry. The 2D ^1H NOESY experiments displayed the expected intramolecular nOe cross peak between the terminal formyl protons and the α-CH_2 methylene that is indicative of the selective inclusion of the *cis,cis*-isomer of **7** in the cavity of **1**. Taken together these observations, we assigned a binding constant of cage **1** towards *cis,cis*-**7** lower than that previously observed for *cis,cis*-**6** (> 10^6 M^{-1}).

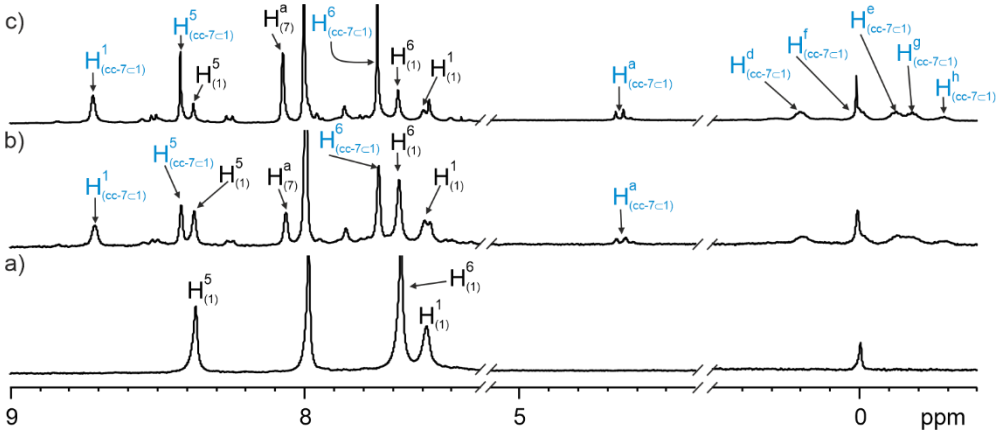

Figure 14. Selected regions of the ^1H NMR spectra (500 MHz, 298 K, $CDCl_3$: CD_3CN 9:1) of (a) octa-imine cage **1**, (b) 1:1 mixture of octa-imine cage **1** and guest **7**. (c) 1:2 mixture of octa-imine cage **1** and guest **7**.

4.2.8 Summary of the binding studies of cage **1** with diformamide series.

Taken all together, octa-imine cage **1** preferentially binds diformamides **2**-**7** in the *cis,cis*-conformation. Formamide guest **2** with only 6 methylene units between the two formamide ends is too short to establish a ditopic interaction between the two distal hemispheres. Consequently, in the **2⊂1** inclusion complex(es) the included

guest is exchanging fast in the ^{1}H NMR timescale between the two binding sites. This results in broad signals in the ^{1}H NMR spectrum (**Figure 15a**).

Formamide **3**, with an additional methylene unit, can establish a ditopic interaction with the two binding sites of cage **1** immediately and exclusively forming the complex *cis,cis*-**3**⊂**1** in solution with the bound *cis,cis*-**3** in an almost extended conformation (**Figure 15b**). The addition of more methylene units between formamide ends (**4**-**6**) results in an increase number of gauche interactions for the bound guests confirming the folded conformation of the included guests. Considering the low concentration of the *cis-cis*- isomers in solution the results of the binding experiments suggested that the binding constant of cage **1** for guests **3-6** is larger than 10^6 M^{-1}.

Interestingly, both pyrrole NH signal of the bound cage **1** (H^1s) and formyl proton of bound formamide (H^a) appear downfield shifted in the inclusion complexes of guests **4-6** (**Figure 15c-e** and **Table 3**) concerning the analogous in the *cis,cis*-**3**⊂**1** counterpart (**Figure 15b**). The downfield shift increases with the increase of the number of methylene spacers (**Figure 15**). This trend could be related to the length of the hydrogen bond interactions which become shorter in inclusion complex with longer guests. When the number of methylene groups increased to 11 (guest **7**), the binding constant dropped at least one order of magnitude. Moreover, the Δδ of the NH protons $H^1_{(cc\text{-}7\subset1)}$ (Δδ) is also reduced compared to $H^1_{(cc\text{-}6\subset1)}$.

Remarkably, the proton located in the central methylene unit of the free diformamides (H^e for **2**, H^f for **3** and **4**; H^g for **5** and **6**; and H^h for **7**), resonate almost at the same chemical shift (1.25 ppm) compared to those of the free guest . The energy minimized structures of the inclusion complexes show these protons located in the center of capsule which might be well-shielded by the phenyl ring of the linker. We hypothesized that the higher packing states (**Table 3**) locate these protons far away from the central axis (C_4) and close to the portals of cage **1**. The high mechanical pressure inside cage **1** in the case of the inclusion of large guests might deform the aromatic walls to a certain degree, resulting in a larger space between two aromatic walls. For protons located close to this region, the shielding effect of the cavity can decrease significantly.[16]

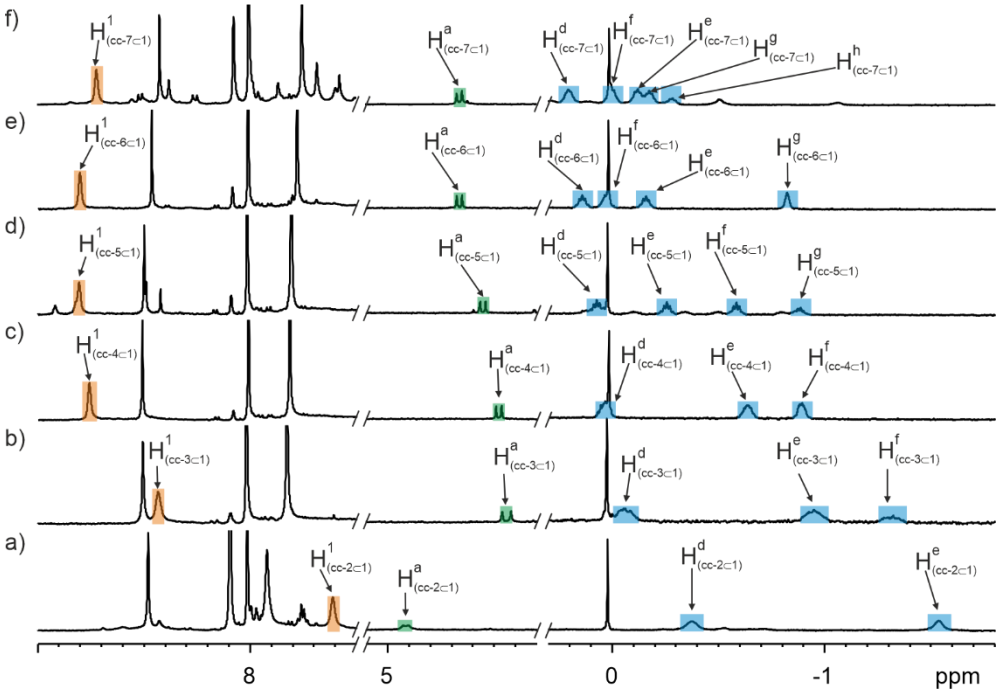

Figure 15. Selected regions of the ^{1}H NMR spectra (500 MHz, 298K, $CDCl_3$: CD_3CN 9:1) of the complexes between cage **1** and guest a) **2**; b) **3**; c) **4**; d) **5**; e) **6**; f) **7**. In the cases of b) to e) 1 equiv. of guest was added to a 2 mM solution of cage **1**. For a) and f) an excess (> 2 equiv.) of the diformamide guests was added.

Table 3. Calculated packing coefficients (PCs), length difference (Δ d) (in Å) between the two oxygen atoms of the formyl groups in the *cis,cis*-conformation of the bound guests and that of the fully extended *cis,cis*-diformamide and induced chemical shift values ($\Delta\delta = \delta$bound - δfree, ppm) for the pyrrole NHs and formyl protons in the inclusion complexes.

Guest	PC %[a]	Δ d (Å)	$\Delta\delta$ H^1 (ppm)	$\Delta\delta$ H^a (ppm)
2	52		0.02	-3.04
3	57	0.3	0.84	-3.51
4	61	1.3	1.17	-3.48
5	66	2.4	1.22	-3.40
6	68	3.9	1.21	-3.30
7	72	5.1	1.13	-3.30

[a] Packing coefficients (PC% =(V_{guest}/V_{host})×100) derived from the energy-minimized inclusion complexes (MM3). The volumes of the bound capsules and the included guests were calculated using SwissPDB Version 4.10.

4.2.9 Pair-wise competitive binding studies of diformamides with the octa-imine cage 1.

We designed a series of pair-wise competitive binding experiments of diformamides **3**-**6** with octa-imine cage **1** to determine the relative thermodynamic stabilities of the corresponding inclusion complexes (**3**-**6**⊂**1**). The thermodynamic stability of the corresponding 1:1 inclusion complexes will mainly depend on the conformations adopted by the diformamides guests in the cavity of cage **1**. On the one hand, we assumed that the inclusion complex **3**⊂**1** was probably the most thermodynamically stable because the bound diformamide **3** adopted an almost fully extended conformation lacking significant gauche interactions. On the other hand, we considered that, most likely, the inclusion complex **6**⊂**1** was the less thermodynamically stable complex. This was attributed not only to the larger number of gauche interactions caused by the folding of the diformamide upon inclusion in cage **1** but also to the high PC value (68%) calculated for the resulting inclusion complex.

*Pair-wise competitive binding of diformamide **3** and **6** with octa-imine cage **1***

We started the pair-wise competitive binding experiments by adding an equimolar amount of diformamide **3** (7 × CH_2) to a solution of the pre-formed inclusion complex **6** (10 × CH_2)⊂**1** (2 mM in $CDCl_3$: CD_3CN 9:1). We monitored the guest exchange process using ^{1}H NMR spectroscopy. The spectrum acquired immediately after adding **3** (~5 min) showed the immediate emergence of the **3**⊂**1** complex. However, its diagnostic proton signals displayed a reduced intensity (**Figure 16a**). After 2 h, the signals for the **6**⊂**1** complex were not visible anymore in the ^{1}H NMR spectrum. Only the signals corresponding to the **3**⊂**1** complex were shown (**Figure 16c**). As expected, the result supported that the inclusion complex of the shorter diformamide **3**⊂**1** was favored thermodynamically over the **6**⊂**1** complex. We estimated an energy difference between the two inclusion complexes (100:1) larger than 2.7 kcal·mol^{-1}. Remarkably, the exchange process between the two guests was slow on the human time scale requiring more than 2 h to reach the equilibrium.

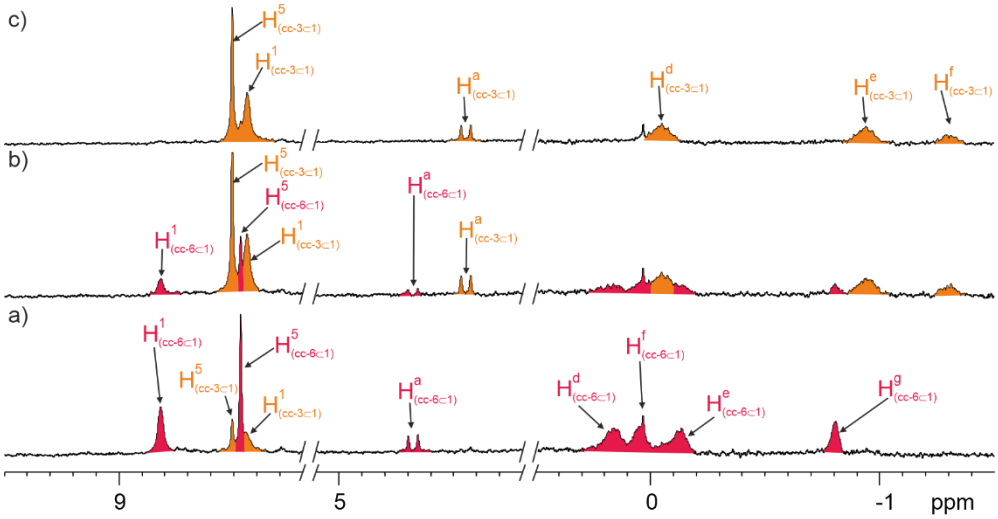

Figure 16. Selected region of the ^{1}H NMR spectra (300 MHz, at 298 K, $CDCl_3$:CD_3CN 9:1 mixture) of a solution mixture of inclusion complex **6** (10 × CH_2)⊂**1** (2 mM) and diformamide **3** (7 × CH_2) (1 equiv.); a) immediately after the addition of **3**, b) 1 h after the addition of **3**, and c) 2 h after addition of **3**.

*Pair-wise competitive binding of diformamide **3** and **5** with octa-imine cage **1***

To a thermodynamically equilibrated solution of complex **5** (9 × CH_2) ⊂**1** (2 mM in $CDCl_3$: CD_3CN 9:1), which contained a mixture of the *cis,cis*-**5⊂1** and *trans,cis*-**5⊂1** isomeric complexes in 65:35 molar ratio, respectively, we added an equimolar amount of **3** (7 × CH_2). We monitored the guest exchange process using ^{1}H NMR spectroscopy. The spectrum acquired following the addition of **3** (5 min), revealed the appearance of *cis,cis*-**3⊂1** complex in solution to a very reduced extent. With time, the signals corresponding to the *cis,cis*-**3⊂1** increased at the expenses of those of the *cis,cis*-**5⊂1** and *cis,trans*-**5⊂1** complexes. After 6h, the intensity of the signals corresponding to the *cis,cis*-**5⊂1** and the *cis,cis*-**3⊂1** was almost the same (**Figure 17b**). The inclusion complex *cis,trans*-**5⊂1** should also be present in the solution to maintain the 65:35 equilibrium isomeric ratio. Probably, its concentration is too low to be detected by ^{1}H NMR spectroscopy.

After 24 h, we could not observe further changes in the ^{1}H NMR spectrum, indicating that the equilibrium was reached (**Figure 17c**). Based on integral values of selected proton signals, we determined an 80:20 ratio for *cis,cis*-**3⊂1**: *cis,cis*-**5⊂1.** This ratio assigned an energy advantage of 0.8 kcal·mol^{-1} to the *cis,cis*-**3⊂1** complex over the *cis,cis*-**5⊂1.** Most likely, the slower rate observed for the exchange of the included guests **5** by **3** compared to that of **6** by **3** is related to the superior reversibility of the

former exchange reaction owing to the reduced difference in thermodynamic stability of the involved inclusion complexes (*cis,cis*-**5⊂1** and *cis,cis*-**3⊂1).**

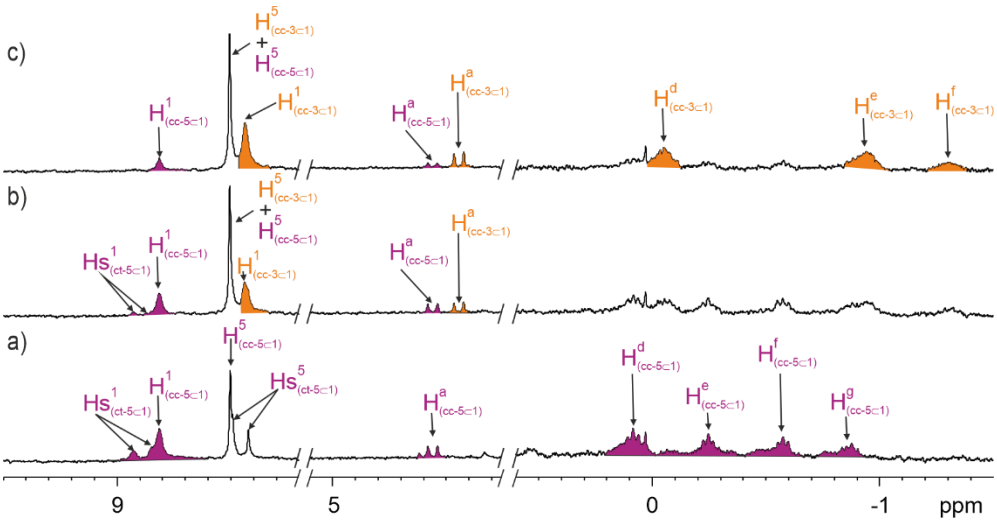

Figure 17. Selected region of the ^{1}H NMR spectra (300 MHz, at 298 K, $CDCl_3$:CD_3CN 9:1 mixture) of a solution mixture of isomeric inclusion complexes cis,cis- and cis-trans-**5** (9 × CH_2)⊂**1** (2 mM) (65:35) and equimolar amount of diformamide **3** (7 × CH_2) a) immediately after the addition of **3** (1 equiv.), b) 6 h after the addition of **3**, c) 24 h after the addition of **3**.

*Pair-wise competitive binding of diformamides **3** and **4** with octa-imine cage **1**.*

To our surprise, the addition of an equimolar amount of formamide **3** (7 × CH_2) to a solution containing the preformed and thermodynamically stabilized *cis-cis*-**4** (8 × CH_2)⊂**1** inclusion complex (2 mM in $CDCl_3$: CD_3CN 9:1) did not produce any detectable changes due to guest exchange even after 1 week. For this reason, we decided to perform the pair-wise competition adding a mixture of the two diformamides (1 equiv. of each) to a solution of the octa-imine cage **1**. The downfield region of ^{1}H NMR spectrum of the mixture acquired following the addition (5 min) showed three sets of NH signals corresponding to the inclusion complexes *cis,cis*-**3⊂1**, *cis,trans*-**4⊂1,** and *cis,cis*-**4⊂1**. The existence of a mixture of complexes was also substantiated by the observation of two partially overlapping doublets, producing a pseudo-triplet, at δ = 4.4 ppm corresponding to the cis-formyl protons of their bound ends (**Figure 18a**). Based on the intensity of the diagnostic proton signals of the complexes, we estimated that the composition of the mixture at this time was approximately 45% of isomeric **4⊂1** complexes and 55% of *cis,cis*-**3⊂1** complex. In short, octa-imine **1** did not show a significant kinetic selectivity for

the inclusion of any of the two formamides. We reanalyzed the solution mixture after 24 h and learned that the ratio of inclusion complexes of the diformamides did not change (**Figure 18c**). However, and in agreement with the previous findings, the *cis,trans*-**4⊂1** complex had almost completely isomerized to the *cis,cis*- counterpart.

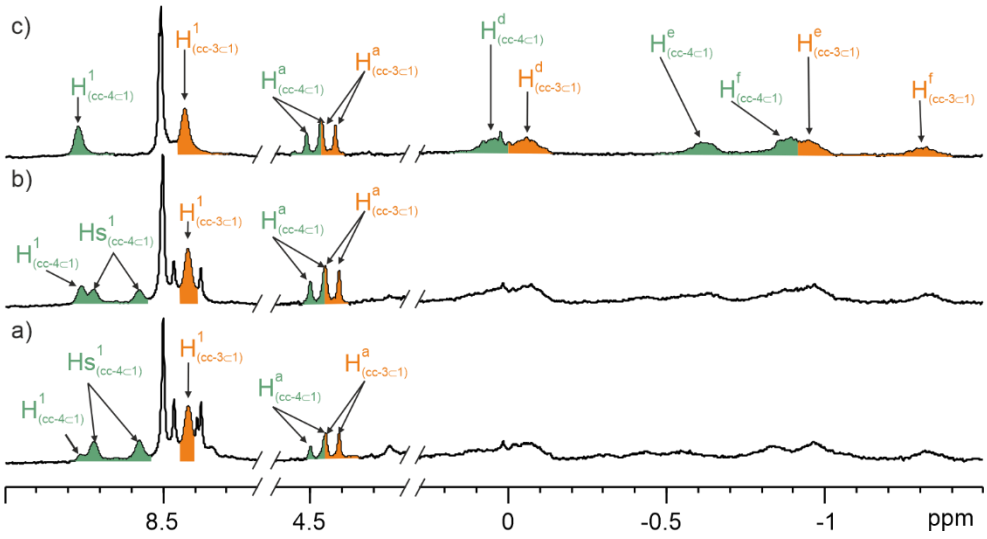

Figure 18. Selected region of the ^{1}H NMR spectra (300 MHz, at 298 K, $CDCl_3$:CD_3CN 9:1 mixture) of a solution mixture of isomeric inclusion complexes cis,cis- and cis-trans-**4** (8 × CH_2)⊂**1** (2 mM) (65:35) and equimolar amount of diformamide **3** (7 × CH_2): a) immediately after the addition; b) 4 h after the addition; c) 24 h after the addition.

The contrasting results of the two competitive pair-wise binding experiments were not easy to reconcile. We concluded that the thermodynamic equilibrium was not reached in any of them. For this reason, we designed a third series of competitive binding experiments in which we added, in separate NMR tubes containing the thermodynamically equilibrated *cis,cis*-**4⊂1** complex, 10, 50, and 100 equiv. of diformamide **3**. We monitored the exchange processes by ^{1}H NMR at different times. After 500 h, we observed the presence of diagnostic signals of the *cis,cis*-**3⊂1** complex to an extent close to 15% in all three cases. From this observation, we inferred that the exchange kinetics seemed to be of zero order concerning the diformamide **3** and that more than 500 h were necessary to reach equilibrium.

We determined an initial guest exchange rate value (from *cis,cis*-**4⊂1** to *cis,cis*-**3⊂1** complex) of 1.67 × 10^{-10} M·s^{-1}. Taking together the initial concentration of *cis,cis*-**4⊂1** (2 × 10^{-3} M), we estimated a rate constant for the exchange to be 8.35 × 10^{-8} s^{-1}. This value served to assign an energy barrier ($\Delta G^{\ddagger}$) of 27.1 kcal·mol^{-1}.

4.2.10 Possible interconversion pathways between the inclusion complexes of the *cis,trans*-diformamide **4** and the *cis,cis*-counterpart.

For the sake of brevity, we will explain this section focusing on the putative behavior of formamide **4** (8 × CH_2). Nevertheless, all provided explanations could be also applicable to the inclusion of diformamide **5** (9 × CH_2) in the octa-imine cage **1**.

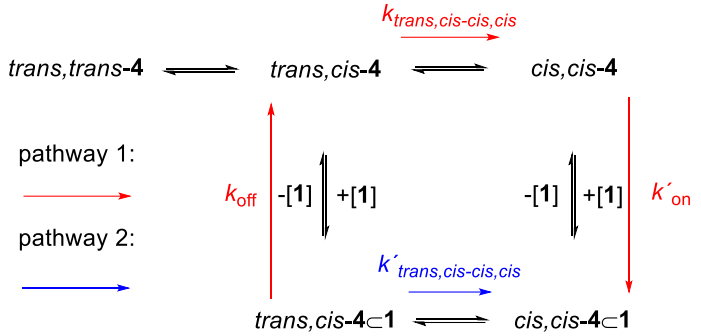

Figure 19. Theoretical model considering the inclusion of different conformers of **4** in the cavity of **1**.

We propose two possible mechanisms for the interconversion of the *trans,cis*-**4⊂1** inclusion complex into the *cis,cis*-**4⊂1** counterpart. The first pathway (red arrows in **Figure 19**) might go through a guest exchange mechanism, in which cage **1** exchanges the kinetically bound *trans,cis*-**4** diformamide with *cis,cis*-**4** isomer present in solution to a very reduced extent (~ 3-5 %). An alternative pathway (blue arrow in **Figure 19**) could involve the isomerization of the bound diformamide *trans,cis*-**4** inside the cavity of cage **1** to the bound *cis,cis*-**4** through a conformational exchange mechanism. Unfortunately, experimentally, it was not possible to identify which mechanism was taking place in the solution.

In an attempt to gain more insight into the interconversion mechanism, we fit the observed changes in concentration of *trans,cis*-**4⊂1** and *cis,cis*-**4⊂1** with time to a reversible theoretical kinetic model A ⇌ B using Parameter Estimation module in the COPASI Software Version 4.25 (**Figure 20**).[17]

$$cis,trans-\mathbf{4}\subset\mathbf{1}\underset{\boldsymbol{k_{-2}}}{\overset{\boldsymbol{k_2}}{\rightleftarrows}}cis,cis-\mathbf{4}\subset\mathbf{1}$$

$$K_a = \frac{[cis, trans - \mathbf{4} \subset \mathbf{1}]}{[cis, cis - \mathbf{4} \subset \mathbf{1}]} = \frac{k_2}{k_{-2}}$$

The fit of the experimental data to the theoretical model was good and returned a rate constant of k_2 = 3.63 × 10^{-5} s^{-1} which assigned an energy barrier of interconversion of 23.5 kcal mol^{-1}.

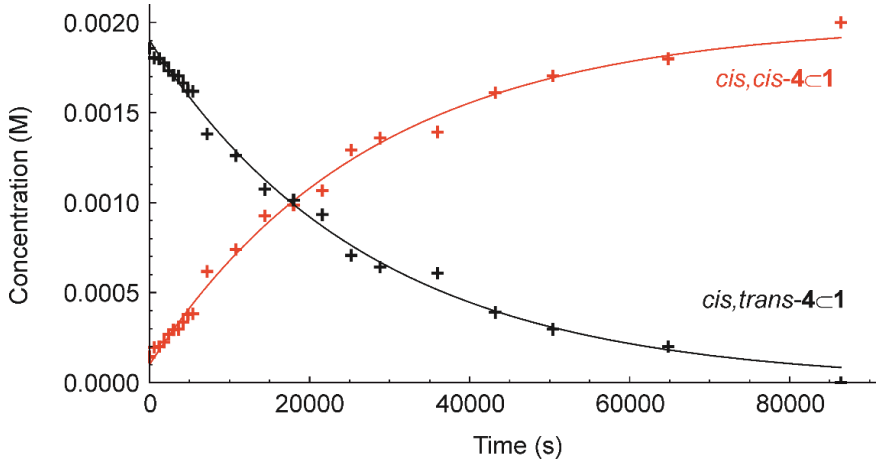

Figure 20. Concentration (M) versus time (s) of *cis,trans*-**4**⊂**1** (black) and *cis,cis*-**4**⊂**1** (red). Initial concentrations: [*cis,trans*-**4**⊂**1**] = 1.9 × 10^{-3} M and [*cis,cis*-**4**⊂**1**] = 1.0 × 10^{-4} M. The lines show the fit of the kinetic data.

We compared this value with that determined in the previous section for the guest exchange process between *cis,cis*-**4**⊂**1** and *cis,cis*-**3**⊂**1** (27.1 kcal·mol^{-1}). The observed difference in energy barriers suggested that most likely the interconversion of *trans,cis*-**4**⊂**1** to *cis,cis*-**4**⊂**1** occurs through a conformational exchange mechanism instead of a guest exchange mechanism.

The relative values determined for the energy barriers of both processes (23.5 vs 27.1 kcal·mol^{-1}) were in agreement with the larger number of interactions (i.e. hydrogen bonds) that need to be broken considering the guest exchange process compared to the conformational exchange counterpart.

The change of the energy barrier of isomerization of amides included in molecular containers has already been reported by groups of Reindhout [18] and Fujita. [19] However, similar observations have not been reported so far for formamide guests. The larger energy barrier of formamide´s isomerization inside cage **1** (23.5 kcal·mol^{-1}) compared to that in the bulk (~ 15-20 kcal·mol^{-1}) might be attributed to the necessary cleavage of multiple hydrogen bonds and the larger steric hindrance of the transition state of isomerization inside the container.

4.3 Conclusions

We described the formation of inclusion complexes between a homologous series of diformamides (**2**-**7**) having a different number of methylene units (5-11) separating the two formamide ends and the molecular octa-imine cage **1** in a mixture of organic solvents. In all cases, the binding of diformamides involves the inclusion of *cis*-enriched isomers. In addition, the alkyl chains of the included guests must fold experiencing an induced-fit conformation because their energetically favorable fully-extended forms are too long to fit the cavity size. The conformational adaption process of the included guests takes place when the binding interactions can overcome the costs associated with the higher energy conformation necessary for binding. The size and shape limitations of cage **1** restricts guests to adopt folded conformations having at least one of their terminal formamides ends in *cis*-form. Remarkably, we detected two semi-stable conformations of the guests in the isomeric inclusion complexes *cis,trans*-**4⊂1** and *cis,trans*-**5⊂1** that interconverted with time to the corresponding *cis,cis*-analogues. The interconversion processes of the semi-stable states into the thermodynamically more stable *cis,cis*-forms of the inclusion complexes are slow on the human time scale (i.e. hours). We suggest two possible interconversion mechanisms: 1) the conformational exchange of the *cis,trans*-isomers into the *cis,cis*-analogues takes place on the bound guest or 2) the interconversion goes through a guest exchange process. The comparison of the energy barrier determined for the interconversion process (23.5 kcal·mol^{-1}) and that derived from the pair-wise competitive binding experiments using **3** and the *cis,cis*-**4⊂1** complex (27.1 kcal·mol^{-1}) suggested that the interconversion of *cis,trans*-isomer into the *cis,cis*-analogue occurs through an isomerization process inside the cage (conformational exchange mechanism).

4.4 Experimental section

4.4.1 General information

Starting materials and reagents were purchased from commercial suppliers and used without further purification. All reactions were performed under an argon atmosphere and protected from light unless specified. Anhydrous solvents were obtained from a solvent purification system SPS-400-6 from Innovative Technologies. All solvents were of HPLC grade quality, commercially obtained, and used without further purification. ^{1}H NMR, ^{13}C NMR, and 2D NMR spectra were recorded on a Bruker Avance 400 (400 MHz for ^{1}H NMR) and Bruker Avance500 (500 MHz for ^{1}H NMR). Deuterated solvents from Sigma Aldrich were used for NMR studies. Chemical shifts are given in ppm, relative to residual solvents.
The synthetic procedure to prepare cage **1** is reported in **Chapter 3**. Diformamides **2**-**7** were synthesized following previously reported procedures in the literature.[12]

4.4.2 Study of the inclusion complex 2⊂1

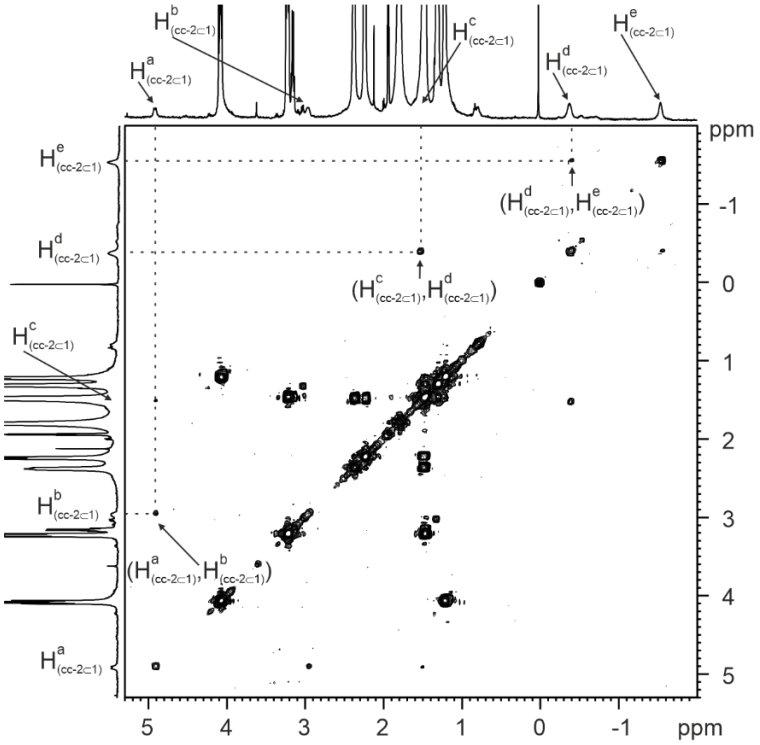

Figure 21. Selective region of the ^{1}H-^{1}H COSY (500 MHz, 298 K, $CDCl_3$: CD_3CN 9:1) spectra of **2⊂1** complex (2 mM). See **Figure 4** for the proton's assignment.

4.4.3 Study of the inclusion complex **3⊂1**

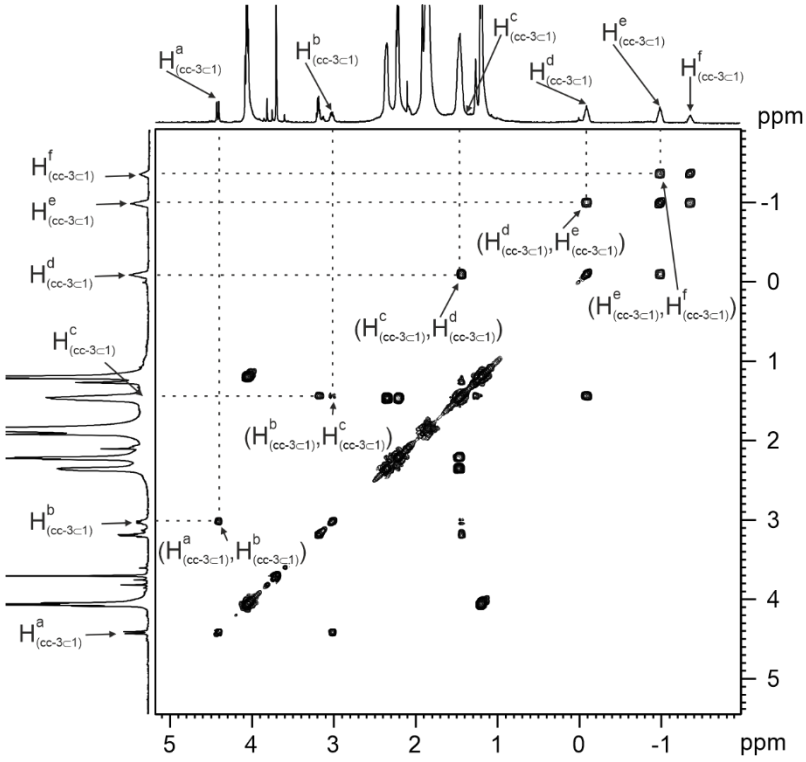

Figure 22. Selective region of the ^{1}H-^{1}H COSY (500 MHz, 298 K, $CDCl_3$: CD_3CN 9:1) spectra of **3⊂1** complex (2 mM). See **Figure 6** for the proton's assignment.

4.4.4 Study of the inclusion complex **4⊂1**

Table 4. Experimental chemical shifts of free (δ_{free}) and bound (δ_{bound}) guest **4** and complexation-induced shifts ($\Delta\delta$).

Signal	δ_{free} (ppm)	Signal	δ_{bound} (ppm)	$\Delta\delta$ (ppm)
$H^{a}_{(cc\text{-}4)}$	7.96	$H^{a}_{(cc\text{-}6\subset1)}$	4.47	-3.59
$H^{b}_{(cc\text{-}4)}$	5.69	$H^{b}_{(cc\text{-}6\subset1)}$	3.04	-2.92
$H^{c}_{(cc\text{-}4)}$	3.13	$H^{c}_{(cc\text{-}6\subset1)}$	1.53	-1.66
$H^{d}_{(cc\text{-}4)}$	1.45	$H^{d}_{(cc\text{-}6\subset1)}$	0.0176	-1.43
$H^{e}_{(cc\text{-}4)}$	1.28	$H^{e}_{(cc\text{-}6\subset1)}$	-0.660	-1.94
$H^{f}_{(cc\text{-}4)}$	1.28	$H^{f}_{(cc\text{-}6\subset1)}$	-0.912	-2.19

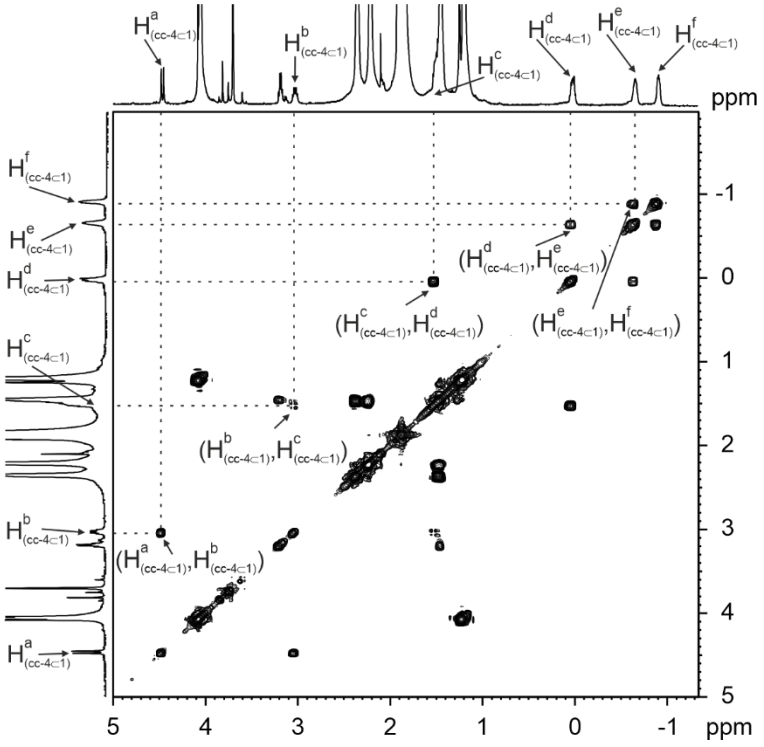

Figure 23. Selective region of the ^{1}H-^{1}H COSY (500 MHz, 298 K, $CDCl_3$: CD_3CN 9:1) spectra of **4⊂1** complex (2 mM). See **Figure 9** for the proton's assignment.

4.4.5 Study of the inclusion complex **5⊂1**

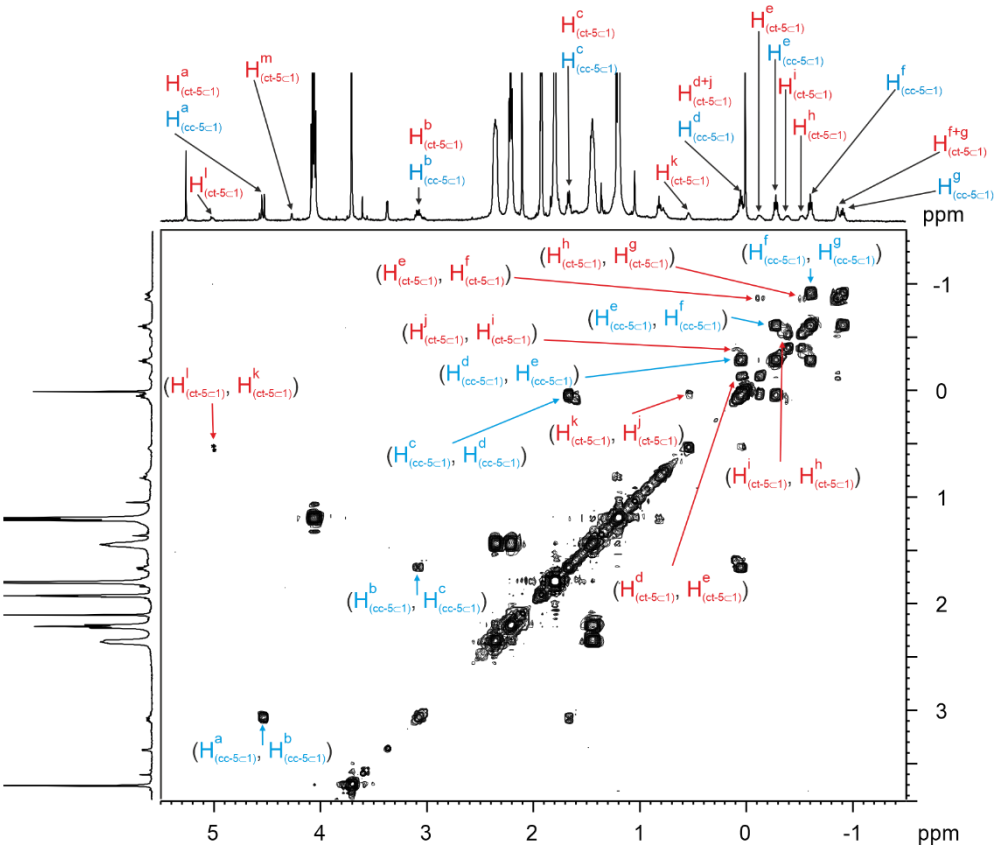

Figure 24. Selective region of the ^{1}H-^{1}H COSY (500 MHz, 298 K, $CDCl_3$: CD_3CN 9:1) spectra of **5⊂1** (2 mM). See **Figure 11** for protons assignment.

4.4.6 Study of the inclusion complex 6⊂1

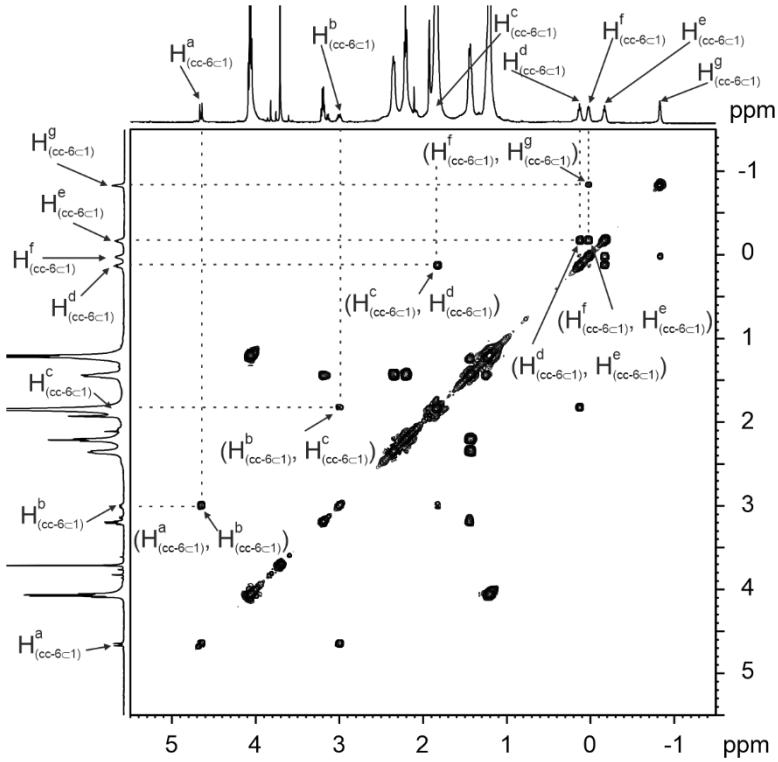

Figure 25. Selective region of the ^{1}H-^{1}H COSY (500 MHz, 298 K, $CDCl_3$:CD_3CN 9:1) spectra of **6⊂1** (2 mM). see **Figure 13** for the protons assignment.

4.4.7 Study of the inclusion complex **7⊂1**

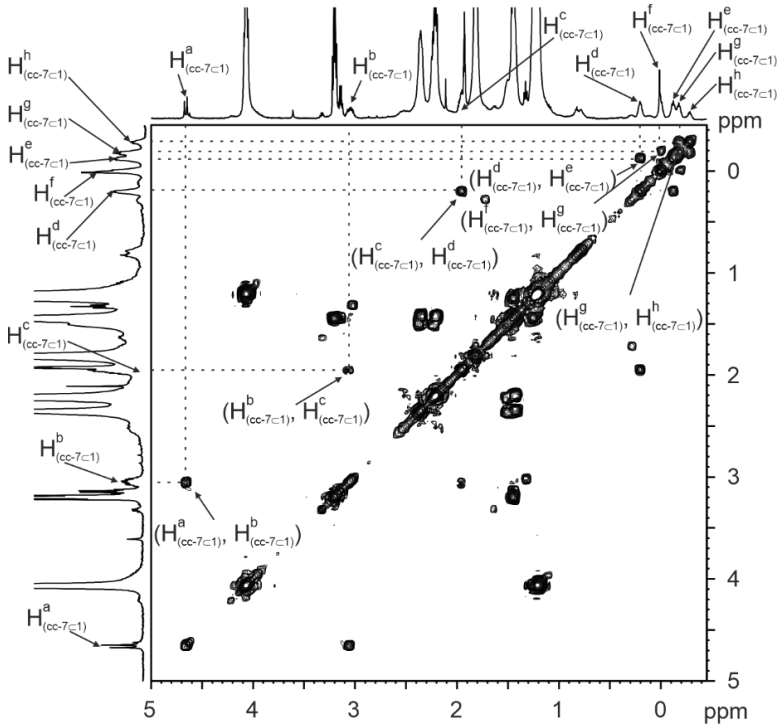

Figure 26. Selective region of the ^{1}H-^{1}H COSY (500 MHz, 298 K, $CDCl_3$:CD_3CN 9:1) spectra of **7⊂1** (2 mM).

Table 5. Calculated packing coefficients (PCs) and dimensions of guests derived from MM3 calculations.

Guest	V_1 (Å^3)	V_{guest} (Å^3)	PC %[a]	d_{free} (Å)[b]	d_{bound} (Å)[c]	Δ d (Å)
2	329	171	52	13.6		
3	334	189	57	14.6	14.3	0.3
4	336	204	61	16.0	14.7	1.3
5	340	223	66	17.2	14.8	2.4
6	352	239	68	18.5	14.6	3.9
7	355	257	72	19.7	14.6	5.1

[a] Packing coefficients (PC % =(V_{guest}/V_{host})×100) derived from the energy-minimized inclusion complexes (MM3). The volumes of the bound capsules and the included guests were calculated using SwissPDB Version 4.10.[b] Distances between the two oxygen atoms of the energy-minimized guests in fully extended *cis,cis*-conformations. [c] Distances between the two oxygen atoms of the guests in the energy-minimized structures of the complexes.

4.5 References and notes

[1] Rebek, J., *Proc. Natl. Acad. Sci.* **2009,** *106* (26), 10423-10424.
[2] Fischer, E., *Ber. Dtsch. Chem. Ges.* **1894,** *27* (3), 2985-2993.
[3] Thoma, J. A.; Koshland, D. E., Jr., *J. Am. Chem. Soc.* **1960,** *82* (13), 3329-3333.
[4] Ajami, D.; Rebek, J., *Nature Chem.* **2009,** *1* (1), 87-90.
[5] Scarso, A.; Trembleau, L.; Rebek, J., *J. Am. Chem. Soc.* **2004,** *126* (41), 13512-13518.
[6] Mecozzi, S.; Rebek, J., Julius, *Chem. Eur. J.* **1998,** *4* (6), 1016-1022.
[7] Valdes, C.; Spitz, U. P.; Toledo, L. M.; Kubik, S. W.; Rebek, J., Jr., *J. Am. Chem. Soc.* **1995,** *117* (51), 12733-12745.
[8] Grimm, L. M.; Spicher, S.; Tkachenko, B.; Schreiner, P. R.; Grimme, S.; Biedermann, F., *Chem. Eur. J.* **2022,** *28* (38), e202200529.
[9] Espelt, M.; Ballester, P., *Org. Lett.* **2012,** *14* (22), 5708-5711.
[10] Escobar, L.; Díaz-Moscoso, A.; Ballester, P., *Chem. Sci.* **2018,** *9* (36), 7186-7192.
[11] Sun, Q.; Escobar, L.; de Jong, J.; Ballester, P., *Chem. Sci.* **2021,** *12* (40), 13469-13476.
[12] Khamphaijun, K.; Namnouad, P.; Docker, A.; Ruengsuk, A.; Tantirungrotechai, J.; Díaz-Torres, R.; Harding, D. J.; Bunchuay, T., *Chem. Commun.* **2022,** *58* (52), 7253-7256.
[13] Li, Y.-S.; Escobar, L.; Zhu, Y.-J.; Cohen, Y.; Ballester, P.; Rebek, J.; Yu, Y., *Proc. Natl. Acad. Sci.* **2019,** *116* (40), 19815-19820.
[14] Karplus, M., *J. Am. Chem. Soc.* **1963,** *85* (18), 2870-2871.
[15] Pastor, A.; Martínez-Viviente, E., *Coord. Chem. Rev.* **2008,** *252* (21), 2314-2345.
[16] Tzeli, D.; Petsalakis, I. D.; Theodorakopoulos, G.; Rahman, F.-U.; Ballester, P.; Rebek Jr., J.; Yu, Y., *ChemPhysChem* **2020,** *21* (19), 2187-2195.
[17] Hoops, S.; Sahle, S.; Gauges, R.; Lee, C.; Pahle, J.; Simus, N.; Singhal, M.; Xu, L.; Mendes, P.; Kummer, U., *Bioinformatics* **2006,** *22* (24), 3067-3074.
[18] Timmerman, P.; Verboom, W.; van Veggel, F. C. J. M.; van Duynhoven, J. P. M.; Reinhoudt, D. N., *Angew. Chem., Int. Ed.* **1994,** *33* (22), 2345-2348.
[19] Takezawa, H.; Shitozawa, K.; Fujita, M., *Nature Chem.* **2020,** *12* (6), 574-578.

Chapter 5

Polar Octa-imine cages as molecular containers for Huisgen 1,3-dipolar cycloaddition reactions

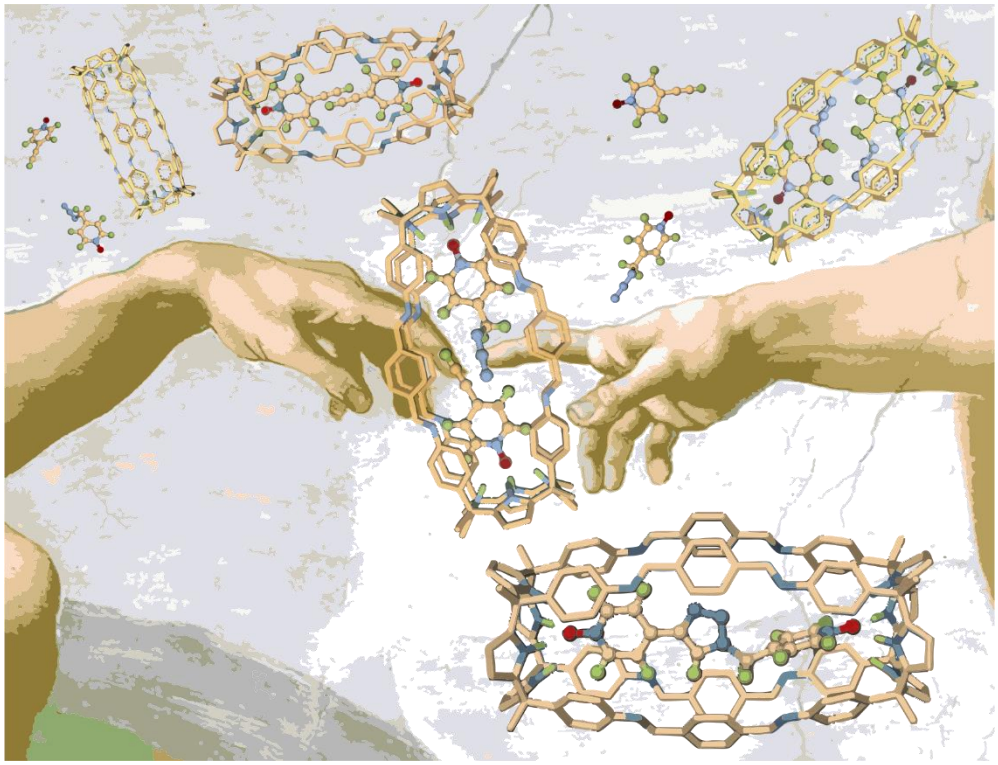

Unpublished results

UNIVERSITAT ROVIRA I VIRGILI
Receptors based on Aryl-extended Calix[4]pyrrole Scaffolds
Yifan Li

5.1 Introduction

The confinement of molecules in nanometric spaces can change their physical and chemical properties. In living systems, enzymes bind substrates in confined environments, *a.k.a*. active sites, to catalyze their chemical transformations under mild conditions.[1, 2] Enzymes place the reacting groups of the bound substrates in close proximity and favorable orientation for their reaction. This results in an effective increase in the concentration of the reactants and endows the reaction with an intramolecular character, resulting in a significant rate increase. It is also proposed that enzymes bind unstable and transient transition states more tightly than substrates or products, causing additional rate acceleration. In close analogy, highly reactive species and substrates´ high energy conformations were stabilized by inclusion in synthetic molecular containers, leading to altered reaction pathways, changes in selectivity, and rate increases compared to the bulk solution.[3,4,5] Entropic effects, particularly the 'Circe effect' proposed by William Jencks, have been instrumental in understanding enzyme catalysis. This phenomenon suggests that for unimolecular reactions, the ground state conformation of the substrate might be destabilized by enzyme binding. The substrate is bound in an optimal orientation for the reaction, in a conformation close to the transition state's geometry, provoking the reaction's acceleration. Relying on the same phenomenon, Page and Jencks estimated that the maximum entropic contribution of enzymatically converting a bimolecular reaction into an unimolecular was *c.a.* - 35 e.u. corresponding to a rate acceleration (effective molarity (EM = $e^{\Delta S/R}$)) between 10^7-10^8 M.[6]

The acceleration experienced by cycloaddition reactions upon inclusion of the reactants in covalent or supramolecular synthetic molecular containers was used to assess their potential use as synthetic enzymes. In the bulk, the azide-alkyne Huisgen 1,3-cycloaddition reaction requires elevated temperatures and often produces a mixture of two regioisomeric 1,2,3-triazoles.[7,8] Copper-[9] and Ruthenium-[10] catalyzed versions of this cycloaddition are well-known to selectively obtain the 1,4- or the 1,5-disubstituted 1,2,3-triazole isomer, respectively.

Mock et al. described the use of cucurbit[6]uril (CB[6]) to accelerate and control the regioselectivity of the intermolecular Huisgen cycloaddition between an azide and an alkyne at room temperature and in the absence of metal catalysts.[11, 12] The inclusion of the two ammonium-substituted reactants into the cavity of CB[6] produced a ternary complex featuring the reactive groups inside the cavity and turned the otherwise bimolecular reaction into an unimolecular one (**Figure 1a**). The acceleration of the reaction was estimated as 10^5 using initial rates ratio ($v_{complex}/v_{bulk}$). Moreover, the reaction was regioselective, producing only the 1,4-

substituted triazole. The authors attributed their results mainly to the increase in local concentration of the reactants inside the cavity. They also proposed that the cycloaddition transition state (TS) was stabilized inside the cavity as an additional factor responsible for the observed acceleration. It is worth noting here that in a separate work, a computational study from Maseras and Carlquist did not find any evidence for the hypothesized stabilization of the TS of the corresponding reaction but only for the reduction of the entropic penalty of pairing the two reactants.[13] For Mock's system, an EM of 1.6 $\times 10^4$ M was determined (i.e. $k_{complex}/k_{bulk}$) = 0.019 s^{-1}/1.16 $\times 10^{-6}$ $M^{-1}s^{-1}$). This value represents the hypothetical concentration of one of the two reactants needed in bulk to proceed at a rate equal to that of the reaction in the ternary inclusion complex.[14]

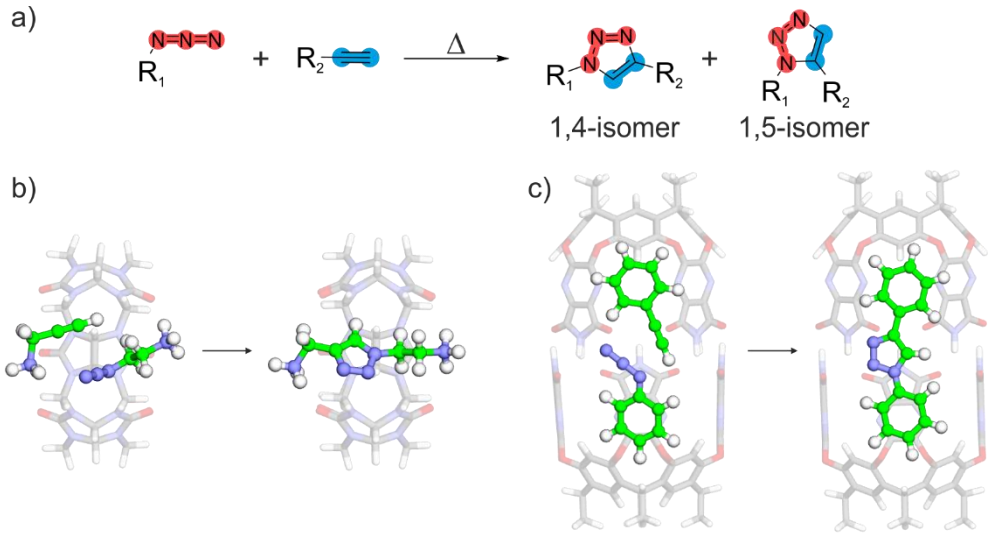

Figure 1. (Top) Reaction scheme of the Huisgen 1,3-cycloaddition of an azide with a terminal alkyne yielding 1,4- and 1,5- disubstituted-1,2,3-triazole isomers. (Bottom) Energy minimized (MM3) structures of the ternary complexes and their corresponding Huisgen 1,3-cycloaddition products in b) CB[6] and c) resorcin[4]arene cavitand dimer. Both reactions selectively yielded the 1,4-cycloaddition product. Some sections of the containers were removed for clarity.

In 2002, Rebek and collaborators reported the use of a self-assembled resorcin[4]arene cavitand dimer to accelerate the cycloaddition reaction between phenyl azide and phenylacetylene, producing exclusively the 1,4-triazole isomer.[15] Adding the two substrates to a mM solution of the resorcin[4]arene cavitand in mesitylene-d_{12} permitted the self-assembly of the dimeric container with the concomitant observation of the ternary complex (*a.k.a.* Michaelis complex) and other encapsulation complexes. The ternary complex consisted of one molecule of

phenylacetylene and one of phenyl azide simultaneously included in the cavity of the dimeric capsule, displaying an arrangement resembling the transition state's geometry producing the 1,4-isomer product (**Figure 1b**). The observation of the Michaelis complex facilitated the quantification of the rate constant in the presence of the capsule. The acceleration of the cycloaddition reaction inside the cavity was calculated as $v_{complex}/v_{bulk} = 240$, while the EM value of the reaction was estimated a few years later by Mandolini et al.[14] to be $k_{complex}/k_{bulk} = 120$ M. The authors proposed that the increase in the local concentration of the substrates inside the capsule was the main source of the observed reaction acceleration. A theoretical reaction rate inside the container was estimated, based on the rate constant of the reaction in the bulk and the effective concentrations of the included substrates (3.7 M), to be $v_{estimated} = k_{bulk} \times (3.7)^2 = 6 \times 10^{-8}$ Ms^{-1}. Interestingly, the measured reaction rate was lower than the theoretically estimated value ($v_{estimated}/v_{complex} = 45$).

Almost 20 years later, in 2017, Daver et al. reported a complete investigation on how the resorcin[4]arene cavitand dimer affected the free energy profile of the cycloaddition reaction.[16] In brief, they concluded that the main factors lowering the energy barrier for the cycloaddition reaction were the reduction of the entropic component associated with bringing the two substrates together (3.3 kcal·mol^{-1}) and the reduction of the steric strain present in the ternary complex (2.4 kcal·mol^{-1}). The contribution of the stabilization of the TS inside the capsule was calculated to be residual (0.7 kcal·mol^{-1}). In parallel to this work, Maseras and co-workers reached similar conclusions and demonstrated that product inhibition was responsible for the lack of efficient catalysis.[17] In other words, the product was the best fit for the cavity of the resorcin[4]arene dimer.

In the two works mentioned above, the two reactive groups are included in the containers' cavities, increasing the effective concentrations of the reactants. Owing to the inclusion of the reactants in the containers, translational, rotational, and conformational reaction entropy is also reduced by converting the bimolecular reaction into unimolecular. These two factors are critical for accelerating and controlling the regioselectivity in the included Huisgen 1,3-cycloaddition.[18]

In this chapter, we describe the binding properties of octa-imine cages based on aryl-extended calxi[4]pyrrole units with several *p*-substituted pyridine *N*-oxides and *N*-substituted 4-pyridone containing terminal alkyne and azide reacting groups. The octa-imine cage **1** was evaluated as a reactor vessel to mediate the 1,3-dipolar cycloaddition reaction between azido- and ethynyl-derived pyridine-*N*-oxides and 4-pyridone guests simultaneously included in its cavity. We expected that the tight binding of the substrates in the bis-calix[4]pyrrole-hemispheres of the cage, through

hydrogen-bonding and π-interactions, and the well-defined and fixed orientation of the reacting groups, facing each other inside the cavity, would produce larger EM values for the reaction occurring in the cage's cavity compared to Rebek's resorcin[4]arene dimer (*vide supra*). We also anticipated that the included cycloaddition reaction would be regioselective toward the 1,4-isomer owing to the reduced fit of the transition state geometry leading to the 1,5- counterpart.

5.2 Results and discussion

5.2.1. Design and synthesis

We designed octa-imine cage **1** to be evaluated as a reactor vessel to mediate the 1,3-dipolar cycloaddition reaction between azido- and ethynyl-derived pyridine-*N*-oxide guests (**2**-**5**) that can be simultaneously included in its cavity (**Figure 2**).

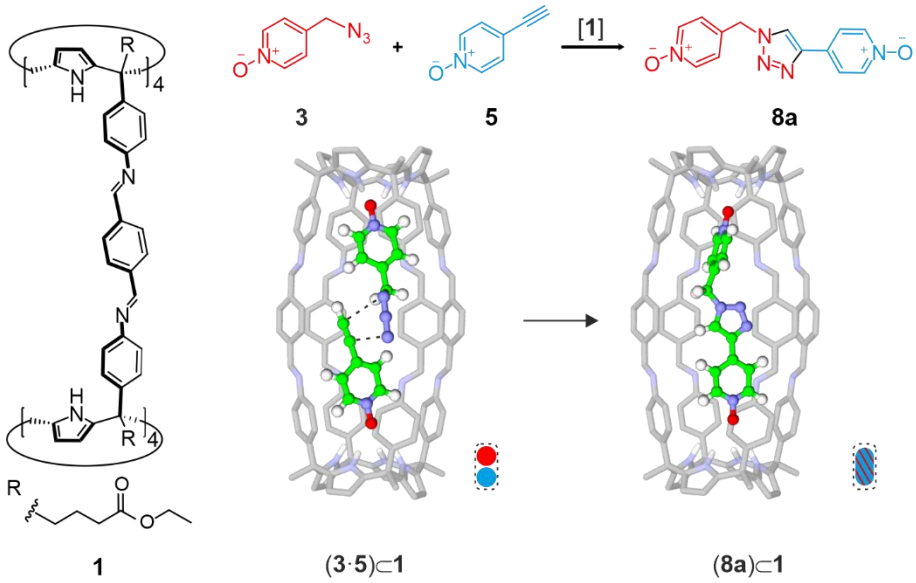

Figure 2. (Left) Line-drawing simplified structure of octa-imine cage **1**. (Right) Scheme of the 1,3-dipolar cycloaddition reaction between azido-pyridine-*N*-oxide **3** and ethynyl-pyridine-*N*-oxide **5** in the bulk (top) and in the cavity of the octa-imine cage **1** (bottom). The energy-minimized structures (MM3) of the (**3**·**5**)⊂**1** ternary complex and the cycloaddition product **8a** are also depicted in the figure with their cartoon representations.

We prepared a series of azide *p*-substituted pyridine-*N*-oxide derivatives featuring a different number of methylene units (CH_2, n = 0-2) between the reacting group and the pyridine-*N*-oxide ring (**2**-**4**). We were interested in studying the influence of the distance and orientation of the reacting groups in the acceleration and

regioselectivity of the Huisgen 1,3-cycloaddition reactions included in **1**. It is worth noting that all our attempts to synthesize 4-propyne pyridine-*N*-oxide were unsuccessful. Alternatively, we prepared the *N*-(2-propynyl) substituted 4-pyridone **6**. The 4-pyridone scaffold turned out to be a good alternative to the pyridine-*N*-oxide as a polar knob driving the inclusion of the reactants in the cavity of **1**.

Octa-imine cage **1** was prepared following the procedure described in **Chapter 3**. The 4-substituted pyridine-*N*-oxide guests **2-5** were synthesized from the corresponding pyridine derivates by oxidation with Oxone® in water, 2-butanone 1:1 solvent mixture. *N*-(2-propynyl) pyridone **6** was synthesized by reacting 4-hydroxypyridine with 3-bromopropyne in acetonitrile solution and in the presence of K_2CO_3 as the base (see experimental section).

The 1,4-tetrazoles isomers **7a-10a** were synthesized by cooper-catalyzed azide-alkyne cycloaddition (CuAAC) reactions of the corresponding substrates **2-6**. The reactions were performed in DCM solution using $Cu(CH_3CN)_4PF_6$ as catalyst and tris-(benzyltriazolymethyl)amine (TBTA) as ligand.

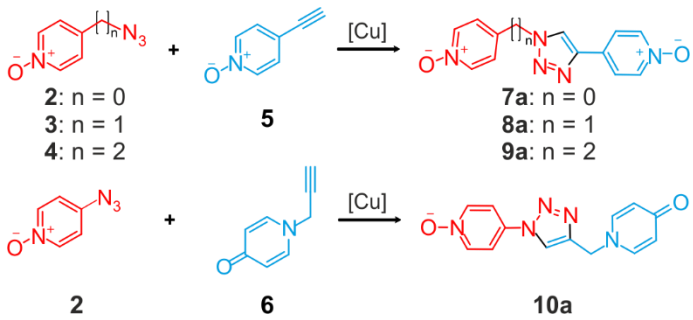

Scheme 1. Synthetic scheme for preparing the 1,4-isomers of the cycloaddition products (**7a**-**10a**) from the corresponding azido derivatives **2-4** and ethynyl derivatives **5-6**.

Molecular modeling studies (MM3) suggested that pyridine-*N*-oxide guests **2**-**6** were adequate in size, shape, and functional group to form 2:1 homo- and hetero-(ternary) inclusion complexes with cage **1** (**Figure 3**). Not surprisingly, the relative thermodynamic stabilities of the complexes depended on the guests' size, shape, and functional groups.

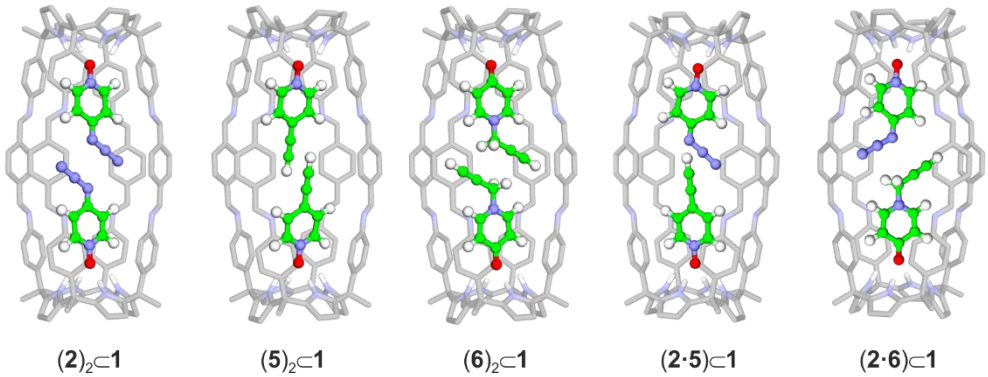

Figure 3. MM3 energy-minimized structures of selected examples of 2:1 homo- and hetero- (ternary) complexes of octa-imine cage **1** with guests **2**, **5,** and **6**. Cage **1** is shown in stick representation with only polar hydrogen atoms. Guests **2**, **5,** and **6** are shown in ball and stick representation with their carbon atoms displayed in green color.

5.2.2. Homo-inclusion complexes of octa-imine cage 1.

We investigated the formation of the 2:1 homo-inclusion complexes of octa-imine cage **1** with guests **2**-**6**, using ^{1}H NMR titration experiments.

5.2.2.1 Study of the inclusion of azide 2 in octa-imine 1

The addition of 1.1 equiv. of **2** to a 2 mM solution of the octa-imine cage **1** in a $CDCl_3$:CD_3CN 9:1 solvent mixture provoked the appearance of two new sets of proton signals that we attributed to bound **1** in two inclusion complexes of different stoichiometry: **2**⊂**1** and (**2**)$_2$⊂**1**. The intensity of the protons of the free octa-imine solvate $(CD_3CN)_2$⊂**1** (**Figure 4b**) was reduced to a similar extent to the new ones. Adding more than 1.1 equiv. of **2** favored the increase of the intensity of the set of signals attributed to the (**2**)$_2$⊂**1** complex. When 2.2 equiv. of **2** were added, we exclusively observed the proton signals of the (**2**)$_2$⊂**1** complex in the ^{1}H NMR spectrum of the mixture(**Figure 4c**). The pyrrole NHs ($H^{2''}$) resonated as a broad singlet at $\delta = 9.54$ ppm. The imine ($H^{5''}$) and the aromatic protons of the spacer ($H^{6''}$) appeared as two sharp singlets at $\delta = 8.06$ and 7.74 ppm, respectively. The aromatic protons of the two molecules of **2** included in **1** resonated as two doublets at $\delta = 5.77$ ($H^{b''}$) and 4.96 ($H^{a''}$) ppm. They were significantly upfield shifted in comparison to the free counterpart ($\Delta\delta$ = - 1.13 ($H^{b''}$) and - 3.14 ppm ($H^{a''}$)). This result supported the inclusion of **2** in the aromatic cavity of **1**. The exclusive observation of the signals of the (**2**)$_2$⊂**1** complex after the addition of 2 equiv. of **2** indicated that its binding constant was larger than 10^8 M^{-2}.

The initially formed **2**⊂**1** complex was a co-inclusion complex with one acetonitrile molecule: (**2**)(CD_3CN)⊂**1** complex. This complex displayed two chemically non-equivalent hemispheres producing two separate signals for the pyrrole NHs ($H^{2'}$ and $H^{11'}$). Using the integral values of selected proton signals in the three sets, we determined that the ratio of the concentrations of the three species ($CD_3CN)_2$⊂**1**:(**2**)(CD_3CN)⊂**1**:(**2**)$_2$⊂**1** was 26%:29%:45% under the used experimental conditions.

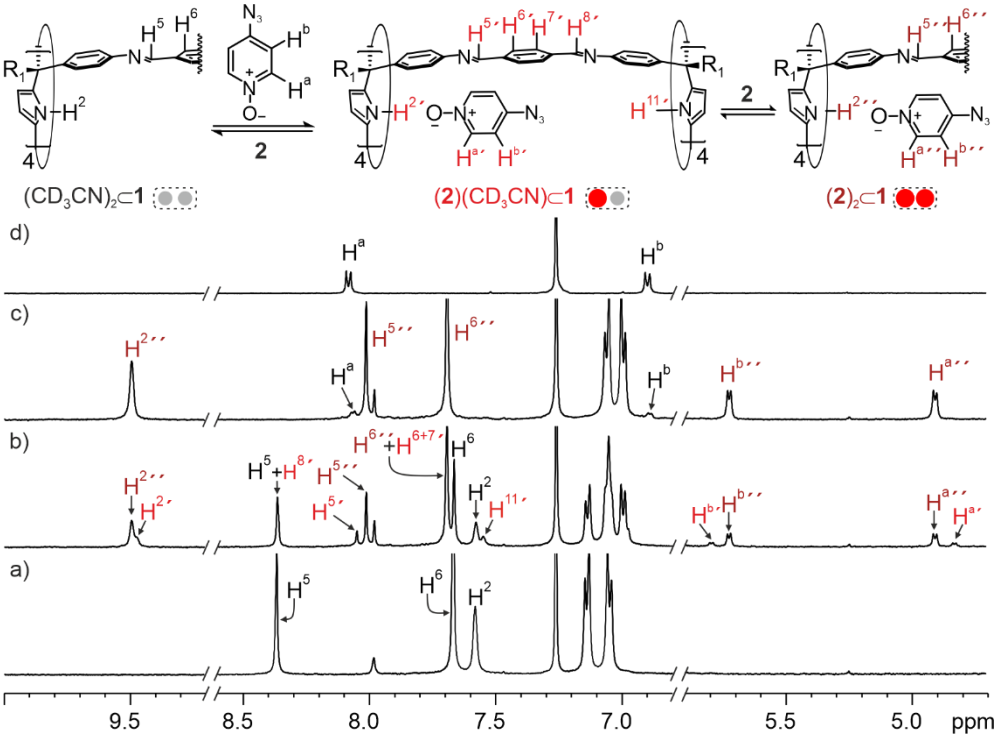

Figure 4. Selected regions of ^{1}H NMR (400 MHz, at 298K, $CDCl_3$:CD_3CN 9:1) spectra of the titration of a 2 mM solution of octa-imine cage **1**, upon addition of a) 0 equiv., b) 1.2 equiv., and c) 2.4 equiv. of **2**. Spectrum d) corresponds to the free **2** in the same solvent mixture. Primed letters indicate the bound proton signals in the 1:1 complex, and double primed letters those in the 2:1 complex.

The addition of more than 2 equiv. of **2** did not produce noticeable changes to the proton signals assigned to the (**2**)$_2$⊂**1** complex. However, we observed the emergence of the proton signals of free **2**. A 2D ^{1}H NOESY experiment did not reveal the existence of cross-peaks between the proton signals of free and bound **2** (**Figure 40** in the experimental section). This result supported that the binding equilibrium featured slow dynamics on the ^{1}H NMR chemical shift and the EXSY timescales

(mixing time = 0.3 s). Based on this result, we estimated that the dissociation rate constant of the complex, k_{off}, should be smaller than 10^{-2} s^{-1} ($k_{exchange} = k' + k_{off} \sim 10^{-2}$ s^{-1}).

Using integral values of selected proton signals of the three species ($(CD_3CN)_2\subset$**1**:(**2**)$(CD_3CN)\subset$**1**:(**2**)$_2\subset$**1**) to determine their ratio of concentrations in the spectra acquired throughout the NMR titration and the Hyperquad Simulation and Speciation (HySS2009) software, we estimated the stepwise and overall macroscopic constants of the binding process to be $K_{1:1} = 2 \times 10^4$ M^{-1}, $K_{2:1 \leftrightarrow 1:1} = 5 \times 10^4$ M^{-1}, and $K_{2:1} = 1 \times 10^9$ M^{-2}. These results revealed a slightly positive binding cooperative in the formation of the (**2**)$_2\subset$**1** complex (**Figure 5a**). Applying the statistical correction to the macroscopic binding constant determined for the first binding event resulted in a $K_{ref} = K_{1:1}/2 = 10^4$ M^{-1}. Next, we determined the cooperativity factor as the ratio of the statistically corrected binding constants of the two binding events obtaining $\alpha = 2 \cdot K_{2:1 \leftrightarrow 1:1}/K_{ref} = (2 \times 5 \times 10^4)/ 10^4 = 10$.

To accurately assess the binding constant values of the formation of the 1:1 and 2:1 complexes, we undertook isothermal titration calorimetry (ITC) experiments **(Figure 5b)**. The stepwise injection of a chloroform: acetonitrile 9:1 solution of guest **2** (16 mM) to a solution of octa-imine cage **1** (1 mM) in the same solvent mixture produced a gradual release of heat attributed to the binding process. The normalized integrated data produced a single sigmoidal binding isotherm with an inflection point centered at a **2**/**1** molar ratio value close to 2 i.e. N = 1.6. This result indicated that the binding cooperativity was not significantly large enough to be detected in the ITC experiment. We fit the ITC data to the theoretical binding model considering one set of sites implemented in the Microcal ITC software. The obtained fit was good and returned the statistically corrected average value of the binding constant for the two sites $K_{average} = 4.6 \times 10^4$ M^{-1}. This value agreed with the magnitude of the binding constants estimated from the NMR titration and their speciation profiles. The sharp exothermic peaks obtained at the beginning of the ITC titration and the relatively broad exothermic peaks appearing after reaching the molar ratio **2**/**1** = 1 agreed with a fast inclusion process ($k_{on} \sim 10^2$ M^{-1} s^{-1}) and a much slower guest dissociation ($k_{off} \sim 10^{-2}$ s^{-1}). The time between injections was set to 600s owing to the slow dissociation of the complex in reaching equilibrium and regenerating the baseline.

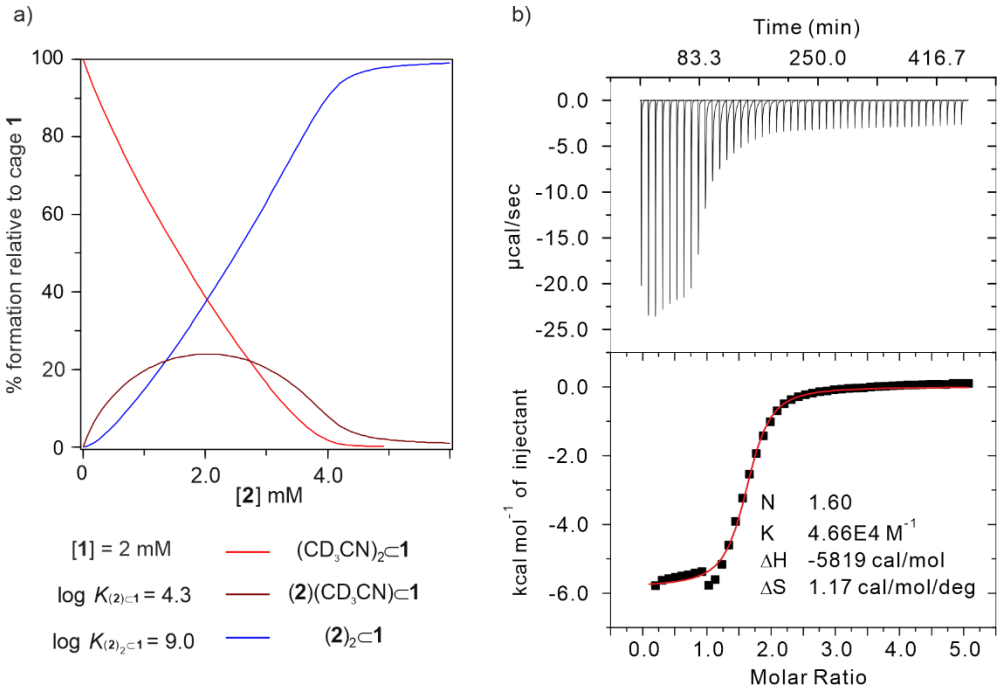

Figure 5. a) Speciation profile of the addition of increasing amounts of **2** (up to 3 equiv.) to a 2 mM solution of cage **1** considering the binding constant values $K_{1:1} = 2 \times 10^4$ M^{-1}, $K_{2:1} = 1 \times 10^9$ M^{-2}. b) Top- Traces of the raw data (heat vs time) of the ITC experiment of cage **1** ([cell] =1×10^{-3} M) with **2** ([syringe] =1.6×10^{-2} M). The solutions were prepared using a chloroform: acetonitrile 9:1 solvent mixture. Bottom- Normalized integrated heat (black squares) vs. **2**/**1** molar ratio. The experimental data were fit to one set of sites binding model (red line).

5.2.2.2 Study of the inclusion of other pyridine *N*-oxdies with cage **1**

We performed analogous ^{1}H NMR titration experiments with pyridine-*N*-oxides **3**-**6** and octa-imine cage **1**.

The results with pyridine *N*-oxide guests **3**-**5** were similar to those described for **2** (**Figure 6**, **Figure 41** and **Figure 43** in the experimental section). In brief, for all titration experiments, the ^{1}H NMR spectra of the equimolar mixture of octa-imine cage **1** and the *N*-oxide showed three separate sets of proton signals for **1**. We attributed these signals to the protons of the solvated free octa-imine cage $(CD_3CN)_2\subset$**1**, the 1:1 complex (**3**-**5**)$(CD_3CN)\subset$**1**, and the 2:1 complex (**3**-**5**)$_2\subset$**1**. The more intense set of signals was assigned to the 1:1 complexes (70%-80%). No signals for the free guests **3**-**5** protons were detected in the equimolar mixtures. This suggested that the binding constants of all 1:1 complexes were larger than 10^4 M^{-1}.

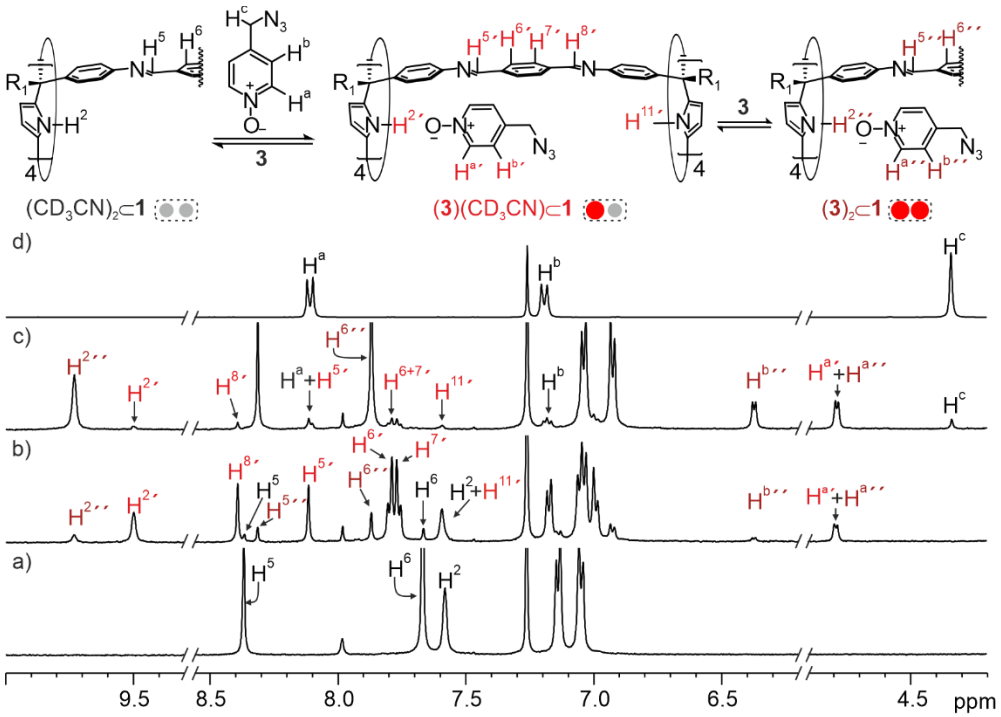

Figure 6. Selected regions of ^{1}H NMR (400 MHz, at 298 K, $CDCl_3$: CD_3CN 9:1) spectra of the titration of a 2 mM solution of octa-imine cage **1**, upon addition of a) 0 equiv., b) 1.1 equiv. ; c) 2.2 equiv. of **3**. Spectrum d) corresponds to the free **3** in the same solvent mixture. Primed letters indicate proton signals in the 1:1 complex and double primed letters in the 2:1 complex.

The addition of 2 equiv. of guests, **3**-**5**, to a 2 mM solution of cage **1** in $CDCl_3$:CD_3CN 9:1 mixture provoked the complete disappearance of the set of signals corresponding to the solvated cage $(CD_3CN)_2$⊂**1**. However, the proton signals corresponding to the 1:1 complexes (**3**-**5**)(CD_3CN)⊂**1** were detectable and coexisted with those of the free guests **3**-**5**. The quantitative formation of the 2:1 complexes (**3**-**5**)$_2$⊂**1** required the addition of more than 2 equiv. of guests **3**-**5** (up to 6 equiv.). We estimated that the binding constant value for the stepwise formation of the 2:1 complex ($K_{1:1\leftrightarrow 2:1}$) was lower than 10^4 M^{-1}. Therefore, contrary to our observations with guest **2**, the second binding event for guests **3**-**5** in cage **1** featured a slightly negative binding cooperativity ($\alpha \sim 0.1$).

5.2.2.3 Assessment of the binding constants for the inclusion process of **3** in cage **1**.

We used the Hyperquad Simulation and Speciation (HySS2009) software to simulate the species' speciation profiles (concentration ratios) observed in the ^{1}H NMR spectra acquired during the titration experiments of **1** with **3**. Specifically, we observed a good coincidence between the simulated and the experimentally measured speciation profiles for the three species present in the inclusion process of **3** by **1** using $K_{1:1} = 3 \times 10^5$ M^{-1} and $K_{2:1} = 3 \times 10^9$ M^{-2} as macroscopic association constants for the 1:1 and 2:1 complexes, respectively (**Figure 7a**).

We performed ITC experiments of cage **1** with guest **3** in conditions similar to those mentioned above for guest **2**. The normalized integrated heat data displayed a double sigmoidal binding isotherm (**Figure 7b**). The inflection points of the two sigmoidal curves were centered at **3/1** molar ratio values of 0.6 and 1.2, respectively. We used a theoretical binding model of two sequential binding sites for the mathematical analysis of the titration data. The fit was good and returned the thermodynamic parameters for the two binding events as: $K_{1:1} = 3.8 \times 10^5$ M^{-1}, $\Delta H_{1:1}$ =-8.2 kcal·mol^{-1}, and $K_{1:1\leftrightarrow2:1} = 3.8 \times 10^3$ M^{-1}, $\Delta H_{1:1\leftrightarrow2:1}$ = - 17.1 kcal·mol^{-1}. These results agreed with the macroscopic association constant values derived from the simulated speciation profiles of the ^{1}H NMR titrations.

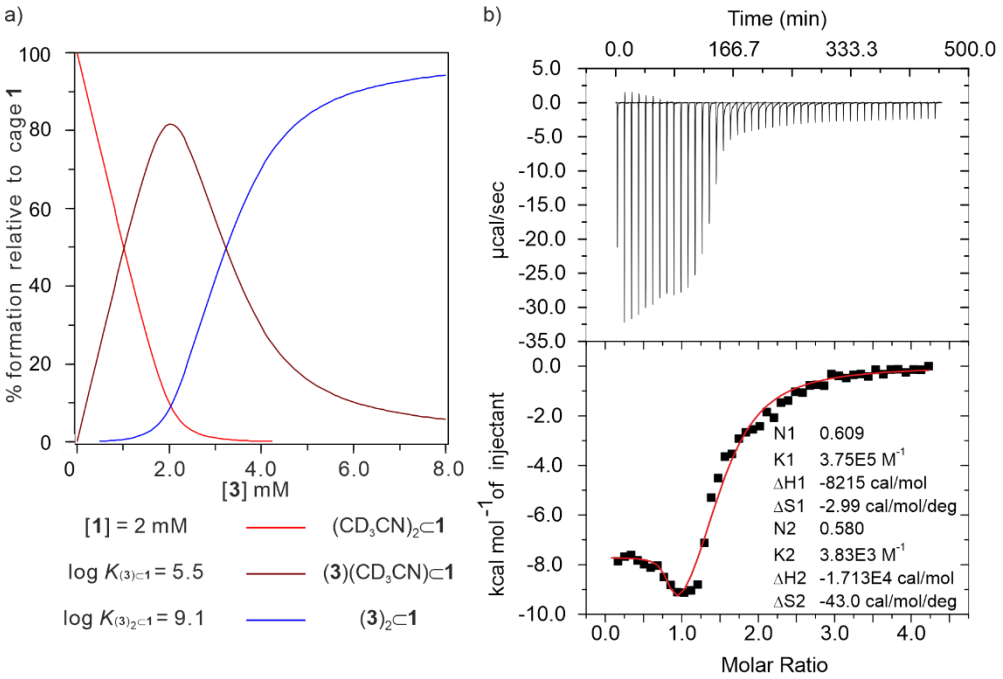

Figure 7. a) Speciation profile of the solutions resulting from the incremental addition of **3** (up to 4 equiv.) to a 2 mM solution of cage **1** considering the binding constant values $K_{1:1} = 3.2 \times 10^5$ M^{-1}, $K_{2:1} = 1.3 \times 10^9$ M^{-2}. b) Top- Traces of the raw data (heat vs time) of the ITC experiment of cage **1** ([cell] = 1×10^{-3} M) with **3** ([syringe]= 1.6×10^{-2} M). The solutions were prepared using a chloroform: acetonitrile 9:1 solvent mixture. Bottom- Normalized integrated heat (black squares) vs. **3**/**1** molar ratio. Experimental data were fit to a sequential two-binding sites model (red line).

5.2.2.4 Study of the inclusion of *N*-(2-propynyl) 4-pyridone **6** in octa-imine cage

Finally, we investigated the binding properties of octa-imine cage **1** with alkynyl-4-pyridone **6**. The ^{1}H NMR spectrum of an equimolar mixture of **1** and **6** showed three separate sets of signals for the protons of cage **1** that were indicative of the existence of three species in solution. We also detected that the protons of free **6** were present as small-intensity signals (**Figure 8b**). This observation indicated that the binding constant of the 1:1 complex, (**6**)(CD_3CN)⊂**1**, must be lower than 10^4 M^{-1}. We assigned the set of signals of **1** having the major intensity to the 2:1 complex (**6**)$_2$⊂**1** (34 %). The addition of 2 equiv. of **6** provoked an increase in the intensity of the signals corresponding to the 2:1 complex at the expense of those of the 1:1 and solvate cage. The observation of proton signals corresponding to the 1:1 complex and the solvated cage in the mixture's ^{1}H NMR spectrum (**Figure 8c**) indicated that

the second binding event to produce the 2:1 complexes featured a binding constant lower than 10^4 M^{-1}.

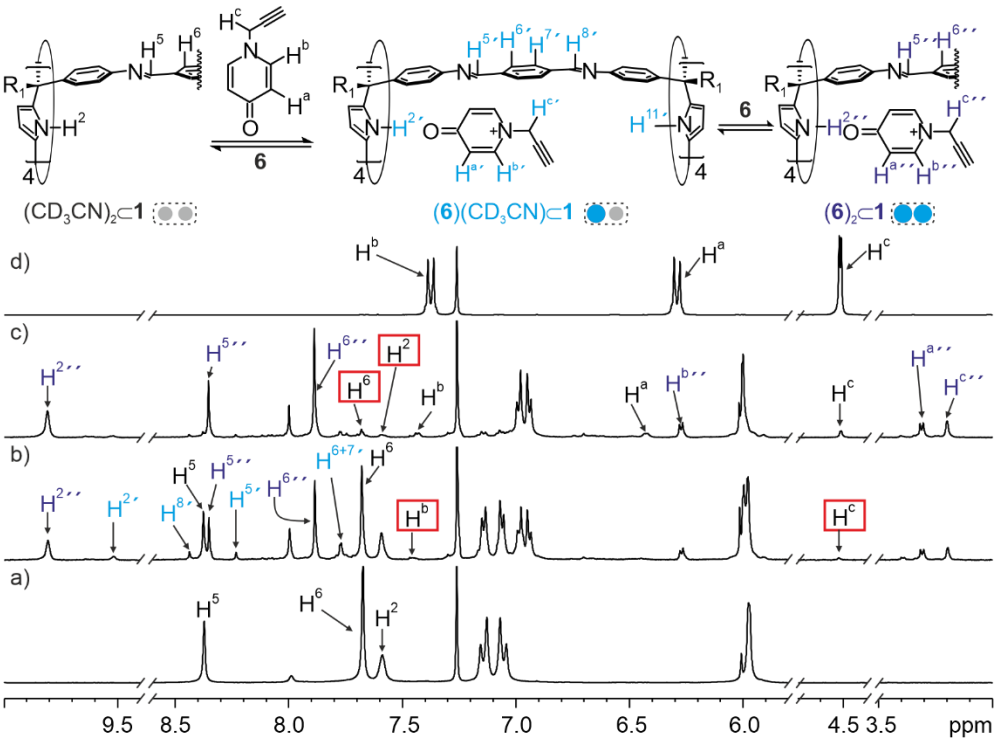

Figure 8. Selected regions of ^{1}H NMR (400 MHz, at 298K, $CDCl_3$:CD_3CN 9:1) spectra of the titration of a 2 mM solution of cage **1**, upon addition of a) 0 equiv., b) 1equiv., and c) 2 equiv. of **6**. Spectrum d) corresponds to the free **6** in the same solvent mixture. Primed letters indicate the proton signals in the 1:1 complex, and double-primed letters indicate the proton signals in the 2:1 complex.

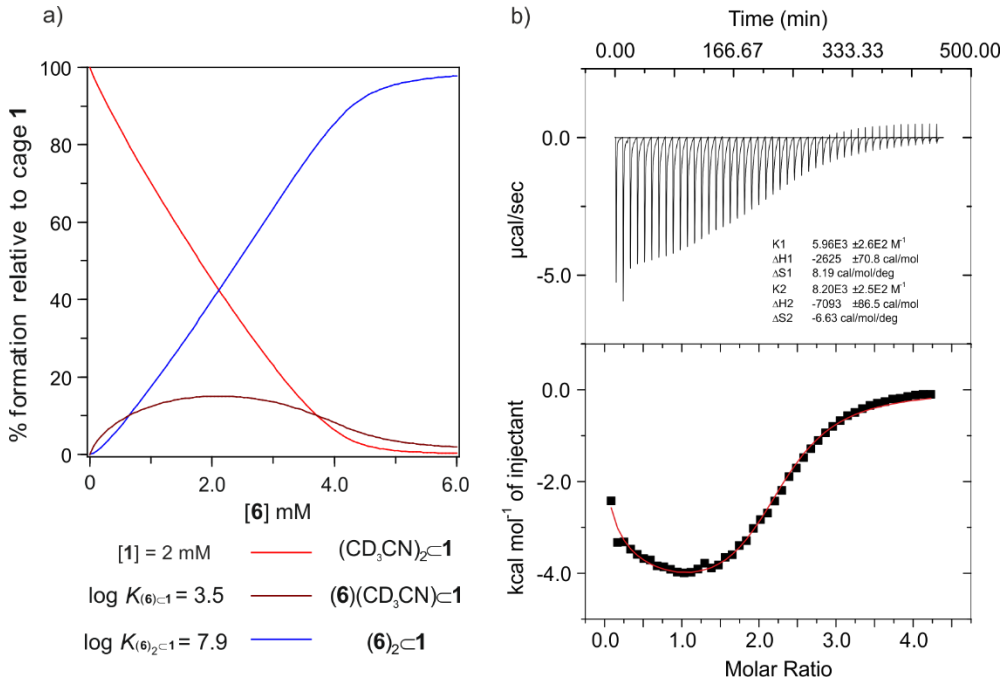

Figure 9. a) Speciation profile of the solutions resulting from the incremental addition of **6** (up to 3 equiv.) to a 2 mM solution of cage **1** considering the binding constant values $K_{1:1} = 3.2 \times 10^3$ M^{-1}, $K_{2:1} = 8 \times 10^7$ M^{-2}. b) Top- Traces of the raw data (heat vs time) of the ITC experiment of cage **1** ([cell] = 1×10^{-3} M) with **6** ([syringe]= 2.0×10^{-2} M). The solutions were prepared using a chloroform: acetonitrile 9:1 solvent mixture. Bottom- Normalized integrated heat (black squares) vs. **6**/**1** molar ratio. Experimental data were fit to a sequential two-binding sites model (red line).

5.2.3. Ternary inclusion complexes of octa-imine cage **1**.

Next, we explored the formation of 1:1:1 ternary hetero-inclusion complexes. To this end, we added 2 equiv. of pyridine-*N*-oxide guests **2** (4-methyl azide) and **5** (4-ethynyl) to a 2 mM solution of cage **1** in $CDCl_3$:CD_3CN 9:1 solvent mixture (final molar ratio of compounds **1**, **2** and **5** was 1:2:2). The resulting solution was analyzed using ^{1}H NMR spectroscopy, evidencing that reaching the thermodynamic equilibrium between inclusion complexes required several minutes. This observation demonstrated that guests' dissociation processes were fast on the human-time scale (seconds to minutes).

After 10 minutes, the ^{1}H NMR spectrum of the thermodynamically equilibrated mixture showed the diagnostic signals of (**2**)$_2\subset$**1** complex. (**Figure 10c**). However, we did not detect the presence of the homo-complex (**5**)$_2\subset$**1** or any of the expected 1:1 complexes (**2**·CD_3CN)$\subset$**1** and (**5**·CD_3CN)$\subset$**1**. We observed an unidentified set of

signals of cage **1** that we assigned to their protons in the (**2·5**)⊂**1** ternary hetero-complex (around 40% of the total amount of bound capsule, 0.8 mM).

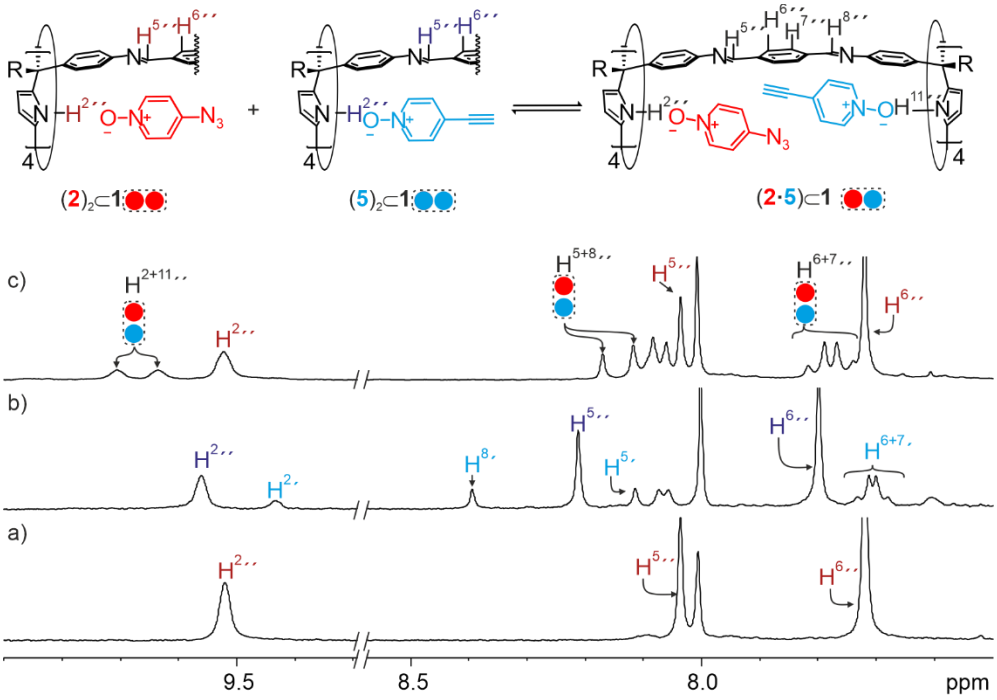

Figure 10. Selected regions of ^{1}H NMR (400 MHz, at 298K, $CDCl_3$:CD_3CN 9:1) spectra of a) 1:2 mixture of cage **1** and **2**; b) 1:2.4 mixture of cage **1** and **5**; c) 1:2:2 mixture of cage **1**, **2** and **5**. Primed letters indicate the proton signals in the 1:1 complex, double-primed letters indicate the proton signals in the 2:1 complex.

Taken together, the results above demonstrated that the ternary hetero-complex (**2·5**)⊂**1** and the homo-complex (**2**)$_2$⊂**1** were thermodynamically favored over the (**5**)$_2$⊂**1** counterpart and the 1:1 complexes (**2**·CD_3CN)⊂**1** and (**5**·CD_3CN)⊂**1**. Considering the experimentally observed speciation profile and using the Hyperquad Simulation and Speciation (HySS2009) software, we derived the binding constant value of the ternary hetero-complex (**2·5**)⊂**1** (**Figure 11**). The theoretical speciation profile approximated to the experimentally observed one (40% (**2·5**)⊂**1** and 60% (**2**)$_2$⊂**1**) by manually adjusting the binding constant value of the hetero-complex (**2·5**)⊂**1**. We obtained a reasonable agreement between the two for $K_{(\mathbf{2\cdot5})\subset\mathbf{1}}$ = 3.9 × 10^9 M^{-2}. The binding constants of the other species were fixed to the values determined in previous sections using ITC experiments and simulated speciation profiles (**Figure 12**).

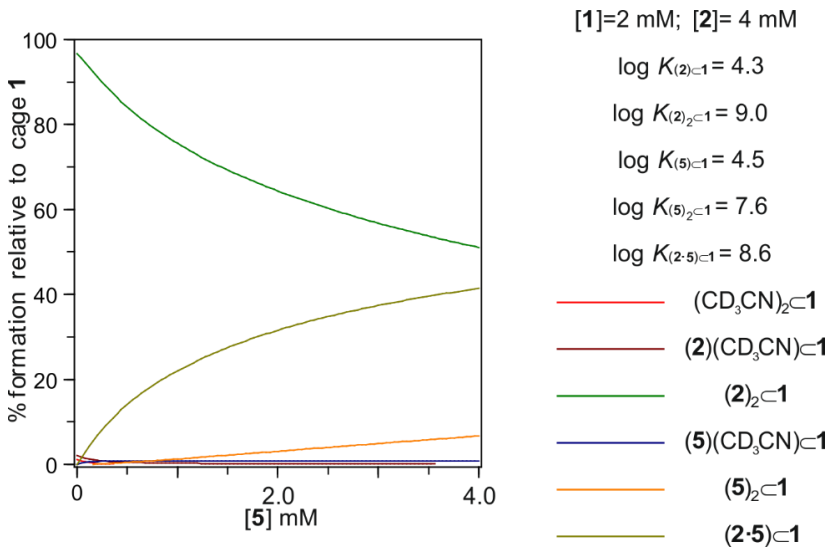

Figure 11. Simulated speciation profile derived from the titration of a solution containing **1** at 2 mM concentration and **2** at 4 mM concentration with incremental amounts of **5** until reaching a 4 mM concentration. The last point considers the overall concentrations of the three components (**1**, **2,** and **5**) used in the solution mixture analyzed by ^{1}H NMR spectroscopy. The association constant values for all the species except the ternary complex, (**2**·**5**)⊂**1**, were derived in previous experiments (NMR speciation profiles and ITC experiments).

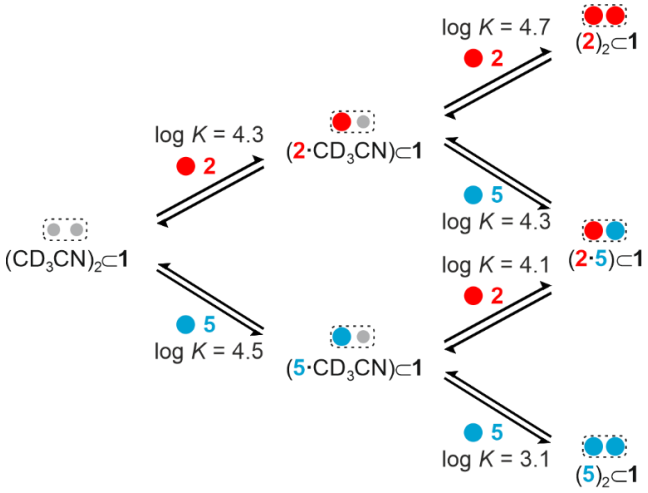

Figure 12. The theoretical model used for the mathematical analysis of the kinetic data of the cycloaddition reaction between **2** and **5** included in the octa-imine cage **1**. The model takes into account all binding equilibria forming the 1:1 and 2:1 homo and hetero complexes**.** The binding constants were determined with separate titration experiments (vide supra).

We analyzed the speciation profiles of cage **1** in the presence of mixtures of other two guests, **3**-**6**, using ^{1}H NMR spectroscopy. We were interested in characterizing the formation of the ternary complexes in the disproportionation equilibria of 1:1 and 2:1 homo- complexes. Not surprisingly, the amount of formed ternary hetero-complex in solution was related to the relative thermodynamic stabilities of the ternary hetero-complex and those of the 1:1 and 2:1 homo- counterparts. Likewise, the used molar ratio of cage and guests influenced the percentage of ternary hetero-complex formed in the solution equilibrium.

For example, adding 2 equiv. of **5** and 1 equiv. of **3** to a 2 mM solution of cage **1** produced a new ternary hetero-complex (**3**·**5**)⊂**1** in 27% extent of (0.54 mM) concerning the total concentration of cage **1**. (**Figure 13**). We also detected homo-complex (**5**)$_2$⊂**1** as major species in solution (30%), homo-complex (**3**)$_2$⊂**1** (20%) and the 1:1 complexes (**3**·CD_3CN)⊂**1** (14%) and (**5**·CD_3CN)⊂**1** (3%).

In contrast, adding 1 equiv. of **5** and 1 equiv. of **3** to a 2 mM solution of cage **1** produced the corresponding ternary complex (**3**·**5**)⊂**1** in 16% extent (**Figure 14b**). A simulation profile predicted that the addition of 5 equiv. of guests **5** and **3** to a 2 mM solution of cage **1** should produce the ternary complex (**3**·**5**)⊂**1** in less than 5% extent. Experimentally, we could not detect the proton signals of the (**3**·**5**)⊂**1** complex in the ^{1}H NMR spectrum of the mixture (**Figure 14c**).

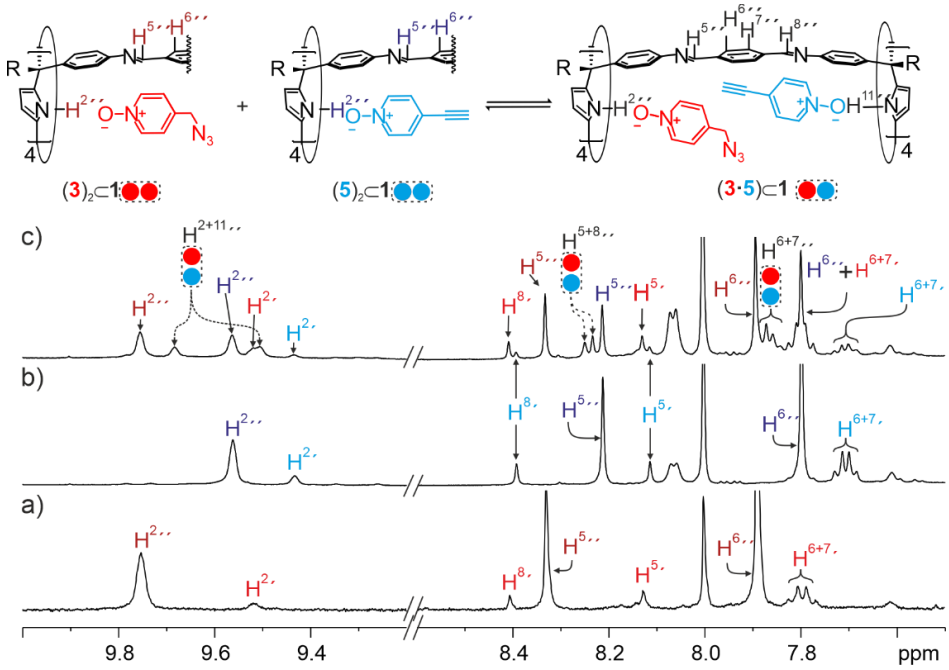

Figure 13. Selected regions of ^{1}H NMR (400 MHz, at 298K, $CDCl_3$:CD_3CN 9:1) spectra of solutions containing: a) 1:2 mixture of cage **1** and **3**; b) 1 mixture of cage **1** and **5**; c) 1:1:2 mixture of cage **1**,**3** and **5** registered immediately after mixing (5 min). Primed letters indicate the proton signals in the 1:1 complex and double primed letters in the 2:1 complex.

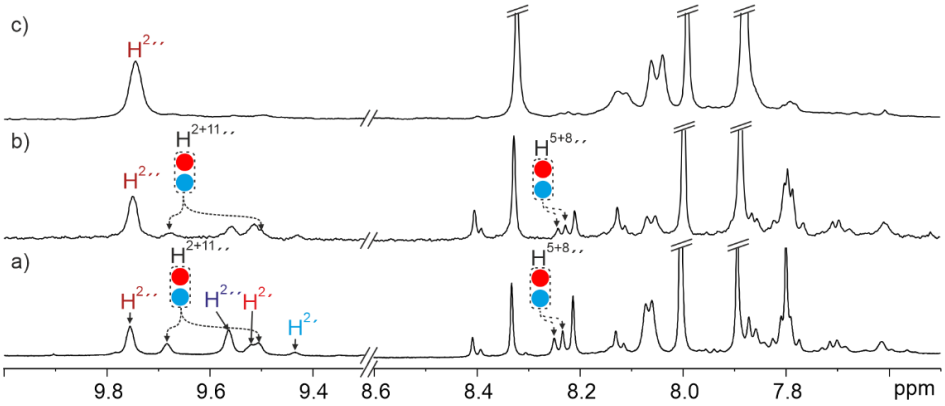

Figure 14. Selected region of the ^{1}H NMR (300 MHz, at 298 K, $CDCl_3$: CD_3CN 9:1) spectra of solutions containing: a) 1:1:2 mixture of cage **1**, **3** and **5**; b) 1:1:1 mixture of cage **1**, **3** and **5**; c) 1:5:5 mixture of cage **1**, **3** and **5**. All spectra are registered immediately after mixing. Primed letters indicate the proton signals of the bound cage and *N*-oxide in the 1:1 complex, double-primed letters indicate the proton signals of the bound cage and *N*-oxide in the 2:1 complex.

5.2.4. Mediation of Huisgen 1,3-cycloaddition reaction by inclusion in cage 1

5.2.4.1. Study of the 1,3-dipolar cycloaddition reaction of 2 and 5 included in 1

To evaluate the potential use of cage **1** for mediating the Huisgen 1,3-cycloaddition reaction between guests **2** and **5**, we monitored, at different time intervals during 2 weeks using ^{1}H NMR spectroscopy, a 2 mM solution of **1** also containing **2** and **5** in 1:2:2 molar ratio (**Figure 10**). We did not detect significant changes in the ^{1}H NMR spectra acquired during this period of time. This result demonstrated that the cycloaddition reaction between **2** and **5** was not accelerated to a measurable extent under the described experimental conditions.

The energy-minimized structures (MM3) of the ternary complex of (**2**·**5**)⊂**1** showed the two reacting groups (azido and ethynyl) located in a suitable orientation for the reaction to take place when included in **1**. The distances between the two reacting groups are slightly larger than those expected for the transition state (**Figure 15**). We calculated an effective concentration for the reactants when included in the cavity of **1** (volume of the cavity around 410 Å^3) of 4.0 M. The increase in local concentration was not enough to induce an observable acceleration to the reaction occurring in the cage's cavity. The octa-imine cage **1** featured reduced conformational flexibility. This could explain why the two reacting groups, when included in the cavity of 1, cannot reach the optimal distance required for achieving the transition-state geometry of the 1,3-cycloaddition reaction. It is worth noting that the polar pyridine-*N*-oxide knobs of the reactants fixed the positions of their reacting groups when included in cage **1**. A putative process to approximate the two reacting groups will involve adapting the length of cage **1**. This process might be energetically highly demanding owing to its reduced conformational flexibility. Alternatively, the *N*-oxide knobs included in the C[4]P hemispheres of **1** could elongate their intermolecular interaction distances. A mechanism that also requires a high energy cost. In short, the 1,3-cycloaddition between **2** and **5** was not significantly accelerated when included in cage **1**.

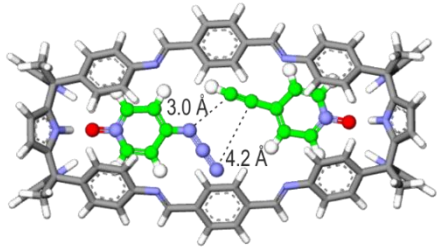

Figure 15. Energy-minimized structures (MM3) of ternary complex **(2·5)⊂1**.

In a separate experiment, we investigated the binding of the bis-pyridine-*N*-oxide **7a** with the octa-imine cage **1** in a $CDCl_3$:CD_3CN 9:1 solvent mixture by a solid-liquid extraction. Compound **7a** is the 1,4-triazole isomer resulting from the CuCAAC of **2** and **5**.[19] After suspension sonication and filtration, the ^{1}H NMR spectrum of the resulting solution did not show signals that could be easily assigned to the protons of **7a** (**Figure 16**). Moreover, some of the proton signals of **1** broadened beyond detection. When the ^{1}H NMR spectrum of the solution was registered at 233 K, we observed the pyrrole NHs of **1** resonating as two pairs of separate signals with different intensities (9.7, 9.4, 8.5, and 8.4 ppm). Each pair of the signals was ascribed to one of the two possible isomeric complexes of **7a⊂1** (**Figure 17**). Most likely, the two isomers were involved in a chemical exchange that was slow on the ^{1}H NMR timescale at 233 K. We hypothesized that the length of the bis-pyridine-*N*-oxide **7a** was too short to adequately span the gap between the two polar hemispheres of cage **1**. For this reason, it experienced a shuttling motion when included in **1**. This process displayed intermediate dynamics on the ^{1}H NMR chemical shift time scale at r.t. and became slow on the same time scale at 233K.

To support this hypothesis, we performed molecular modeling studies. The energy-minimized structures (MM3) of one of the two isomeric complexes of **7a⊂1** showed that the N-O···N-H hydrogen bonding distances of its two hemispheres were significantly different (3.1 Å and 3.9 Å). (**Figure 17**, left). This result supported the observation of different chemical shifts for the NH protons of the two hemispheres in each one of the **7a⊂1** isomeric complex.

This result provided experimental support to our previous suggestion indicating that reaching the transition state of the 1,3-dipolar cycloaddition between **2** and **5** inside the cavity of **1** required that at least one of the *N*-oxide guests moved towards the other to shorten the distance between the reacting groups. To do so, the hydrogen bonds of the *N*-oxide with the C[4]P NHs should be elongated, producing a concomitant increase in energy of the complex and the putative transition state that could be formed. The reduced fit between the length of cage **1** and the reactants **2**

and **5** in reaching the transition-state geometry explained why the included 1,3-cycloaddition reaction was not accelerated.

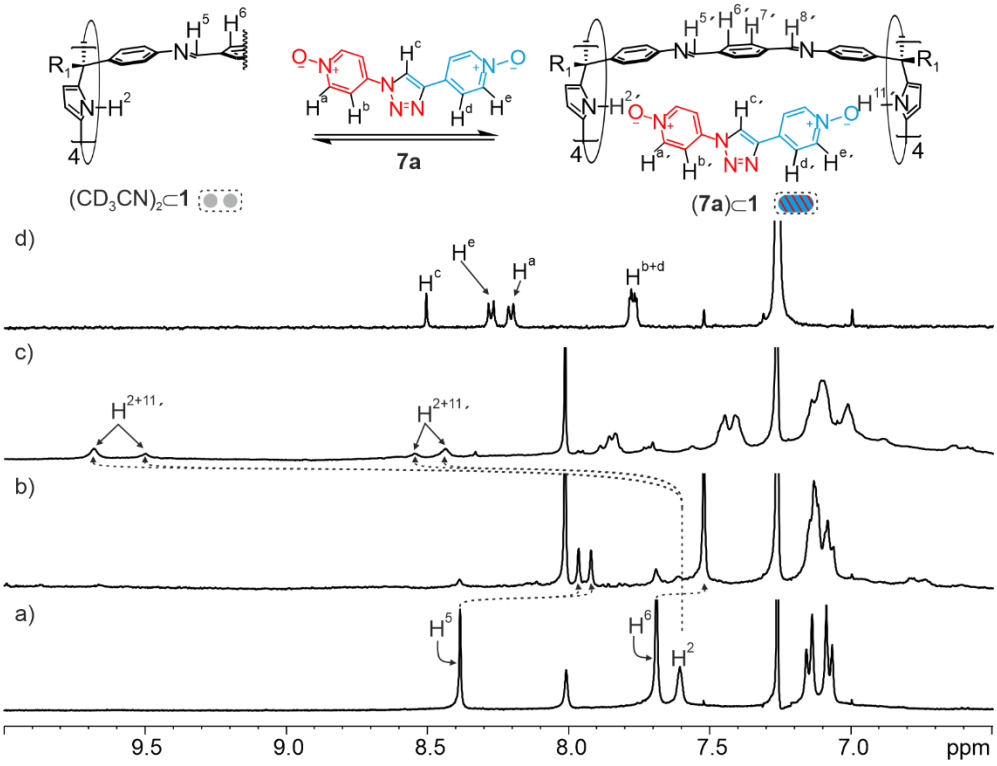

Figure 16. (Top) Binding equilibria of **7a** with cage **1**. (Bottom) Selected regions of the1H NMR (300 MHz, $CDCl_3$: CD_3CN 9:1) spectra of a) 2 mM solution of cage **1** at 298 K, b) the solution resulting from the solid-liquid extraction of **7a** with a 2mM solution of cage **1** (298K), and c) the same solution at 233 K. Spectrum d) corresponds to the free **7a** in the same solvent mixture at 298 K. Primed letters indicate the proton signals of bound **1** in the 1:1 complex.

We performed the cycloaddition reaction between **2** and **5** in the bulk solution (absence of cage **1**). The reaction was performed using a 25 mM concentration of the starting *N*-oxides at 298 K in a chloroform: acetonitrile 9:1 mixture containing 4-methyl pyridine *N*-oxide (1 mM) as an internal standard. We monitored the reaction using HPLC.[20]

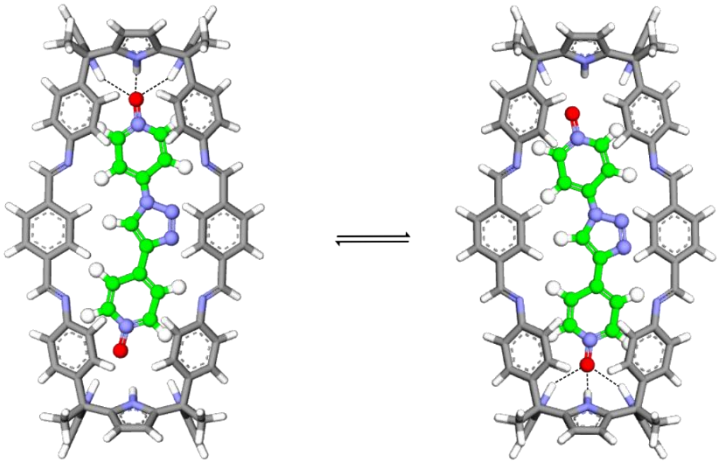

Figure 17. Energy-minimized structures (MM3) of two isomers of **7a⊂1** complex. The equilibrium between them shows fast dynamics of the chemical shift time scale at room temperature. Most likely, one molecule of water is involved in bringing the *N*-oxide with the NHs in the non-directly hydrogen bonded hemisphere.

The chromatogram of the cycloaddition reaction between **2** and **5** monitored by HPLC (λ = 300 nm) shows two peaks with different retention times (10.3 min and 11.3 min). The intensity of these peaks increased with time compared to that of the internal standard (i.s., appearing at t = 8.2 min) (**Figure 74** in experimental section). The peak with a retention time of 11.3 min corresponded with the 1,4-disubstituted triazole product **7a**. We verified this point by using analogous analytic conditions and injecting a sample of pure **7a** from the CuCAAC reaction of **2** and **5**. The other peak was assigned to the 1,5-disubstituted triazole product **7b**. We plotted the peak area corresponding to the 1,4-isomer of **7a** normalized by the area of the i.s. ($A_{\mathbf{7a}}/A_{i.s.}$) at different reaction times (**Figure 75** in experimental section).[21] With these data and the help of a calibration curve, we determined the initial rate for forming **7a** in the bulk as ($v_{0(bulk)7a}$ = 3.1 × 10^{-11} Ms^{-1}). Considering a second-order kinetic reaction model and the determined reaction rate, we calculated the rate constant for the reaction in the bulk $k_{bulk7a} = v_{0(bulk)7a} / (0.025M)^2$ = 5.0 × 10^{-8} $M^{-1}s^{-1}$. This corresponds to a half-life[22] of around 23 years. The HPLC integral of the peak produced by **7a** is approximately two times larger than that of **7b**. Assuming that **7a** and **7b** have similar extinction coefficients at 300 nm, the rate constant of **7b** can be estimated to be half of the value of $k_{bulk7a.}$

5.2.4.2. Study of the 1,3-dipolar cycloaddition reaction of 3 and 5 included in 1

We changed the 4-azido pyridine-*N*-oxide **2** by 4-azidomethyl pyridine-*N*-oxide **3** as the 1,3-dipolar compound of the cycloaddition reaction. Based on molecular modeling studies (**Figure 2**), the ternary complex of (**3•5**)⊂**1** placed the two reacting groups in closer spatial proximity in comparison to the (**2•5**)⊂**1** analog. Likewise, the energy-minimized complex structure with the 1,4-triazole bis-*N*-oxide **8a**, **8a**⊂**1**, revealed a good fit with the cavity length of **1.** This resulted in a ditopic interaction with optimal hydrogen bonding distances between the two *N*-oxide polar ends of **8a** and the pyrrole NHs of both hemispheres of **1**.

We added azide **3** and ethynyl **5** to a 2 mM solution of **1** to obtain a final mixture of **1**, **3** and **5** in 1:1:2 molar ratio. The ^{1}H NMR spectrum of the mixture acquired after the sample's preparation showed the diagnostics peaks of the different species in solution. We detected the signals of the protons in ternary hetero-complex (**3**·**5**)⊂**1** (0.54 mM).

We used ^{1}H NMR spectroscopy to monitor changes in solution with time. From the beginning (t= 30 min), we detected a new set of well-defined proton signals that did not coincide with any known inclusion complexes of **1** with **3** and **5**. The pyrrole NH signals resonated for this new species as two separated singlets ($H^{11'}$ and $H^{2'}$ in **Figure 18b**) at $\delta = 9.2$ and 8.9 ppm. This observation hinted at forming a new octa-imine **1** inclusion complex having non-chemically equivalent hemispheres. Likewise, the imine protons of the new species were also split into two singlets at $\delta = 8.1$ and 8.0 ($H^{5'}$ and $H^{8'}$). Four new doublets ($H^{\varepsilon'}$, $H^{\beta'}$, $H^{\alpha'}$, and $H^{\phi'}$) were detected and assigned to the protons of the included guest(s) at 6.8, 6.5, 5.2, and 4.9 ppm in this new species. The intensity of the new set of signals increased with time at the expense of those attributed to the homo-inclusion complexes (**3**)$_2$⊂**1** and (**5**)$_2$⊂**1**. The concentration of the ternary complex (**3**·**5**)⊂**1** seemed almost constant at the initial phases of the monitoring process (around 0.54 mM). After 48 h, the ^{1}H NMR spectrum of the reacting solution showed exclusively the signals corresponding to the new inclusion complex (**Figure 18c**). Together, these results augur well for the acceleration of the 1,3-dipolar cycloaddition between **3** and **5** when included in cage **1**. Moreover, only one of the two possible cycloaddition regio-isomers seemed to be formed. We performed separate binding studies to confirm that the 1,4-regioisomer **8a** was exclusively produced in the cycloaddition reaction of **3** and **5** included in cage **1**. The signals of the ^{1}H NMR spectrum of the **8a**⊂**1** encapsulation complex coincided with those of the new species observed when **3** and **5** were

included in cage **1** (**Figure 45** in experimental section). Most likely, the bad fit of the 1,5-isomer for the cavity of **1** precluded its formation when the cycloaddition reaction of **3** and **5** is included in it.

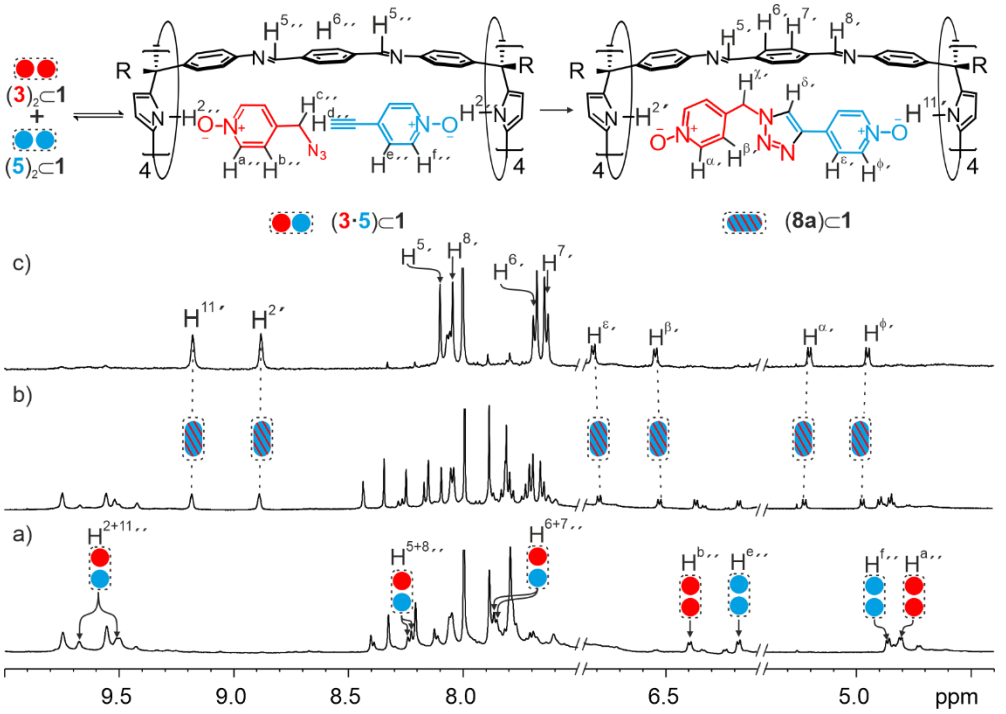

Figure 18. (Top) Left) Disproportionation equilibrium of homo- inclusion complexes (**3**)$_2$⊂**1** and (**5**)$_2$⊂**1** to yield the ternary complex (**3**·**5**)⊂**1**. Right) The 1,3-dipolar cycloaddition reaction between **3** and **5** included in the octa-imine cage **1** yielded the complex **8a**⊂**1**. (Bottom) Selected regions of the ^{1}H NMR (300 MHz, at 298 K, $CDCl_3$: CD_3CN 9:1) spectra corresponding to the monitoring of the formation of complex **8a**⊂**1** starting from a 1:1:2 molar mixture of compounds **1, 3,** and **5**, respectively, after a) 0 h, b) 8 h, c) 48 h. Primed letters indicate the proton signals in the 1:1 complexes, double-primed letters are used for the 2:1 homo- and hetero-complexes.

We used the integral values of selected proton signals of the new species formed **8a**⊂**1** to determine its concentration changes with time. By plotting the changes in concentration with time we determined the initial reaction rate for the formation of **8a** inside cage **1** (t = 0-4 h; < 20% reaction progress). Using the described experimental conditions, we determined an initial rate value of $v_{complex}$ = (3.2 ± 0.1) × 10^{-8} M s^{-1} (

Figure 19). We detected the proton signals of the ternary complex (**3·5**)⊂**1** in the ^{1}H NMR spectrum of the initial reacting mixture. Using selected integral values, we calculated its concentration, allowing the determination of the rate constant of the included cycloaddition reaction $k_{complex} = v_{complex}/[(\mathbf{3{\cdot}5})\subset\mathbf{1}] = 5.9 \times 10^{-5}$ s^{-1}.

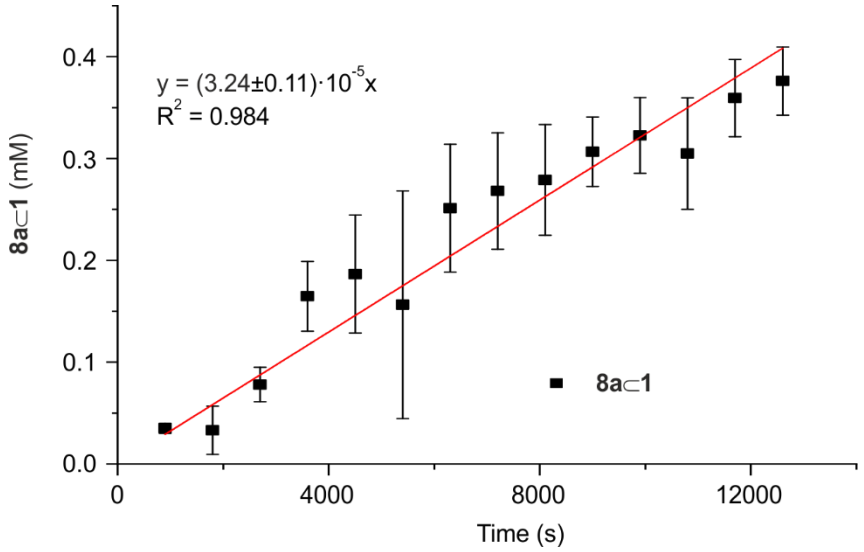

Figure 19. Kinetic profile concentration of complex **8a⊂1** (mM) with time (s) for the 1:1:2 molar mixture of **1**, **3,** and **5** in a solution of $CDCl_3$:CD_3CN 9:1 solvent mixture. The red line represents the fit of the initial reaction´s rate. Concentrations were calculated as the average of two different experiments and the error bars correspond to the standard deviations.

We performed the cycloaddition reaction of **3** with **5** in the bulk solution using the abovementioned conditions for the reaction of **2** with **5** (**Figure 77** in experimental section). The initial rate measured for the formation of **8a** ($v_{0(bulk)8a} = 3.5 \times 10^{-11}$ Ms^{-1}) was almost analogous to that determined for **7a** ($v_{0(bulk)7a} = 3.1 \times 10^{-11}$ Ms^{-1}). We determined the rate constant for the reaction of **3** with **5** to be $k_{bulk8a} = 5.6 \times 10^{-8}$ M^{-1}s^{-1}. In brief, the background reaction in the bulk is negligible at millimolar concentrations.

Moreover, using the determined k_{bulk}, we estimated the initial reaction rate (v_{bulk}) for the reaction performed at mM concentration. Specifically, for the concentrations of reactants used in the 1:1:2 molar mixture of compounds **1, 3,** and **5**, respectively, the initial reaction v_{bulk} can be estimated as k_{bulk} x [**3**] x [**5**] = 5.6×10^{-8} M^{-1}s^{-1} · 2×10^{-3} M · 4×10^{-3} M = 4.5×10^{-13} M s^{-1}. Using this value, we determined the acceleration factor of the reaction as 7.1×10^4 from the initial rates ratio

$v_{complex}/v_{bulk}$. It was also possible to derive an acceleration factor of EM = 1058 M for the reaction occurring in the cage's cavity using the rate constants $k_{complex}/k_{bulk}$ ratio.

We undertook analogous kinetic experiments in the presence of different molar ratios of compounds **1**, **3** and **5**, (1:1:1 and 1:5:5). As we mentioned above, the use of different molar ratios of guests and cage **1** affected the concentration in which the ternary complex is assembled (0.32 mM for 1:1:1 and < 0.1 mM for 1:5:5). As expected, a decrease in the concentration of the ternary complex resulted in a diminution of the cycloaddition initial rates ($(1.5 \pm 0.3) \times 10^{-8}$ Ms^{-1} for 1:1:1 and $(6.6 \pm 0.4) \times 10^{-9}$ Ms^{-1} for 1:5:5). The rate constant was maintained with a value of 5×10^{-5} s^{-1} for all investigated molar ratios. The initial rates method to determine rate constant values is associated with large experimental errors related to determining the product concentration at the initial reaction stages (less than 20% reaction conversion). We decided to fit the complete kinetic data to a suitable theoretical kinetic model, using COPASI software version 4.25, as an alternative method to derive the reaction's rate constant.[23]

To mathematically analyze the kinetic data, we used a theoretical model considering the reversible formation of the 1:1 and 2:1 homo- and hetero-complexes and the irreversible formation of the included cycloaddition product, **8a⊂1** complex (**Figure 20**). We manually fixed the k_{on}s and k_{off}s values of the equilibria for the formation of 1:1 and 2:1 inclusion complexes. To do so, we set the k_{off}s for all inclusion complexes as 0.01 s^{-1} in agreement with the slow guest exchange rate constant estimated from the lack of exchange cross-peaks in the EXSY experiments (t_{mix} = 0.3 s, *vide supra*). The k_{on}s for each binding equilibria were determined using the association constant values derived from the thermodynamic characterization studies and the relationship $K_a = k_{on} / k_{off}$ (**Figure 20**). The rate constant of the cycloaddition reaction included in the octa-imine cage **1**, $k_{complex}$, was the only variable parameter used for the fit. The fit of the experimental kinetic data to the elaborated theoretical kinetic model was good for all three ratios of compounds **1**, **3**, and **5** (**Figure 21**). We used the values of $k_{complex}$ returned from the three fits to calculate an average value as $k_{complex} = 7 \pm 0.7 \times 10^{-5}$ s^{-1} .

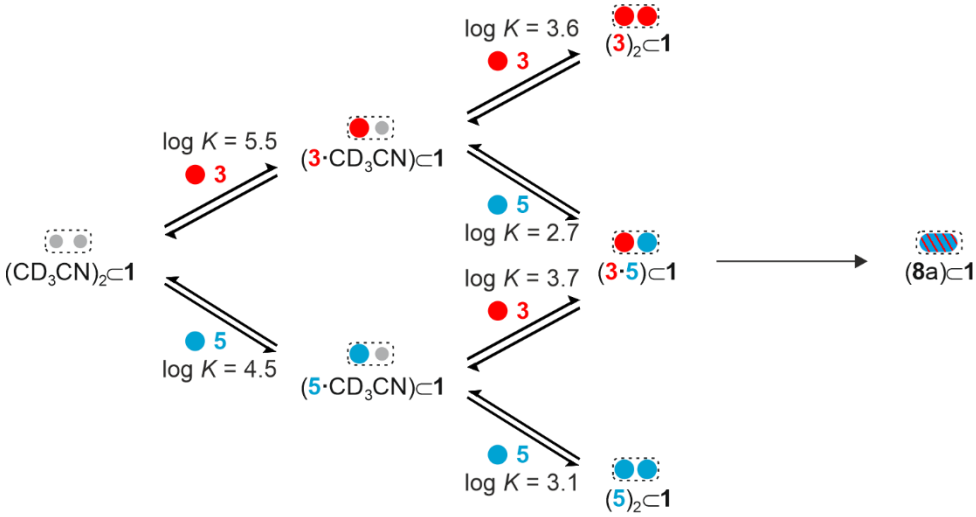

Figure 20. The theoretical model used for the mathematical analysis of the kinetic data of the cycloaddition reaction between **3** and **5** included in the octa-imine cage **1**. The model takes into account all binding equilibria forming the 1:1 and 2:1 homo and hetero complexes and the irreversible formation of the included cycloaddition product**, 8a⊂1** complex**.** The binding constants were determined with separate titration experiments (vide supra). See text for details on k_{on} and k_{off} fixed values used for the fit.

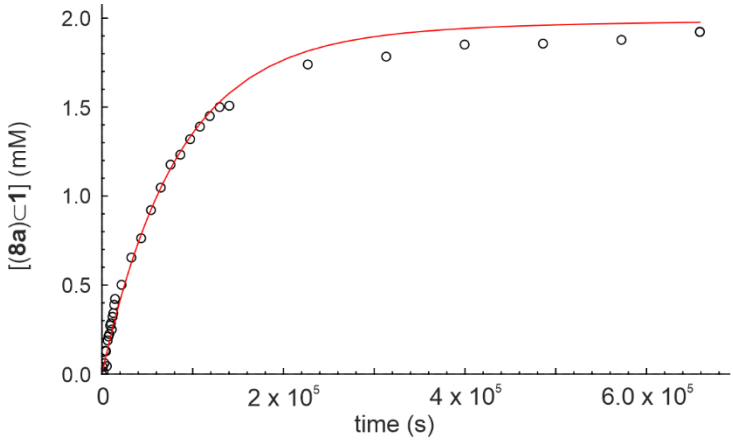

Figure 21. Changes in the concentration of complex **8a⊂1** (mM) vs time (s) following the addition of 1 equiv. of **3** and 2 equiv. of **5**, respectively, to a 2 mM solution of octa-imine cage **1**. Solid line represents the fit of the kinetic data to the elaborated model depicted in **Figure 21**.

We calculated the acceleration factor provoked by including the cycloaddition reaction between **3** and **5** inside the cavity of cage **1** from the ratio of the rate constants, $k_{complex}/k_{bulk}$, obtaining an EM = 1250 M. The magnitude of EM agrees with the one derived using the value of $k_{complex}$ using initial rates method. This result afforded an indication of the quality of the fit of the kinetic data to the complete kinetic model in determining a more accurate value for the $k_{complex}$.

We hypothesized that the increase in the effective concentration of the reactants inside the cavity of the octa-imine cage **1** could be one of the reasons of the observed acceleration. Considering the rate constant of the reaction in the bulk solution and the local concentration calculated for the reagents inside the cavity, we estimated a maximum theoretical reaction rate of $v_{estimated} = k_{bulk} \times (4.0)^2 \approx 8.9 \times 10^{-7}$ Ms^{-1}.

The theoretical estimated initial rate for the reaction in cage **1** is approximately 60-fold larger than the experimentally measured counterpart. The later value ($v_{complex}$ = 1.5 ± 0.3 × 10^{-8} Ms^{-1}) was extracted from a kinetic experiment using equimolar amounts of **1**, **3** and **5** at 2 mM.

Although we consider comparing these values as relevant, Rebek and Jia reported a close ratio of the corresponding rates ($v_{estimated}/v_{complex}$ = 45) for the reaction included in the resorcin[4]arene cavitand dimer. We expected that the tighter binding and well-defined orientation of the substrates included in **1**, compared to the resorcin[4]arene inclusion complex, would endow a superior initial rate compared to this theoretical estimate. The tight binding of the substrates and the lack of adaptability of the cage might compromise the achievement of an energetically more favorable transition state. We know that the transition state inside the cage differs from that in the bulk despite considering the k_{bulk} value for the theoretical estimate.

5.2.4.3. Study of the 1,3-dipolar cycloaddition reaction of **4** with **5** included in cage **1**

To gain some understanding on the factors influencing the selectivity and acceleration achieved by including the Huisgen reaction between 4-ethynyl-pyridine-*N*-oxide **5** with 4-azidomethyl-pyridine-*N*-oxide **3** in the octa-imine cage **1**, we evaluated the inclusion of similar reactions involving substrates featuring additional methylene units between the pyridine ring and the azide (**4** (2 CH_2)) and alkyne reacting groups (**6** (1 CH_2)).

First, we studied the kinetics of the 1,3-dipolar cycloaddition reaction between 2-azido-4-ethylpyridine-*N*-oxide **4** and 4-ethynyl-pyridine-*N*-oxide **5** included in the

octa-imine cage **1**. Azide **4** presents one more methylene unit than azide **3**. A 2mM equimolar mixture of **1**, **4,** and **5** in a 9:1 $CDCl_3$:CD_3CN solvent mixture produced a complex mixture of 1:1, and 2:1 homo- and hetero-complexes. Using the integral values of the pyrrole NH signals of the complexes, we calculated that the initial concentration of ternary hetero-complex was 0.18 mM (9% of the total mixture). observed a new set of proton signals that grew in intensity with time. We attributed these signals to the inclusion complex of the 1,4-triazole isomer **9a** included in **1**. We used the changes in the integral values of selected proton signals of the appearing **9a⊂1** complex to determine its concentration changes with time. We fit the experimental kinetic data to a similar theoretical kinetic model (**Figure 56**)used above and determined the reaction rate constant as $5.9 \times 10^{-5} s^{-1}$.

We measured the rate constant for the cycloaddition reaction of **4** and **5** in the bulk solution**,** k_{bulk9a}, using kinetic HPLC experiments. We used analogous conditions to those described above for similar reactions and determined a ratio of isomeric products and k_{bulk} values in line with previous ones (3.5×10^{-8} $M^{-1}s^{-1}$, **Figure 79** in experimental section). Not surprisingly, this result demonstrated that adding one methylene unit between the pyridine ring and the azide group did not significantly impact the kinetics nor the regioselectivity of the reaction in the bulk.

Next, we determined the acceleration factor of the cycloaddition reaction of **4** and **5** included in **1** to be EM = $k_{complex}$ / k_{bulk} = 1685 M, which is similar to the acceleration factor obtained between **3** and **5** included in **1**. This result demonstrated that adding one methylene unit between the pyridine ring and the azide group did not significantly impact the kinetics nor the regioselectivity of the of the cycloaddition of **4** and **5** upon inclusion in cage **1**.

*Study of the 1,3-dipolar cycloaddition reaction of **2** with **6** included in cage **1***

The good results obtained in the acceleration of the cycloaddition reactions of 4-(2-azidomethyl)-pyridine-*N*-oxide **3** with 4-ethynyl-pyridine-*N*-oxide **5** included in cage **1** (vide supra), prompted us to study the reaction of the substrates having the terminal reacting groups in the opposite scaffolds. That is, to study the cycloaddition reaction between 4-azide-pyridine-*N*-oxide **2** and 4-(2-propynyl)-pyridine *N*-oxide. Unfortunately, all our attempts to prepare 4-(2-propynyl)-pyridine *N*-oxide were unsuccessful. For this reason, we decided to use the synthetically accessible *N*-propynyl 4-pyridone **6** as a suitable analog scaffold of 4-(2-propynyl)-pyridine *N*-oxide.

A 2 mM equimolar mixture of **1**, **2**, and **6** in a 9:1 $CDCl_3$:CD_3CN solvent mixture produced the self-assembly of a combination of 1:1, and 2:1 homo- and hetero-

complexes. Similarly to above, we determined the concentration of the ternary complex [(**2•6**)⊂**1**] to be 0.47 mM. We observed a new set of proton signals that grew in intensity with time. We assigned this set of signals to the **10a**⊂**1** complex. The inclusion complex of the 1,4-isomer **10a** of the 1,3-cycloaddition reaction between **2** and **6** remained included in **1.** We determined the rate constant 2.9×10^{-6} s^{-1} in the same way measured above. From the rate constant measured in bulk solution for the formation of **10a** ($k_{bulk} = 6.13 \times 10^{-8}$), we quantified the acceleration factor of the included cycloaddition reaction as EM = 47 M.

Two single bonds need to be frozen in the transition states of the cycloaddition reactions of 4-(2-azidomethyl)-pyridine-*N*-oxide **3** with 4-ethynyl-pyridine-*N*-oxide **5**, and 4-azide-pyridine-*N*-oxide **2** with *N*-propynyl 4-pyridone **6**, when included in cage **1**. However, the EM values of the two reactions are noticeably different, 1250 M for the former and 47 M for the latter. EM values might be related to the entropy reduction experienced by the transition state of reactions occurring in the cage's cavity compared to those in the bulk. In the present case, other factors played a significant role.

Molecular modeling (MM3) studies revealed different relative orientations of the two reacting groups in the (**3**·**5**)⊂**1** and the (**2**·**6**)⊂**1** ternary Michaelis complexes when approaching the geometries of the cycloaddition reaction transition states. Most likely, energy differences of the two transition states of the reactions, included in **1,** are responsible for the significant changes measured in their acceleration factors (**Table 1**). In the bulk solution, the transition states of the two reactions can achieve similar geometries. However, including the reactions in cage **1** imposed steric constraints on the geometries of their transition states owing to the tight binding of the polar knobs of the reacting substrates in the hemispheres of the cage (**Figure 22**). The same reasoning was used to explain the high regioselectivity toward the 1,4-isomer observed for the Huisgen 1,3-dipolar-cycloaddition reactions included in **1**, which were described above.

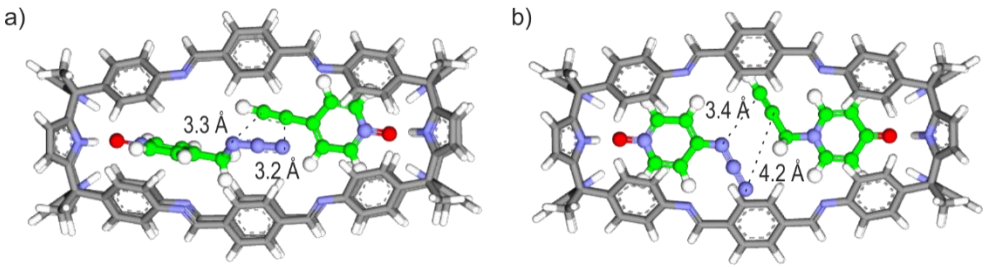

Figure 22. Energy-minimized structures (MM3) of ternary complex (**3·5**)⊂**1** (a) and (**2·6**)⊂**1** (b).

We summarize in **Table 1** the results of our kinetic investigations of the inclusion of several Huisgen 1,3-dipolar-cycloaddition reactions in cage **1**.

Table 1. Rate constants of the 1,3-cycloaddition reactions between azides derivatives **2-4** and alkyne derivatives **5-6** in the bulk and inside octa-imine cage **1** producing the 1,4-cycloaddition isomer and their respectively derived effective molarities.

entry	reactants	$k_{complex}$ (s^{-1})	k_{bulk} ($M^{-1}s^{-1}$)	EM (M)
1	**2+5**	n.m.[a]	5.0×10^{-8}	-
2	**3+5**	7.0×10^{-5}	5.6×10^{-8}	1250
3	**4+5**	5.9×10^{-5}	3.5×10^{-8}	1685
4	**2+6**	2.9×10^{-6}	6.1×10^{-8}	47

[a] not measurable

We draw the following conclusions from the above-tabulated data:

1) The inclusion of azido derivative **2** (n = 0) and alkyne **5** in cage **1** did not produce any measurable acceleration of the cycloaddition reaction (entry 1). The included reacting groups (azide and alkyne) are correctly oriented but need to be closer to react. The container is conformationally locked and cannot adapt to bring the two reacting groups to an optimal distance for the reaction to occur.

2) The maximum reaction acceleration was observed by including in cage **1** the reaction between azide derivative **3** or **4** (n=1-2) and 4-ethynyl-pyridine-*N*-oxide **5**. The acceleration factor of the included cycloaddition reaction between alkynyl **5** and azide **4** (n=2), having one more methylene unit between the pyridine-*N*-oxide ring and the terminal azide group than **3**, has no obvious difference compared to that with **3**. (entry 2 *vs* entry 3, **Table 1**).

3) The addition of one methylene unit between the polar knob (4-pyridone) and the reacting alkynyl group in **6** produced a deleterious effect on the reaction with **2** when the reactants are included in cage **1**. The acceleration factor of the reaction was reduced by one order of magnitude compared to that of **3** with **5**, which requires the freezing of the same number of single bond rotations in the transition state of the included cycloaddition reaction (entry 2 vs. entry 4, **Table 1**).

4) Including the cycloaddition reactions in cage **1** imposes geometric and steric constraints on their transition states. This can be used to explain the observed acceleration factors and the regioselectivity.

5.2.5. Control experiments to support the effect of acceleration of the Huisgen 1,3-dipolar cycloadditions by inclusion in the octa-imine cage 1.

We performed several control experiments to support the role of the polar cavity on the acceleration observed for the Huisgen cycloaddition included in cage **1**.

First, we prepared a 20 mM equimolar solution of tetra-amine tetra-ester aryl-extended calix[4]pyrrole **12**, azidomethyl pyridine **11**, and ethynyl pyridine *N*-oxide **5**. We did not detect the formation of the cycloaddition products after several days (**Figure 23**). We concluded that the binding of the ethynyl-pyridine-*N*-oxide substrate to a calix[4]pyrrole host does not substantially modify the reactivity of the dipolarophile (i.e. alkyne group). Therefore, we concluded that this factor was not responsible for the observed accelerations in the cycloaddition reactions.

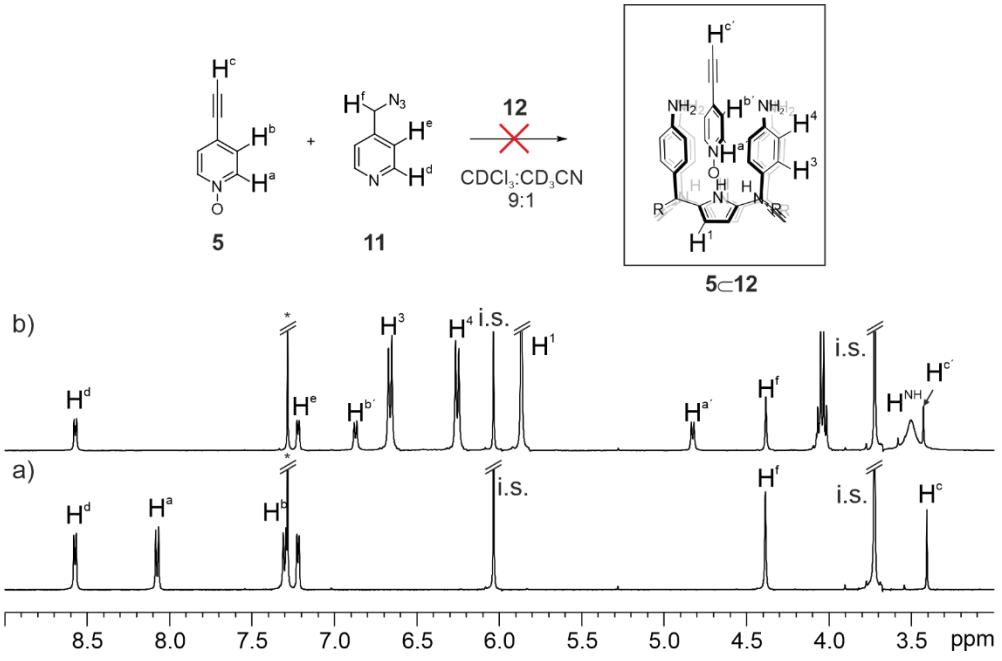

Figure 23. Selected region of the ^{1}H NMR spectra (400 MHz, at 298 K, $CDCl_3$:CD_3CN 9:1) of a)**5**:**11** 1:1 20 mM mixture; and b) **5**:**11**:**12** 1:1:1 20 mM mixture. No changes

were detected in any of the ^{1}H NMR spectra after 1 month suggesting that **12** does not act as catalyst in the 1,3-dipolar cycloaddition reaction.

Next, we monitored the evolution of an equimolar solution mixture of the octa-imine cage **1**, ethynyl pyridine-*N*-oxide **5**, and two azido- derivatives, **2** and **3**. Based on our previous findings, we expected this mixture to yield the exclusive formation of the cycloaddition product **8a** included in the cavity of **1**. The ^{1}H NMR spectrum of the initial combination showed multiple sets of proton signals, indicating the coexistence of several complexes in the solution. At t = 5 min, we could identify the homo- complexes (**2**)$_2$⊂**1** and (**3**)$_2$⊂**1** and the ternary complexes (**2**·**5**)⊂**1** and (**3**·**5**) ⊂**1**. We monitored the evolution of this reaction mixture with time using ^{1}H NMR spectroscopy. After 20 hours, we detected a new set of proton signals assigned to the **8a**⊂1 complex. We did not detect signals for the protons of free or bound **7** (**7a** or **7b**), which resulted from the cycloaddition reaction of **2** and **5**. The reaction selectivity exhibited by the octa-imine cage **1** for the acceleration of the included Huisgen cycloaddition of **5** with **3** over **2**, is most likely because, as already mentioned, the arrangement of the substrates in the (**2**·**5**)⊂**1** complex cannot reach the geometry of the transition state of the reaction.

5.3 Conclusions

We utilized the [4+2] octa-imine cage as a reaction vessel to accelerate bimolecular reactions in confined spaces. To this end, we synthesized a series of polar guests bearing either azide (**2**–**4**) or alkyne (**5**, **6**) terminal groups. The octa-imine cage readily forms thermodynamically and kinetically stable 1:1 and 2:1 homo- and hetero-inclusion complexes with monotopic guests. Although complex formation is fast on a human timescale, these complexes exhibit slow exchange kinetics on the NMR timescale.

In ternary complexes, two guests with distinct reactive groups (azido and ethylene) are brought into close proximity within the octa-imine cages, aligning their reactive functionalities and effectively increasing the local concentration of reactants. This setup imparts an intramolecular-like quality to the bimolecular reaction, resulting in a significant rate enhancement.

Notably, in contrast to the Huisgen 1,3-dipolar cycloaddition reaction in bulk, which typically produces both 1,5- and 1,4-disubstituted 1,2,3-triazole products in similar proportions, the same reaction within the encapsulated complex selectively yields only the 1,4-isomer.

In most instances, the calculated effective molarity for the reaction inside the molecular container was on the order of 10^3 M. However, in one case, the effective molarity was lower (10^2 M), likely due to the tight binding and restricted adaptability of the substrates within the cage, which impeded transition state (TS) formation. With the shortest azido and ethylene reactants, no measurable acceleration was observed in the ternary encapsulation complex, likely because the transition state (TS) requires higher energy within the cage due to tight hydrogen bonding between the cage and guest, which limits the reaction.

5.4 Experimental section

5.4.1. General information

Starting materials and reagents were purchased from commercial suppliers and used without further purification. All reactions were performed under an argon atmosphere and protected from light unless specified. Anhydrous solvents were obtained from a solvent purification system SPS-400-6 from Innovative Technologies. All solvents were of HPLC-grade quality, commercially obtained, and used without further purification. ^{1}H NMR, ^{13}C NMR and 2D NMR spectra were recorded on a Bruker Avance 300 (300 MHz for ^{1}H NMR and 75 MHz for ^{13}C NMR), Bruker Avance 400 (400 MHz for ^{1}H NMR and 100 MHz for ^{13}C NMR), Bruker Avance 500 (500 MHz for ^{1}H NMR and 125 MHz for ^{13}C NMR) or Bruker Avance 500 with cryoprobe (500 MHz for ^{1}H NMR and 125 MHz for ^{13}C NMR). Deuterated solvents used are indicated in the characterization and chemical shifts are given in ppm.

UV-Vis absorption measurements were carried out with Shimadzu UV-1603 spectrophotometer. All measurements were performed at room temperature (RT) in quartz cuvettes of 1 cm optical pathlength.

ITC experiments were performed in a MicroCal VP-ITC Micro Calorimeter with the VP Viewer 2000 software. All the titrations were carried out in chloroform: acetonitrile 9:1 solution mixture at 288 K. Titrations were carried out by adding small aliquots (8 μL, 16 s) of a solution of the guest into a solution of the host in the same solvent. The spacing time was set as 600 s due to the observed slow kinetics. The concentration of guest solution was approximately sixteen times more concentrated than the host solution. The association constants and the thermodynamic parameters were obtained from the fit of the titration data to either a simple one set of sites binding model for guest **2** or sequential binding sites model for guest **3** by using the Microcal ITC Data Analysis module.

The HPLC system used for monitor reactions was an Agilent technologies 1200 series and the analytical column was BEH HILIC (3.5 μm, 4.6×150 mm, Waters Xbridge®), protected by a BEH HILIC precolumn (3.5 μm, 3.9 mm × 5mm, Waters Xbridge®). The mobile phase gradient starting from ACN/H_2O 98:2, increase H_2O from 2% to 40% in 15 min, and then hold 40% 10 min, finally back to 2% in 5 min and stabilize phase for 10 min. Flux: 1 mL/min. Injection volume: 5 μL. Detection wavelength 300 nm.

High Resolution Mass Spectra (HRMS) were obtained on a Bruker HPLC-TOF (MicroTOF Focus). All ions were generated by electrospray ionization (ESI) in the positive mode.

The synthetic procedure to prepare cages **1** is reported in Chapter 3. Guest **2** was synthesized, adapting the previously reported procedure. [24] Guest **6** was synthesized, through modification of the reported alkylation of 4-hydroxypridine procedure in literature. [25]

5.4.2. Synthesis and Characterization

General procedure for the synthesis of para-substituted pyridyl N-oxide: para-substituted pyridyl *N*-oxide derivatives were obtained by oxidation of the corresponding pyridine analogues using the following general procedure. The para-substituted pyridine derivative (1.00 mmol) was dissolved in a 1:1 mixture of water/2-butone (60 mL). Then $NaHCO_3$ (1.68 g, 20.0 mmol, 20 equiv.) was added into the two-phase mixture under stirring. 20 mL of a water solution of OXONE® (2.50 g, 4.00 mmol, 4 equiv.) was added dropwise to the mixture in 30 minutes under stirring. After 24 h, the mixture was diluted with chloroform (50 mL) and the water phase was washed with chloroform (2x50mL). The organic layers were collected, dried over anhydrous Na_2SO_4, filtered, and concentrated under reduced pressure. The crude was purified by column chromatography (neutral alumina, chloroform: i-propanol 95:5) to obtain the pyridyl *N*-oxide derivates in 40-60% yield.

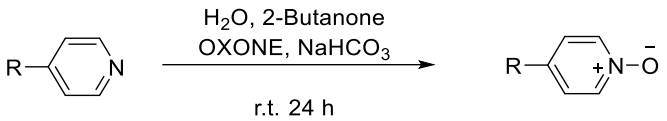

Scheme 2. Synthesis of pyridyl *N*-oxide derivatives **2** (R = N_3), **3** (R = $-CH_2N_3$), **4** (R = $-C_2H_4N_3$), **5** (R = -C≡CH).

General procedure for the synthesis of 1,4-disubstituted 1,2,3-triazole derivatives: 1,4-disubstituted triazole derivatives were obtained by 1,3-dipolar cycloaddition reaction between the para-substituted pyridine *N*-oxide precursors with alkyne and azide terminal groups. In general, the pyridyl *N*-oxide alkyne derivatives (100 μmol) and pyridyl *N*-oxide azide derivative (100 μmol) were dissolved in 5 mL of dry dichloromethane under argon. Then $Cu(CH_3CN)_4PF_6$ (5.00 μmol, 0.05 equiv.) and TBTA (5.00 μmol, 0.05 equiv.) were added to the mixture and stirred for 2 h at r.t. protected from light. After two hours a white solid precipitated in the reaction mixture. The white precipitate was collected via filtration and washed with dichloromethane (5 mL) and acetonitrile (5 mL) to give the pure compound.

5.4.2.1. Characterization of guest 3

^{1}H NMR (400 MHz, 298 K, $CDCl_3$): δ (ppm) = 8.19 (d, J = 6.8 Hz, 2H), 7.22 (d, J = 6.8 Hz, 2H), 4.39 (s, 2H).

^{13}C NMR (100 MHz, 298 K, $CDCl_3$) δ (ppm) = 139.4, 134.3, 125.1, 52.43.

HR-MS (ESI TOF) m/z: $[M+H]^+$ calculated for $C_6H_7N_4O^+$ = 151.0620, found 151.0613.

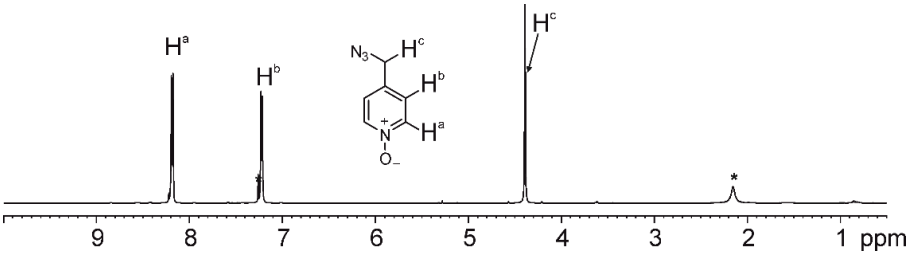

Figure 24. ^{1}H NMR spectrum (400 MHz, 298 K, $CDCl_3$) of **3**. *Residual solvent peaks.

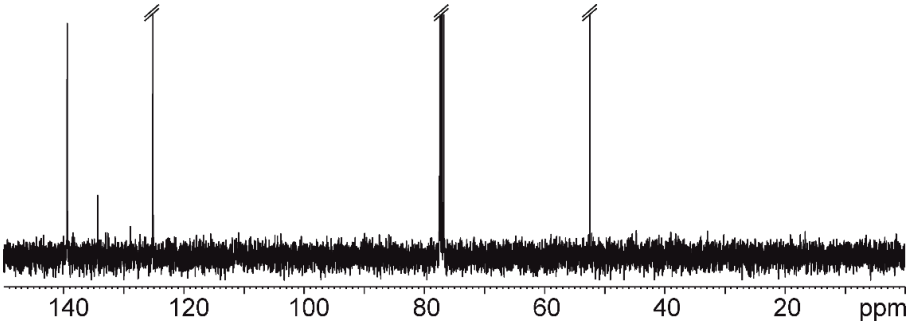

Figure 25. ^{13}C NMR (100 MHz, at 298 K, $CDCl_3$) of **3**.

5.4.2.2. Characterization of guest **4**

^{1}H NMR (400 MHz, 298 K, $CDCl_3$): δ (ppm) = 8.16 (d, J = 6.8 Hz, 2H), 7.14 (d, J = 6.8 Hz, 2H), 3.57 (t, J = 6.6 Hz, 2H), 2.86 (t, J = 6.6 Hz, 2H).

^{13}C NMR (100 MHz, 298 K, $CDCl_3$): δ (ppm) = 139.3, 137.4, 126.6, 51.20, 33.93.

HR-MS (ESI TOF) m/z: $[M+Na]^+$ calculated for $C_7H_9N_4O^+$ = 165.0776, found 165.0771.

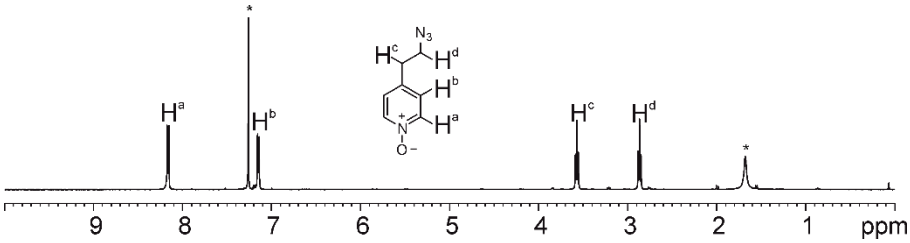

Figure 26. ^{1}H NMR spectrum (400 MHz, 298 K, $CDCl_3$) of **4**. *Residual solvent peaks.

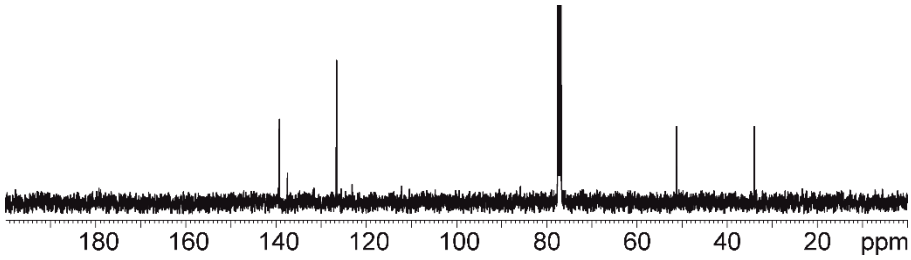

Figure 27. ^{13}C NMR (100 MHz, at 298 K, $CDCl_3$) of **4**.

5.4.2.3. Characterization of guest **5**

^{1}H NMR (400 MHz, 298 K, $CDCl_3$): δ (ppm) = 8.12 (d, *J* = 7.2 Hz, 2H), 7.32 (d, *J* = 7.2 Hz, 2H), 3.39 (s, 1H).
^{13}C NMR (100 MHz, 298K, $CDCl_3$): δ (ppm) = 139.2, 129.1, 119.8, 83.5, 80.0.
HR-MS (ESI TOF) m/z: $[M+H]^+$ calculated for $C_7H_6NO^+$=120.0449, found 120.0447.

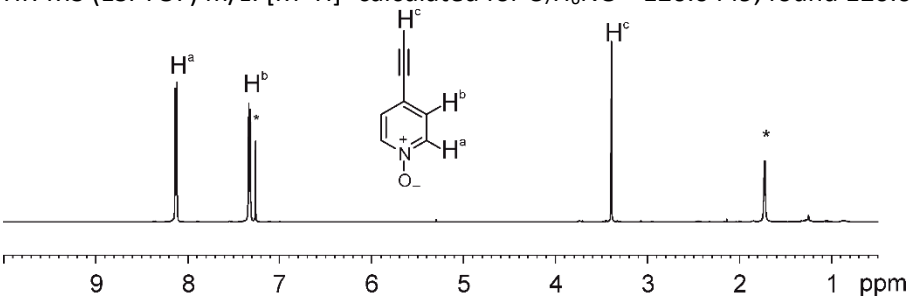

Figure 28. ^{1}H NMR spectrum (400 MHz, 298 K, $CDCl_3$) of **5**. *Residual solvent peaks.

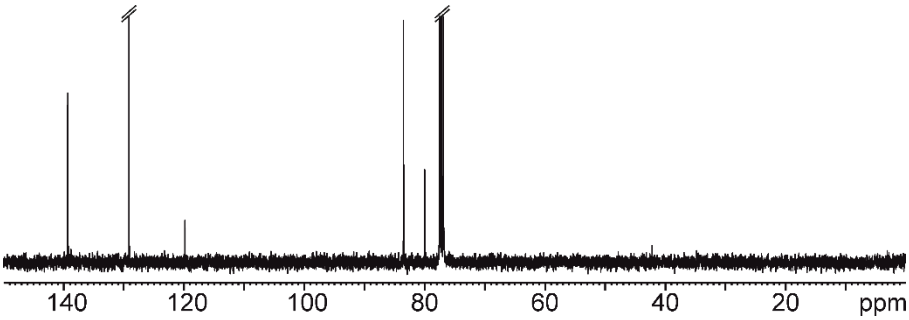

Figure 29. ^{13}C NMR (100 MHz, at 298 K, $CDCl_3$) of **5**.

5.4.2.4. Synthesis of guest 6

Under Ar, propargyl bromide (1.60 g, 11.0 mmol, 1.1 mL, 1 equiv.)was added to a suspension of 4-hydroxypridine (1.00 g, 11.0 mmol, 1 equiv.) and K_2CO_3 (3.04 g, 22.0 mmol, 2 equiv.) in acetonitrile (50 mL). The reaction mixture was then refluxed at 83 °C for 24 h. On completion of the reaction, as indicated by TLC, the mixture was filtered and the filtrate was evaporated under vacuum to give the crude product. The crude product was purified by column chromatography (neutral alumina, DCM:*i*-propanol 97:3) to give the product **6** a white solid in 80% yield (8.80 mmol, 1.1 g).

^{1}H NMR (400 MHz, 298 K, $CDCl_3$): δ (ppm) = 7.40 (d, *J* = 7.8 Hz, 2H), 6.40 (d, *J* = 7.8 Hz, 2H), 4.56 (d, *J* = 2.6 Hz, 2H), 2.62 (t, J= 2.6 Hz, 1H).

^{13}C NMR (100 MHz, 298K, $CDCl_3$): δ (ppm) =179.1, 139.1, 119.3, 75.4, 45.6.

HR-MS (ESI TOF) m/z: $[M+H]^+$ calculated for $C_8H_8NO^+$ = 134.0600, found 134.0603.

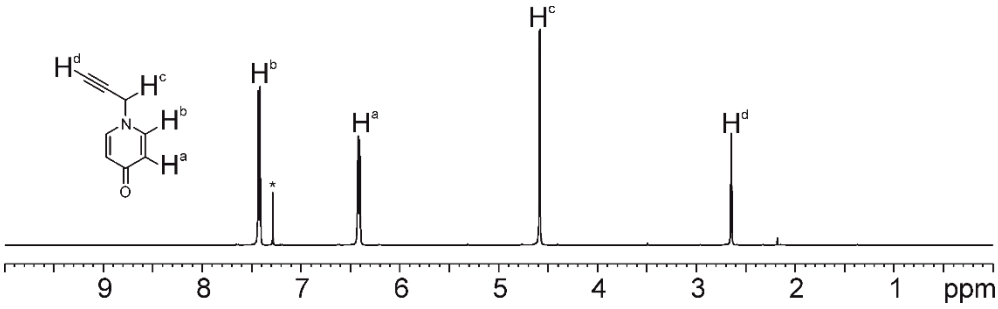

Figure 30. ^{1}H NMR spectrum (400 MHz, 298 K, $CDCl_3$) of **8**. *Residual solvent peaks.

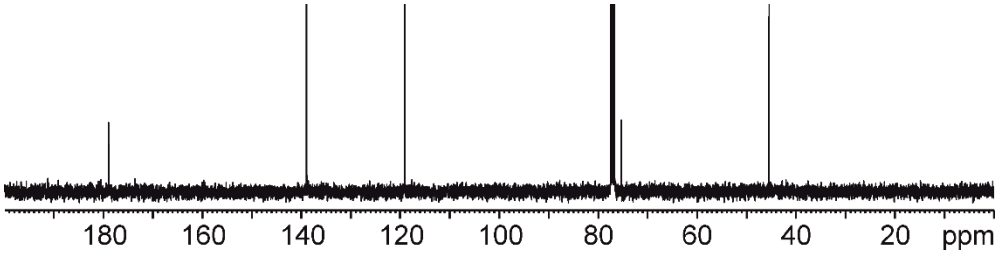

Figure 31. ^{13}C NMR (100 MHz, at 298 K, $CDCl_3$) of **6**.

5.4.2.5. Characterization of guest **7a**

^{1}H NMR (400 MHz, 298 K, d_6-DMSO): δ (ppm) = 9.55 (s, 1H), 8.46 (d, J = 7.3 Hz, 2H), 8.35 (d, J = 7.0 Hz, 2H), 7.99 (d, J = 7.3 Hz, 2H), 7.88 (d, J = 7.0 Hz, 2H) ppm.

^{13}C NMR (100 MHz, 298K, d_6-DMSO): δ (ppm) = 144.5, 140.2, 139.5, 131.9, 126.2, 122.5, 120.9, 1172.

HR-MS (ESI TOF) m/z: $[M+Na]^+$ calculated for $C_{12}H_9N_5NaO_2^+$ = 278.0660, found 278.0648.

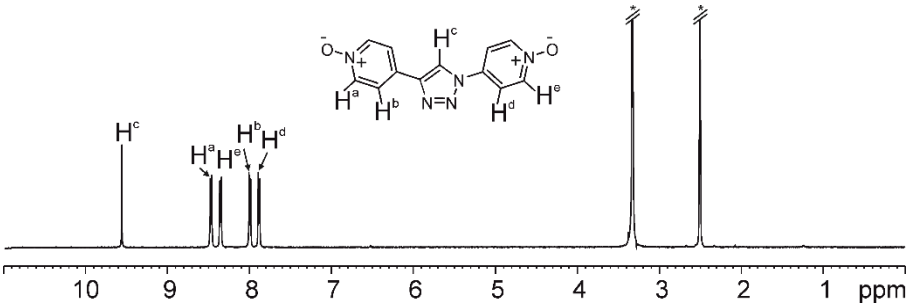

Figure 32. ^{1}H NMR spectrum (400 MHz, 298 K, d_6-DMSO) of **7a**. *Residual solvent peaks.

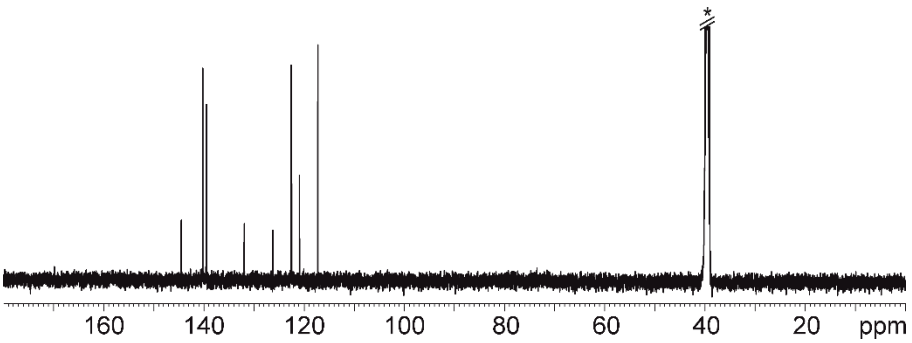

Figure 33. ^{13}C NMR (100 MHz, at 298 K, d_6-DMSO) of **7a**.

5.4.2.6. Characterization of guest **8a**

^{1}H NMR (400 MHz, 298 K, d_6-DMSO): δ (ppm) = 8.80 (s, 1H), 8.28 (d, J = 6.6 Hz, 2H), 8.23 (d, J = 6.4 Hz, 2H), 7.85 (d, J = 6.6 Hz, 2H), 7.35 (d, J = 6.4 Hz, 2H), 5.71 (s, 2H) ppm.
^{13}C NMR (100 MHz, 298K, d_6-DMSO): δ (ppm) = 144.1, 139.7, 139.4, 133.2, 127.5, 126.5, 123.7, 122.8, 51.52.
HR-MS (ESI TOF) m/z: $[M+Na]^+$ calculated for $C_{13}H_{11}N_5NaO_2^+$ = 292.0806, found 292.0805.

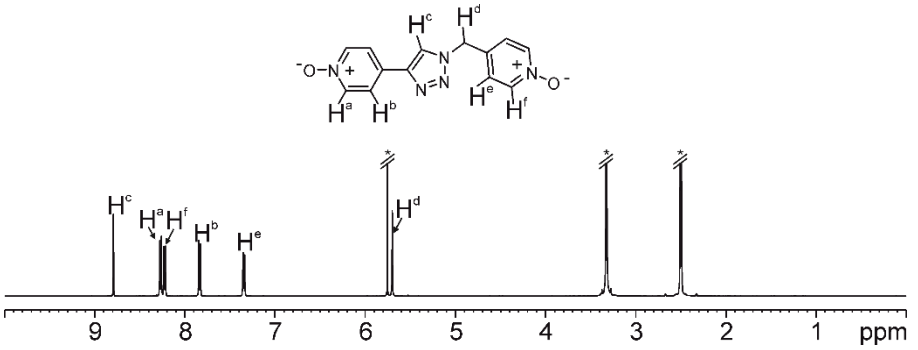

Figure 34. ^{1}H NMR spectrum (400 MHz, 298 K, d_6-DMSO) of **8a**. *Residual solvent peaks.

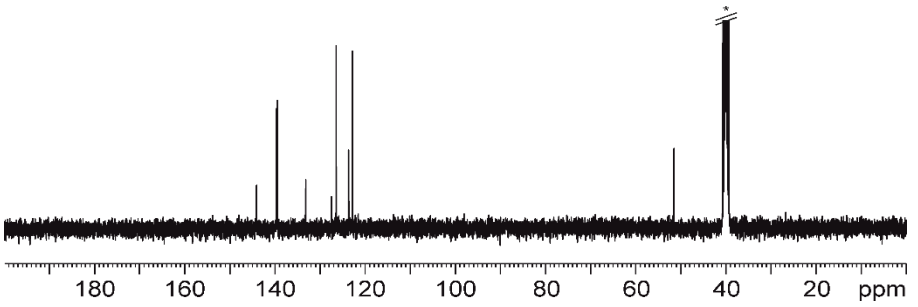

Figure 35. ^{13}C NMR (100 MHz, at 298 K, d_6-DMSO) of **8a**.

5.4.2.7. Characterization of guest **9a**

^{1}H NMR (400 MHz, 298 K, d_6-DMSO): δ (ppm) = 8.67 (s, 1H), 8.25 (d, J = 7.0 Hz, 2H), 8.10 (d, J = 6.8 Hz, 2H), 7.78 (d, J = 7.0 Hz, 2H), 7.23 (d, J = 6.8 Hz, 2H), 4.71 (t, J = 7.0 Hz, 2H) 3.21 (t, J = 7.0 Hz, 2H) ppm.

^{13}C NMR (100 MHz, 298K, d_6-DMSO): δ (ppm) = 143.6, 139.7, 138.9, 136.0, 127.7, 127.2, 123.2, 122.7, 50.20, 34.11.

HR-MS (ESI TOF) m/z: $[M+H]^+$ calculated for $C_{14}H_{14}N_5O_2^+$ = 284.1143, found 284.1142.

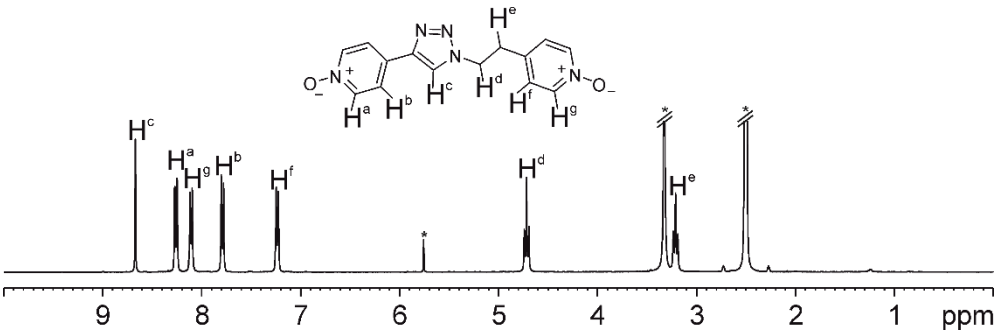

Figure 36. ^{1}H NMR spectrum (400 MHz, 298 K, d_6-DMSO) of **9a**. *Residual solvent peaks.

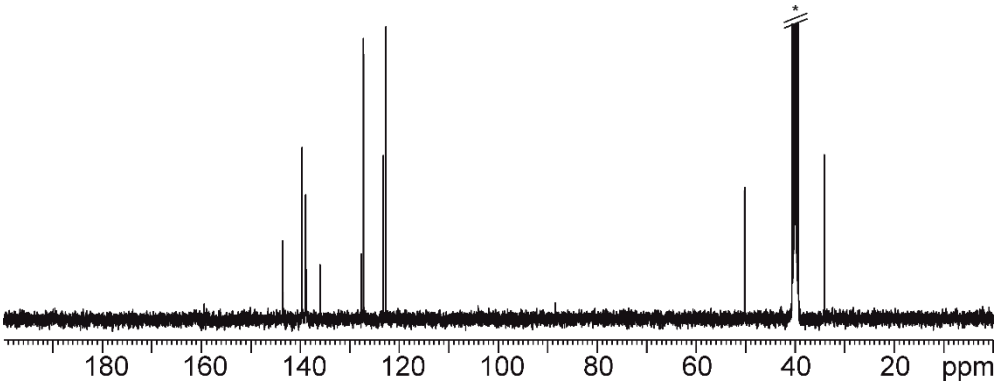

Figure 37. ^{13}C NMR (100 MHz, at 298 K, d_6-DMSO) of **12a**.

5.4.2.8. Characterization of guest **10a**

^{1}H NMR (400 MHz, 298 K, d_6-DMSO): δ (ppm) = 8.93 (s, 1H), 8.40 (d, J = 6.8 Hz, 2H), 8.00 (d, J = 6.8 Hz, 2H), 7.81 (s, 2H), 6.11 (s, 2H), 5.27 (s, 2H).

^{13}C NMR (100 MHz, 298K, d_6-DMSO): δ (ppm) = 144.5, 141.6, 140.7, 132.6, 122.7, 117.8, 50.1.

HR-MS (ESI TOF) m/z: $[M+Na]^+$ calculated for $C_{13}H_{11}N_5NaO_2^+$ = 292.0805, found 292.0810.

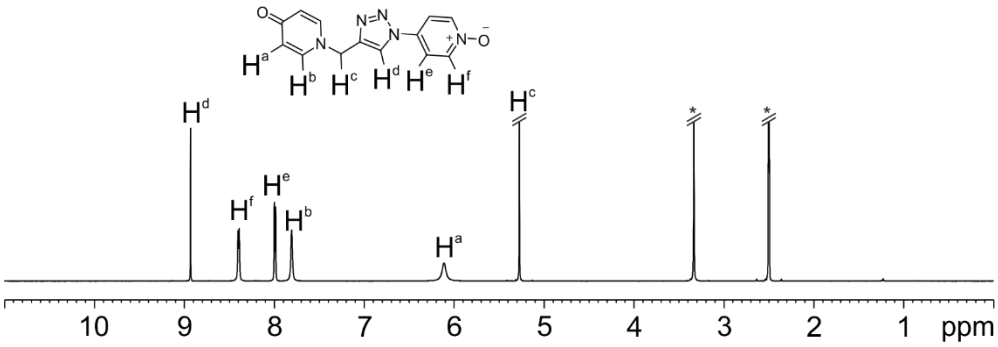

Figure 38. ^{1}H NMR spectrum (400 MHz, 298 K, d_6-DMSO) of **10a**. *Residual solvent peaks.

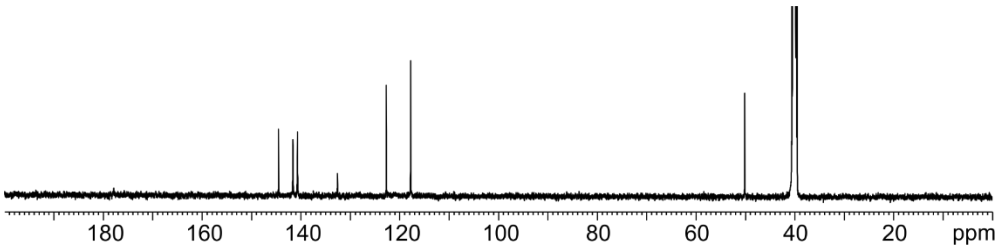

Figure 39. ^{13}C NMR (100 MHz, at 298 K, d_6-DMSO) of **10a**.

5.4.3. Binding studies of monotopic and ditiopic guests in cage **1**

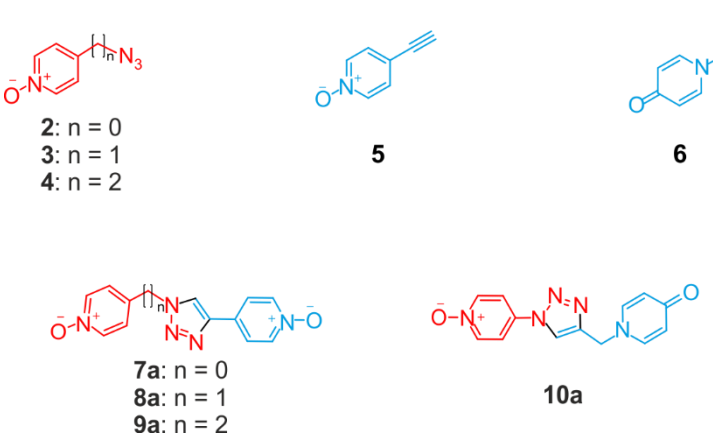

Scheme 3. Line-drawing structure of guests used for the binding studies with cage **1**.

5.4.3.1. Binding studies of **2** with octa-imine cage **1**.

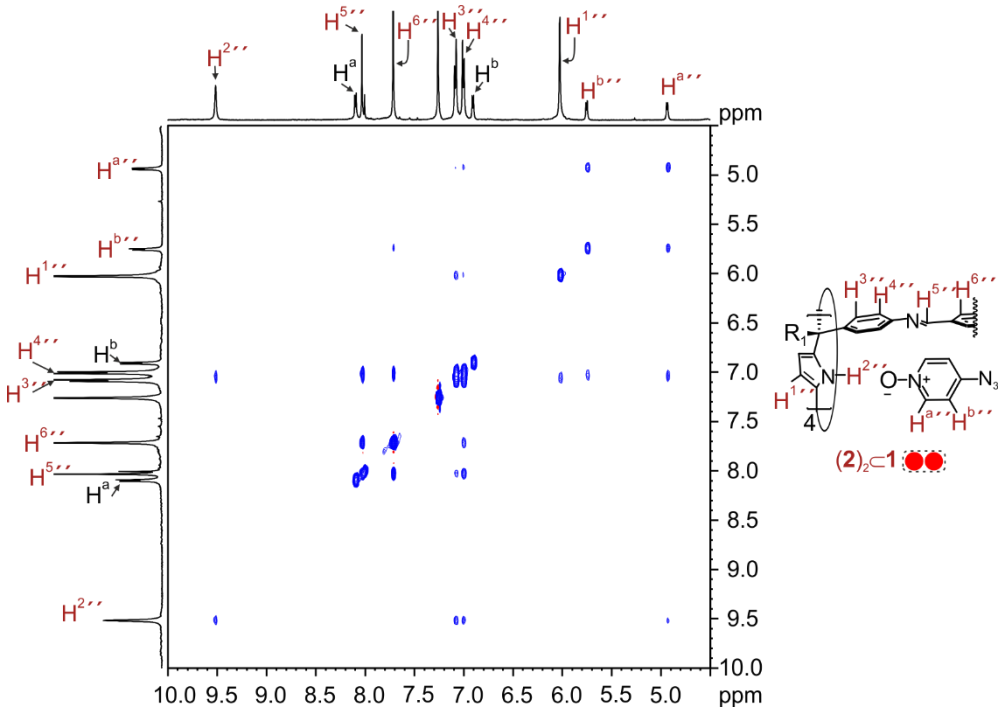

Figure 40. 2D ^{1}H NOESY NMR (500 MHz, at 298 K, $CDCl_3$:CD_3CN 9:1, d8 (mixing time) = 0.3 s) of (**2**)$_2$⊂**1** with 2 equiv. of free **2**.

5.4.3.2. Binding studies of **4** with octa-imine cage **1**.

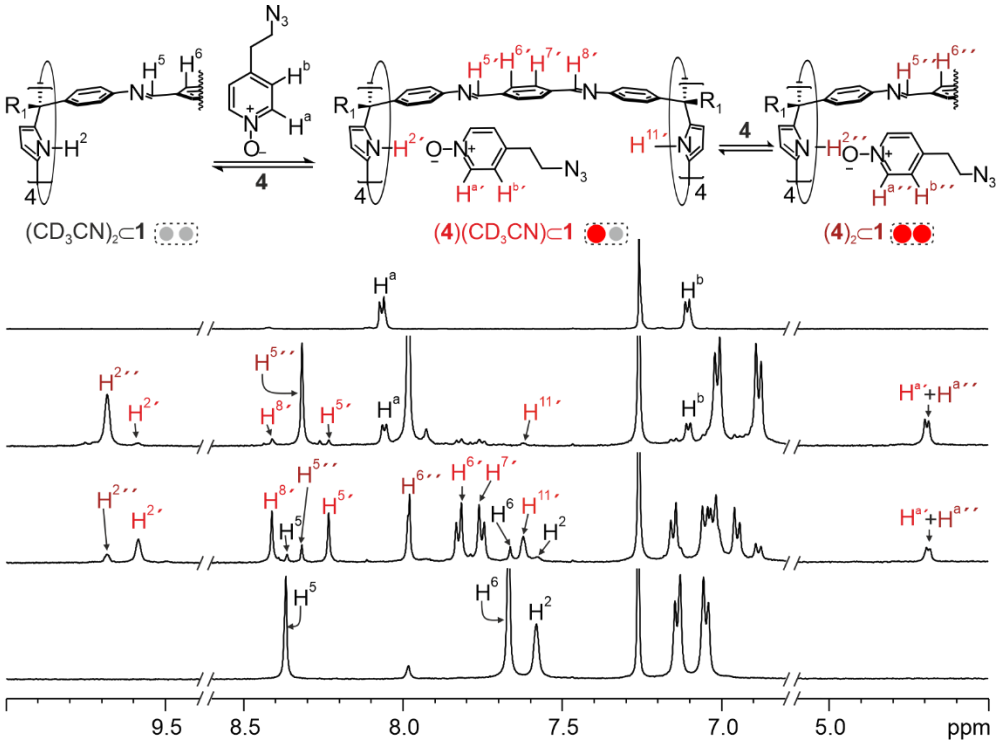

Figure 41. Selected regions of ^{1}H NMR (400 MHz, at 298 K, $CDCl_3$: CD_3CN 9:1) spectra of the titration of a 2 mM solution of cage **1**, upon addition of a) 0 equiv., b) 1 equiv. ; c) 2 equiv. of **6**. Spectrum d) corresponds to the free **6** in the same solvent mixture.

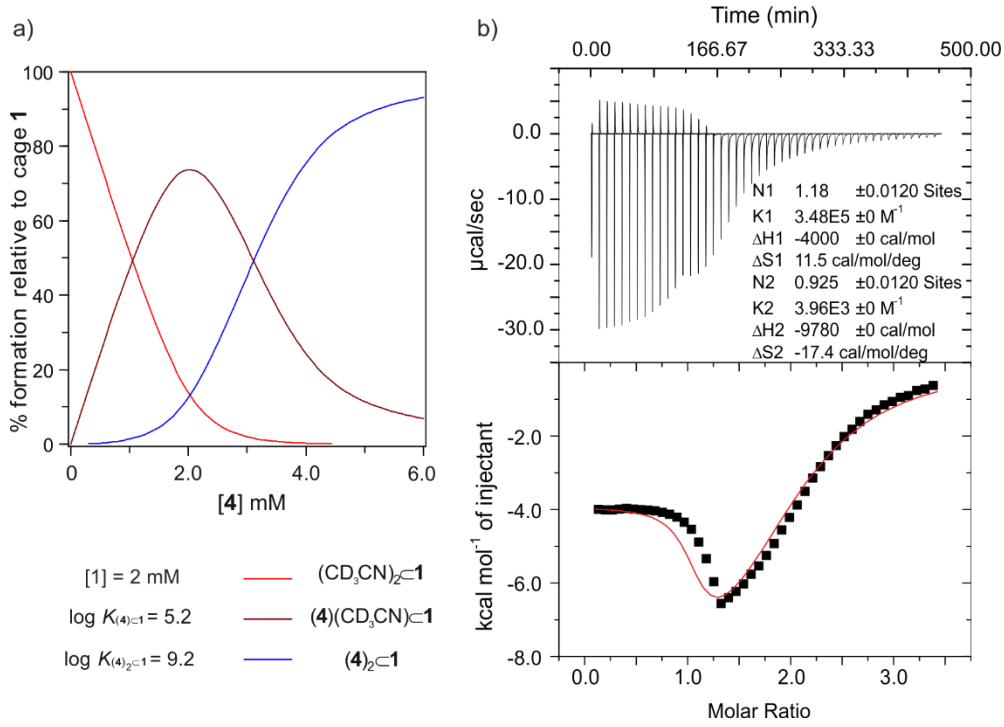

Figure 42. . a) Speciation profile of the solutions resulting from the incremental addition of **4** (up to 6 equiv.) to a 2 mM solution of cage **1** considering the binding constant values $K_{1:1} = 2 \times 10^5$ M^{-1}, $K_{2:1} = 2 \times 10^9$ M^{-2}. b) Top- Traces of the raw data (heat vs time) of the ITC experiment of cage **1** ([cell] = 1×10^{-3} M) with **4** ([syringe]= 1.6×10^{-2} M). The solutions were prepared using a chloroform: acetonitrile 9:1 solvent mixture. Bottom- Normalized integrated heat (black squares) vs. **4**/**1** molar ratio. Experimental data were fit to a sequential two binding sites model (red line).

5.4.3.3. Binding studies of **5** with octa-imine cage **1**.

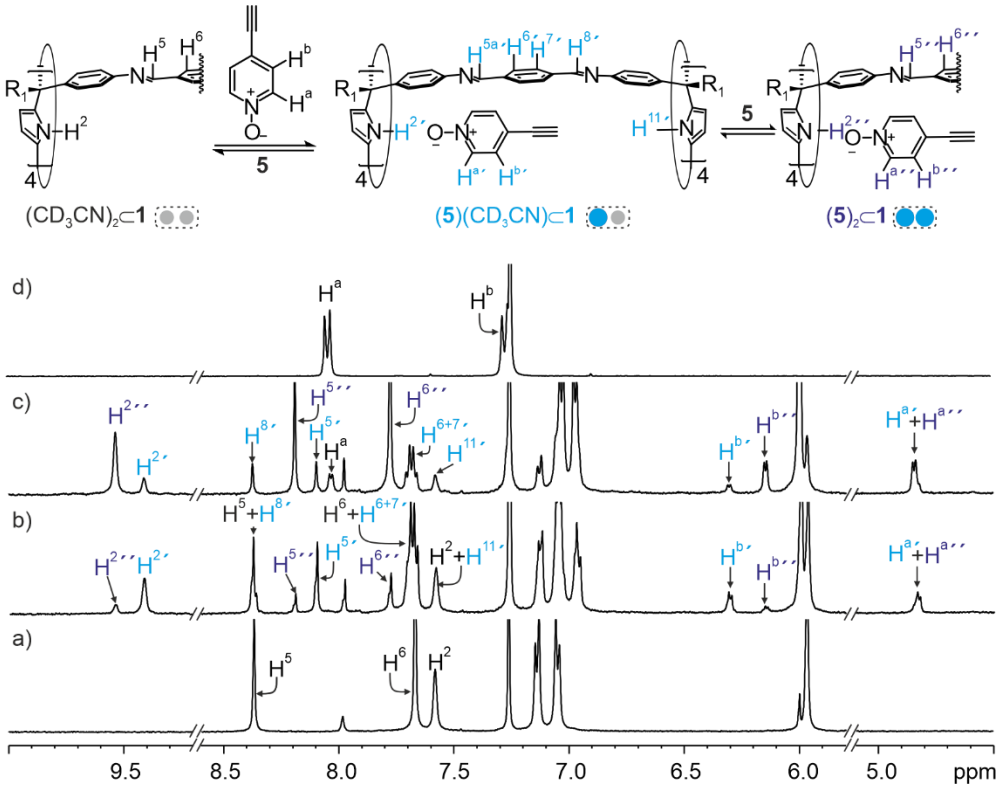

Figure 43. Selected regions of ^{1}H NMR (400 MHz, at 298 K, $CDCl_3$: CD_3CN 9:1) spectra of the titration of a 2 mM solution of cage **1**, upon addition of a) 0 equiv., b) 1 equiv. ; c) 2 equiv. of **5**. Spectrum d) corresponds to the free **5** in the same solvent mixture.

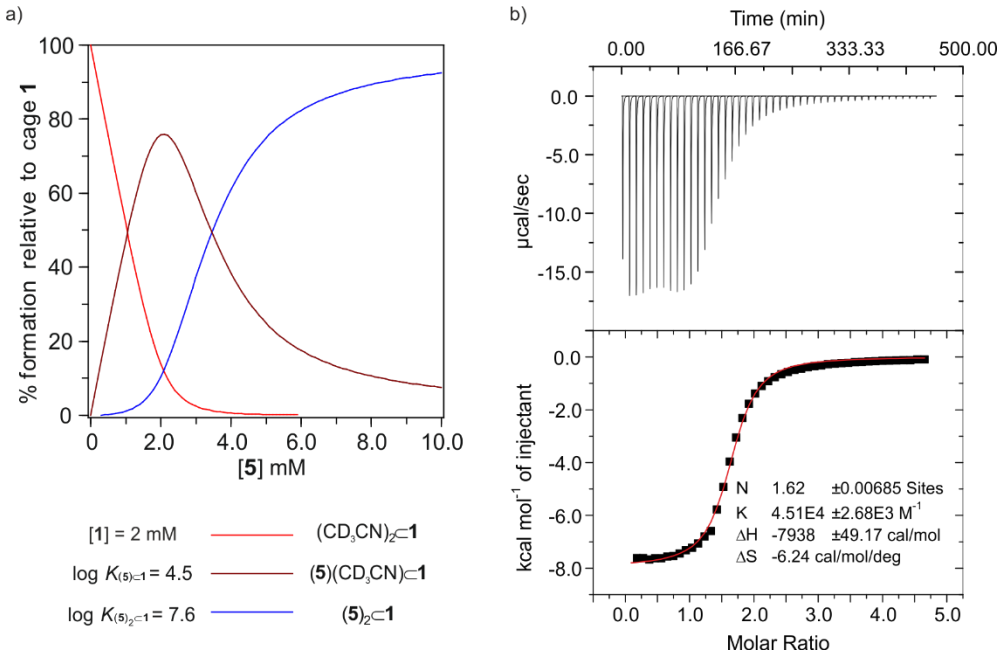

Figure 44. a) Speciation profile of the addition of increasing amounts of **5** (up to 5 equiv.) to a 2 mM solution of cage **1** considering the binding constant values $K_{1:1} = 3 \times 10^4$ M^{-1}, $K_{2:1} = 4 \times 10^7$ M^{-2}. b) Top- Traces of the raw data (heat vs time) of the ITC experiment of cage **1** ([cell] =1×10^{-3} M) with **5** ([syringe] =2.0×10^{-2} M). The solutions were prepared using a chloroform: acetonitrile 9:1 solvent mixture. Bottom- Normalized integrated heat (black squares) vs. **5**/**1** molar ratio. The experimental data were fit to one set of sites binding model (red line).

5.4.3.4. Binding studies of **8a** with octa-imine cage **1**.

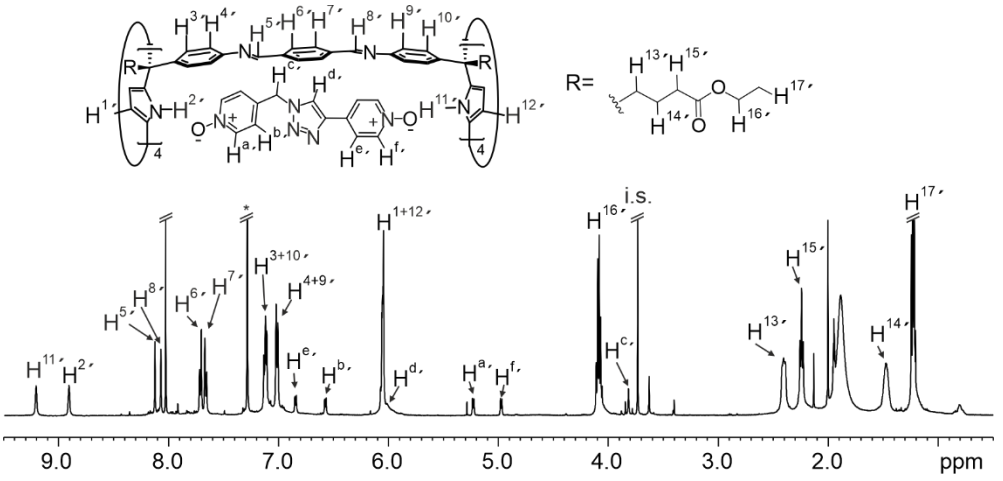

Figure 45. ^{1}H NMR (400 MHz, at 298 K, $CDCl_3$: CD_3CN 9:1) spectra of a 2 mM solution of **8a⊂1** prepared by solid liquid extration. (1.2 equiv. of **8a** was added into 2 mM solution of cage **1** in solid state)

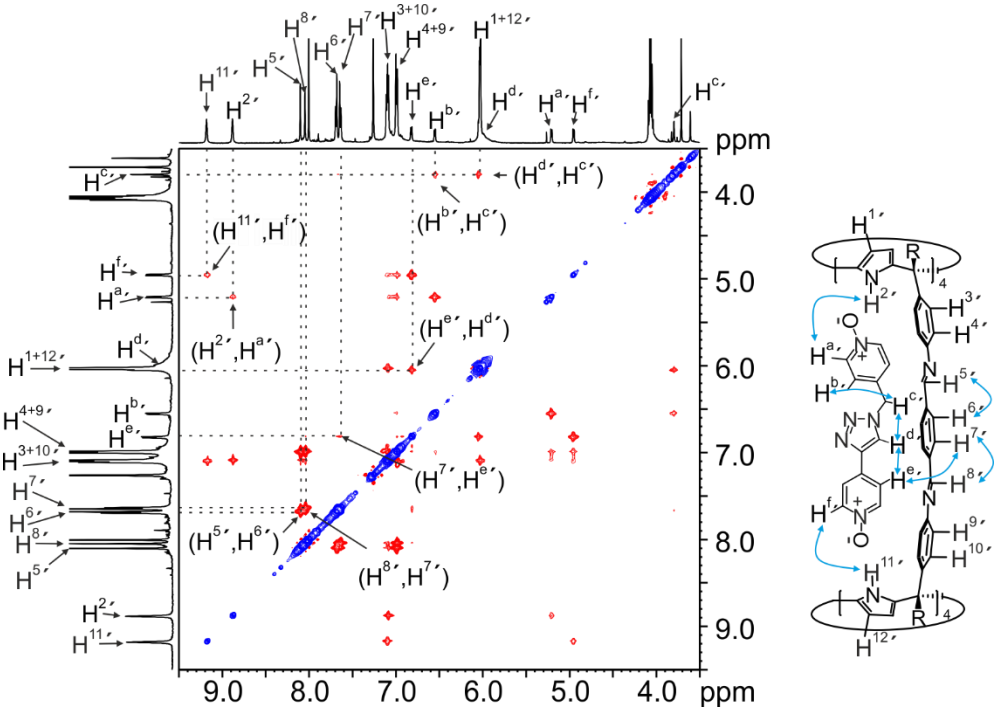

Figure 46. 2D ^{1}H ROESY NMR (500 MHz, at 298 K, $CDCl_3$:CD_3CN 9:1, d8 (mixing time) = 0.3 s) of **8a⊂1.**

5.4.3.5. Binding studies of **9a** with octa-imine cage **1**.

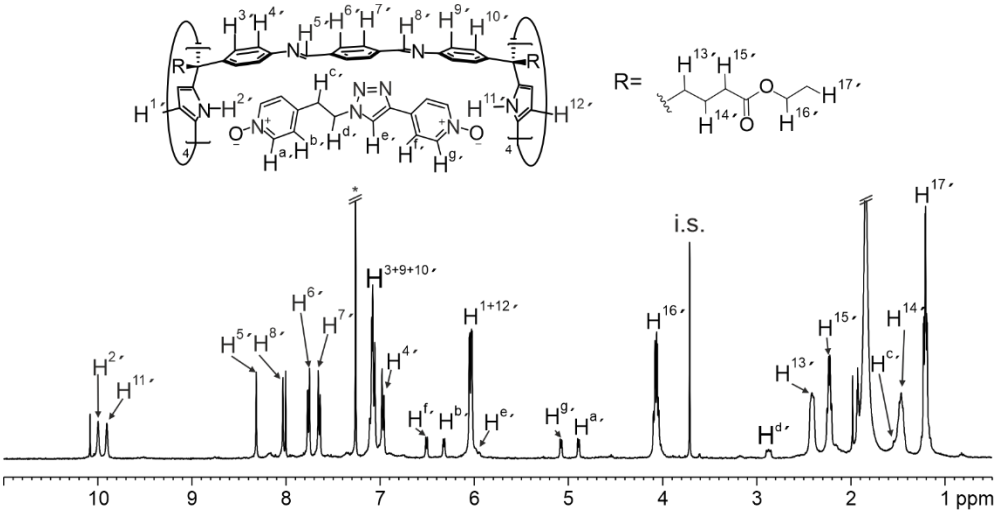

Figure 47. Selected regions of ^{1}H NMR (400 MHz, at 298 K, $CDCl_3$: CD_3CN 9:1) spectra of a 2 mM solution of **9a⊂1** prepared by solid liquid extration.

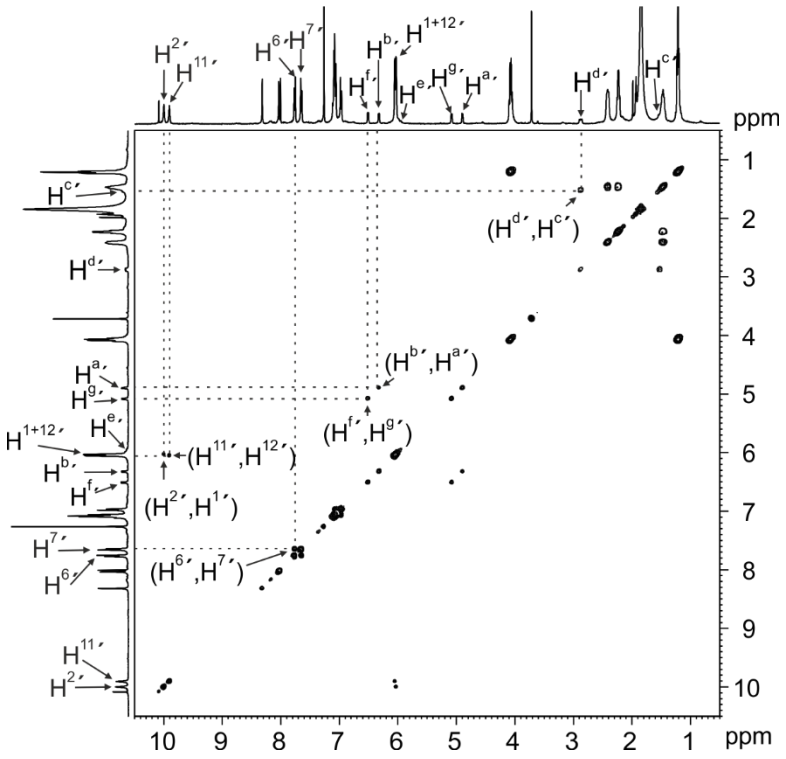

Figure 48. 2D ^{1}H COSY NMR (500 MHz, at 298 K, $CDCl_3$:CD_3CN 9:1) of **9a⊂1.**

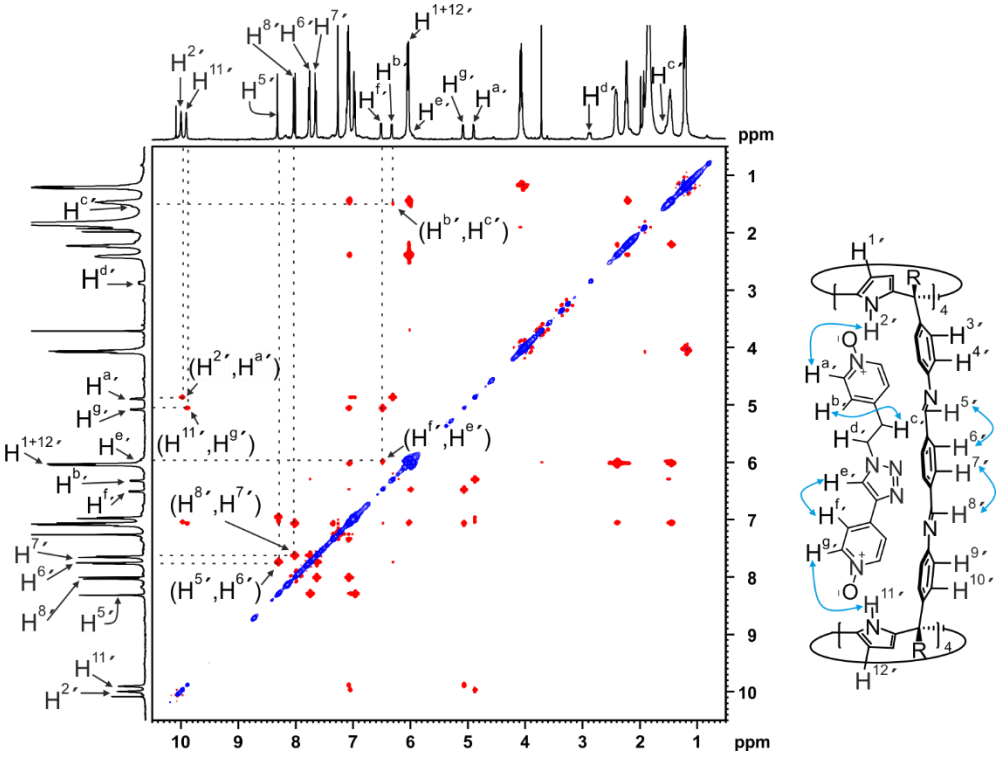

Figure 49. 2D ^{1}H ROESY NMR (500 MHz, at 298 K, $CDCl_3$:CD_3CN 9:1, d8 (mixing time) = 0.3 s) of **9a⊂1.**

5.4.3.6. Binding studies of **10a** with octa-imine cage **1**.

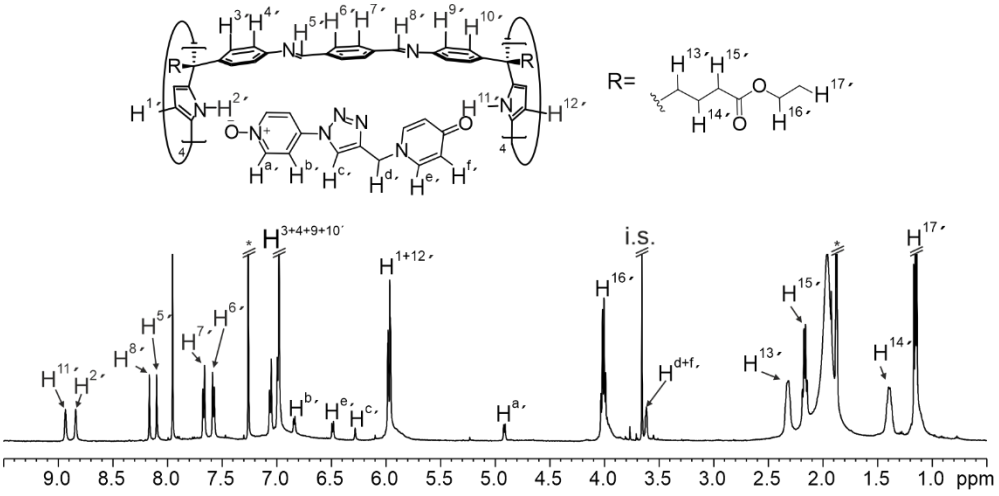

Figure 50. ^{1}H NMR (400 MHz, at 298 K, $CDCl_3$: CD_3CN 9:1) spectra of a 2 mM solution of of **10a⊂1** prepared by solid liquid extration.

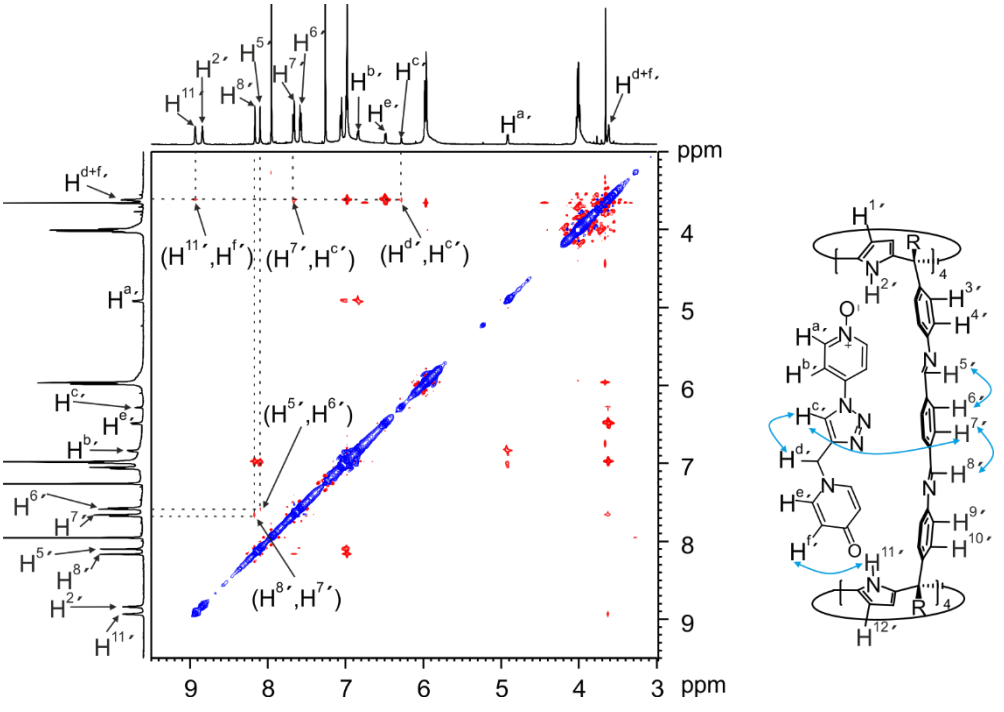

Figure 51. 2D ^{1}H ROESY NMR (500 MHz, at 298 K, $CDCl_3$:CD_3CN 9:1, d8 (mixing time) = 0.3 s) of **10a⊂1.**

5.4.3.7. Binding studies of **4** and**5** with octa-imine cage **1**.

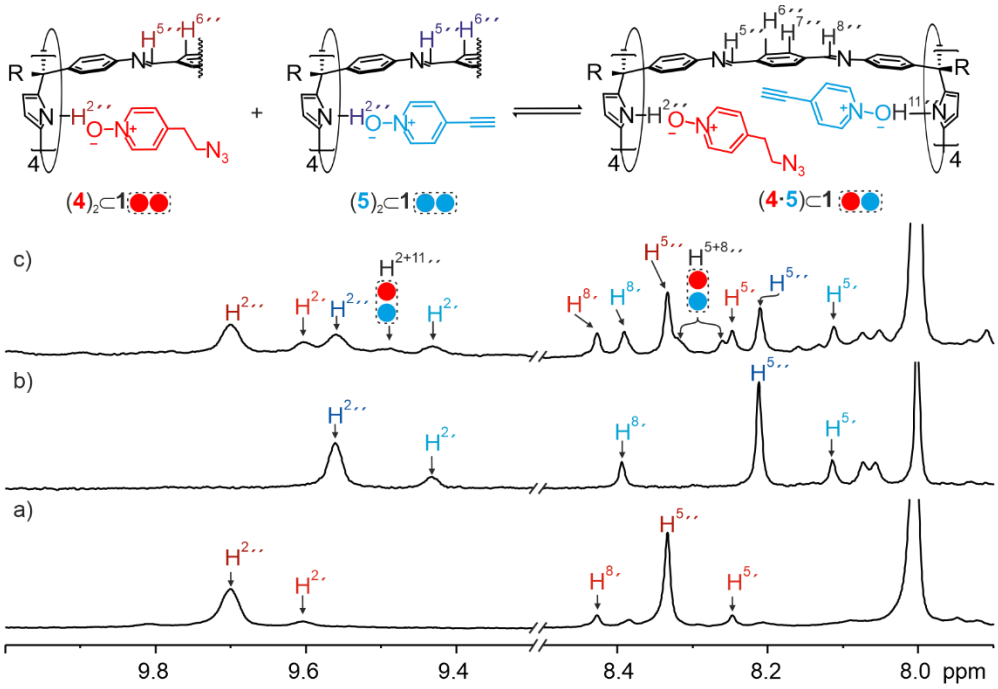

Figure 52. (Top) Thermodynamic equilibrium constants between different inclusion complexes containing guests**4** and **5**. (Bottom) Selected regions of ^{1}H NMR (400 MHz, at 298K, $CDCl_3$:CD_3CN 9:1) spectra of a) 1:2 mixture of cage **1** and **4**; b) 1:2 mixture of cage **1** and **5**; c) 1:1:1 mixture of cage **1**,**4** and**5** registered immediately after mixing.

5.4.3.8. Binding studies of2 and 6 with octa-imine cage 1.

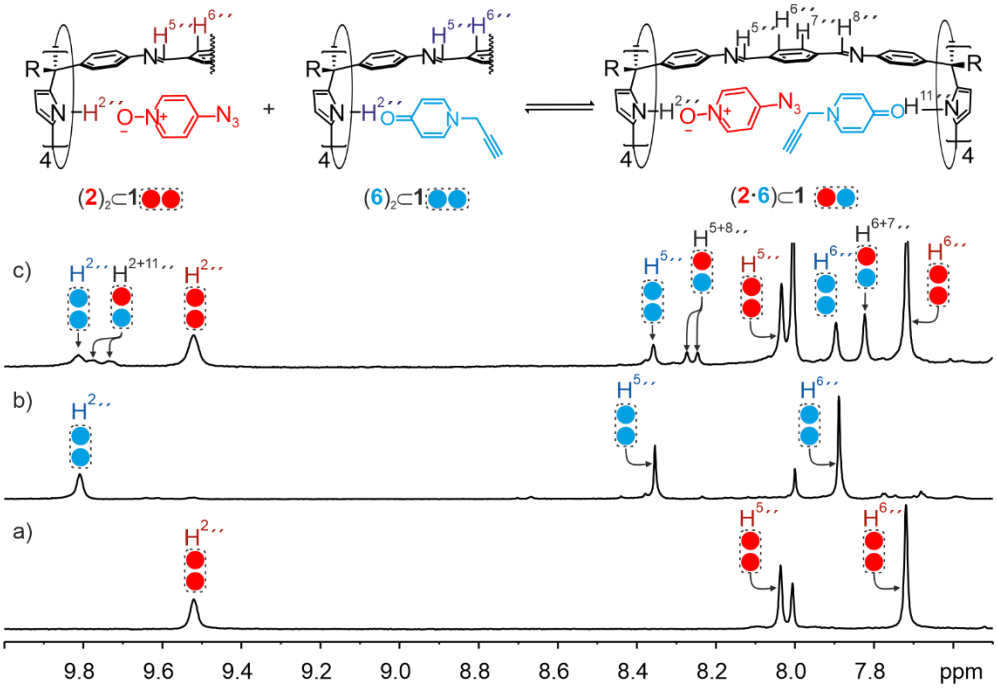

Figure 53. (Top) Thermodynamic equilibrium constants between different inclusion complexes containing guests **2** and **6**. (Bottom) Selected regions of ^{1}H NMR (400 MHz, at 298K, $CDCl_3$:CD_3CN 9:1) spectra of a) 1:2 mixture of cage **1** and ; b) 1:2 mixture of cage **1** and **6**; c) 1:1:1 mixture of cage **1**, **2** and **6** registered immediately after mixing.

5.4.4. Kinetic characterization of cycloaddition reaction in cage **1**.

5.4.4.1. Kinetic study of 1:3:5 mixture with different ratios.

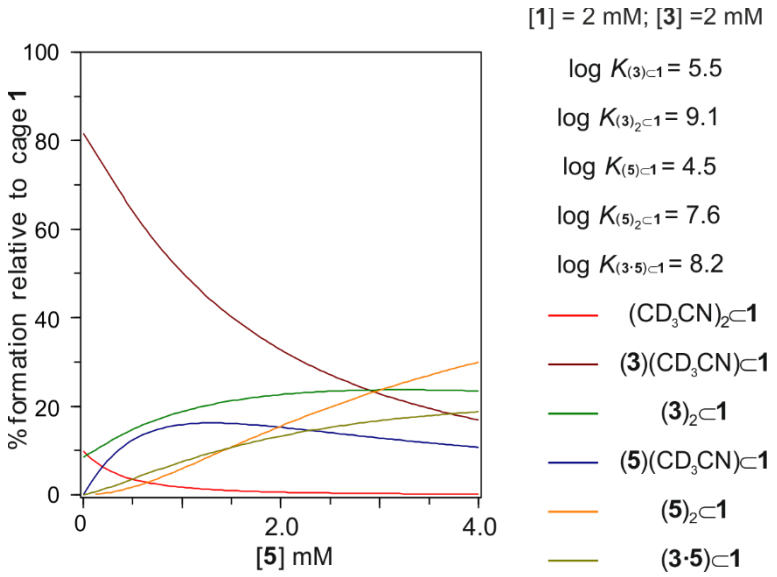

Figure 54. Simulated speciation profile derived from the titration of a solution containing **1** and **3** at 2 mM concentration with incremental amounts of **5** until reaching a 2 mM concentration. The last point considers the overall concentrations of the three components (**1**, **3** and **5**) used in the solution mixture analyzed by ^{1}H NMR spectroscopy. The association constant values for all the species except the ternary complex, **(3·5)⊂1**, were derived in previous experiments (NMR speciation profiles and ITC experiments).

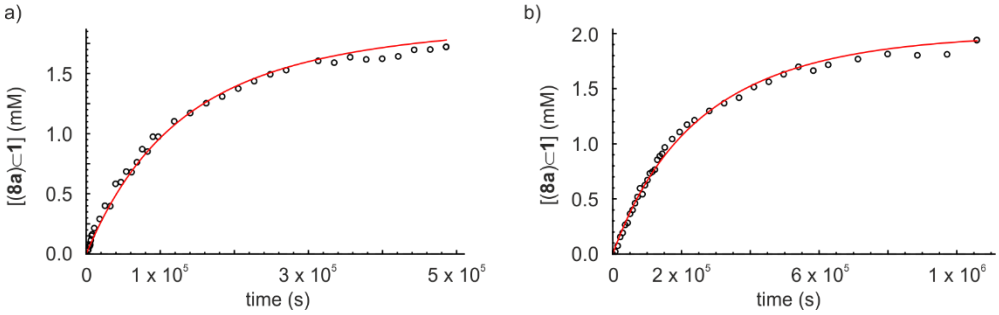

Figure 55. Kinetic profiles of the concentration of complex **8a⊂1** (mM) vs time (s) for the 1,3-dipolar cycloaddition reaction mediate in cage **1**: a) addition of 1 equiv. of **3** and **5**, respectively, b) addition of 5 equiv. of **3** and **5**, respectively, to a 2 mM solution of octa-imine cage **1**. Solid line represents the fit of the kinetic data to the elaborated model depicted in **Figure 21**

5.4.4.2. Kinetic study of 1:4:5 1:1:1 mixture

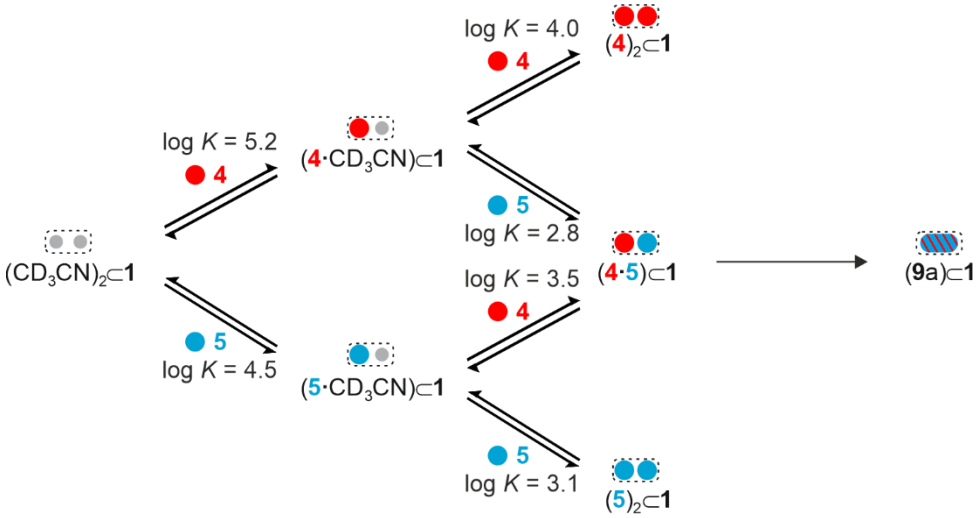

Figure 56. The theoretical model used for the mathematical analysis of the kinetic data of the cycloaddition reaction between **4** and **5** included in the octa-imine cage **1**. The model considers all binding equilibria forming the 1:1 and 2:1 homo and hetero complexes and the irreversible formation of the included cycloaddition product**, 9a⊂1** complex**.** The binding constants were determined with separate titration experiments (vide supra).

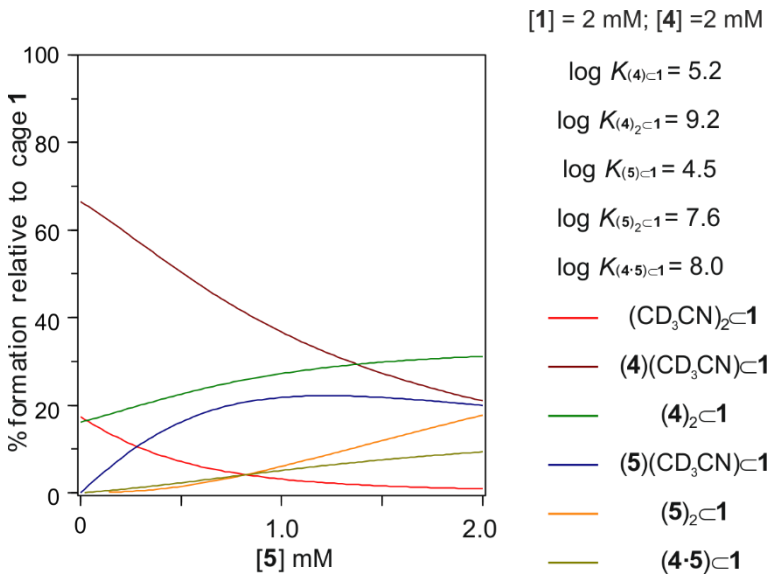

Figure 57. Simulated speciation profile derived from the titration of a solution containing **1** and **4** at 2 mM concentration with incremental amounts of **5** until reaching a 2 mM concentration. The last point considers the overall concentrations of the three components (**1**, **4** and **5**) used in the solution mixture analyzed by ^{1}H NMR spectroscopy. The association constant values for all the species except the ternary complex, **(3·5)⊂1**, were derived in previous experiments (NMR speciation profiles and ITC experiments).

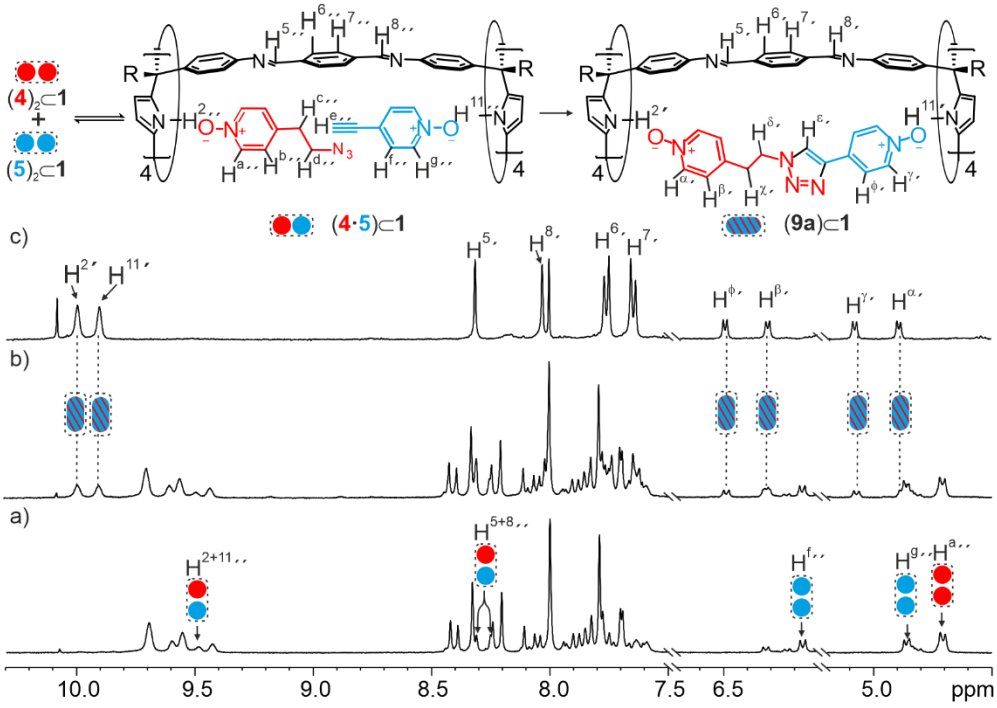

Figure 58. (Top) Left) Disproportionation equilibrium of homo- inclusion complexes (**4**)$_2$⊂**1** and (**5**)$_2$⊂**1** to yield the ternary complex (**4**·**5**)⊂**1**. Right) The 1,3-dipolar cycloaddition reaction between **4** and **5** included in the octa-imine cage **1** yielded the complex **9a**⊂**1**. (Bottom) Selected regions of the ^{1}H NMR (300 MHz, at 298 K, $CDCl_3$: CD_3CN 9:1) spectra corresponding to the monitoring of the formation of complex **9a**⊂**1** starting from a 1:1:1 molar mixture of compounds **1, 3,** and **5**, respectively, after a) 0 h, b) 36 h. Primed letters indicate the proton signals in the 1:1 complexes, double-primed letters are used for the 2:1 homo- and hetero-complexes.

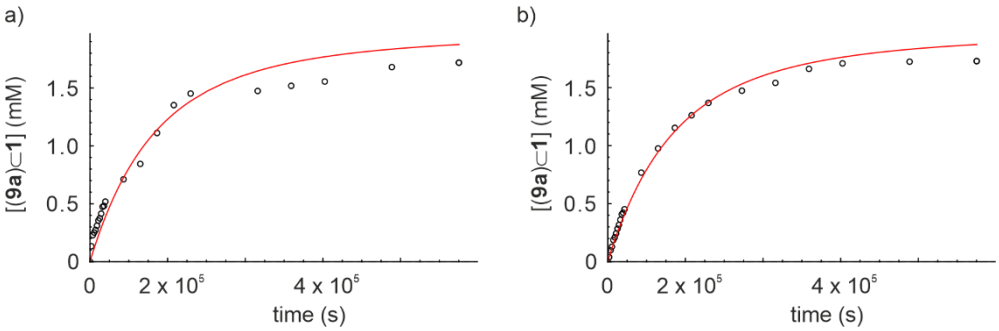

Figure 59. Kinetic profiles of the concentration of complex **9a⊂1** (mM) vs time (s) for the 1,3-dipolar cycloaddition reaction mediate in cage **1.** Two parallel experiments (a) and (b) were conducted by adding 1 equiv. of **4** and **5** to a 2 mM solution of octa-imine cage **1**. The solid line represents the model fit to the kinetic data, as depicted in **Figure 56**.

5.4.4.3. Kinetic study of 1:2:6 1:1:1 mixture

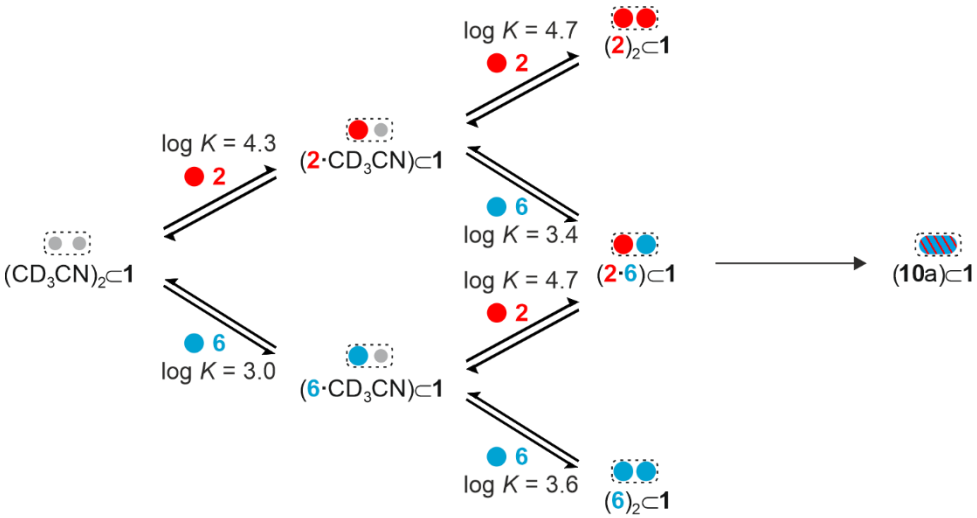

Figure 60. The theoretical model used for the mathematical analysis of the kinetic data of the cycloaddition reaction between **2** and **6** included in the octa-imine cage **1**. The model takes into account all binding equilibria forming the 1:1 and 2:1 homo and hetero complexes and the irreversible formation of the included cycloaddition product**, 10a⊂1** complex**.** The binding constants were determined with separate titration experiments (vide supra).

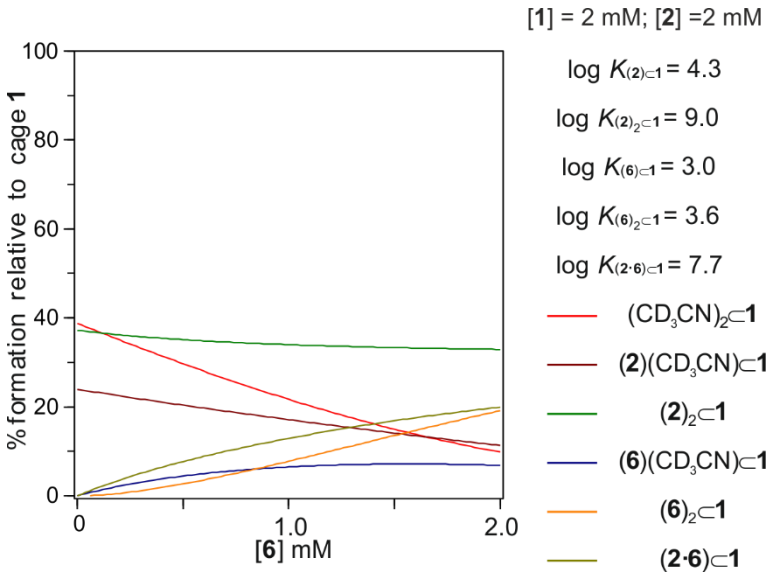

Figure 61. Simulated speciation profile derived from the titration of a solution containing **1** and **2** at 2 mM concentration with incremental amounts of **6** until reaching a 2 mM concentration. The last point considers the overall concentrations of the three components (**1**, **2** and **6**) used in the solution mixture analyzed by ^{1}H NMR spectroscopy. The association constant values for all the species except the ternary complex, **(2·6)⊂1**, were derived in previous experiments (NMR speciation profiles and ITC experiments).

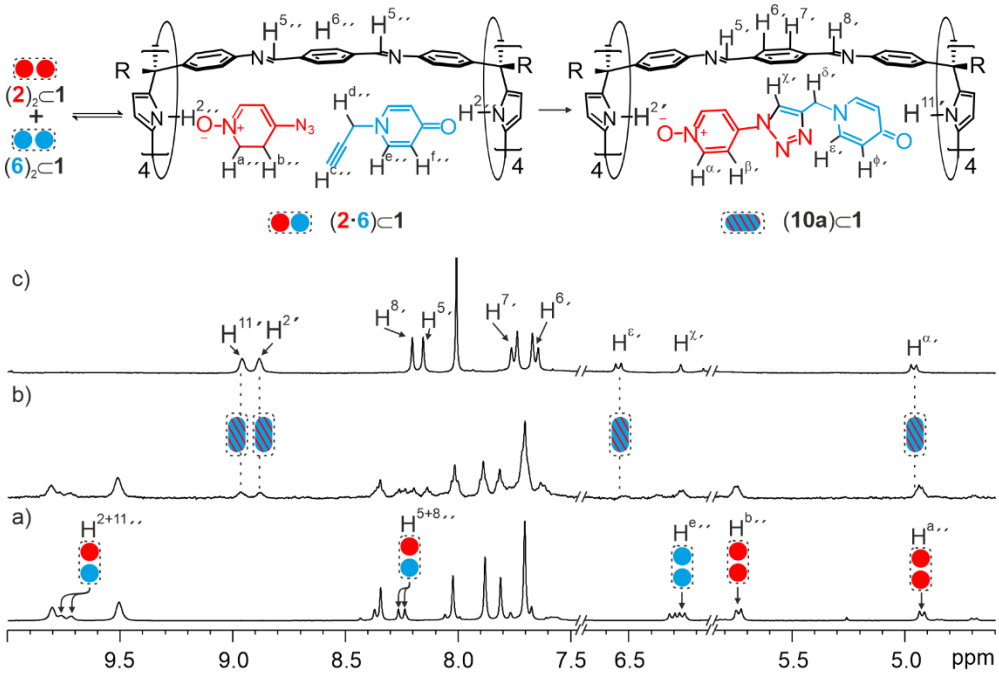

Figure 62. (Top) Left) Disproportionation equilibrium of homo- inclusion complexes (**2**)$_2$⊂**1** and (**6**)$_2$⊂**1** to yield the ternary complex (**2**·**6**)⊂**1**. Right) The 1,3-dipolar cycloaddition reaction between **2** and **6** included in the octa-imine cage **1** yielded the complex **10a**⊂**1**. (Bottom) Selected regions of the ^{1}H NMR (300 MHz, at 298 K, $CDCl_3$: CD_3CN 9:1) spectra corresponding to the monitoring of the formation of complex **10a**⊂**1** starting from a 1:1:1 molar mixture of compounds **1, 2,** and **6**, respectively, after a) 0 h, b) 72 h. Primed letters indicate the proton signals in the 1:1 complexes, double-primed letters are used for the 2:1 homo- and hetero-complexes.

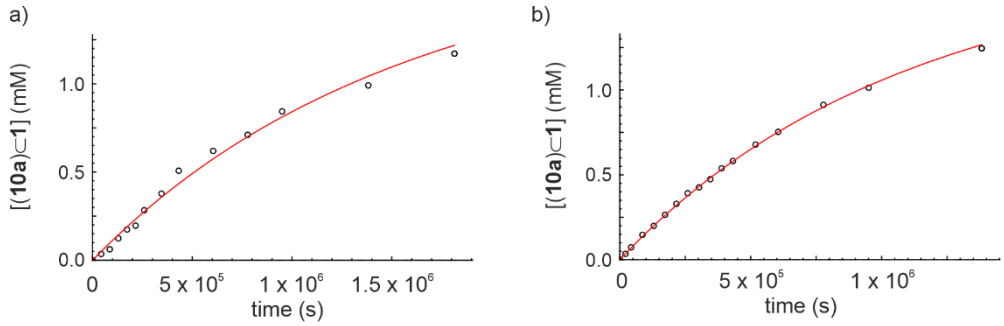

Figure 63. Kinetic profiles of the concentration of complex **10a⊂1** (mM) vs time (s) for the 1,3-dipolar cycloaddition reaction mediate in cage **1.** Two parallel experiments (a) and (b) were conducted by adding 1 equiv. of **2** and **6** to a 2 mM solution of octa-imine cage **1**. The solid line represents the model fit to the kinetic data, as depicted in **Figure 60**.

5.4.5. UV-vis study of monotopic and ditopic guests

In order to monitor the Huisgen cycloaddition reaction in bulk by HPLC, the UV-vis absorption of reactants (**2**-**6**) and 1.4-product isomers (**7a**-**10a**) were first measured in chloroform acetonitrile 9:1 mixture.

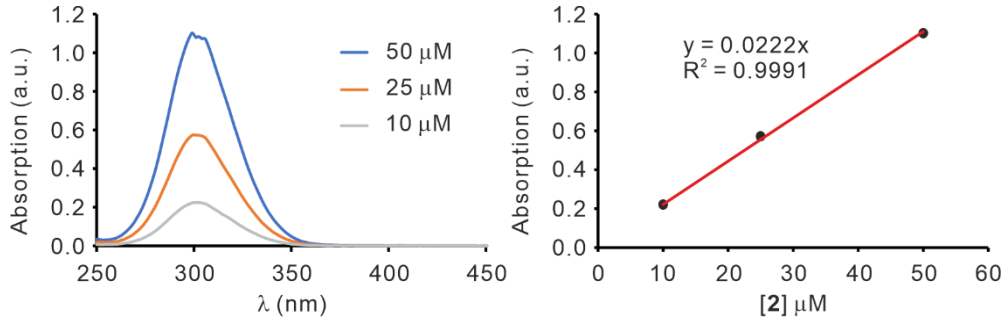

Figure 64. Left- UV-vis absorption spectrum of **2** with varied concentrations (λ_{max} =299 nm). Right- Plot of the absorption change at 299 nm vs concentration of **2**. The slope of red line corresponds to the extinction coefficient in λ_{max} (ε = 21700 $M^{-1}\cdot cm^{-1}$).

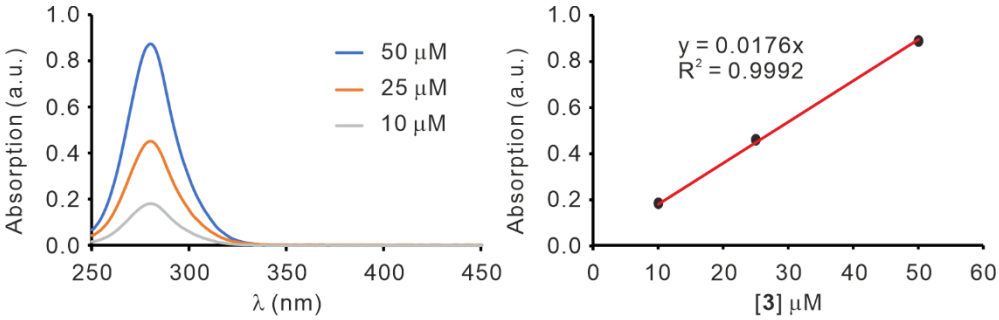

Figure 65. Left- UV-vis absorption spectrum of **3** with varied concentrations (λ_{max} =280 nm) Right - Plot of the absorption change at 280 nm vs concentration of **3**. The slope of red line corresponds to the extinction coefficient in λ_{max} (ε = 17600 $M^{-1}\cdot cm^{-1}$).

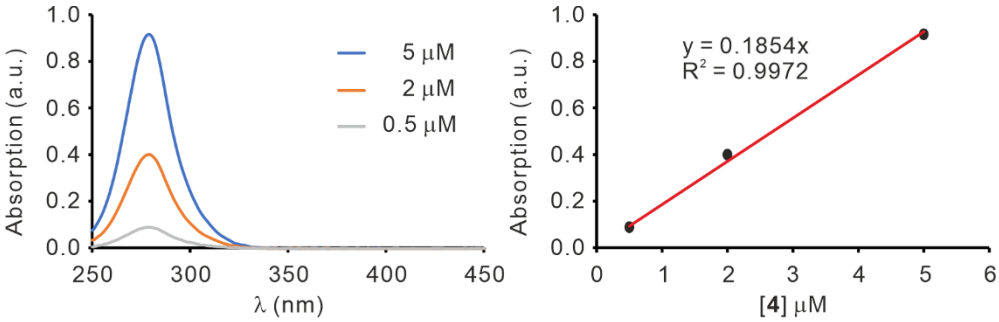

Figure 66. Left- UV-vis absorption spectrum of **4** with varied concentrations (λ_{max} =279 nm). Right- Plot of the absorption change at 279 nm vs concentration of **4**. The slope of red line corresponds to the extinction coefficient in λ_{max} (ε = 200000 $M^{-1}\cdot cm^{-1}$).

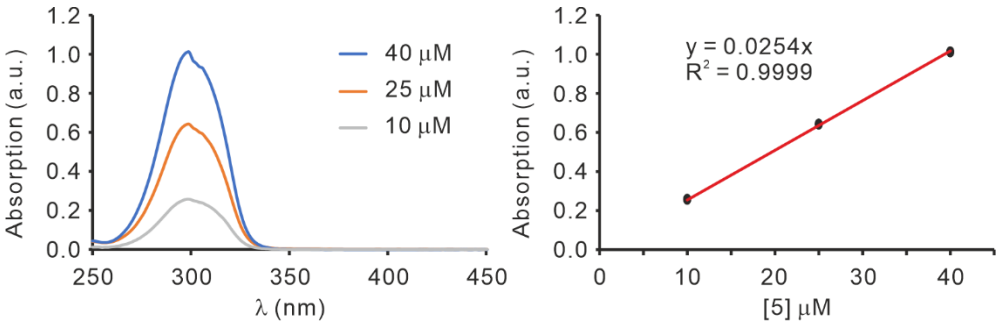

Figure 67. Left- UV-vis absorption spectrum of **5** with varied concentrations (λ_{max} =299 nm). Right- Plot of the absorption change at 299 nm vs concentration of **5**. The slope of red line corresponds to the extinction coefficient in λ_{max} (ε = 25400 $M^{-1}\cdot cm^{-1}$).

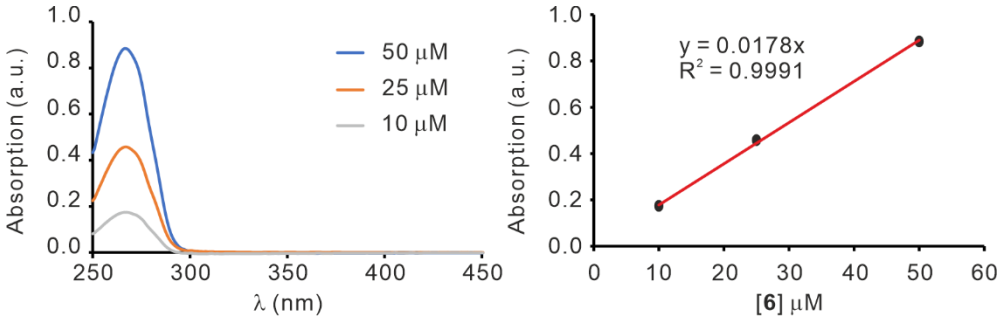

Figure 68. Left- UV-vis absorption spectrum of **6** with varied concentrations (λ_{max} =267 nm). Right- Plot of the absorption change at 267 nm vs concentration of **6**. The slope of red line corresponds to the extinction coefficient in λ_{max} (ε = 17800 $M^{-1}\cdot cm^{-1}$).

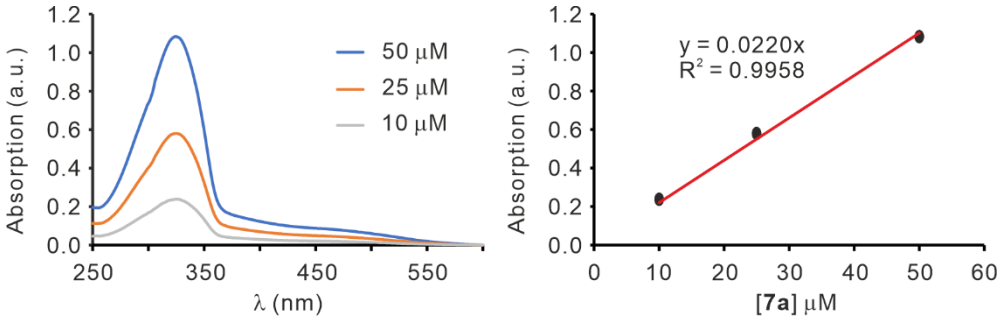

Figure 69. Left- UV-vis absorption spectrum of **7a** with varied concentrations (λ_{max} =325 nm). Right- Plot of the absorption change at 325 nm vs concentration of **7a**. The slope of red line corresponds to the extinction coefficient in λ_{max} (ε = 22000 $M^{-1}\cdot cm^{-1}$).

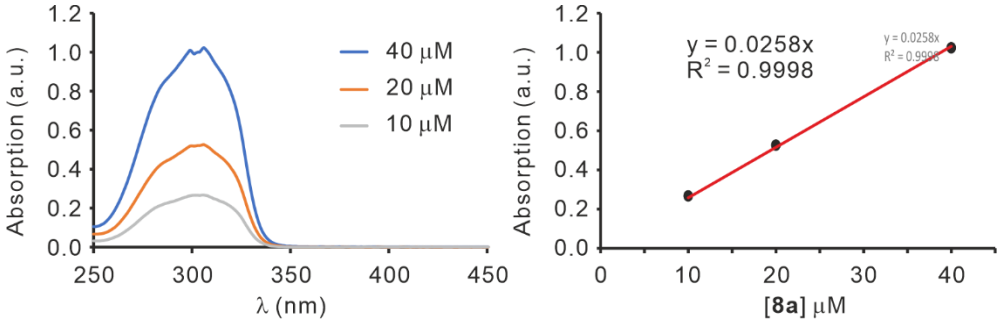

Figure 70. Left- UV-vis absorption spectrum of **8a** with varied concentrations (λ_{max} =306 nm). Right- Plot of the absorption change at 306 nm vs concentration of **8a**. The slope of red line corresponds to the extinction coefficient in λ_{max} (ε = 25800 $M^{-1}\cdot cm^{-1}$).

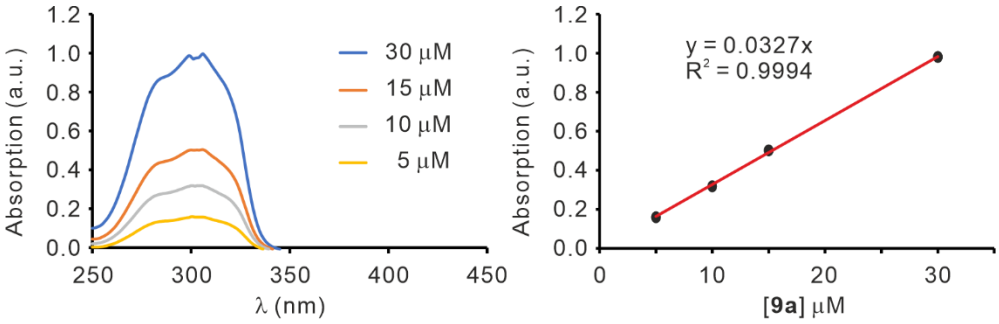

Figure 71. Left- UV-vis absorption spectrum of **9a** with varied concentrations (λ_{max} =300 nm). Right- Plot of the absorption change at 300 nm vs concentration of **9a**. The slope of red line corresponds to the extinction coefficient in λ_{max} (ε = 32700 $M^{-1}\cdot cm^{-1}$).

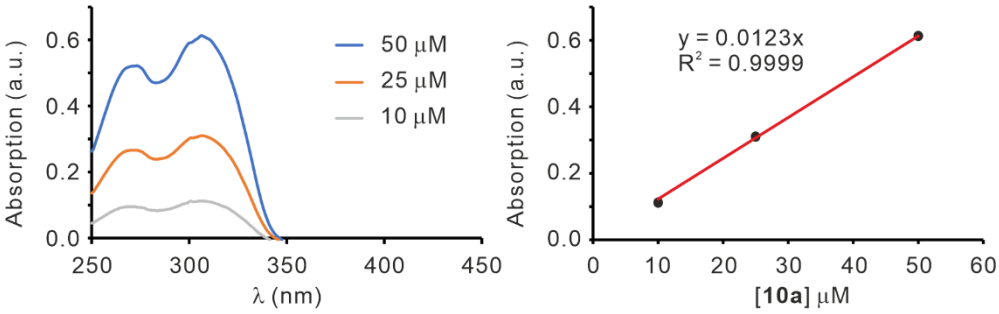

Figure 72. Left- UV-vis absorption spectrum of **10a** with varied concentrations (λ_{max} =306 nm). Right- Plot of the absorption change at 306 nm vs concentration of **10a**. The slope of the red line corresponds to the extinction coefficient in λ_{max} (ε = 12200 $M^{-1}\cdot cm^{-1}$).

5.4.6. Kinetic characterization of the cycloaddition reaction in bulk

We carried out the cycloaddition reactions in the bulk in chloroform: acetonitrile 9:1 solvent mixture. All reactants and products showed a very large extinction coefficient in maximum absorption wavelength (ε = 16600-32700 L/mol·cm). We used 4-methylpyridine *N*-oxide as the internal standard (i.s.) which has a distinct retention time compared to either reactants or products (**Table 2**). Products **7a**-**10a** have good absorption in 300 nm, in which wavelength the i.s. shows reduced absorption. To have comparable intensity of peaks for both product and i.s. in the HPLC chromatogram, 1 mM concentration of i.s. and four different concentrations of **7a-10a** (0.1, 0.05, 0.02, 0.01 mM) were used for the calibration curve ($A_{product}/A_{i.s.}$).

Table 2. The retention times and UV-Vis absorption propterities of guests.

Entry	retention time (min)	λ_{max} (nm)	ε (L/mol·cm)
2	7.4	299	21700
3	6.4	280	17600
4	6.8	279	200000
5	5.3	299	25400
6	7.3	267	17800
i.s.	8.2	277	16600
7a	11.3	325	22000
8a	12.3	306	25800
9a	13.1	300	32700
10a	12.7	306	12200

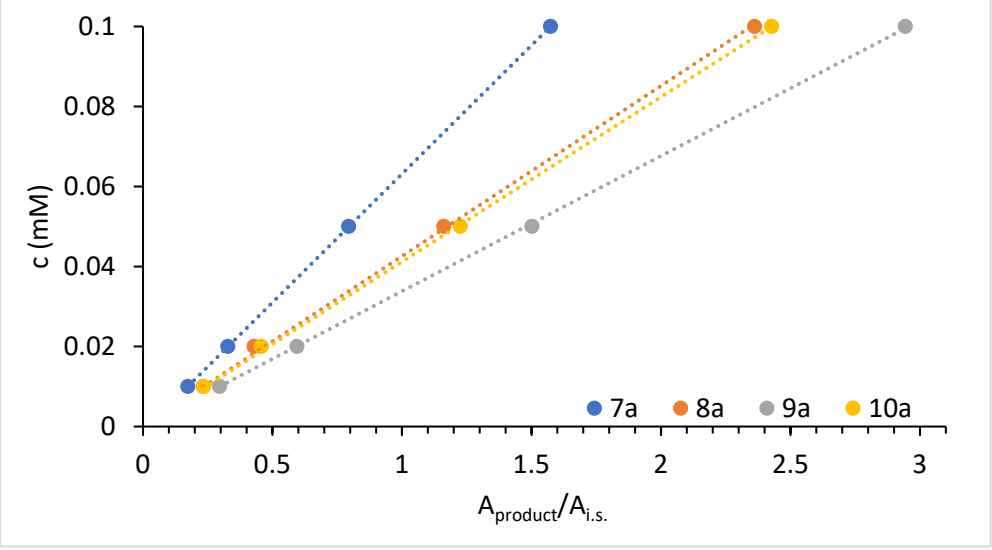

Figure 73. Calibration curves of 1,4-cycloaddition products **7a-10a** using 4-methyl pyridine *N*-oxide as i.s. (1 mM) and considering ($A_{product}/A_{i.s.}$) ratio at 300 nm.

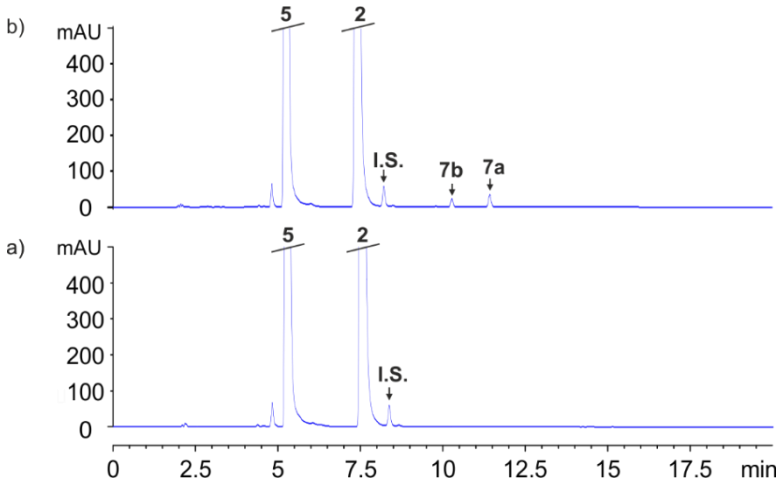

Figure 74. HPLC trace of the reaction crude between **2** and **5** ($CDCl_3$:CD_3CN 9:1, 25 mM for each and r.t.) a) 0h and b) 361 h. The presence of both isomers **7a** and **7b** were observed. 1 mM 4-metylypyridine *N*-oxide was used as internal standard.

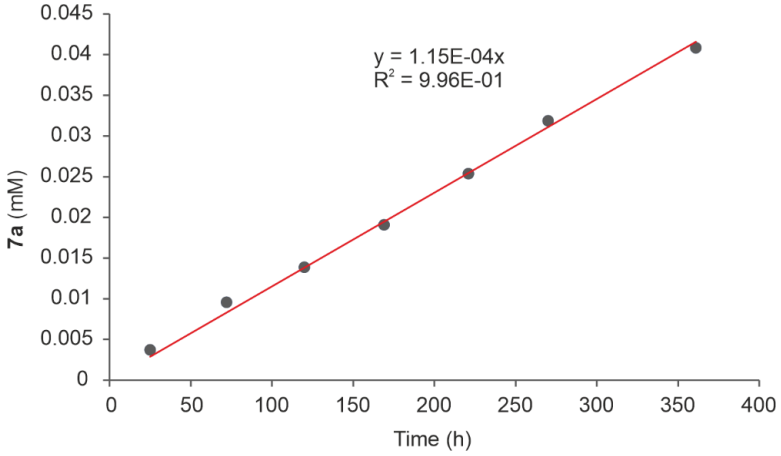

Figure 75. Linear fit of the determined concentration of **7a** at different times used to determine the initial reaction rate in bulk.

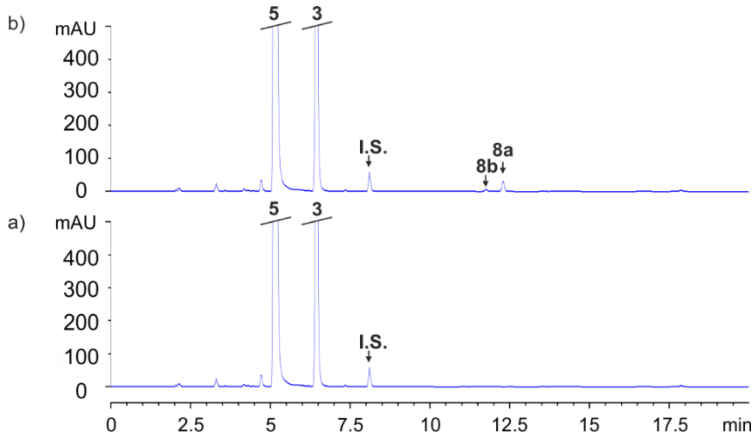

Figure 76. HPLC trace of the reaction crude between **3** and **5** ($CDCl_3$:CD_3CN 9:1, 25 mM for each and r.t.) a) 0h and b) 361 h. The presence of both isomers **8a** and **8b** were observed. 1 mM 4-metylypyridine *N*-oxide was used as internal standard.

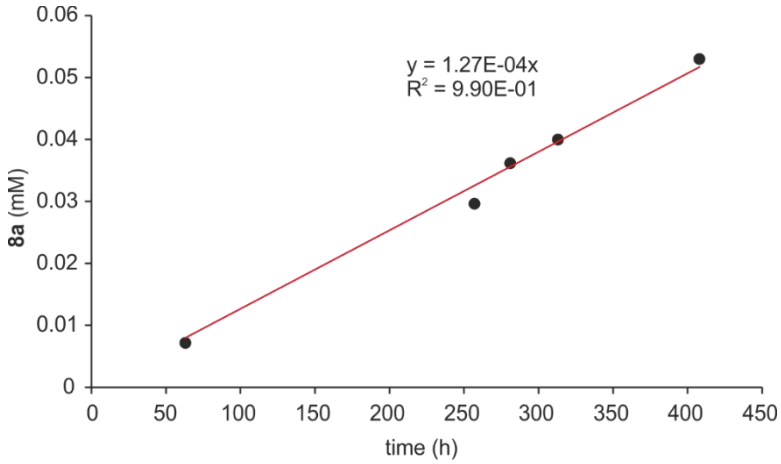

Figure 77. Linear fit of the determined concentration of **8a** at different times used to determine the initial reaction rate in bulk.

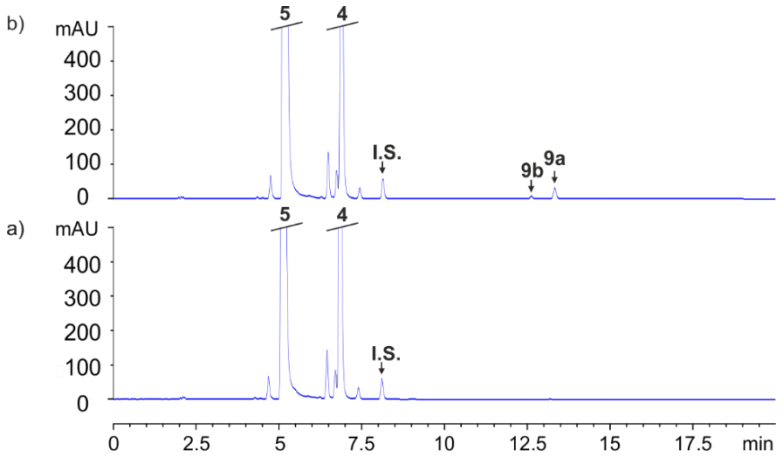

Figure 78. HPLC trace of the reaction crude between **4** and **5** ($CDCl_3$:CD_3CN 9:1, 25 mM for each and r.t.) a) 0h and b) 361 h. The presence of both isomers **9a** and **9b** were observed. 1 mM 4-metylypyridine *N*-oxide was used as internal standard.

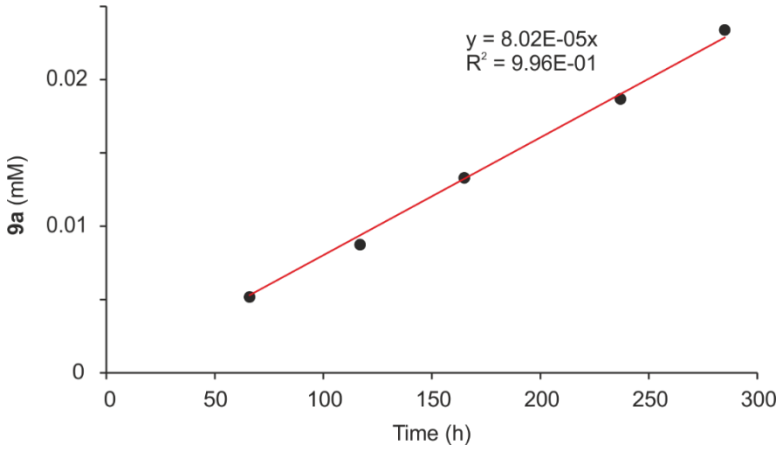

Figure 79. Linear fit of the determined concentration of **9a** at different times used to determine the initial reaction rate in bulk.

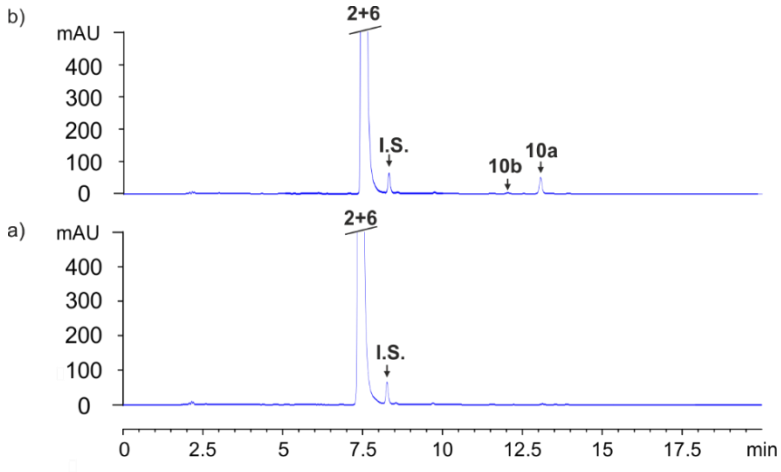

Figure 80. HPLC trace of the reaction crude between **2** and **6** ($CDCl_3$:CD_3CN 9:1, 25 mM for each and r.t.) a) 0h and b) 361 h. The presence of both isomers **10a** and **10b** were observed. 1 mM 4-metylypyridine *N*-oxide was used as internal standard.

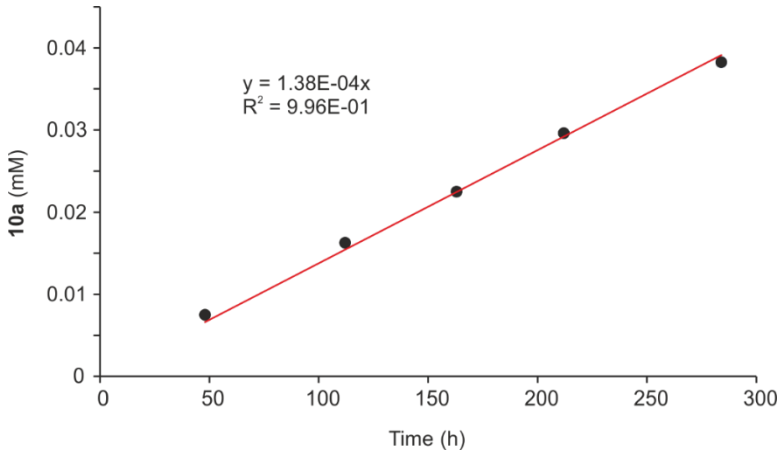

Figure 81. Linear fit of the determined concentration of **10a** at different times used to determine the initial reaction rate in bulk.

Table 3. The initial reaction rates and rate constants of cycloaddition reactions in the bulk.

Entry	$v_{(0)bulk}$ ($M \cdot s^{-1}$)	k_{bulk} ($M^{-1} \cdot s^{-1}$)
7a	3.14×10^{-11}	5.02×10^{-8}
8a	3.48×10^{-11}	5.58×10^{-8}
9a	2.18×10^{-11}	3.49×10^{-8}
10a	3.83×10^{-11}	6.13×10^{-8}

5.5 References and notes

[1] Richard, J. P., *Biochemistry* **2013,** *52* (12), 2009-2011.
[2] Pauling, L., *Nature* **1948,** *161* (4097), 707-709.
[3] Wang, R.; Yu, Y., *Beilstein J. Org. Chem.* **2022,** *18*, 309-324.
[4] Yu, Y.; Yang, J.-M.; Rebek, J., *Chem* **2020,** *6* (6), 1265-1274.
[5] Liu, W.; Stoddart, J. F., *Chem* **2021,** *7* (4), 919-947.
[6] Jencks, W. P., Binding Energy, Specificity, and Enzymic Catalysis: The Circe Effect. In *Advances in Enzymology and Related Areas of Molecular Biology*, 1975; pp 219-410.
[7] Huisgen, R., *Proceedings of the Chemical Society* **1961,** (October), 357-396.
[8] Huisgen, R., *Angew. Chem., Int. Ed.* **1963,** *2* (11), 633-645.
[9] Hein, J. E.; Fokin, V. V., *Chem. Soc. Rev.* **2010,** *39* (4), 1302-1315.
[10] Johansson, J. R.; Beke-Somfai, T.; Said Stålsmeden, A.; Kann, N., *Chem. Rev.* **2016,** *116* (23), 14726-14768.
[11] Mock, W. L.; Irra, T. A.; Wepsiec, J. P.; Manimaran, T. L., *J. Org. Chem.* **1983,** *48* (20), 3619-3620.
[12] Mock, W. L.; Irra, T. A.; Wepsiec, J. P.; Adhya, M., *J. Org. Chem.* **1989,** *54* (22), 5302-5308.
[13] Carlqvist, P.; Maseras, F., *Chem. Commun.* **2007,** (7), 748-750.
[14] Cacciapaglia, R.; Di Stefano, S.; Mandolini, L., *Acc. Chem. Res.* **2004,** *37* (2), 113-122.
[15] Chen, J.; Rebek, J., *Org. Lett.* **2002,** *4* (3), 327-329.
[16] Daver, H.; Harvey, J. N.; Rebek, J., Jr.; Himo, F., *J. Am. Chem. Soc.* **2017,** *139* (43), 15494-15503.
[17] Goehry, C.; Besora, M.; Maseras, F., *Eur. J. Org. Chem.* **2018,** *2018* (18), 2103-2109.
[18]Hema, K.; Sureshan, K. M., *Acc. Chem. Res.* **2019,** *52* (11), 3149-3163.
[19] Compound **7a** has low solubility in $CDCl_3$:CD_3CN 9:1 solvent mixture.
[20] NMR spectroscopy was not useful to calculate initial rates under these conditions.
[21] Another peak at 12.5 min was detected and attributed to the 1,5-isomer.
[22] $t_{1/2}= 1/(k[\mathbf{5}]_0)$
[23] Hoops, S.; Sahle, S.; Gauges, R.; Lee, C.; Pahle, J.; Simus, N.; Singhal, M.; Xu, L.; Mendes, P.; Kummer, U., *Bioinformatics* **2006,** *22* (24), 3067-3074.
[24] Adriaenssens, L.; Acero Sánchez, J. L.; Barril, X.; O'Sullivan, C. K.; Ballester, P., *Chem. Sci.* **2014,** *5* (11), 4210-4215.
[25] Yang, Q.-Y.; Lehn, J.-M., *Angew. Chem., Int. Ed.* **2014,** *53* (18), 4572-4577.

Chapter 6

Self-assembly of a tetra-imine cage and its application as a molecular container for Huisgen cycloaddition reactions

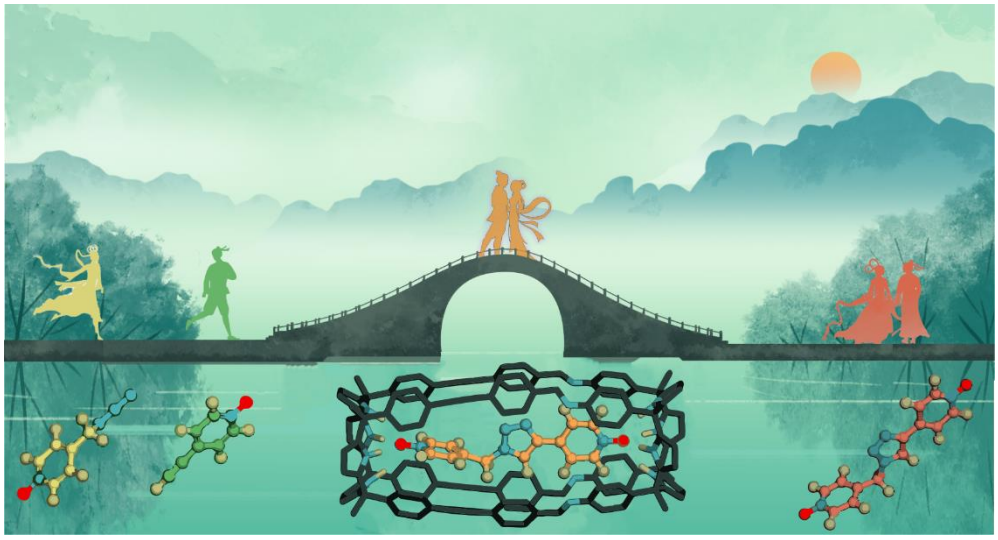

Unpublished results

UNIVERSITAT ROVIRA I VIRGILI
Receptors based on Aryl-extended Calix[4]pyrrole Scaffolds
Yifan Li

Self-assembly of a tetra-imine cage and its application as a molecular container for Huisgen cycloaddition reactions

6.1 Introduction

Including chemical reactions in molecular containers aims to mimic and gain insight into the function of enzymes.[1] For bimolecular reactions included in molecular containers, the increase in rate acceleration is not derived from a significant modification of the reaction mechanism occurring in the bulk. The primary sources of the rate acceleration experienced by the reaction occurring in the container's cavity derive from the isolation of the substrates from the bulk (desolvation), their increase in local concentrations owing to inclusion in the container's cavity, and the entropy gain caused by the conversion of an intermolecular reaction into an intramolecular counterpart.[2] Additional factors, like the packing coefficient of the inclusion complex,[34] the shape complementarity between the guests and the cavity,[5] the orientation of the reacting groups, and the electrostatic potential offered by the cavity surface,[6] can also influence the acceleration factor of the reactions occurring in the container's cavity.

Recently, Nau and co-workers studied the acceleration of the dimerization of cyclopentadiene (CPD) by inclusion in different cucurbit[*n*]uril (*n* = 5-8) receptors (**Figure 1**). Some reactions showed turnover, rendering the molecular containers sub-stoichiometric catalysts. The authors suggested that the packing coefficient values of the Michaelis (ternary) complexes played a significant role in the acceleration factor experienced by the reaction occurring in the container's cavity.[7] This putative contribution to reaction acceleration was supposed to derive from the known negative activation volume for Diels-Alder reactions.[8] However, cucurbit[*n*]uril are not ideal molecular containers for studying the contribution of the packing coefficient in the acceleration of the included chemical reactions. Cucurbit[*n*]uril receptors show significant differences in cavity size (more than 70 $Å^3$). Accurate values for their internal volumes are difficult to measure because of the two opposed wide-open portals exhibited by their scaffolds. In addition, the study of the acceleration effect caused by a suitable orientation of two reacting groups, diene, and dienophile, in the Michaelis complex was not investigated due to the symmetry of the dimerization reaction of CPD.

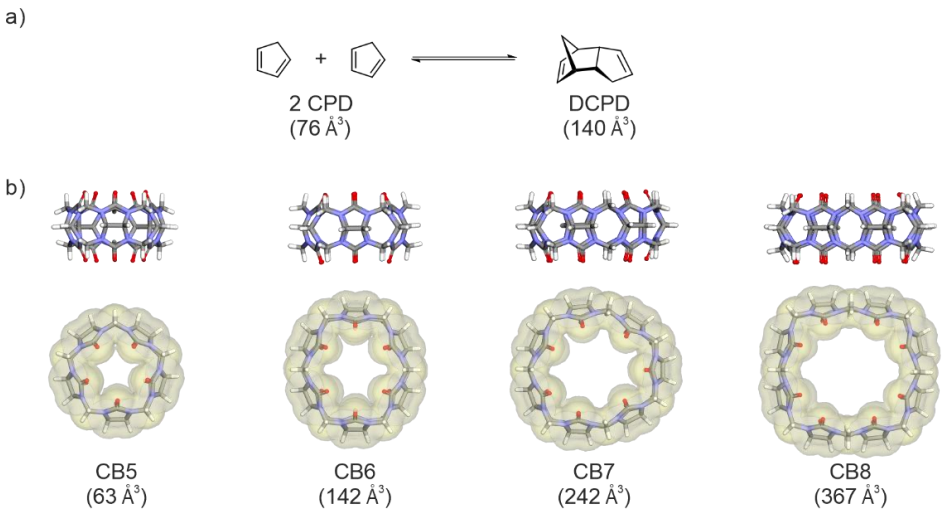

Figure 1. a) Reaction scheme of Diels-Alder reaction of cyclopentadiene (CPD) to endo-dicyclopentadiene (DCPD). b) Side and top views of energy minimized (MM3) structures of Cucurbit[*n*]urils, CB*n*, *n* = 5-8.

In **Chapter 4** we explored how minor variations in the length of guest molecules can significantly influence their molecular recognition. In **Chapter 5**, we investigated the acceleration and regioselectivity of bimolecular Huisgen 1,3-dipolar cycloaddition reactions upon inclusion in a molecular container featuring a polar and shape-persistent cavity. We found that varying the length of one of the two reactants by one or two methylene units—resulting in differences of ca. 1.4 -2.8 Å—markedly impacted the reactions' acceleration in the container's cavity. To further underscore the importance of shape, size, and function complementarity between the included guests/substrates and the container's cavity in mediating reactions in the cavity, in the present chapter, we investigate the self-assembly of a tetra-imine cage based on two different calix[4]pyrrole components. The self-assembled tetra-imine cage featured a cylindrical cavity slightly longer than the octa-imine counterparts described in the previous chapters. In analogy to its predecessors, the polar cavity of the tetra-imine cage can potentially be used as a reaction vessel for the intramolecular Huisgen cycloaddition reaction.

We hypothesized that the relatively longer cavity provided by the tetra-imine cage, compared to that of the octa-imine counterpart reported in previous chapters, would also influence the packing coefficient of the ternary Michaelis complexes. The different aromatic panels of the two cages could also modify the relative orientation of the two included reacting groups. These changes may alter the reaction kinetics of the cycloaddition reaction when included in the dissimilar polar cavities of the two containers.

6.2 Results and discussions

6.2.1 Synthesis

Based on our previous results on the self-assembly of tetra-imine cage **5**[9] and octa-imine cage **6** (**chapter 5**) using acetonitrile as a template, we investigated the self-assembly of the unprecedented tetra-imine cage **1 (Figure 2)**. The construction of the molecular scaffold of **1** was based on the condensation reaction of a tetra-aldehyde SAE-C[4]P **2** with tetra-amino AE-C[4]P **3** (**Scheme 1**).

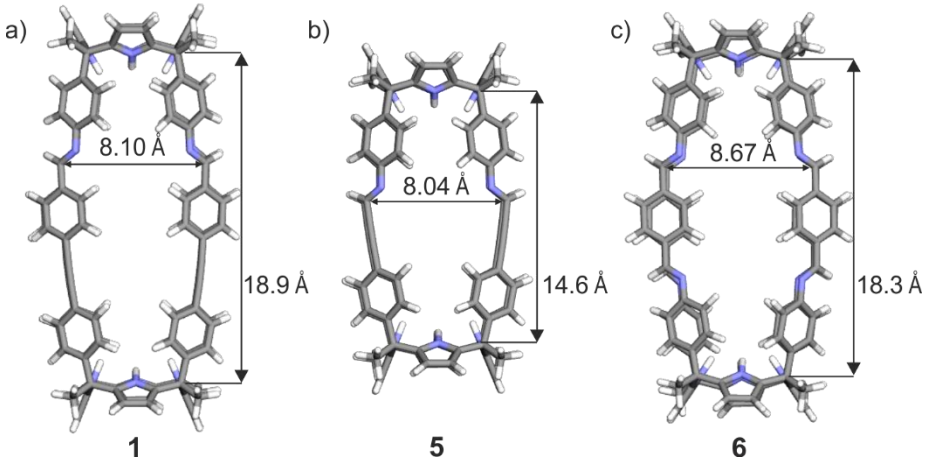

Figure 2. Side views of the MM3 energy-minimized structures of poly-imine cages **1, 5,** and **6**. The length of the three cages' cavity (from meso-carbon to meso-carbon) is indicated. The numbering of the cages is independent in each chapter (i.e. cage **6** in this chapter corresponds to cage **1** in **Chapter 3**).

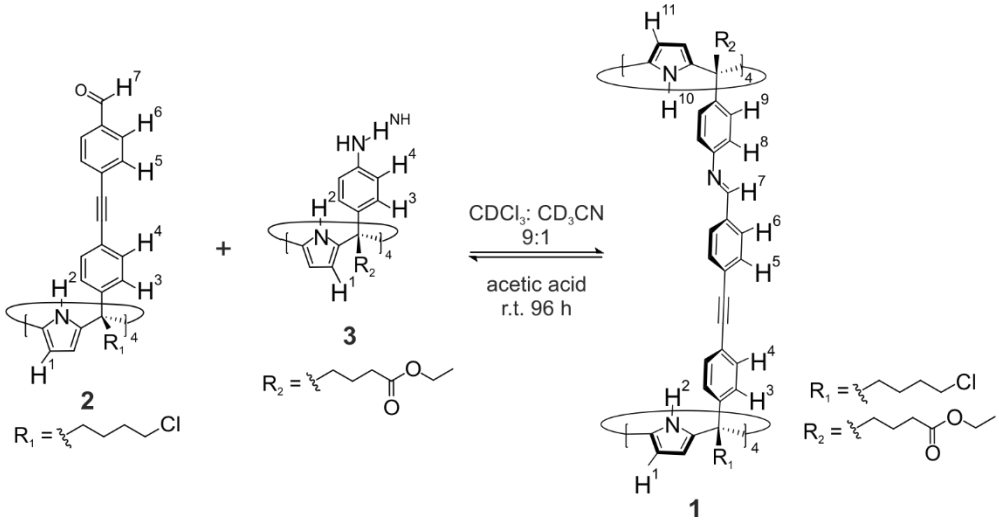

Scheme 1. Synthetic scheme of the self-assembly of tetra-imine cage **1.**

In turn, tetra-aldehyde SAE-C[4]P **2** was synthesized from the corresponding tetra-iodo calix[4]pyrrole **12** precursor (**Scheme 3** in the experimental section). The four-fold Sonogashira coupling reaction of the tetra-iodo calix[4]pyrrole **12** with 4-ethynylbenzaldehyde **13** in a 1:1 mixture of DIPA/THF yielded the tetra-aldehyde SAE calix[4]pyrrole **2** as a yellow powder in 80% yield after column chromatography purification of the reaction crude.

The ^{1}H NMR spectra of tetra-aldehyde SAE-C[4]P **2** in chlorinated solvents (e.g. $CDCl_3$, CD_2Cl_2) at 298 K show broad proton signals in the aromatic region (**Figure 3a**). The addition of 1 equiv. of 4-phenylpyridine *N*-oxide **4** to the above solution of **2** provoked the appearance of sharp signals for all aromatic protons (**Figure 3b**). Broad aromatic signals for **2** were also observed in d_6-acetone and d_3-acetonitrile solutions. In contrast, a d_7-DMF solution of **2** produced a ^{1}H NMR spectrum with well-defined signals for all protons. These observations suggested that tetra-aldehyde SAE-C[4]P **2** experienced aggregation in most of the tested organic solvents.

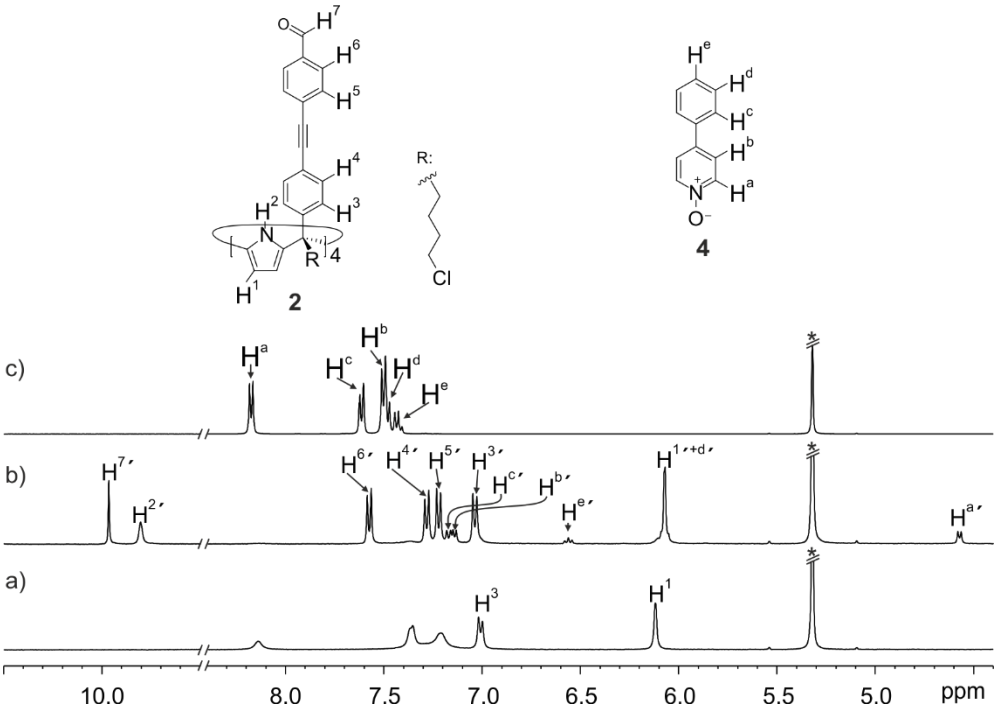

Figure 3. Selected region of the ^{1}H NMR spectra (400 MHz, at 298 K, CD_2Cl_2) acquired during the titration of tetra-aldehyde calix[4]pyrrole [**2**] = 1 mM with incremental amounts of PhPyNO **4**; a) free **2**; b) **2** with 1 equiv. of PhPyNO **4**, c) free PhPyNO **4**. Primed letters indicate the proton signals for the bound host and guest.

A single-crystal of **2** suitable for X-ray diffraction grew from a 1:1 CH_2Cl_2/CH_3CN solution. The solution of the diffracted data revealed the dimerization of the tetra-aldehyde SAE-C[4]P **2** in the solid state (**Figure 4**). The two calix[4]pyrrole units involved in the dimer adopted the cone conformation, including one aromatic panel with the terminal aldehyde group in the aromatic cavity of each other. Most likely, in the chlorinated solvents, acetone, and acetonitrile the tetra-aldehyde SAE-C[4]P **2** is also present as a dimer driven by intermolecular hydrogen bonding and π–π, CH–π interactions. DMF is known to be included in the polar aromatic cavity of AE-C[4]P by forming hydrogen bonding and CH-π interactions.[10] DMF efficiently competes with the dimerization process of **2**, as evidenced by the well-defined ^{1}H NMR spectrum obtained in this solvent.

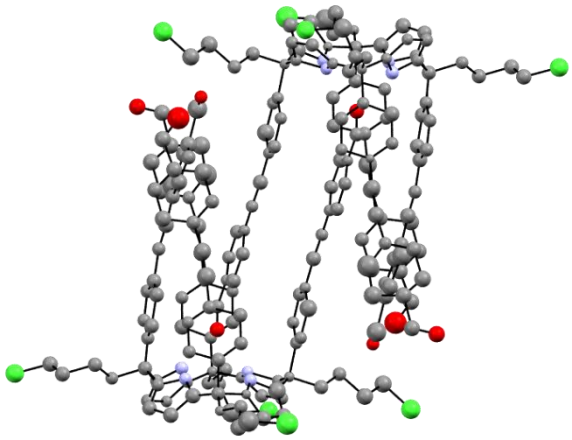

Figure 4. Single crystal structure of the dimer of **2**. The two C[4]Ps adopted the cone conformation. Hydrogen atoms and additional solvent molecules were omitted for clarity.

We monitored the self-assembly of the tetra-imine cage **1** using ^{1}H NMR spectroscopy and 1,3,5-trimethoxybenzene as internal standard (i.s.). The ^{1}H NMR spectrum registered after mixing the equimolar mixture of the two molecular components of **1**, tetra-aldehyde SAE-C[4]P **2** and tetra-amine AE-C[4]P **3** (2mM for each) in a 9:1 CD_3Cl:CD_3CN mixture containing 0.01 mM acetic acid, exclusively showed the expected proton signals for **2** and **3** in solution (**Figure 5a**). This observation indicated that the SAE-C[4]P **2** still exists as a dimer in the presence of tetra-amine **3**. The quantitative self-assembly of the tetra-imine cage **1** required standing the solution for 4 days at room temperature. The ^{1}H NMR spectra of the thermodynamically equilibrated solutions showed sharp and well-defined proton signals, which were diagnostic for the self-assembly of the tetra-imine cage **1 (Figure 5b**). We did not detect residual signals of precursors **2** and **3**. It is worth noting that the quantitative self-assembly of the previously described tetra-imine cage **5** (reference 9, **Figure 4**) required only 3 hours at r.t. In short, the dimerization of **2** harmed the kinetics of the self-assembly of the tetra-imine cage **1** owing to the low availability of free **2** in solution.

The sharp singlet resonating at δ = 8.2 ppm in the ^{1}H NMR spectrum of the mixture after 4 days was assigned to the CHs of the imine bonds (H^{7}). We also observed two signals for the pyrrole NHs (H^{2} and H^{10}) corresponding to the two chemically non-equivalent C[4]P hemispheres resonating as broad singlets at δ = 7.4 and 7.5 ppm, respectively. The β-pyrrole protons (H^{1} and H^{11}) appeared as two separated doublets close to δ = 5.9 ppm. This observation agreed with the existence of two

different calix[4]pyrrole hemispheres of the tetra-imine cage **1**. The chemical shifts of some of the protons of **1**, compared to those in the free components, **2** and **3**, were indicative of the C[4]P units adopting cone conformation. Using integral values of selected proton signals of the tetra-imine cage **1** and the i.s., we determined that the cage assembly occurred to an extent larger than 90%.

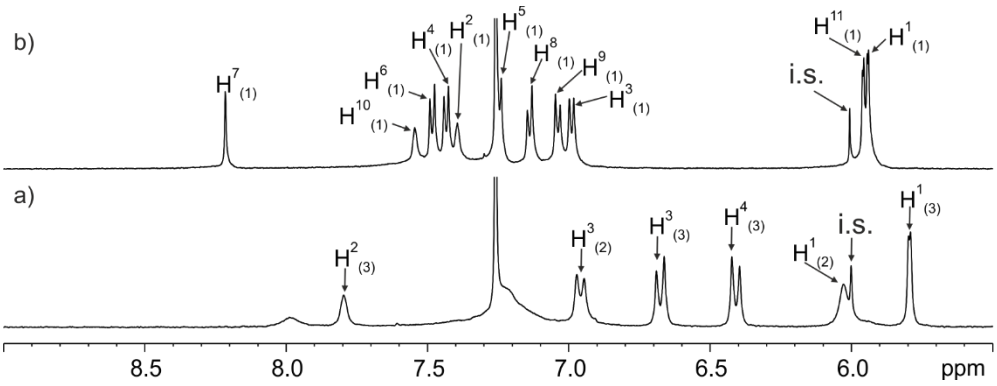

Figure 5. Selected region of the ^{1}H NMR spectra (500 MHz, at 298 K, $CDCl_3$:CD_3CN 9:1 mixture) of (a) 1:1 mixture of **2** and **3** immediately after mixing the two components and (b) after 336h at 298 K. The proton signals in panel (b) are diagnostic of the quantitative self-assembly of the tetra-imine cage **1**. See Scheme 1 for the proton assignment. The numbers in parentheses shown as subscripts indicate the species to which the proton belongs.

We characterized the tera-imine cage **1** by a complete set of high-resolution spectra (1D and 2D NMR experiments and HRMS). The number of signals present in the ^{1}H NMR spectrum of cage **1** agrees with C_{4v} symmetry. A ROESY experiment showed nOe cross-peaks between the imine protons (H^7) and the two *ortho*-aromatic protons of the connected panels (H^6 and H^8) (**Figure 6**).

We performed a ^{1}H DOSY NMR experiment in $CDCl_3$ solution (**Figure 7**). The experimentally measured diffusion coefficient (- log $D_{measured}$ = 9.39) agreed with that calculated for a cylindrical object with geometrical parameters coinciding with those determined from the energy-minimized structure of cage **1** (10.2 Å diameter and 30.5 Å height, see **Figure 29** in the experimental section).

To prepare cage **1** on a relatively larger scale, we assembled the cage at the same concentration mentioned above (2 mM for precursors **2** and **3**) in a larger volume (10 mL) using 0.01 mM acetic acid as catalyst. After 120 hours, the solvent was removed under vacuum, and the solid residue was dissolved in 5 mL of DCM. The

addition of 0.5 mL of methanol and the slow evaporation of the solvent (up to 1 mL) in reduced pressure provoked the precipitation of cage **1**. The solid was filtered, washed with methanol, and dried in a vacuum to afford pure cage **1** as a yellow solid.

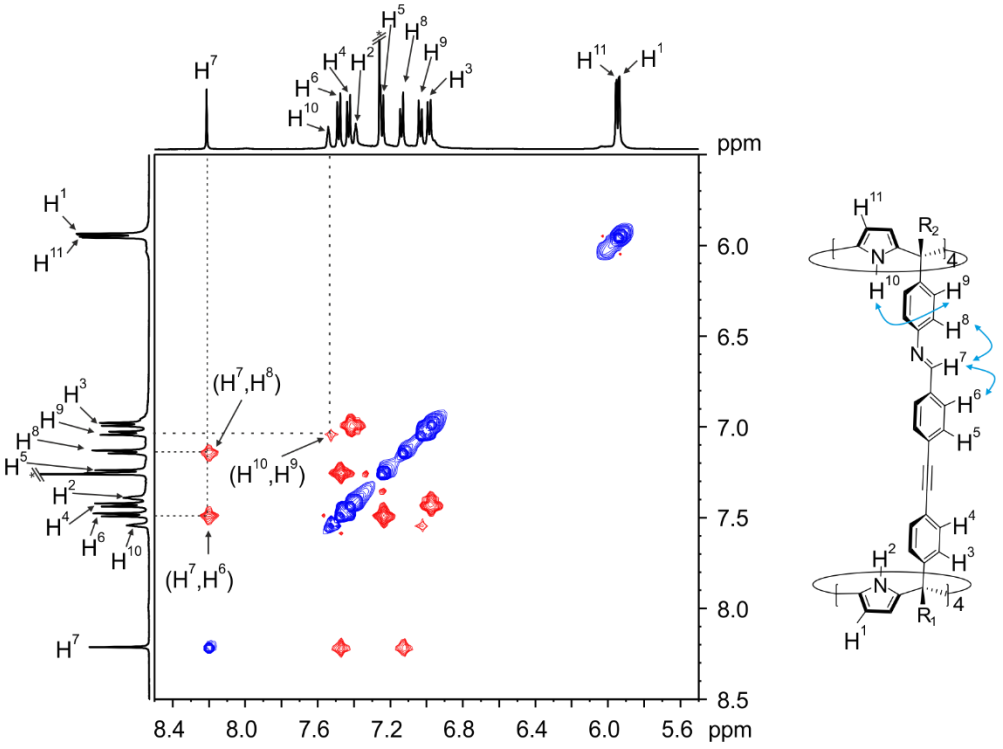

Figure 6. 2D ^{1}H ROESY NMR (500 MHz, at 298 K, $CDCl_3$:CD_3CN 9:1, d8 (mixing time) = 0.3 s) of tetra-imine cage **1.**

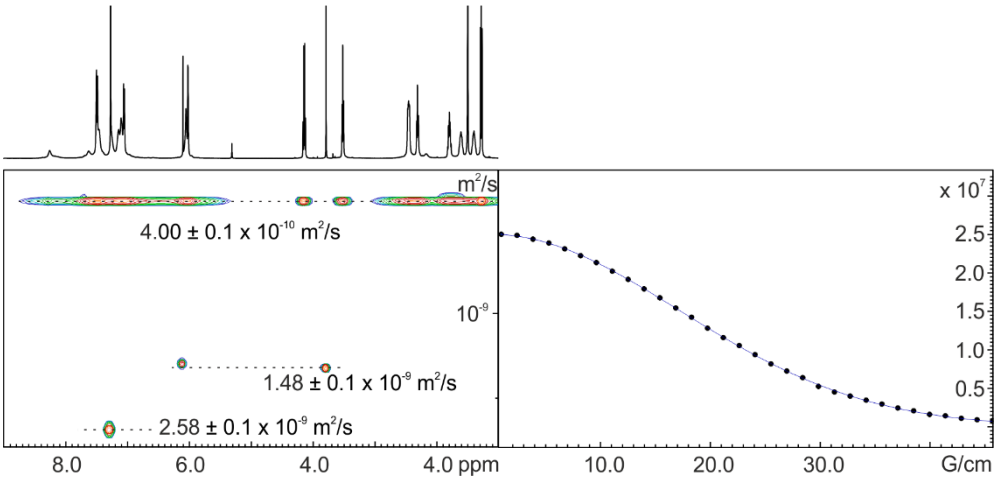

Figure 7. (left) ^{1}H pseudo 2D plot of the DOSY experiment (500 MHz, 298k, $CDCl_3$, D20 = 0.10 s; P30 = 0.20 ms) of **1**. (right) Fit of the decay of the proton signal resonating at δ= 6.1 pm to a mono-exponential Stejskal–Tanner function. Errors are indicated as standard deviation.

6.2.2 Study of the effect of the aromatic walls of the imine cages in the in-out chemical exchange process of acetonitrile molecules.

Using a solvent-template-assisted self-assembly strategy, our group has successfully prepared three different bis-calix[4]pyrrole poly-imine cages **1**, **5**, and **6** (**Figure 2**). These imine cages possess a polar, shape-persistent cavity due to the conformational constraints imposed by the imine bonds and aromatic spacers. On the one hand, tetra-imine cage **1** and octa-imine cage **6** exhibit almost identical cavity lengths, diameters, and volumes because the lengths of the aromatic panels used as spacers are similar. The tetra-imine **5** has a reduced cavity length and diameter. On the other hand, the size and shape of the portals, defined by the different aromatic panels connecting the two calix[4]pyrrole hemispheres, in the three containers **1**, **5**, and **6** are notably different.

The X-ray crystal structures of cages **5** and **6,** described in **Chapter 3**, revealed that these containers displayed two portals with different shapes and sizes in the solid state. The energy-minimized structure of cage **1** also suggested the existence of two different portals. The in-out exchange process of the guests through a “French doors” mechanism is expected to have a lower energy barrier when occurring through a larger portal. Thus, the shape and size of the portals in the poly-imine cages are crucial in determining the energy barriers of the guest exchange

processes. Owing to the D_{4h} symmetry of octa-imine cage **6**, the shape and size of any portal should be identical in the two calix[4]pyrrole hemispheres. Thus, the two ends of the cage are expected to have identical properties in guest exchange processes. Conversely, for tetra-imine cages **1** and **5**, displaying a reduced apparent C_{4v} symmetry in solution, the shape and size of the portals for the two calix[4]pyrrole hemispheres are different. As a consequence of their different symmetry (D_{4h} vs C_{4v}), octa-imine **6** possesses two chemically equivalent calix[4]pyrrole binding sites. However, those in tetra-imines **5** and **1** are chemically non-equivalent.

To characterize the role played by the different aromatic panels of the three cages in the kinetics of the in-out guest exchange processes involving acetonitrile molecules, we performed 1D-^{1}H GOESY experiments.[11] We used three separate 2 mM solutions of cages **1**, **5**, and **6** in a 9:1 $CDCl_3$:CH_3CN solvent mixture (**Figure 8**). Please note that we employed non-deuterated acetonitrile in the preparation of the solutions. The selective excitation (gaussian pulse) of the singlet corresponding to the free CH_3CN (δ= 1.94 ppm) produced 1D-GOESY spectra displaying, in addition to the excited singlet, one or more in-phase low-intensity upfield shifted singlet/s. These upfield-shifted signals were assigned to protons of acetonitrile molecules included in the cages, which experienced slow chemical exchange processes on the proton chemical shift time scale. The two separate signals were spaced by at least 470 Hz. Nevertheless, the solvent exchange must be fast on the 1D-GOESY timescale. That is, a significant amount of saturation transfer was produced in the 0.3 s used as GOESY mixing time. The number and shape of the upfield shifted signals, corresponding to the types of included acetonitrile molecules, differed for the three cages **1**, **5**, and **6**.

In the case of cage **1**, the 1D-GOESY spectrum shows two sharp signals resonating at δ = 0.3 and 1.0 ppm. We assigned these signals to the protons of the two different acetonitrile molecules in the two non-equivalent calix[4]pyrrole hemispheres of cage **1** (**Figure 8a**). The similar sharpening observed for the two signals assigned to the acetonitrile molecule included in the two polar ends of tetra-imine cage **1** suggested that the energy barrier for their in-out exchange processes was close and significantly large. However, in the case of tetra-imine cage **5** (**Figure 8b**), we observed two upfield-shifted signals at δ = 0.2 and 0.8 ppm, one as a sharp and the other as a broad singlet. The different shapes of the two signals suggested that the energy barriers for their exchange mechanism were dissimilar. In short, the two acetonitrile molecules in the non-chemically equivalent hemispheres of tetra-imine **5** underwent energetically different in-out exchange processes.

It is worth remembering that the analogous 1D-GOESY experiment of cage **6** described in **Chapter 3** (**Figure 8c**) showed only one broad and upfield-shifted signal for the bound acetonitrile molecules, indicating a lower barrier and faster in-out exchange process.

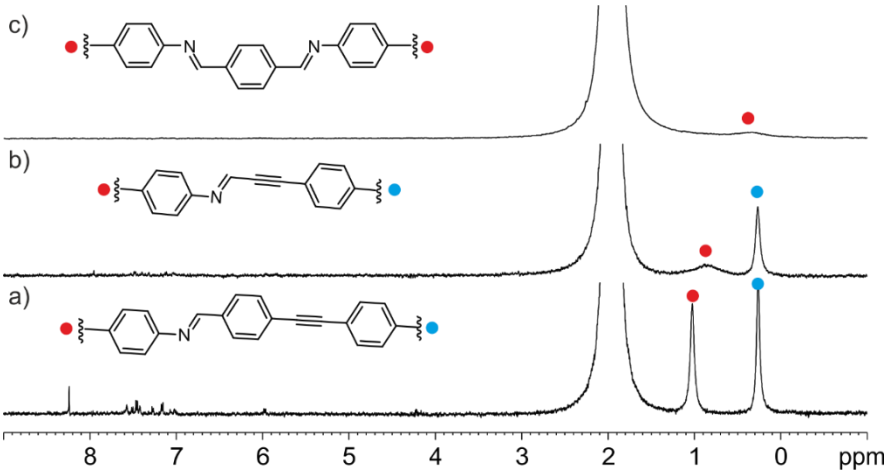

Figure 8. 1D-GOESY ^{1}H NMR spectra of $CDCl_3$:CH_3CN solutions of poly-imine cages (a) **1**, (b) **5**, (c) **6** performed by selective irradiation of the CH_3CN solvent peak (δ = 1.94 ppm). The observation of upfield-shifted singlets with the same phase as the selectively excited signal of the CH_3CN supports the inclusion of CH_3CN molecules in the cages. The signals assigned to included acetonitrile protons in the chemically non-equivalent calix[4]pyrrole hemispheres are indicated with circles of different colors.

Together, these results indicated that the in-out exchange barriers for the acetonitrile molecules included in the polar poly-imine cages are influenced by the shape and size of the portals defined by their aromatic spacers. The energy barrier of the in-out exchange process is expected to increase for bulkier guests requiring more significant portal enlargements. A putative change in the exchange mechanism demanding the temporal cleavage of imine bonds may also be foreseen in the case of extremely large monotopic and ditopic guests.

6.2.3 Binding properties of the tetra-imine cage **1** with pyridine *N*-oxides

Next, we decided to characterize the binding properties of the tetra-imine cage **1** towards the reactants and products of the Huisgen cycloaddition reactions suitable for inclusion (**Scheme 2**). We selected three 4-substituted pyridine *N*-oxides (**7-9**) already used as guest/reactants for the octa-imine cage **6** (see **Chapter 5**). We also picked two relevant 1,4-disubstituted 1,2,3-triazole bis-*N*-oxides (**10a, 11a**). These bis-*N*-oxides are the 1,4-isomer products of the Huisgen cycloaddition reactions of the mono-pyridine *N*-oxides **7**-**9**. We monitored the binding processes of the five guests with cage **1** using ^{1}H NMR spectroscopic titrations.

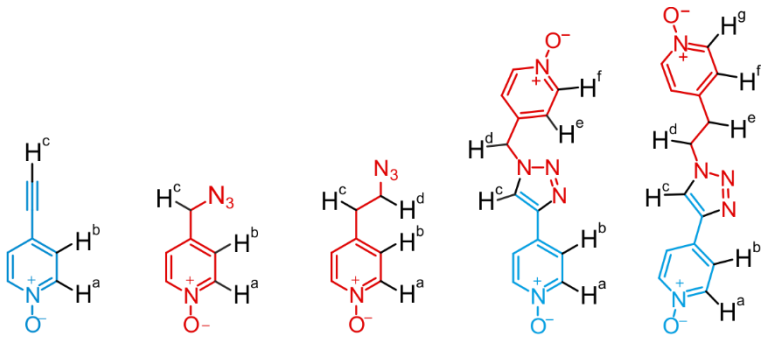

Scheme 2. Line-drawing structures of monotopic (**7**-**9**) and ditopic (**10a**, **11a**) *N*-oxide guests were used in the study of the binding properties of cage **1**.

6.2.3.1 Inclusion of 4-ethynylpyridine *N*-oxide **7** in cage **1**.

We added 1 equiv. of 4-ethynylpyridine *N*-oxide **7** to a 2 mM solution of tetra-imine cage **1** in a $CDCl_3$:CD_3CN 9:1 mixture. We analyzed the resulting solution using ^{1}H NMR spectroscopy immediately after adding the *N*-oxide (approximately 5 min after). We observed the appearance of several sets of separate proton signals for the tetra-imine cage **1**. We assigned the different sets of signals to free **1** and its inclusion complexes (**7**)⊂**1** and (**7**)$_2$⊂**1** (**Figure 9b**). We detected four separate signals for the imine proton (H^7) resonating at δ = 8.34, 8.22, 8.14, and 8.04 ppm, corresponding to the three species. It is worth noting that the (**7**)⊂**1** complex produced two imine signals owing to the slow chemical exchange of included **7** between the two non-chemically equivalent hemispheres of **1**. The ratio of the integral values of the four imine proton signals did not change with time, indicating that the kinetics of complexes' formation were fast, and the binding system quickly reached the thermodynamic equilibrium. We did not detect signals for the protons of the free guest **7** in the equimolar mixture. This result led us to estimate that the

stepwise binding constants for forming the (**7**)⊂**1** and (**7**)$_2$⊂**1** complexes were larger than 10^4 M^{-1}.

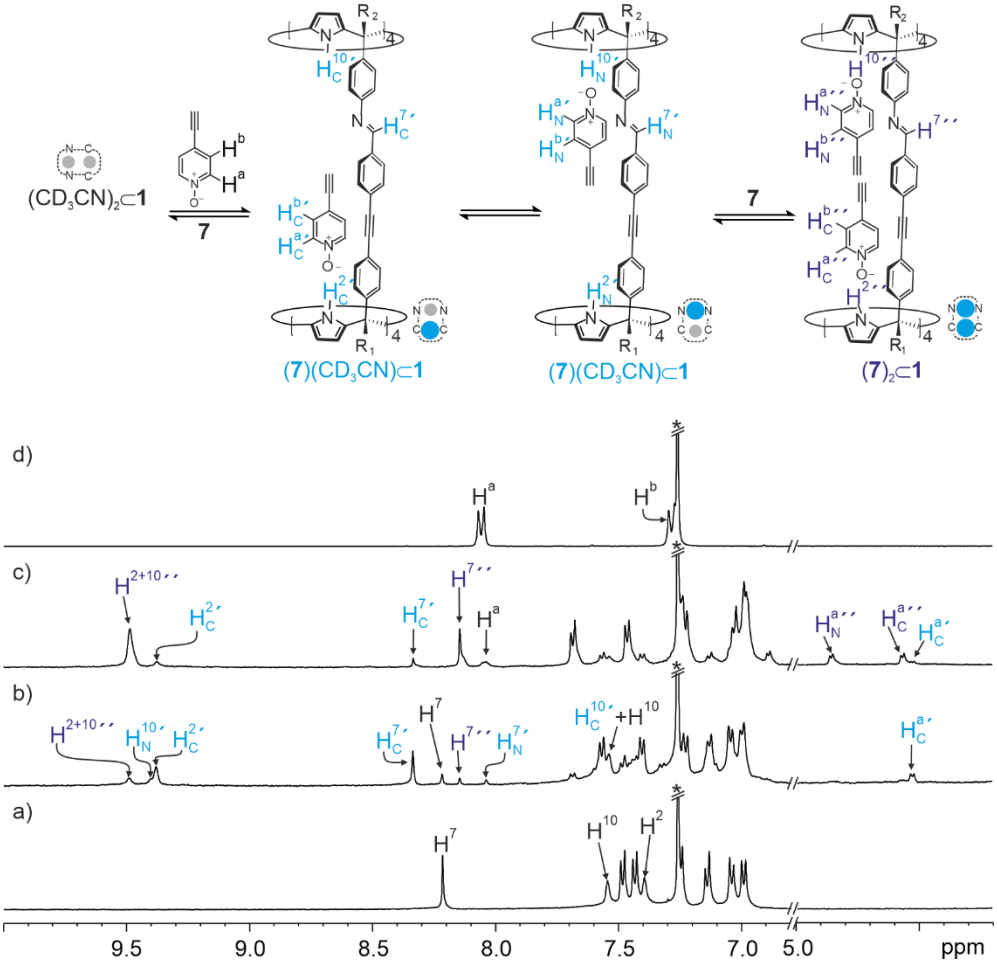

Figure 9. Selected region of the ^{1}H NMR (500 MHz, at 298K, $CDCl_3$:CD_3CN 9:1) spectra acquired during the titration of a 2 mM solution of cage **1** with incremental additions of **7**: a) 0 equiv., b) 1 equiv., c) 2 equiv. Spectrum d) corresponds to the free **7** in the same solvent mixture. Primed letters indicate the bound proton signals in the 1:1 complex, and double primed letters those in the 2:1 complex. Subscripts "C" and "N" are used to distinguish the two isomers of **7**⊂**1** complexes, specifically referring to the proximity of the bound guest **7** to the alkyne carbon “C” and imine nitrogen “N” connected to the aromatic spacer. Similarly, these subscripts were also used to differentiate the two guests in the (**7**)$_2$⊂1 complex.

The addition of more than 1 equiv. of **7** increased the intensity of the signals assigned to **7**$_2$⊂**1** to the expenses of those of **7** and **7**⊂**1**. When 2 equiv. of **7** were added (**Figure 9c**), we only observed the proton signals of **1** in the(**7**)⊂**1** and (**7**)$_2$⊂**1** complexes and the emergence of the signals of the protons of free **7**. The addition of more than 2 equiv. of **7** provoked the exclusive observation of the signal of the (**7**)$_2$⊂**1** complex and the increase of those of free **7**. For the (**7**)$_2$⊂**1** complex, we detected one broad singlet for the pyrrole NHs (H^{2+10}") and a sharp singlet for the imine counterparts (H^{7}"), resonating at $\delta = 9.48$ ppm and $\delta = 8.14$ ppm, respectively. The aromatic protons of the two copies of **7** in the two chemically non-equivalent hemispheres of the **7**$_2$⊂**1** complex experienced different complexation-induced upfield shifts (H_C^a" and H_N^a"). The dissimilar *meso*-aryl substituents of the two hemispheres provoked distinguishable magnetic anisotropies.

Based on our previous results in **Chapter 5** with octa-imine cage **6**, we inferred that in the two isomeric 1:1 complexes, (**7**)⊂**1**, one molecule of **7** is co-included with one acetonitrile molecule in the opposite hemisphere ((**7**)(CD$_3$CN)⊂**1**).

The integral values of selected imine proton signals ($H_C^{7\prime}$, $H_N^{7\prime}$) indicated an energy difference of approximately 0.65 kcal·mol^{-1} (ΔG = -RT ln$K$) between the two isomers of (**7**)(CD$_3$CN)⊂**1** complex. We putatively assigned the energetically more favorable isomer to a binding geometry locating the included alkynyl-*N*-oxide **7** in the SAE-C[4]P hemisphere of **1** owing to the establishment of more favorable CH-π and π-π intermolecular interactions.

6.2.3.2 Inclusion of the monotopic azido pyridine *N*-oxides 8 and 9 in the tetra-imine cage 1.

We performed analogous binding experiments of the tetra-imine cage **1** with azido pyridine-*N*-oxides **8** and **9**. Cage **1** showed very similar binding properties for the two azido-*N*-oxides. In turn, they also resembled those described above for the ethynyl-pyridine-*N*-oxide **7**. In short, the addition of 1 equiv. of any of the two azido-*N*-oxides produced four sets of proton signals for the imine protons of cage **1**. We attributed these signals to the imine protons in free **1**, the two isomers of the 1:1 complex, and the 2:1 complex. We did not detect the proton signals of the free guests, **8** and **9,** in the equimolar mixtures.

In contrast to the observations made for 4-ethynylpyridine *N*-oxide **7** in the binding studies with cage **1**, the integral values of the imine protons assigned to the four species involving cage **1** formed after the addition of 1 equiv. of the 4-azido-pyridine-*N*-oxide **8** or **9** changed with time. This observation indicated that reaching

the thermodynamic binding equilibrium after the addition of 1 equiv. of guests, **8** or **9,** was slow on the human timescale (minutes). The most noticeable changes occurred between the integral values of the imine proton signals assigned to two 1:1 isomeric complexes ($H_C^{7\prime}$, $H_N^{7\prime}$). In the specific case of azidoethylpyridine *N*-oxide **9**, the ^{1}H NMR spectrum acquired following the addition of the guest showed the presence of one of two 1:1 isomeric complexes in a larger extent ($H_N^{7\prime}$, **Figure 10b**). We surmise that the binding geometry of this kinetically favored inclusion complex involved the location of the bound guest **9** in the AE-C[4]P hemisphere of cage **1**. After 30 minutes, we reanalyzed the solution using ^{1}H NMR spectroscopy. Surprisingly, we observed that the ratio of the integral values of the two 1:1 isomeric complexes changed significantly. At this point, the (**9**)(CD_3CN)⊂**1** isomeric complex putatively locating the *N*-oxide **9** in the SAE-C[4]P hemisphere of cage **1** experienced a significant increase in concentration (($H_C^{7\prime}$, **Figure 10c**). The integral values of the imine protons corresponding to the 2:1 complex, (**9**)$_2$⊂**1**, and the free cage **1** ($H^{7\prime\prime}$ and H^7) were less affected by reaching the equilibrium. These observations supported that the tetra-imine cage **1** is kinetically favored in including the azido-pyridine-*N*-oxides **8** and **9** in its AE-C[4]P hemisphere. In contrast, cage **1** is thermodynamically favored in including the *N*-oxides **8** and **9** in the SAE-C[4]P hemisphere. Depending on the nature of the formation process, a different mixture of the complex is reached. Both complexes are kinetically and thermodynamically stable. The energetically more favored complex is obtained to a major extent under thermodynamic conditions.

The addition of more than 1 equiv. of azido-pyridine-*N*-oxides **8** and **9** produced results similar to those described for the alkynyl-*N*-oxide **7**. In the presence of 2 equiv. of azidoethyl-pyridyne-N-oxide **9**, we neither detected the imine signals corresponding to free cage **1** (H^7), nor the kinetically favored 1:1 isomeric complex ($H_N^{7\prime}$). Conversely, we observed the imine proton signals assigned to the thermodynamically favored 1:1 isomeric complex, (**9**)(CD_3CN)⊂**1**, and the 2:1 complex (**9**)$_2$⊂**1**. We also detected the signals for the protons of free **9** (**Figure 10d**). The quantitative formation of the 2:1 complex (**9**)$_2$⊂**1** required the addition of *ca.* 3 equiv. of **9**.

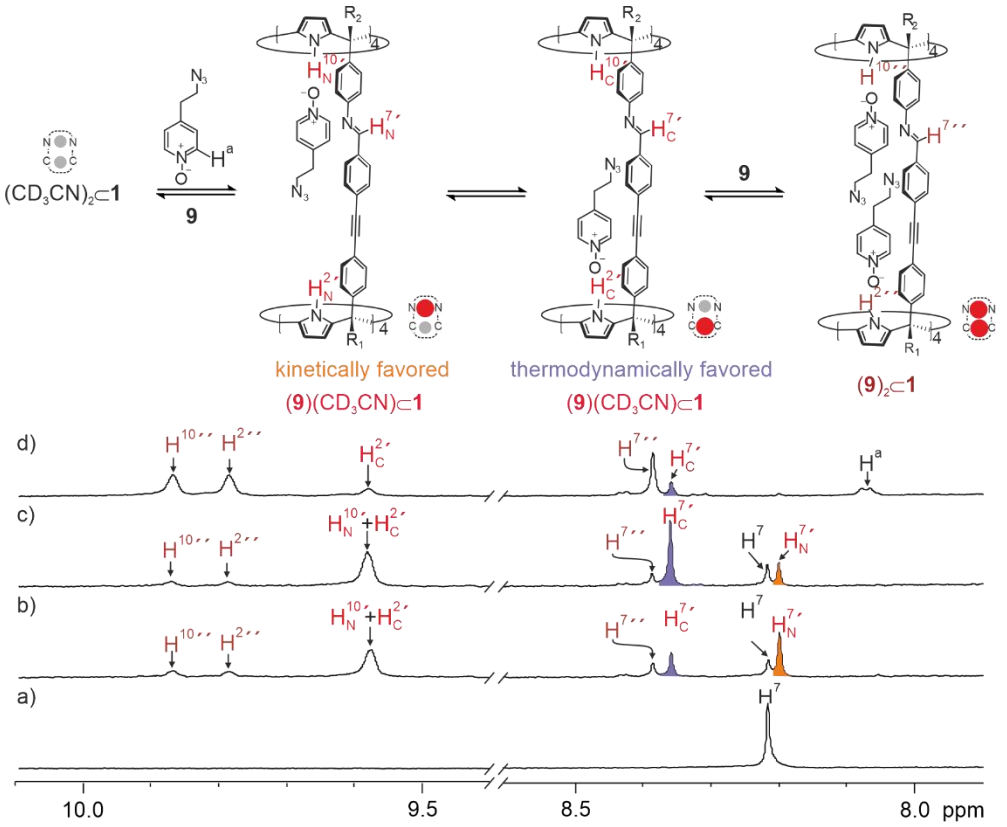

Figure 10. Selected region of the ^{1}H NMR (400 MHz, at 298K, $CDCl_3$:CD_3CN 9:1) spectra acquired during the titration of a 2 mM solution of cage **1** with increasing amounts of azide-*N*-oxide **9**: a) 0 equiv., b) 1 equiv. (5 min after addition), c) 1 equiv. (35 min after addition), d), 2 equiv. (35 min after addition). Subscripts "C" and "N" are used to distinguish the two isomers of **9⊂1** complexes, specifically referring to the proximity of the bound guest **9** to the alkyne carbon "C" and imine nitrogen "N" connected to the aromatic spacer. Similarly, these subscripts were also used to differentiate the two guests in the $(\mathbf{9})_2\subset 1$ complex.

6.2.3.3 ITC studies of cage **1** with monotopic guests

We undertook isothermal titration calorimetry (ITC) experiments to assess accurate binding constants for the formation of 1:1 and 2:1 complexes. The incremental addition of chloroform:acetonitrile 9:1 solution of guests (**7**-**9**, ~10 mM) to a solution of cage **1** in the same solvent mixture (~0.5 mM) produced a gradual release of heat. The normalized integral values of the heat data produced binding isotherms with a single inflection point centered at a host/guest molar ratio close to 2. This result indicated that the binding cooperativity was not significantly large enough to be detected in the ITC experiment. In all experiments, we fit the ITC data to the theoretical binding model considering one set of sites implemented in the Microcal ITC software. The obtained fit was good and returned the statistically corrected average value of the binding constant for the two sites, $K_{average}$, in the range of 1.2-5.4 × 10^4 M^{-1}. Based on these values we estimated the stepwise and overall macroscopic constants of the binding processes for all three guests (**7**-**9**) to be $K_{1:1} = 2 \times K_{average}$ M^{-1}, $K_{2:1 \leftrightarrow 1:1} = K_{average}/2$ M^{-1}, and $K_{2:1} = (K_{average})^2$ M^{-2}. These values agreed with the magnitude of the binding constants estimated from the NMR titration and their speciation profiles (**Figure 30**, **32**, **33** in the experimental section).

In summary, the three monotopic pyridine-*N*-oxides, **7**-**9**, displayed similar binding properties for the tetra-imine cage **1**. Firstly, more than 2 equiv. of the guest are required for the quantitative formation of the (**G**)$_2$⊂**1** complexes indicating that the binding constants for the 2:1 complexes were in the order of 10^8 M^{-2}. Values of 10^9 M^{-2} or larger will induce the quantitative formation of the 2:1 complexes for the 2 mM concentration of **1** used for the titrations. Secondly, in the three binding processes, we estimated the binding constants for the formation of the 1:1 isomeric complexes to be larger than the 10^4 M^{-1} because we did not detect the signals of the free *N*-oxide in an equimolar mixture with **1**.

The ITC experiments of octa-imine cage **6**, studied in **Chapter 5**, showed observable negative cooperativity for guests **8** and **9** in producing the corresponding 2:1 (**G**)$_2$⊂**6** complexes. However, all ITC experiments of tetra-imine cage **1** with guests **7**-**9** show non-cooperativity in forming analogous (**G**)$_2$⊂**1** complexes. We hypothesized that the steric clashes between the two included *N*-oxides guests in the (**G**)$_2$⊂**1** complex were reduced compared to that of the octa-imine cage **6** owing to the increase in the cavity length of cage **1**.

We observed slow kinetics on the human time scale for reaching equilibrium after the addition of 1 equiv. of **8** and **9** to cage **1**. We attributed this finding to the larger

size of the guests compared to the ethynyl-pyridine-*N*-oxide counterpart **7** and the different sizes of the portals of tetra-imine cage **1** compared to **6**. The MM3 minimized the structure of cage **1** (**Figure 11**) showed that the larger portal displays different-sized windows for each hemisphere. That is on the AE-C[4]P hemisphere the longest distance is between the two adjacent imine CHs, d(C_{im}-C_{im}) = 8.1 Å. On the other hand, on the SAE-C[4]P hemisphere, the longest distance is between two adjacent alkyne carbons directly connected to the aromatic spacer, that is d(C_{alkyne}-C_{alkyne}) = 7.3 Å, which is almost 1 Å shorter than the former. These differences in size could be responsible for the kinetically preferred entrance of the guest through the hemisphere portal with the wider window (i.e. AE-C[4]P hemisphere).

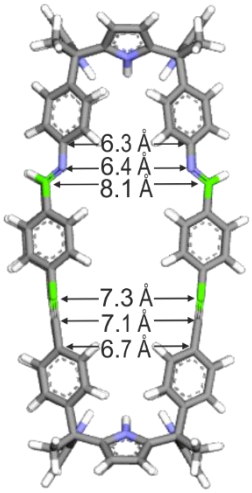

Figure 11. MM3 energy minimized structure of solvated cages **1**. The included solvent molecules were removed for clarity. Alkyl chains were truncated to methyl groups to ease calculations.

6.2.3.4 Inclusion studies of ditopic 1,4-triazole bis-pyridyl *N*-oxides 10a and 11a in tetra-imine cage 1.

To assist in the subsequent kinetic studies of the cycloaddition reactions included in cage **1**, we characterized the cage binding process with the ditopic 1,4-triazole bis-pyridyl *N*-oxide **10a**. The ditopic *N*-oxide **10a** was obtained from the copper(I) catalyzed azide-alkyne cycloaddition (CuAAC) reaction of the mono-topic *N*-oxides **7** (alkyne) and **8** (azide). Due to the reduced solubility of bis-*N*-oxide **10a** in the 9:1 $CDCl_3$:CD_3CN solvent mixture (maximum solubility ~ 0.5 mM, calculated by ^{1}H NMR using an internal standard), we suspended 2 equiv. of **10a** in solid form on a 2 mM solution of cage **1**. After sonication for 2 minutes and filtration, we analyzed the resulting filtrate solution using ^{1}H NMR spectroscopy. We observed two sets of well-defined signals of different intensities, which were assigned to the protons of bound cage **1**. We also detected the signals of the protons of free guest **10a** (**Figure 12b**). The proton signals of the free cage **1** were not detected. Taken together, the obtained results indicated the quantitative formation of two isomeric inclusion complexes of cage **1** which was fats on the human timescale. Notably, the relative intensities of the two sets of proton signals assigned to the bound cage **10a⊂1** complexes changed with time. After two hours, the intensities of the two sets of signals became identical and remained constant (**Figure 12c**).

A careful analysis of the ^{1}H ROESY NMR spectrum registered after the thermodynamic equilibrium was reached allowed us to assign the two sets of proton signals to the two isomers of the 1:1 complex, **10a⊂1** (**Figure 13**). The two chemically non-equivalent binding sites of cage **1** are responsible for the formation of the two isomeric complexes with non-symmetric *N*-oxide **10a**. The kinetic stability of the two isomeric complexes on the chemical shift timescale allowed their detection using ^{1}H NMR spectroscopy. The change in the relative concentrations of the two isomeric **10a⊂1** complexes supported that cage **1** featured a kinetic selectivity for the inclusion of guest **10a** that differed from its thermodynamic counterpart.

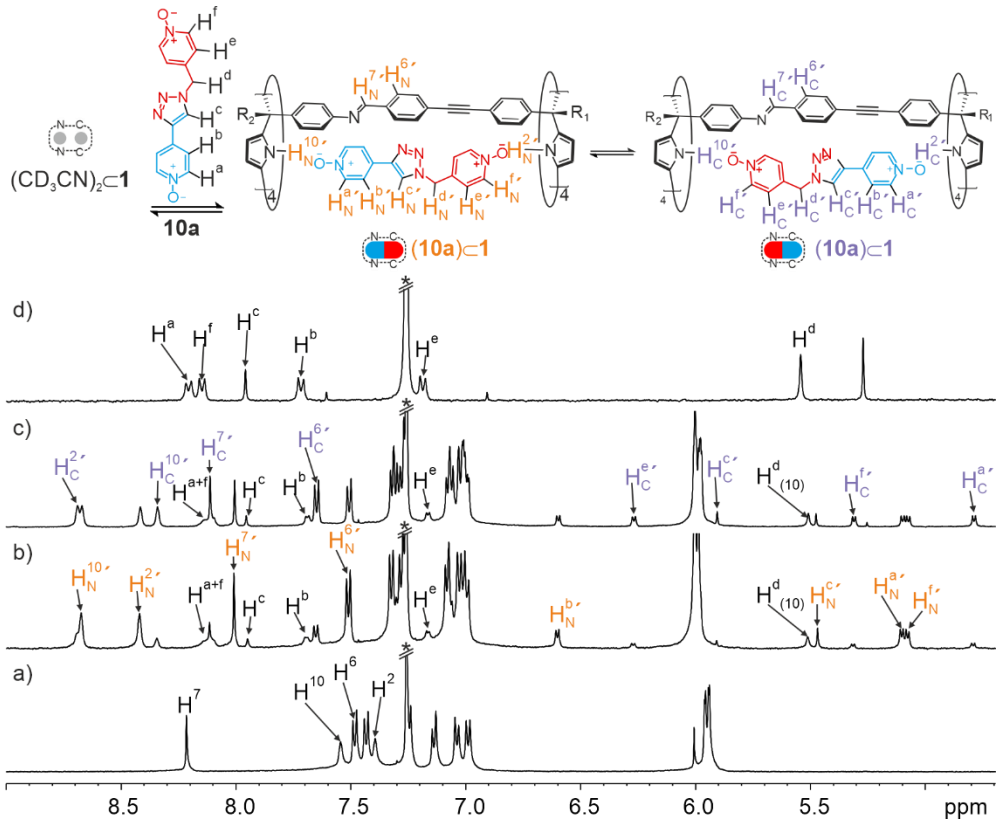

Figure 12. Selected region of the ^{1}H NMR spectra (500 MHz, at 298K, $CDCl_3$:CD_3CN 9:1) of a) 2 mM solution of cage **1** upon addition; b) immediately after the addition of 2 equiv. of **10a**, and c) 2 h after the addition of 2 equiv. of **10a**. Spectrum d) corresponds to that of free **10a** in the same solvent mixture. Subscripts "C" and "N" are used to distinguish the two isomers of **10a⊂1** complexes, specifically referring to the binding of the triazole to the SAE hemisphere ("C") or to the AE one (imine nitrogen "N").

The kinetic binding selectivity of cage **1** for the ditopic guest **10a** produced a mixture of the isomeric complexes **10a⊂1** that is consistent with our previous observations in the selective inclusion of monotopic pyridyl-*N*-oxides **8** and **9** in one of two cage's binding sites (hemispheres). The mono-topic *N*-oxides produced a kinetic mixture of two isomeric complexes **G⊂1**, favoring the location of the included guest in the cage's AE hemisphere (imine substituted). In the case at hand, the inclusion of **10a** in cage **1** might be expected to take place through a lower energy barrier when the bulkier *para*-triazole substituent (triazole *vs.* methylene) of the bis-*N*-oxide spacer passes through the slightly larger portal defined by a conformation of the two imine groups with diverging CHs (see **Figure 11**). The binding geometry of the kinetically

favored isomer of the inclusion complex **10a⊂1** (triazole at the AE hemisphere) was derived from a ^{1}H ROESY NMR experiment. We observed intense intermolecular nOe cross-peaks between the aromatic $H_N^{b\prime}$ protons, *ortho* to the triazole substituent, of the bis-*N*-oxide **10a**, and the center panel protons $H_N^{6\prime}$ of cage **1**. This finding supported the preferential inclusion of the bulkier end of the bis-*N*-oxide **10a** in the AE hemisphere of cage **1**. In another isomeric complex (triazole at the SAE hemisphere), we detected the expected nOe cross-peaks relating the $H_C^{e\prime}$ aromatic protons of the benzyl-substituted end of the bis-*N*-oxide **10a** and the imine protons $H_C^{7\prime}$ of cage **1**.

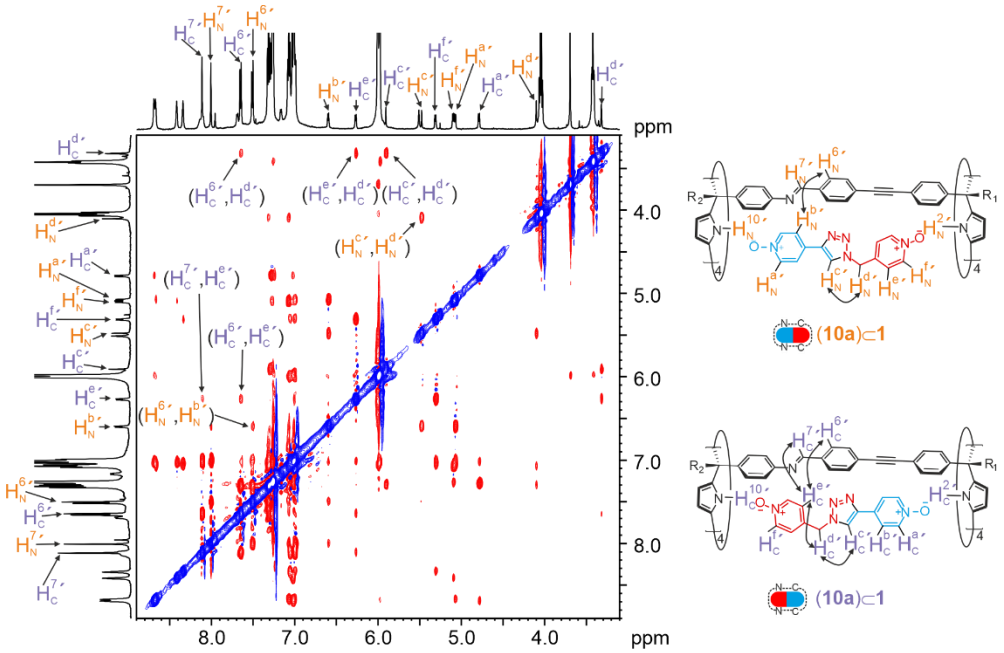

Figure 13. 2D ROESY NMR (500 MHz, at 298 K, $CDCl_3$:CD_3CN 9:1 mixture) spectrum of cage **1** with 2 equiv. of **10a**, taken two hours after the addition of the bis-*N*-oxide.

Reaching the thermodynamic equilibrium of the two isomeric complexes in less than two hours indicated that the energy barriers for their dissociation were not extremely large, i.e., 20 kcal/mol. Because the complex dissociation energy barrier directly relates to its thermodynamic stability, we rationalized that the stability constants of the two complexes were probably lower than 10^8 M^{-1}.

We reached a similar conclusion by considering that the binding constant of a mono-topic pyridyl-*N*-oxide of a hemisphere of poly-imine cage based on AE or SAE C[4]P

scaffolds is in the order of K_{ref} =10^4 M^{-1}. Consequently, the binding constant of a ditopic bis-pyridyl-*N*-oxide included in a poly-imine cage can be estimated as K_{ref}^2 × EM. The effective molarity (EM) factor is directly related to the goodness of the fit between the shape and size of the binding partners. For good fits, EM values range from 1 to 10^3 M. Conversely, sub-optimal fits render EM values from 0.1 to 10^{-3} M or even smaller. The reduced complexation-induced shifts (CIS) of the pyrrole NHs (H^2 and H^{10}) in the **10a⊂1** complexes supported a lack of fit between the cage and the *N*-oxide lengths. Compared to the average CIS values of 2-2.5 ppm observed for the pyrrole NHs in the 1:1 and 2:1 complexes of cage **1** with different monotopic guests (**7**-**9**), the CIS value of pyrrole protons for the isomers of **10a⊂1** complexes was smaller than $\Delta\delta = 1.5$ ppm. This result indicated the formation of longer hydrogen bonding interactions between the pyrrole NHs and the oxygen atoms of the bis-*N*-oxide **10a** in the **10a⊂1** complex.

To confirm our previous hypothesis, we performed a ^{1}H NMR pair-wise competitive experiment of monotopic guest **7** with ditopic guest **10a** and cage **1**. The addition of 0.9 equiv. of **10a** to a solution of cage **1** produced a ^{1}H NMR spectrum with well-defined proton signals diagnostic of the isomeric mixture of **10a⊂1** complexes and the solvated cage **1**. No proton signals of free **10a** were detected (**Figure 14a**). The addition of 1 equiv. of monotopic guest **7** to the previous mixture of isomers provoked the appearance of the proton signals assigned to the (CD_3CN)(**7**)⊂**1**, (**7**)$_2$⊂**1,** and free **10a** species, along with a simultaneous decrease in intensity of the signals assigned to the **10a**⊂**1** isomeric complexes. Adding more than 4 equiv. of **7** provoked almost the complete disappearance of the proton signals of **10a⊂1** isomers and the concomitant increase of the intensity of the signals corresponding to (**7**)$_2$⊂**1** and free guest **10a**. Considering these results and using the Hyperquad Simulation and Speciation (HySS2009) software, we estimated an apparent binding constant of **10a** for cage **1** as 3 × 10^5 M^{-1} (**Figure 15**).

Before adding monotopic guest **7** to cage **1** containing 0.9 eq of **10a**, the relative intensities of the two sets of proton signals assigned to the two isomeric complexes of **10a⊂1** were almost maintained in a 75:25 molar ratio with time. The slow isomerization was attributed to the low availability of free **10a** in the solution. After adding 1 equiv. of monotopic guest **7**, the replaced free **10a** by **7** effectively accelerated the isomerization of **10a⊂1**. The molar ratio of two isomeric complexes quickly reached 50:50 in 10 min after addition.

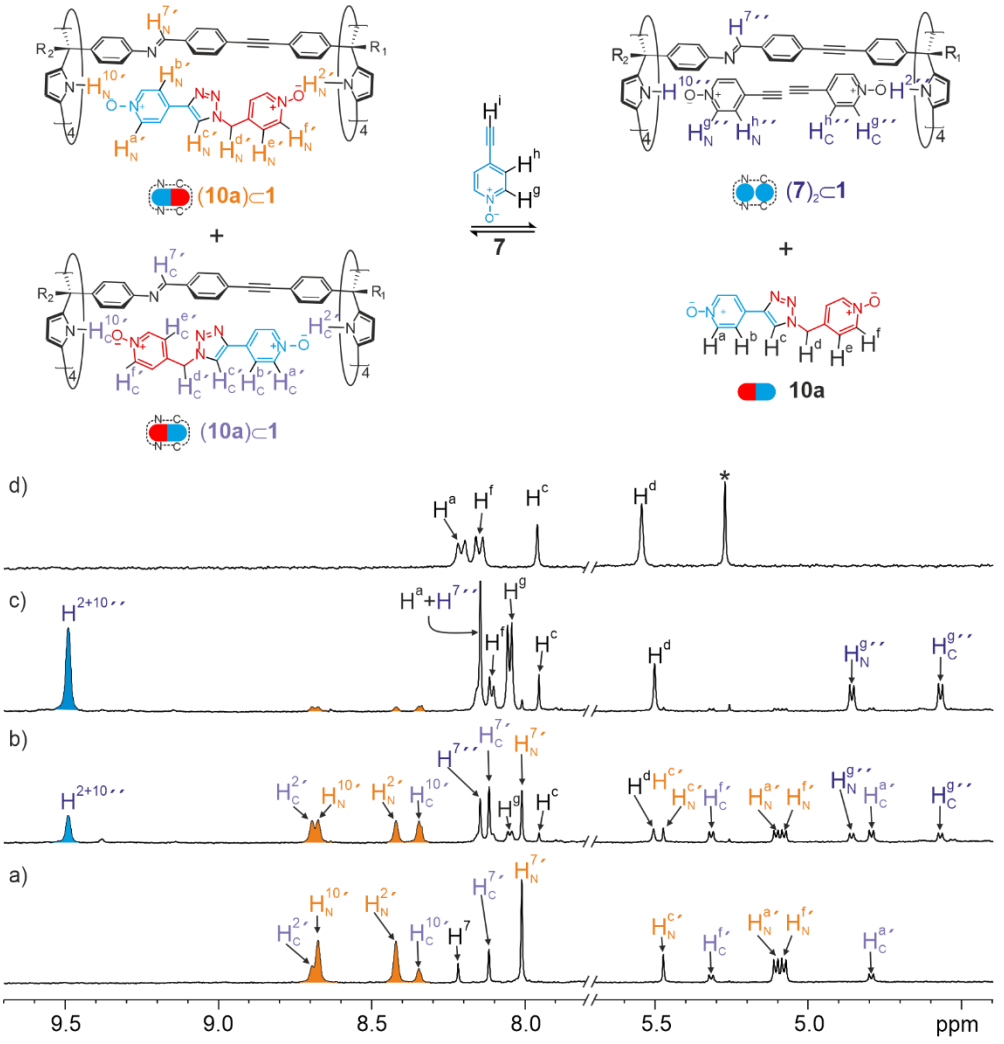

Figure 14. Selected region of ^{1}H NMR spectra (500 MHz, 298K $CDCl_3$:CD_3CN 9:1 mixture) of a) 2mM solution of cage **1** containing 0.9 equiv. of **10a** upon addition of; b) 1 equiv. of **7**, c) 4 equiv. of **7**. Spectrum d) corresponds to that of free **10a** in the same solvent mixture. All NMR spectra were measured 1 hour after each addition to reach the thermodynamic equilibrium.

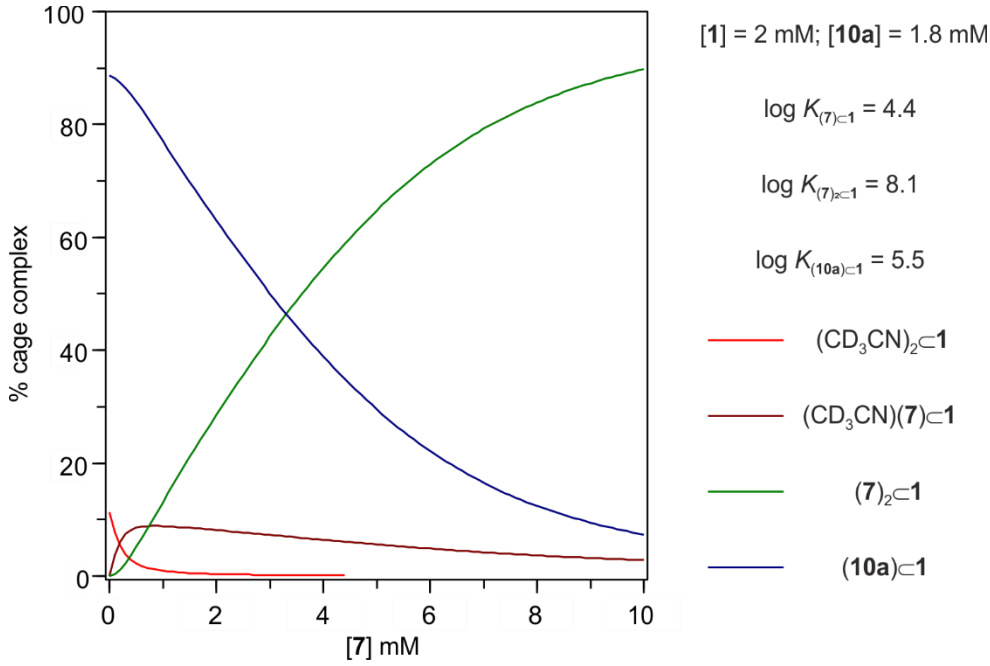

Figure 15. Speciation of the pair-wise competitive experiment of cage **1** (2 mM), with monotopic guest **7** (0-10 mM)**,** and ditopic guest **10a** (1.8 mM).

We also performed the inverse ^{1}H NMR pair-wise competitive experiment. That is, we added 1 equiv. of **10a** to a solution of cage **1** containing 2 equiv. of **7** and monitored the mixture by ^{1}H NMR spectroscopy. Just after the addition of **10a**, we observed the proton signals diagnostic of the two isomeric **10a⊂1** complexes in a 50:50 molar ratio which gradually increased with time (**Figure 16b**). After 2 h, the thermodynamic equilibrium was reached (**Figure 16c**). The obtained results indicated that the exchange of the included guests (from (**7**)$_2$**⊂1** to **10a⊂1)** was slow on the human timescale. The integral values of selected proton signals corresponding to the ratio of (**7**)$_2$**⊂1** and **10a⊂1** complexes at the equilibrium was 65:35. This value was in agreement with the estimated binding constant of **10a** with cage **1** (3×10^5 M^{-1}).

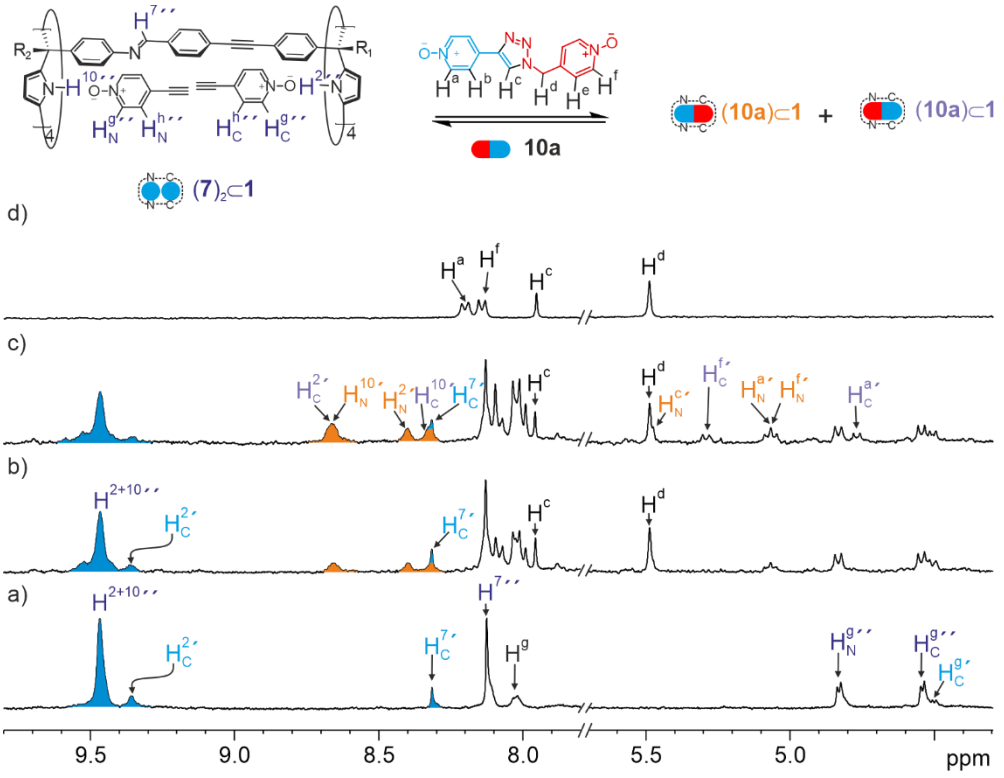

Figure 16. Selected region of ^{1}H NMR spectra (300 MHz, 298K $CDCl_3$:CD_3CN 9:1 mixture) of a) 2mM solution of cage **1** containing 2 equiv. of **7** upon addition of; b) 1 equiv. of **10a** after 5 min, c) after 2 h. Spectrum d) corresponds to that of free **10a** in the same solvent mixture. For proton assignments see **Figure 14**.

In short, a K_a value of 10^5 M^{-1} for both isomers of the **10a⊂1** complexes would result in an EM value of 10^{-3} M. The EM value is related to the concentration of a monotopic guest at which the formation of the 2:1 species (**7**)$_2$⊂**1** competes with the 1:1 chelate complex **10a⊂1**. The results of the theoretical speciation demonstrated that the monotopic guest **7** competes for binding with the ditopic **10a** counterpart in the chelate complex **10a⊂1** at concentrations higher than 10^{-3} M. Considering a similar binding constant for (**8**)$_2$⊂**1** complex, this result hinted at the possible existence of reaction turnover when cage **1** is used as a molecular vessel for promoting the Huisgen cycloaddition reaction between **7** and **8** producing **10a**.

Next, we performed binding experiments of bis-pyridine-*N*-oxide **11a** with cage **1**. Following the addition of 2 equiv. of guest **11a** as solid form and sonication of the resulting suspension for 2 minutes, the ^{1}H NMR spectrum of the filtrated mixture

evidenced the presence of two sets of proton signals of unequal intensity that were assigned to the two isomers of the **11a⊂1** complex. We also detected the signals of the protons of free guest **11a** (**Figure 17b**). After two weeks, we did not detect noticeable changes in the ^{1}H NMR spectrum. This result indicated that either the thermodynamic equilibrium of the complexes was reached very quickly or it was a much slower process than in the case of **10a**. The CISs experienced by the pyrrole NHs in the two isomers of the **11a⊂1** complex were in the range of 2-2.5 ppm. These values agreed well with the CISs observed for the 1:1 and 2:1 complexes with different monotopic *N*-oxide guests (**7**-**9**). We concluded that the bis-pyridyl-*N*-oxide **11a** displayed a better fit for the cavity length of **1** than the analog **10a**. The **11a⊂1** isomeric complexes featured shorter hydrogen bonds between the pyrrole NHs and the oxygen atoms of **11a** than in the case of **10a**. Probably, the stability constants of the **11a⊂1** isomeric complexes were larger than 10^6 M^{-1} due to an increase in EM. Consequently, in this specific case, cage **1** should not show turnover when used as molecular vessels to accelerate the included Huisgen cycloaddition producing bis-*N*-oxide **11a**.

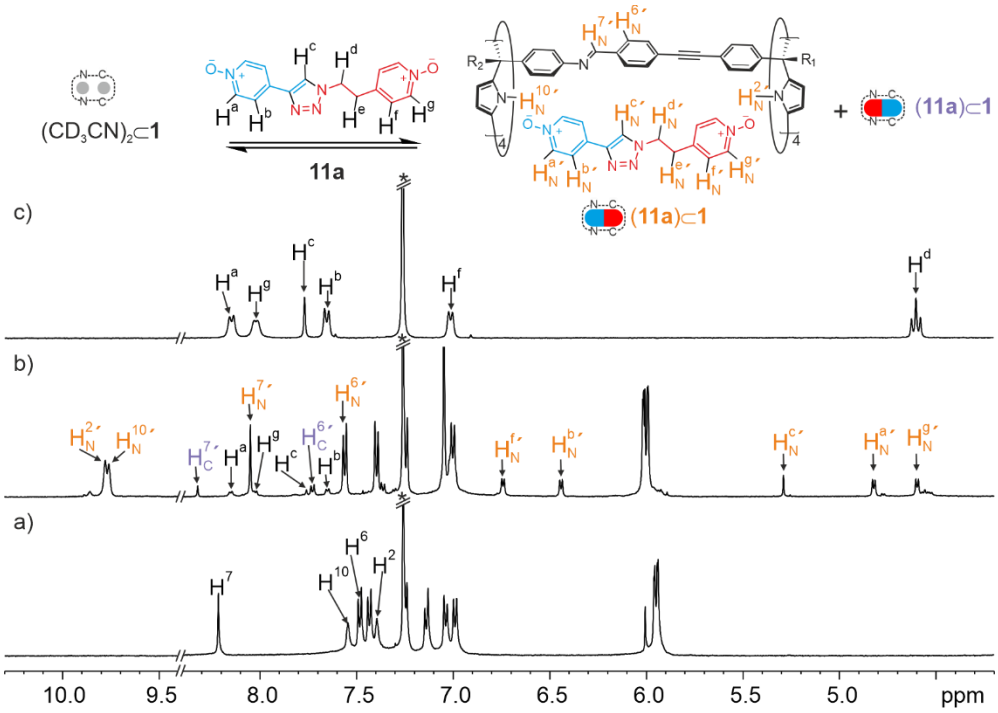

Figure 17. Selected region of the ^{1}H NMR (500 MHz, at 298K, $CDCl_3$:CD_3CN 9:1) spectra acquired for a) a 2mM solution of tetra-imine cage **1** and b) following the addition of 2 equiv. of **11a**. Spectrum c) corresponds to free **11a** in the same solvent mixture.

6.2.4 Kinetic studies of the Huisgen cycloaddition reactions included in the tetra-imine cage **1**.

6.2.4.1 Huisgen cycloaddition reaction between the 4-ethynyl-pyridine-*N*-oxide **7** and 4-(azidomethyl)pyridine-*N*-oxide **8** included in the tetra-imine cage **1**.

First, we investigated the cycloaddition reaction between the two pyridine-*N*-oxides **7** and **8** included in tetra-imine cage **1**. Based on the results of the competitive binding experiments described in the previous section, using **1** as a molecular vessel, we expected to achieve turnover for the included Huisgen cycloaddition reaction involving alkyne **7** and azide **8** and yielding 1,4-disubstituted triazole **10a** as an exclusive product.

We prepared a 2 mM solution of tetra-imine cage **1** in a $CDCl_3$:CD_3CN 9:1 solvent mixture and added equimolar amounts of the ethynyl-pyridine-*N*-oxide **7** and the 4-(azidomethyl)pyridine-*N*-oxide **8**. The ^{1}H NMR spectrum of the resulting mixture showed five different signals for the imine protons of cage **1** (**Figure 18c**). We could assign four of the five signals by comparing their chemical shift values with those of the inclusion complexes characterized in the separate ^{1}H NMR titration experiments of cage **1** with the two *N*-oxide derivatives (**Figure 18a** and **b**). The assigned signals corresponded to the two homo 2:1 inclusion complexes (**7**)$_2$⊂**1**, (**8**)$_2$⊂**1** and the two thermodynamically favored 1:1 complexes (**7**)(CD_3CN)⊂**1**, (**8**)(CD_3CN)⊂**1**. Most likely, the concentrations of the kinetically formed 1:1 complexes were below the detection limit of the ^{1}H NMR spectrometer. The unassigned imine signal was attributed to the (**7**·**8**)⊂**1** ternary complex, *a.k.a.* Michaelis complex (around 10% of the total amount of bound cage, 0.2 mM). Proton signals for the free ethynyl-pyridine-*N*-oxide **7** were also detected in the ^{1}H NMR spectrum of the mixture.

Taken together, the results above demonstrate that the ternary hetero-complex (**7**·**8**)⊂**1** is less thermodynamically favored than the two homo complexes (**7**)$_2$⊂**1** and (**8**)$_2$⊂**1**. Considering the experimentally observed speciation profile and using the Hyperquad Simulation and Speciation (HySS2009) software, we derived the binding constant value of the ternary hetero-complex (**7**·**8**)⊂**1**. The theoretical speciation profile approximated to the experimentally observed one (10% (**7**·**8**)⊂**1**, 30% (**7**)$_2$⊂**1**, 40% (**8**)$_2$⊂**1**, 10% (**7**)(CD_3CN)⊂**1**, and 10% (**8**)(CD_3CN)⊂**1**) by manually adjusting the binding constant value of the hetero-complex (**7**·**8**)⊂**1**. We obtained a reasonable agreement between the two for $K_{(7\cdot8)\subset1} = 2.5 \times 10^8$ M^{-2}. The binding

constants of the other species were fixed to the values determined in previous sections using ITC experiments and simulated speciation profiles.

To our delight, the ^{1}H NMR spectra of the mixture changed with time. After 4 days, we detected two sets of low-intensity signals corresponding to the protons of the two isomers of the **10a⊂1** complexes. The intensity of these new sets of signals increased at the expense of those attributed to the homo-inclusion complexes (**7**)$_2$⊂**1,** (**8**)$_2$⊂**1**, the 1:1 complexes (**7**)(CD_3CN) ⊂**1**, (**8**)(CD_3CN) ⊂**1**.

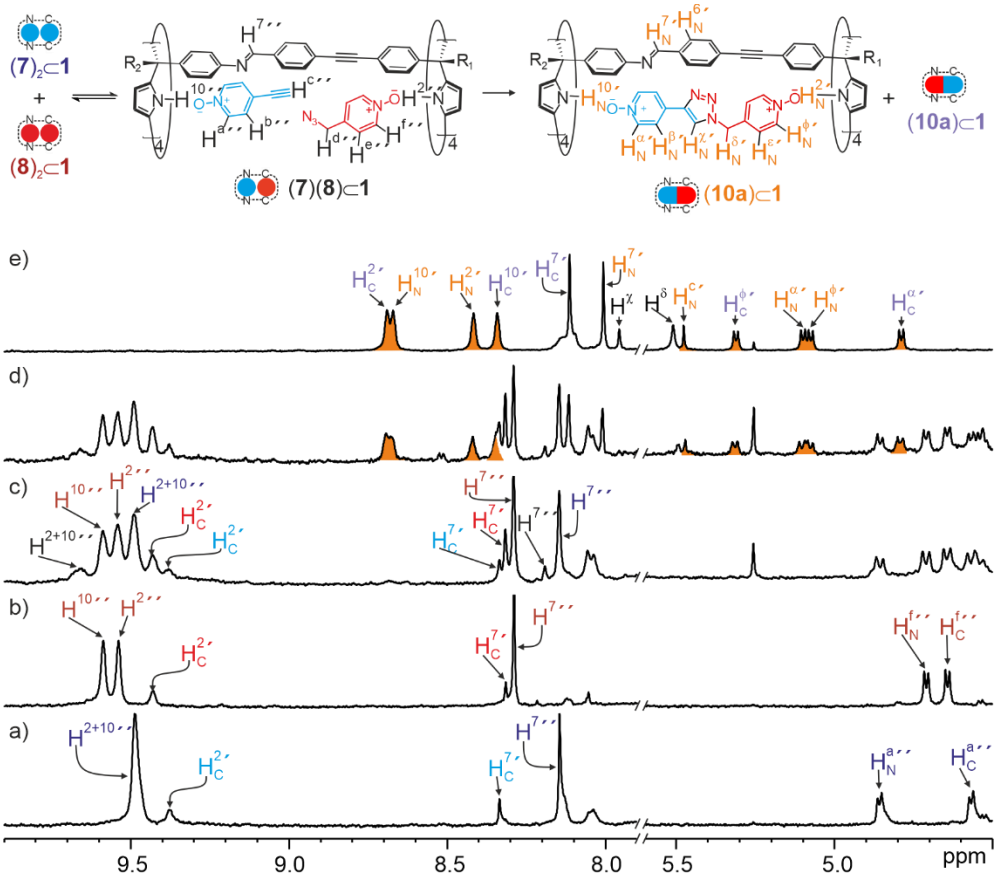

Figure 18. Selected regions of the ^{1}H NMR (500 MHz, at 298K, $CDCl_3$:CD_3CN 9:1) spectra corresponding to the kinetic study of the formation of **10⊂1** complex starting from a 1:1:1 mixture of cage **1**, alkyne **7** and azide **8**. a) cage **1** with 2 equiv. of **7**; b) cage **1** with 2 equiv. of **8**; c) equimolar mixture of **1**, **7**, and **8** at t = 0 h; d) the same mixture after 19 days, e) cage **1** with 2 equiv of **10a**. The cartoon representation of the inclusion complexes of **1** with the different *N*-oxides is used in the assignments of the signals.

We also performed a similar kinetic experiment under substoichiometric conditions, that is with an excess of guest **7** (4 equiv.) maintaining the concentrations of cage **1** and guest **8** at 2 mM. As might be expected, changes in the molar ratio of the molecular components translated into different compositions of inclusion complexes in the resulting mixtures. The **1**:**7**:**8** = 1:4:1 mixture produced the (**7**)$_2$⊂**1** complex as the major species in solution (70%) (**Figure 19a**). We also detected the signals of the protons in the inclusion complexes (**8**)$_2$⊂**1** (20%) and (**7**·**8**)⊂**1** (10%)**.**

The ^{1}H NMR spectra of the mixture changed with time. After 2 days, we did not detect the proton signals corresponding to the isomers of the (**10a**)⊂**1** complexes but the proton signals of free **10a** in solution (**Figure 19b**). Notably, the intensity of the proton signals of **10a** increased with time. This observation indicated that the triazole bis-*N*-oxide **10a**, obtained as the product of the included Huisgen reaction in cage **1**, was replaced by competitive inclusion of the excess of any of the reactants **7** and **8**. These results also supported that cage **1** was capable of reaction turnover.

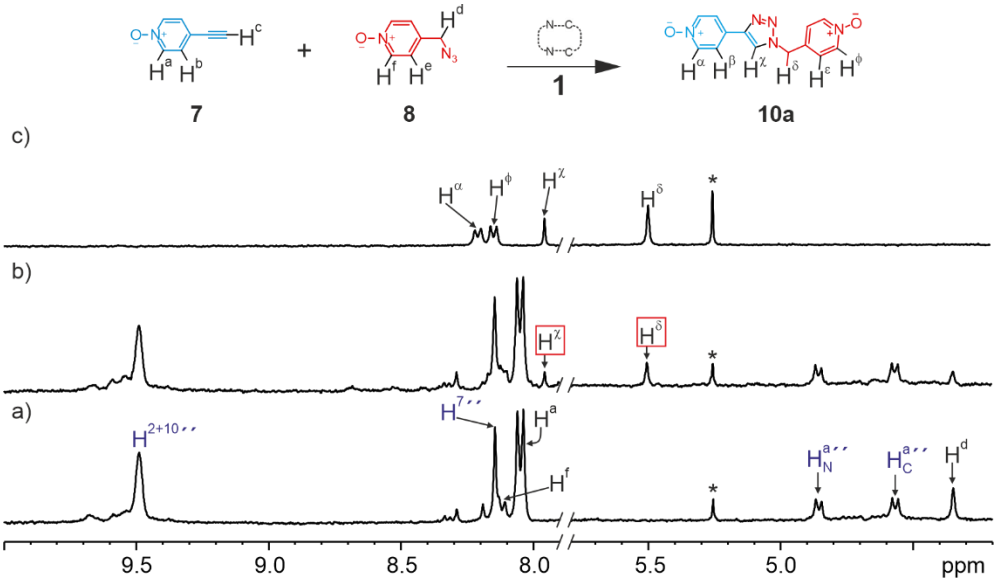

Figure 19. Selected regions of the ^{1}H NMR (500 MHz, at 298K, $CDCl_3$:CD_3CN 9:1) spectra corresponding to the kinetic study of the formation of **10a** starting from a 1:4:1 mixture of **1**:**7**:**8**. a) 1:4:1 mixture of **1**:**7**:**8** (t = 0 h); b) 1:4:1 mixture of **1**:**7**:**8** (t = 20 days). Spectra c) corresponds to the free **10a** in the same solvent mixture.

To mathematically analyze the kinetic data, we used a theoretical model considering: a) the reversible formation of the 1:1 and 2:1 homo- and hetero-complexes from mono-topic reactants **7** and **8**, b) irreversible transformation from the ternary complex (**7**·**8**)⊂**1** into the (**10a**)⊂**1** counterpart (included Husigen 1,3-dipolar cycloaddition reaction), and c) the reversible dissociation of product complex into their binding partners (**Figure 20**). We manually fixed the k_{on}s and k_{off}s values of the equilibria for the formation of 1:1 and 2:1 inclusion complexes. To do so, we set the k_{off}s for all inclusion complexes as 0.01 s^{-1} in agreement with the slow guest exchange rate constant estimated in **Chapter 5**. The k_{on}s for each binding equilibria were determined using the association constant values derived from the thermodynamic characterization studies and the relationship $K_a = k_{on} / k_{off}$. The rate constant of the cycloaddition reaction included in the tetra-imine cage **1**, $k_{included}$, was the only variable in the elaborated model.

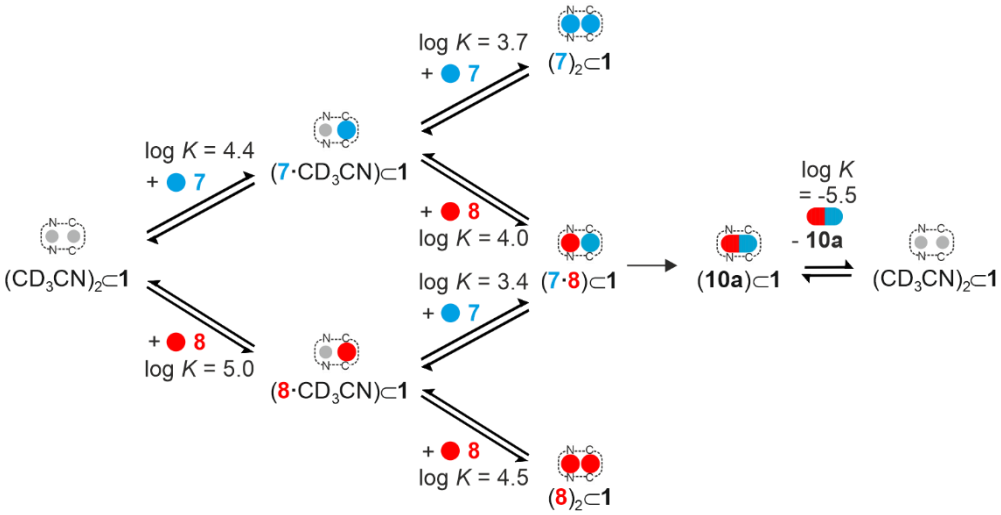

Figure 20. The theoretical model used for the mathematical analysis of the kinetic data of the cycloaddition reaction between **7** and **8** included in the tetra-imine cage **1**. The model considers all binding equilibria forming the 1:1 and 2:1 homo and hetero complexes and the reversible formation of the included cycloaddition product**, 10a⊂1** complex**.** The binding constants were determined with separate titration experiments (vide supra). Only one isomer is shown for each complex for clarity.

We fit the kinetic experimental data to the theoretical model mentioned above using COPASI kinetic modeling software. The fit of the experimental kinetic data to the theoretical kinetic model for included Huisgen 1,3-dipolar cycloaddition

between **7** and **8** was good for both experimental conditions (**1**:**7**:**8** = 1:1:1 and 1:4:1; **Figure 21**). We used the fit to calculate an average value of $k_{included}$ = (1.8 ± 0.3) × 10^{-6} s^{-1}. The rate constant of the Huisgen cycloaddition reaction of **7** and **8** yielding **10a** in the bulk solution was determined in **Chapter 5** as k_{bulk} =5.6 × 10^{-8} $M^{-1}s^{-1}$. We assessed the acceleration factor experienced by the reaction occurring in the cage's cavity from the ratio of the determined rate constants (included and bulk). This procedure returned an EM = $k_{included}/k_{bulk}$ = 32 M. The EM value is almost two orders of magnitude smaller than the EM determined for the same reaction when included in the octa-imine cage **6** (1250 M). This result demonstrated the importance of differences in the nanometric dimensions of the reaction vessels for the acceleration of the reactions occurring in the cage's cavity.

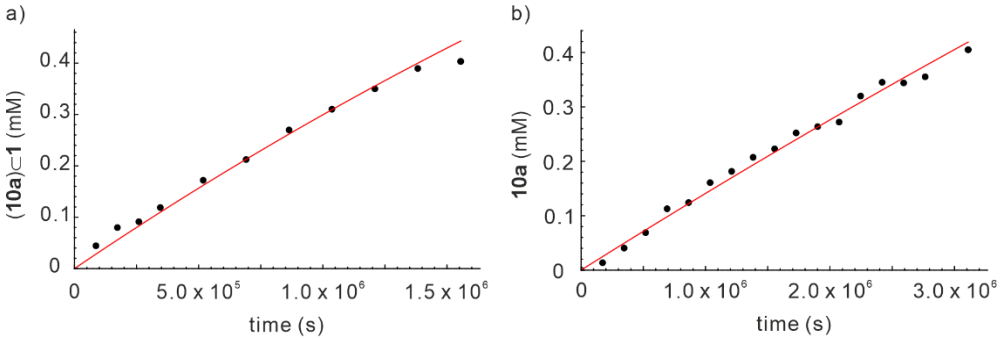

Figure 21. Kinetic profiles of the concentration of species (mM) vs time (s) for the 1,3-dipolar cycloaddition reaction in the presence of 2 mM cage **1**: a) after the addition of 1 equiv. of **7** and **8**, b) after the addition of 4 equiv. of **7** and 1 equiv. of **8**. Red lines represent the fit of the kinetic data to the elaborated model depicted in **Figure 20**.

6.2.4.2 Acceleration of the Huisgen cycloaddition reaction of 4-(ethynyl)pyridine-*N*-oxide **7** and 4-(azidoethyl)pyridine-*N*-oxide **9** by inclusion in the tetra-imine cage **1**.

We prepared a 2 mM equimolar solution of ethynyl pyridine *N*-oxide **7**, azidoethyl pyridine *N*-oxide **9,** and cage **1** in 9:1 $CDCl_3$:CD_3CN mixture of solvents. The ^{1}H NMR spectrum of the solution acquired immediately after adding the *N*-oxides (5 min) showed seven separate signals for the imine protons H^7 of cage **1** (**Figure 22c**). We assigned five of the seven signals by comparing their chemical shifts with those in previous ^{1}H NMR spectra deriving from binding experiments of separate *N*-oxides (**7**, **9** and **11a**) (**Figure 22a** and **b**). The identified signals corresponded to the two homo 2:1 complexes (**7**)$_2$⊂**1**, (**9**)$_2$⊂**1**, the two thermodynamically favored 1:1 complexes (**7**)(CD_3CN) ⊂**1**, (**9**)(CD_3CN) ⊂**1,** and one of the two isomers of the inclusion complex of the bis-*N*-oxide triazole, **11a**⊂**1**. Most likely, the H^7 proton signal of the other **11a**⊂**1** complex isomer appeared overlapped with protons H^a and H^g from free **7** and **9**. The two additional imine signals were attributed to the (**7**·**9**)⊂**1** ternary complexes. Using the integral values of selected imine proton signals, we determined that the ternary hetero-complex (**7**·**9**)⊂**1** was thermodynamically favored over the 2:1 complexes (**7**)$_2$⊂**1**, (**9**)$_2$⊂**1** and the 1:1 complexes (**7**·CD_3CN)⊂**1**, (**9**·CD_3CN)⊂**1**. Considering the experimentally observed speciation profile and using the Hyperquad Simulation and Speciation (HySS2009) software, we derived the ternary hetero-complex binding constant value (**7**·**8**)⊂**1** as 2.0×10^8 M^{-2} (**Figure 37** in the experimental section).

After 4 hours, we analyzed the solution using ^{1}H NMR spectroscopy and were delighted to find the exclusive presence of the signals assigned to the two isomers of the **11a**⊂**1** complex (**Figure 22d**). Remarkably, the kinetics of the cycloaddition reaction of **7** and **9** included in cage **1** was much faster than the cycloaddition between **7** and **8**. The first ^{1}H NMR spectrum acquired immediately after adding the reactants (5 min) showed that the reaction had already progressed to around 30% extent considering the two **11a**⊂**1** complex isomers. A similar kinetic model used to study cycloaddition between **7** and **8** was applied to fit the kinetic experimental data without considering the product dissociation after the included cycloaddition reaction. We set the k_{off}s for all inclusion complexes as 0.01 s^{-1} as mentioned before. The k_{on}s values of the equilibria for the formation of 1:1 and 2:1 inclusion complexes were fixed based on the thermodynamic characterization studies and the relationship $K_a = k_{on} / k_{off}$ (**Figure 38**).

We fit the kinetic experimental data to the theoretical model mentioned above using COPASI kinetic modeling software (**Figure 23**). We used the fit to calculate a

value of $k_{included}$ = 2.2 × 10^{-3} s^{-1}. In **Chapter 5**, we determined that the rate constant for the cycloaddition reaction of **7** and **9** yielding **11a** in the bulk solution was 3.5 × 10^{-8} $M^{-1}s^{-1}$. Using these values, we estimated an acceleration factor of EM = 6.3 x 10^4 M to the included cycloaddition reaction of **7** and **9** in cage **1**; this value is almost two orders of magnitude larger than the one determined for cage **6** (1685 M). The magnitude of the acceleration is close to the theoretical maximum EM = 10^6 M estimated by Page and Jenks by converting an intermolecular cycloaddition Diels-Alder reaction into an intramolecular counterpart or binding the substrates into an enzyme active site.[12]

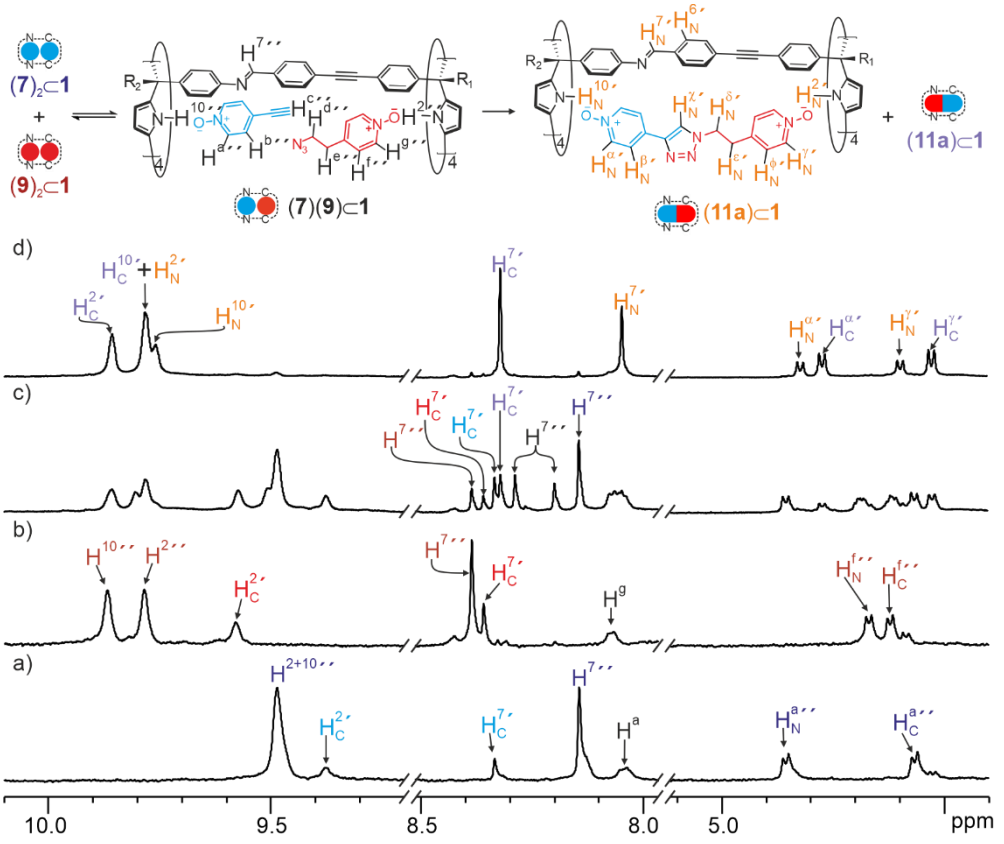

Figure 22. Selected regions of the ^{1}H NMR (500 MHz, at 298K, $CDCl_3$:CD_3CN 9:1) spectra acquired during the kinetic study of the Huisgen cycloaddition reaction of **7** and **9** included in cage **1** and leading to the formation of two isomeric **11a⊂1** complexes: a) cage **1** with 1 equiv. of **7**; b) cage **1** with 1 equiv. of **9**; c) 1:1:1 equimolar mixture of **1**, **7**, and **9** at t= 5 min ; d) same mixture at t = 5 h.

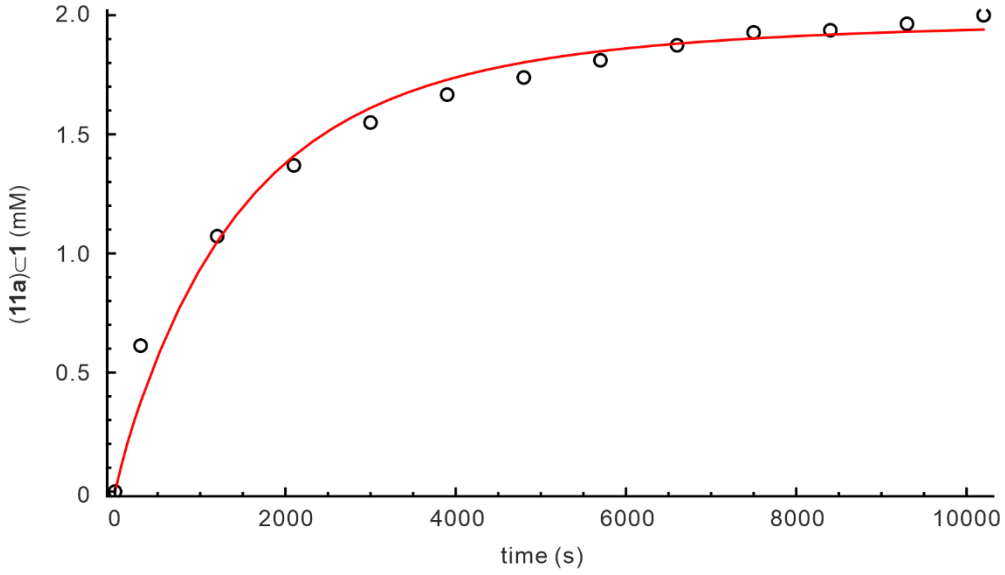

Figure 23. The plot of the changes in concentrations of the **11a⊂1** isomeric complexes with time for a 1:1:1 mixture of **1**, **7** and **9** in 9:1 $CDCl_3$:CD_3CN mixture of solvents.

In **Table 1** we summarized the results of our kinetic investigations for the inclusion of two Huisgen 1,3-dipolar cycloaddition reactions in cages **1** and **6**.

Table 1. Rate constants of the 1,3-cycloaddition reactions between alkyne **7** and azide derivatives **8-9** in the bulk and inside cage **1** and **6** producing the 1,4-cycloaddition isomer and their respectively derived effective molarities.

entry	host	Reactants	k_{bulk} ($M^{-1}s^{-1}$)	$k_{complex}$ (s^{-1})	EM(M)
1	**1**	**7+8**	5.6×10^{-8}	1.8×10^{-6}	32
2	**6**			7.0×10^{-5}	1250
3	**1**	**7+9**	3.5×10^{-8}	2.2×10^{-3}	6.3×10^{4}
4	**6**			5.9×10^{-5}	1685

6.3 Conclusions

We describe the self-assembly of a [1+1] tetra-imine cage **1** via a condensation reaction between tetra-aldehyde SAE-C[4]P **2** and tetra-amino AE-C[4]P **3** in a 9:1 $CDCl_3$:CD_3CN solvent mixture in the presence of 0.01 mM acetic acid as catalyst. The tetra-imine cage **1** was used as a supramolecular reaction vessel to promote the Huisgen 1,3-cycloaddition between an alkyne and azide pyridine-*N*-oxide derivatives simultaneously included in the cavity.

Compared to octa-imine cage **6**, described in **Chapter 5**, tetra-imine cage **1** exhibited a reduced acceleration for the reaction of included guests ethynyl pyridine *N*-oxide **7** and azidomethyl pyridine *N*-oxide **8**. However, our preliminary results augur well for the achievement of reaction turnover under substoichiometric conditions.

In contrast, the Huisgen cycloaddition between guests **7** and azidoethyl pyridine *N*-oxide **9** in the tetra-imine cage **1** showed an EM two orders of magnitude larger than that determined for the octa-imine cage analog **6**.

The result described in this chapter highlighted the importance of shape, size, and length complementarity between the included substrates and the cavity of the molecular reactor for achieving high acceleration factors. The importance of the adequate relative orientation of the reacting groups and the steric constraints imposed on the transition state by the container were also revealed in our studies. We also disclose the thermodynamic requirements of the different inclusion complexes in the use of molecular containers to accelerate included bimolecular reactions and achieve reaction turnover.

6.4 Experimental section

6.4.1 General information

Starting materials and reagents were purchased from commercial suppliers and used without further purification. All reactions were performed under an argon atmosphere and protected from light unless specified. Anhydrous solvents were obtained from a solvent purification system SPS-400-6 from Innovative Technologies. All solvents were of HPLC-grade quality, commercially obtained, and used without further purification. ^{1}H NMR, ^{13}C NMR and 2D NMR spectra were recorded on a Bruker Avance 300 (300 MHz for ^{1}H NMR and 75 MHz for ^{13}C NMR), Bruker Avance 400 (400 MHz for ^{1}H NMR and 100 MHz for ^{13}C NMR), Bruker Avance 500 (500 MHz for ^{1}H NMR and 125 MHz for ^{13}C NMR) or Bruker Avance 500 with cryoprobe (500 MHz for ^{1}H NMR and 125 MHz for ^{13}C NMR). Deuterated solvents used are indicated in the characterization and chemical shifts are given in ppm.

ITC experiments were performed in a MicroCal VP-ITC Micro Calorimeter with the VP Viewer 2000 software. All the titrations were carried out in chloroform: acetonitrile 9:1 solution mixture at 288 K. Titrations were carried out by adding small aliquots (8 μL, 16 s) of a solution of guest into a solution of host in the same solvent. The spacing time was set as 600 s due to the observed slow kinetics. The concentration of guest solution was approximately sixteen times more concentrated the host solution. The association constants and the thermodynamic parameters were obtained from the fit of the titration data to a simple one set of sites binding model by using the Microcal ITC Data Analysis module.

Tetra-amino calix[4]pyrrole **3** [13], tetra-iodo calix[4]pyrrole **12** [14], and 4-ethynyl-benzaldehyde **13**[15] were synthesized by adapting previously reported procedures. The synthesis of monotopic guests **7**-**9** and ditopic guests **10a**-**11a** were discussed in **Chapter 5.** Please note that the number of guests (**7**-**9**, **10a**-**11a**) are different in this chapter from **Chapter 5**.

6.4.2 Synthesis and Characterization

6.4.2.1 Synthesis of calix[4]pyrrole **2**

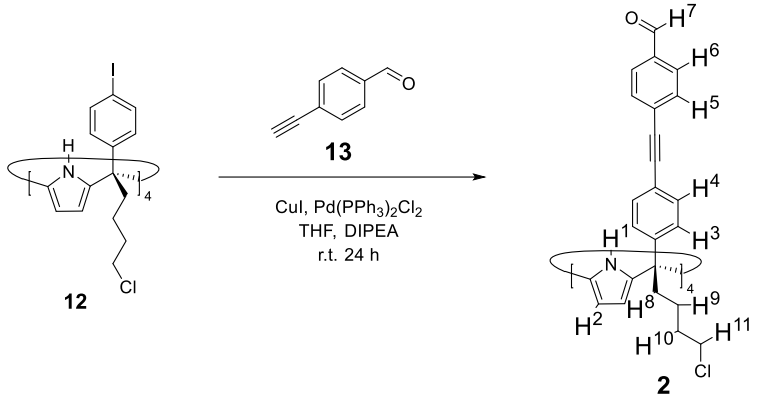

Scheme 3. Synthesis of tetra-aldehyde calix[4]pyrrole **2**.

In a Schlenk flask 25 mL, tetra-α 4-iodophenyl-4'-chlorobutyl calix[4]pyrrole **12** (43.0 mg, 28.9 µmol, 1 equiv.), $Pd(PPh_3)_2Cl_2$ (1.00 mg, 1.45 µmol, 0.05 equiv.), CuI (551 µg, 2.89 µmol, 0.1 equiv.) and 4-ethynylbenzaldehyde **13** (30.1 mg, 231 µmol, 8 equiv.) were kept under the argon atmosphere. Dry THF (5.0 mL) and dry diisopropylamine (5.0 mL) were added dropwise. The reaction was stirred at r.t. for 24 h. After that, the crude was concentrated, redissolved in DCM (10 mL) and washed with brine (2x10 mL) and water (10 mL). The organic layer was dried (Na_2SO_4), filtered and concentrated. The crude was purified by column chromatography on silica gel (3 g, 100:0 → 97:3 CH_2Cl_2:EtOAc) to afford the product as a yellow solid. The product was further purified by recrystallization from 1:1 CH_2Cl_2:CH_3CN (37.1 mg, 17.3 µmol, 60% yield). Rf = 0.4 (DCM, 5%EtOAc).

^{1}H NMR (500 MHz, 298 K, d_7-DMF): δ = 10.05 (s, 4H), 8.88 (s, 4H), 7.79 (d, *J* = 8.2 Hz, 8H), 7.75 (d, *J* = 8.1 Hz, 8H), 7.60 (d, *J* = 8.2 Hz, 8H), 7.10 (d, *J* = 8.1 Hz, 8H), 6.13 (d, *J* = 2.6 Hz, 8H), 3.66 (t, J = 6.6 Hz, 8H), 2.46 (t, *J* = 8.4 Hz, 8H), 1.79 (tt, *J* = 6.9 Hz, 6.6 Hz, 8H), 1.31 (tt, J = 6.9 Hz, 8.4 Hz, 8H).

^{13}C NMR: Solubility of the compound is too low to record ^{13}C NMR.

HRMS (MALDI+) m/z : $[M]^+$ calculated for $C_{96}H_{80}Cl_4N_4O_4^+$ = 1492.4928, found 1492.4940.

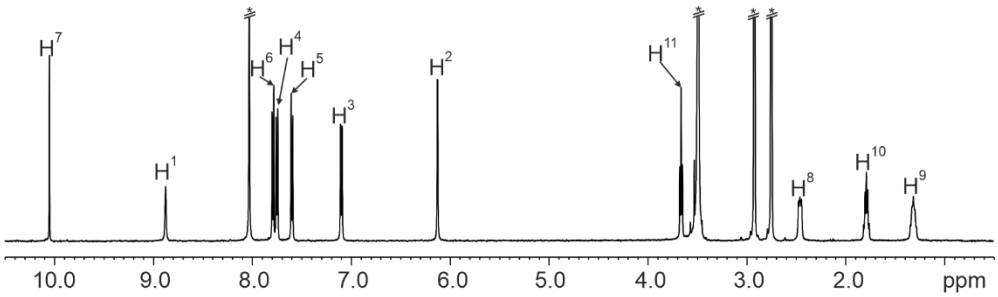

Figure 24. ^{1}H NMR spectrum (500 MHz, at 298 K, d_7-DMF) of **2.**

6.4.2.2 Synthesis of tetra-imine cage **1**

Procedure A:

In an NMR tube, tetra-formylphenyl SAE-C[4]P **2** (1.50 mg, 1.00 µmol, 1 equiv.) and tetra-aminophenyl AE-C[4]P **3** (1.10 mg, 1.00 µmol, 1 equiv.) were mixed in an NMR tube with 500 µL 9:1 $CDCl_3$:CD_3CN containing 0.01 mM acetic acid. The mixture was then left at room temperature for 48 hours. The mixture turned yellow color and provided cage **1** in 90% yields (based on the relative integrals of the signals of the cage and those of the i.s. in solution)

^{1}H NMR (500 MHz, 298 K, 9:1 $CDCl_3$:CD_3CN) δ = 8.21 (s, 4H), 7.54 (bs, 4H), 7.48 (d, *J* = 7.9 Hz, 8H), 7.43 (d, *J* = 7.9 Hz, 8H), 7.39 (bs, 4H), 7.25 (d, *J* = 8.1 Hz, 8H), 7.14 (d, *J* = 8.1 Hz, 8H), 7.03 (d, *J* = 8.1 Hz, 8H), 6.98 (d, *J* = 8.1 Hz, 8H), 5.95 (d, *J* = 2.7 Hz, 8H), 5.94 (d, *J* = 2.7 Hz, 8H), 4.05 (d, *J* = 7.1 Hz, 8H), 3.44 (t, *J* = 6.6 Hz, 8H), 2.34 (dt, *J* = 13.2, 4.4 Hz, 16H), 2.21 (t, *J* = 7.3 Hz, 8H), 1.70 (t, *J* = 7.3 Hz, 8H), 1.54 – 1.44 (m, 8H), 1.34 – 1.26 (m, 8H), 1.18 (t, *J* = 7.1 Hz, 12H).

^{13}C NMR (124 MHz, 298K, 9:1 $CDCl_3$:CD_3CN) δ = 173.4, 159.9, 158.5, 158.0, 148.6, 147.7, 146.8, 144.5, 137.1, 136.9, 135.6, 131.6, 131.0, 130.9, 130.6, 130.0, 128.6, 125.7, 120.4, 120.0, 105.0, 104.8, 90.8, 89.0, 60.2, 48.3, 48.0, 44.8, 38.6, 38.3, 34.4, 32.9, 22.2, 20.5, 14.2, 14.1 ppm.

Procedure B:

In a dry Schlenk SAE-C[4]P **2** (29.8 mg, 20.0 µmol, 1 equiv.) and AE C[4]P **3** (22.8 mg, 20.0 µmol, 1 equiv.) were dissolved in 10 mL chloroform: acetonitrile 9:1 mixture containing 0.01 mM of acetic acid. The mixture was stirred at 298K under Ar and protected from light for 120h. Afterwards, the solvent mixture was removed under

vacuum. The crude cage was then dissolved in 5 mL of DCM and 0.5 mL of methanol was added. The solution was concentrated under reduced pressure and produced cage **1** precipitated as a yellow solid. The precipitate was filtered out and washed with methanol to give pure cage **1** in 70% yield.

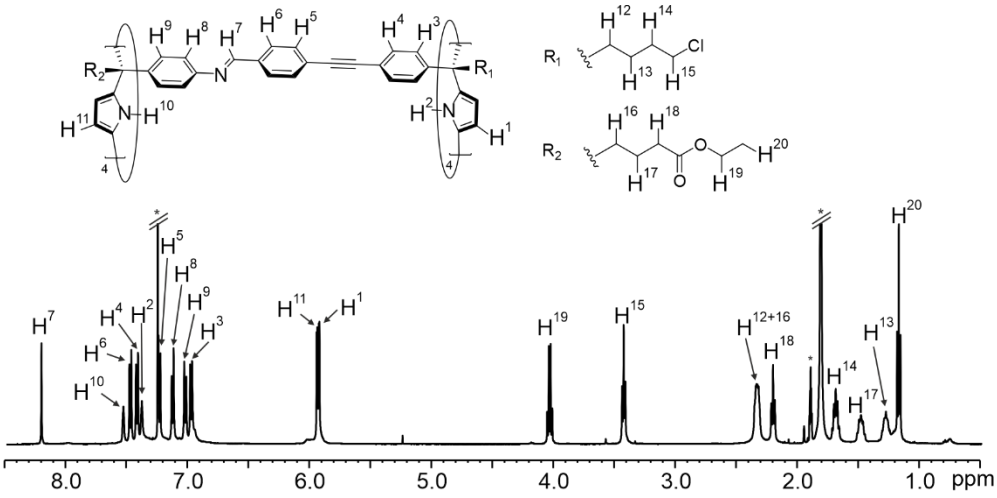

Figure 25. ^{1}H NMR spectrum (500 MHz, at 298 K, $CDCl_3$: CD_3CN 9:1) of $(CD_3CN)_2\subset$**1.**

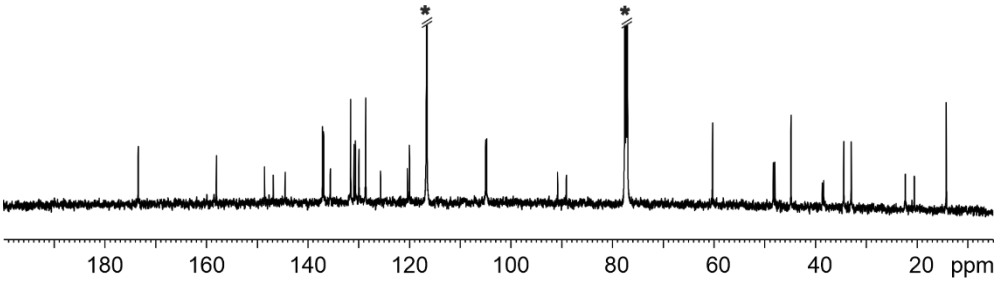

Figure 26. ^{13}C NMR spectrum (124 MHz, at 298 K, $CDCl_3$: CD_3CN 9:1) of $(CD_3CN)_2\subset$**1.**

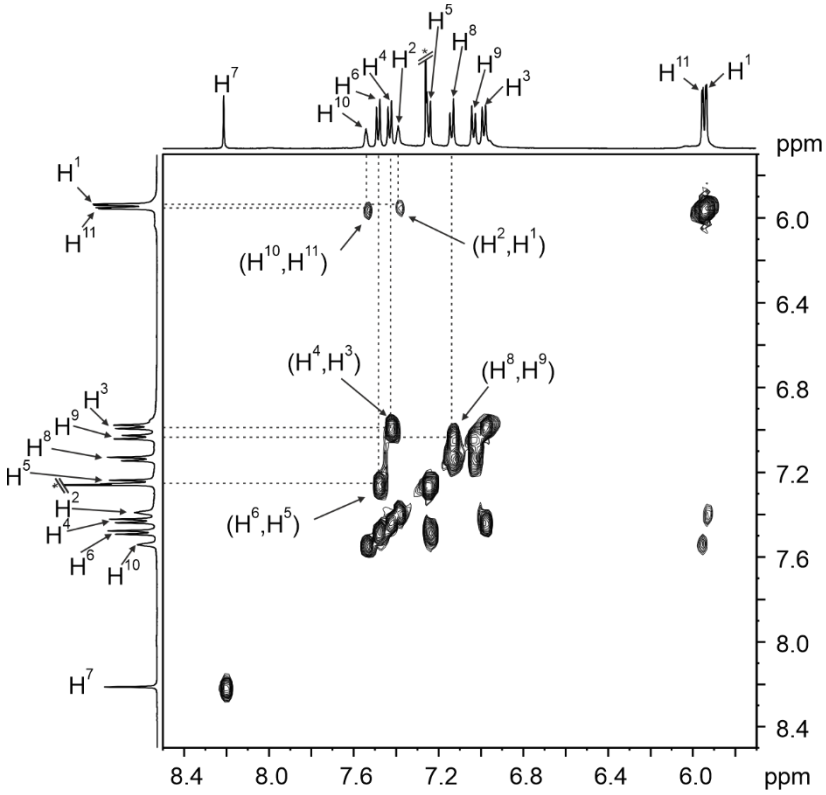

Figure 27. Selected region of ^{1}H-^{1}H COSY NMR (500 MHz, at 298 K, $CDCl_3$: CD_3CN 9:1) of a 2 mM solution of $(CD_3CN)_2 \subset$ **1**. See **Figure 25** for the protons´ assignment.

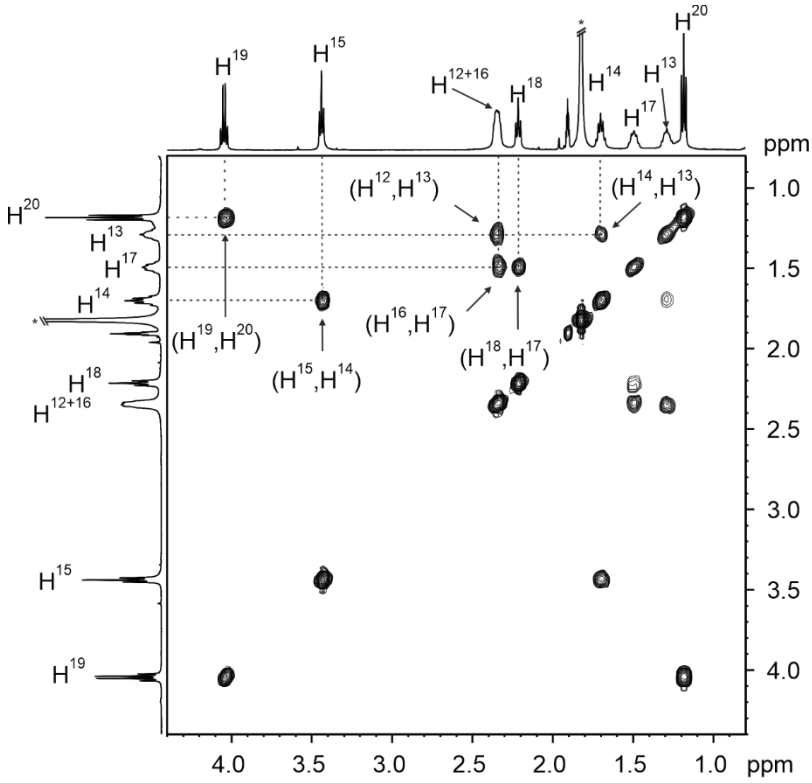

Figure 28. Selected region of ^{1}H-^{1}H COSY NMR (500 MHz, at 298 K, $CDCl_3$: CD_3CN 9:1) of a 2 mM solution of $(CD_3CN)_2\subset$**1**. See **Figure 25** for the protons' assignment.

6.4.2.3 ^{1}H DOSY NMR experiment of cage 1 in CD_3Cl.

The tetra-imine cage **1** is better represented by a cylindrical-shaped object than a sphere. We determined the dimensions of the cylinders using the equations 1-3. First, we estimated the *a* and *b* values from the energy-minimized structure (MM3) of **1**. These values were further refined manually to minimize the difference between the calculated coefficient values and those measured experimentally ($D_{measured}$-$D_{calculated}$ < 1 × 10^{-12} m^2/s). The cylindrical object corresponding to the optimized values is superimposed with the compounds to verify that the geometrical parameters have a physical significance (**Figure 29**).

1) $R = \sqrt[3]{\frac{3(a/b)b^2}{2}}$; a= length (30.5 Å) ang b = diameter (10.2 Å)

2) $f = \frac{(2/3)^{1/3}p^{2/3}}{\ln(2P)-0.3}$; p = a/b

3) $D = \frac{k_B T}{6\pi\eta R f}$

The experimentally measured diffusion coefficients for cage **1** is very similar to the one estimated using the geometrical parameters determined from the energy-minimized structure of cage **1**

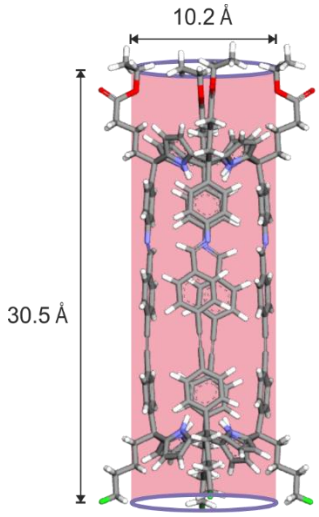

Figure 29. Energy minimized structure (MM3) of the cage **1** and cylinder indicating its dimensions. [16]

6.4.3 Binding studies of monotopic and ditopic guests in cage **1**

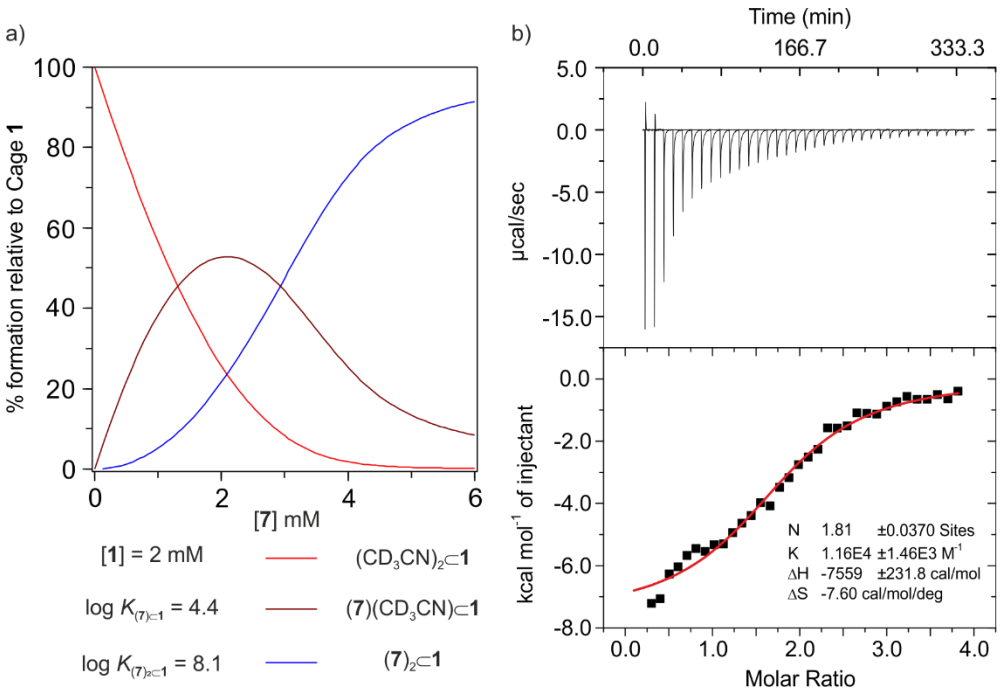

Figure 30. a) Speciation profile of the addition of increasing amounts of **7** (up to 3 equiv.) to a 2 mM solution of cage **1** considering the binding constant values $K_{1:1}$ = 2.5 × 10^4 M^{-1}, $K_{2:1}$ = 1.3 × 10^8 M^{-2}. b) Top- Traces of the raw data (heat vs time) of the ITC experiment of cage **1** ([cell] =5 × 10^{-4} M) with **7** ([syringe] =8 × 10^{-3} M). The solutions were prepared using a chloroform: acetonitrile 9:1 solvent mixture. Bottom- Normalized integrated heat (black squares) vs. **7**/**1** molar ratio. The experimental data were fit to one set of sites binding model (red line).

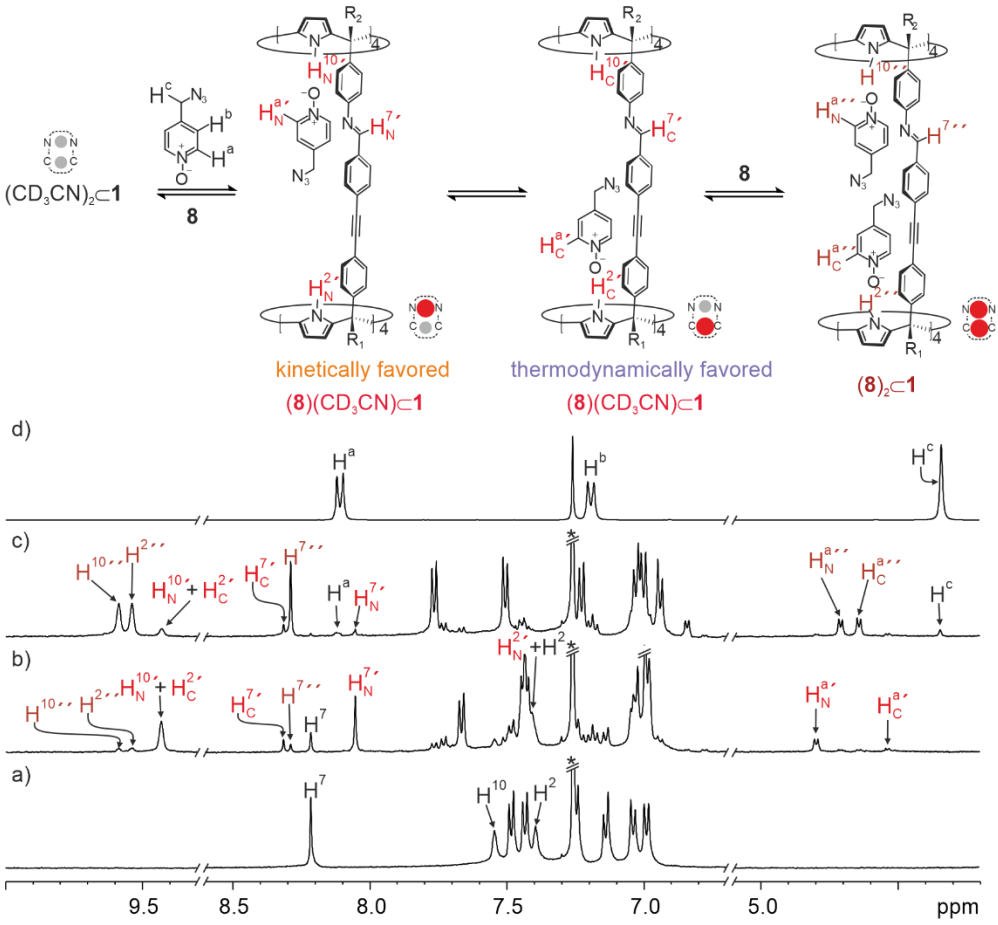

Figure 31. Selected region of the ^{1}H NMR (400 MHz, at 298K, $CDCl_3$:CD_3CN 9:1) spectra acquired during the titration of a 2 mM solution of cage **1** with incremental additions of **8** : a) 0 equiv., b) 1equiv., c) 2 equiv. Spectrum d) corresponds to the free **8** in the same solvent mixture.

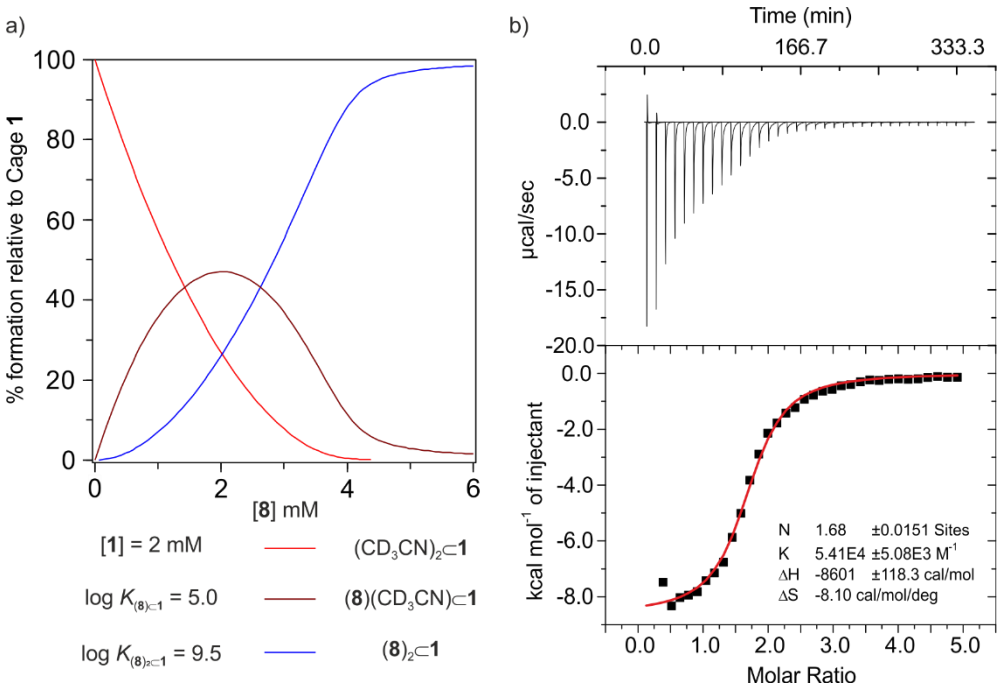

Figure 32. a) Speciation profile of the addition of increasing amounts of **8** (up to 3 equiv.) to a 2 mM solution of cage **1** considering the binding constant values $K_{1:1}$ = 1.0×10^5 M^{-1}, $K_{2:1}$ = 3.3×10^9 M^{-2}. b) Top- Traces of the raw data (heat vs time) of the ITC experiment of cage **1** ([cell] = 5×10^{-4} M) with **8** ([syringe] =11×10^{-3} M). The solutions were prepared using a chloroform: acetonitrile 9:1 solvent mixture. Bottom- Normalized integrated heat (black squares) vs. **8**/**1** molar ratio. The experimental data were fit to one set of sites binding model (red line).

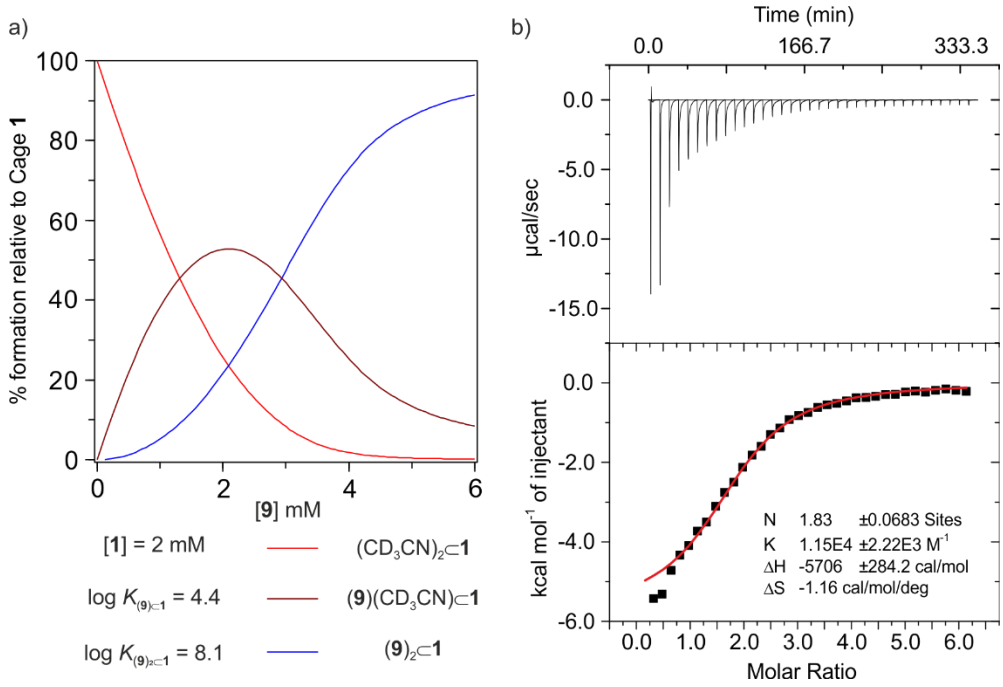

Figure 33. a) Speciation profile of the addition of increasing amounts of **9** (up to 3 equiv.) to a 2 mM solution of cage **1** considering the binding constant values $K_{1:1}$ = 2.5 × 10^4 M^{-1}, $K_{2:1}$ = 1.3 × 10^8 M^{-2}. b) Top- Traces of the raw data (heat vs time) of the ITC experiment of cage **1** ([cell] =5 × 10^{-4} M) with **9** ([syringe] = 13 × 10^{-3} M). The solutions were prepared using a chloroform: acetonitrile 9:1 solvent mixture. Bottom- Normalized integrated heat (black squares) vs. **9/1** molar ratio. The experimental data were fit to one set of sites binding model (red line).

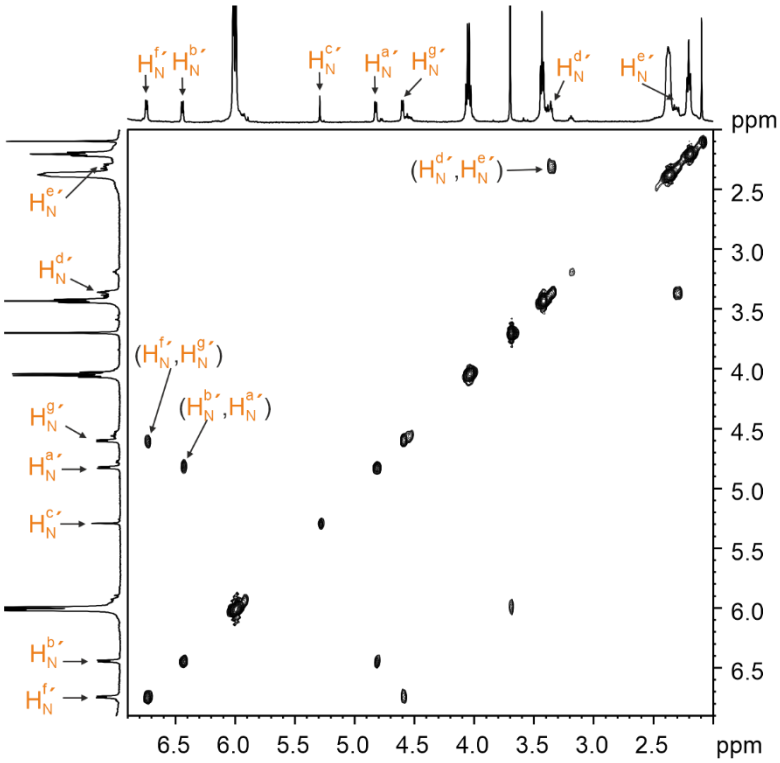

Figure 34. ^{1}H-^{1}H COSY NMR (500 MHz, at 298 K, $CDCl_3$:CD_3CN 9:1 mixture) spectrum of cage **1**, taken two hours after the addition of 2 equiv. of **11a**. See **Figure 17** for the proton's assignment.

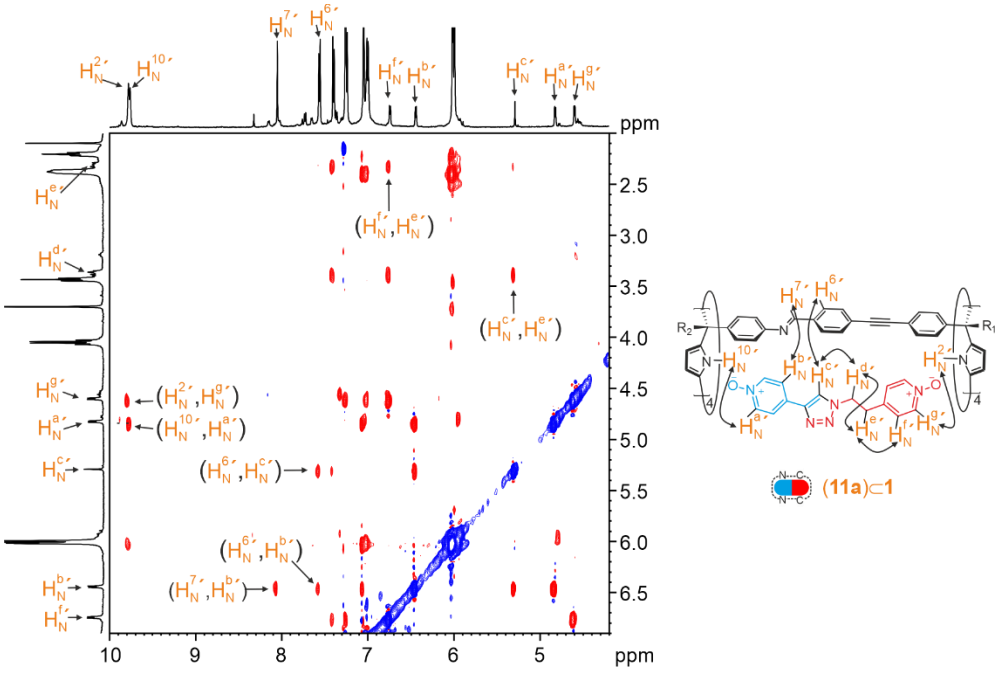

Figure 35. 2D ROESY NMR (500 MHz, at 298 K, $CDCl_3$:CD_3CN 9:1 mixture) spectrum of cage **1**, taken two hours after addition of 2 equiv. of **11a**. See **Figure 17** for the proton's assignment.

6.4.4 Kinetic characterization of cycloaddition reaction in cage **1**.

6.4.4.1 Kinetic study of **1**:**7**:**8** mixture with different ratios.

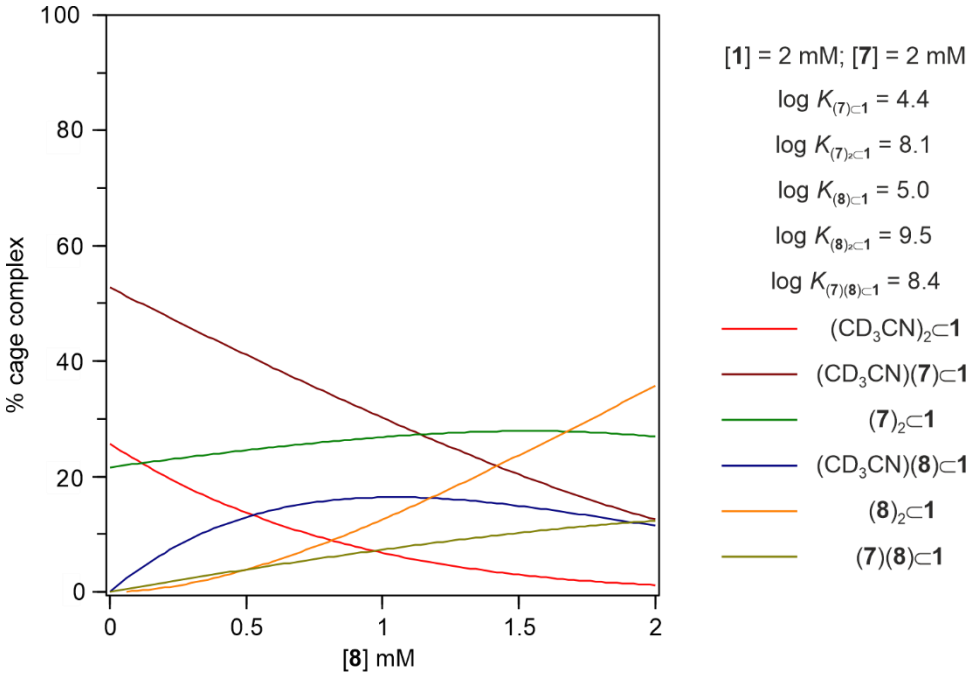

Figure 36. Simulated speciation profile derived from the titration of a solution containing **1** and **7** at 2 mM concentration with incremental amounts of **8** until reaching a 2 mM concentration. The last point considers the overall concentrations of the three components (**1**, **7,** and **8**) used in the solution mixture analyzed by ^{1}H NMR spectroscopy. The association constant values for all the species except the ternary complex, **(7·8)⊂1**, were derived in previous experiments (NMR speciation profiles and ITC experiments).

6.4.4.2 Kinetic study of 1:7:9 mixture

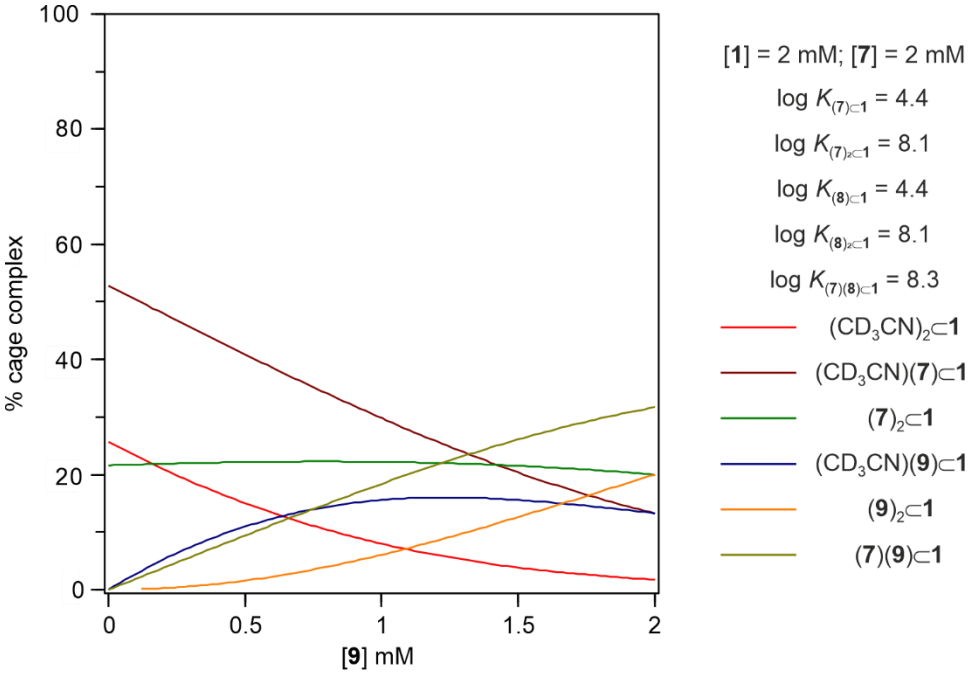

Figure 37. Simulated speciation profile derived from the titration of a solution containing **1** and **7** at 2 mM concentration with incremental amounts of **9** until reaching a 2 mM concentration. The last point considers the overall concentrations of the three components (**1**, **7,** and **9**) used in the solution mixture analyzed by ^{1}H NMR spectroscopy. The association constant values for all the species except the ternary complex, **(7·9)⊂1**, were derived in previous experiments (NMR speciation profiles and ITC experiments).

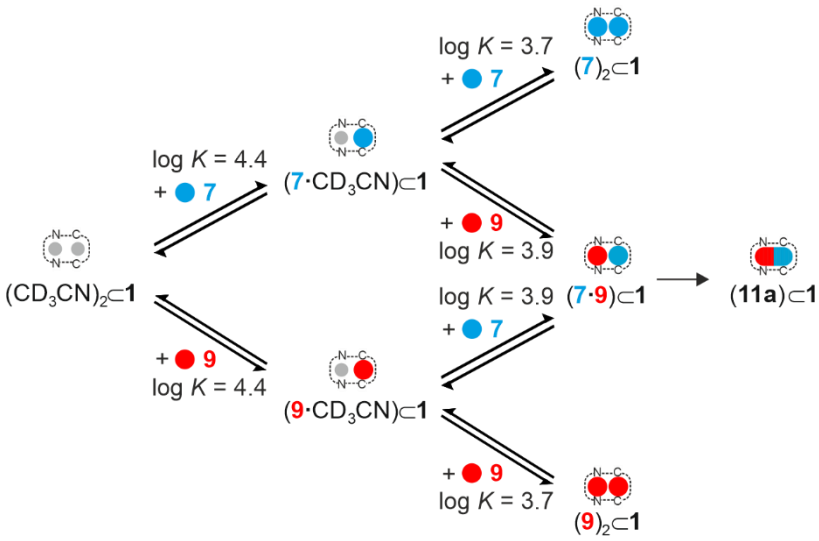

Figure 38. The theoretical model used for the mathematical analysis of the kinetic data of the cycloaddition reaction between **7** and **9** included in the tetra-imine cage **1**. The model takes into account all binding equilibria forming the 1:1 and 2:1 homo and hetero complexes and the irreversible formation of the included cycloaddition product**, 11a⊂1** complex**.** The binding constants were determined with separate titration experiments (vide supra). Only one isomer is shown in the theoretical model for clarity.

6.5 References and notes

[1] Cramer, F.; Kampe, W., *J. Am. Chem. Soc.* **1965,** *87* (5), 1115-1120.
[2] Cacciapaglia, R.; Di Stefano, S.; Mandolini, L., *Acc. Chem. Res.* **2004,** *37* (2), 113-122.
[3] Murase, T.; Horiuchi, S.; Fujita, M., *J. Am. Chem. Soc.* **2010,** *132* (9), 2866-2867.
[4] Fang, Y.; Murase, T.; Fujita, M., *Chem. Lett.* **2015,** *44* (8), 1095-1097.
[5] Yoshizawa, M.; Tamura, M.; Fujita, M., *J. Am. Chem. Soc.* **2004,** *126* (22), 6846-6847.
[6] Wang, K.; Cai, X.; Yao, W.; Tang, D.; Kataria, R.; Ashbaugh, H. S.; Byers, L. D.; Gibb, B. C., *J. Am. Chem. Soc.* **2019,** *141* (16), 6740-6747.
[7] Tehrani, F. N.; Assaf, K. I.; Hein, R.; Jensen, C. M. E.; Nugent, T. C.; Nau, W. M., *ACS Catalysis* **2022,** *12* (4), 2261-2269.
[8] Pindur, U.; Lutz, G.; Otto, C., *Chem. Rev. (Washington, DC, U. S.)* **1993,** *93* (2), 741-761.
[9] Mirabella, C. F. M.; Aragay, G.; Ballester, P., *Chem. Sci.* **2023,** *14* (1), 186-195.
[10] Bonomo, L.; Solari, E.; Toraman, G.; Scopelliti, R.; Floriani, C.; Latronico, M., *Chem. Commun.* **1999,** (23), 2413-2414.
[11] Stott, K.; Stonehouse, J.; Keeler, J.; Hwang, T.-L.; Shaka, A. J., *J. Am. Chem. Soc.* **1995,** *117* (14), 4199-4200.
[12] Page, M. I.; Jencks, W. P., *Proc. Natl. Acad. Sci. U.S.A.* **1971,** *68* (8), 1678-1683.
[13] Escobar, L.; Arroyave, F. A.; Ballester, P., *Eur. J. Org. Chem.* **2018,** *2018* (9), 1097-1106.
[14] Escobar, L.; Ballester, P., *Org. Chem. Front.* **2019,** *6* (11), 1738-1748.
[15] Cummings, S. P.; Cao, Z.; Fanwick, P. E.; Kharlamova, A.; Ren, T., *Inorg. Chem.* **2012,** *51* (14), 7561-7568.
[16] Hansen, S., *J. Chem. Phys.* **2004,** *121* (18), 9111-9115.

General conclusions

In this thesis, we report our results on the design and synthesis of a series of supramolecular receptors featuring well-defined endo-functionalized aromatic cavities based on AE-C[4]P scaffolds. We determine the binding properties of supramolecular and self-assembled molecular receptors using anionic and neutral guests. We also evaluate the self-assembled cages as molecular reactor vessels to mediate the Huisgen cycloaddition reaction.

We draw the following general conclusions from the results obtained in this PhD Thesis:

1) A newly synthesized neutral [2]rotaxane receptor forms 1:1:1 ion-paired complexes with tetraalkylammonium salts of chloride, nitrate, and cyanate anions in chloroform solution. The presence of two chemically non-equivalent binding sites in the macrocyclic component of the receptor provoked the observation of two isomeric complexes differing in the relative location of the bound anion and the axle component. In acetone solution, the interlocked receptor mainly forms 1:1 anionic complexes featuring larger binding constant values than those determined for the ion-paired analogs in chloroform solution. We attributed this finding to the increased dissociation of the ion pairs and the reduced solvation of the anions in the acetone solution. In both solvents, the [2]rotaxane receptor showed a remarkable selectivity for nitrate binding compared to chloride and cyanate. The trigonal shape of the nitrate anion likely allows for a better fit within the three-dimensional polar cavity of the interlocked receptor, enabling more effective non-covalent intermolecular interactions.

2) The use of catalytic amounts of a Brønsted acid favors the quantitative and reproducible self-assembly of [4+2] and [1+1] octa- and tetra-imine cages in a 9:1 chloroform:acetonitrile solvent mixture.

3) The [4+2] octa-imine cage forms 1:1 inclusion complexes with a series of di-formamide guests featuring different alkyl spacers (n= 6-11, number of methylene units between the two formamide ends). The inclusion of some of the guests in the cage cavity forces them to adopt folded and coiled conformations with at least one of the two formamide ends exclusively in the *cis*-form.

4) Some di-formamide guests (n=8 and 9 methylene units) form meta-stable (kinetically stable) 1:1 complexes with the octa-imine cage featuring the terminal formamide groups in a *cis,trans*-conformation. With time, the *cis,trans*-semi-stable complexes are converted to the corresponding thermodynamically stable *cis,cis*-counterparts. We propose that the interconversion process occurs on the included guest rather than requiring an in-out exchange.

5) The [4+2] octa-imine cage displays an endohedrally functionalized cavity larger than other poly-imine cages previously described in our group. The [4+2] self-assembled cage forms thermodynamically and kinetically stable 1:1 and 2:1 homo- and hetero-inclusion complexes with *p*-substituted pyridine *N*-oxide and *N*-substituted 4-pyridone guests. The substituents are azido and ethynyl functional groups. The 1:1 inclusion complexes display binding constants in the 10^4-10^5 M^{-1} range in a $CDCl_3$:CD_3CN 9:1 solvent mixture. The 2:1 homo-complexes showed different levels of binding cooperativity (positive or negative) depending on the guest's substituents. The formation of the complexes is fast on the human timescale. However, they show slow exchange kinetics on the NMR timescale (separate signals for free and bound species).

6) The [4+2] octa-imine cage accelerates the included 1,3-dipolar cycloaddition reaction of 4-azidomethyl and 4-azidoethyl pyridine *N*-oxide with 4-ethynyl pyridine *N*-oxide. The corresponding ternary inclusion hetero-complexes are spectroscopically detected, facilitating the kinetic data analysis. The calculated effective molarity(EM = $k_{included}/k_{bulk}$) for the reaction included in the molecular container is on the order of 10^3 M. Moreover, the reaction occurring in the cage's cavity is regioselective producing exclusively the 1,4-isomer. In contrast, the reaction in bulk produces both the 1,5- and the 1,4- 1,2,3-triazole isomers in comparable amounts. The observed acceleration is one order of magnitude larger than that described for a related reaction included in Rebek's resorcin[4]arene capsular dimer. We attributed the enhancement to the fixed and well-oriented positioning of the substrates within the cavity of the [4+2] cage, favoring achieving the transition state geometry (TS).

7) The product of the included cycloaddition reactions produced highly thermodynamically and kinetically stable 1:1 inclusion complexes. The large

binding affinity of the octa-imine cage for the 1,4-isomer of the Huisgen cycloaddition prevented the observation of catalytic turnover.

8) The [4+2] octa-imine cage also accelerates the 1,3-dipolar cycloaddition reaction between 4-azido pyridine *N*-oxide and N-ethynyl 4-pyridone. However, the reaction occurring in the cage's cavity showed a slower acceleration (10^2 M) compared to the previous ones (10^3 M). Notably, the reaction between 4-azido pyridine *N*-oxide and 4-ethynyl pyridine *N*-oxide was not accelerated to a measurable extent when included in the [4+2] octa-imine cage. These results were attributed to the cage's tight binding and limited flexibility, which imposes geometric and steric constraints in achieving the corresponding TS geometry.

9) We self-assemble a [1+1] tetra-imine cage by coupling a tetra-amino AE-C[4]P with a tetra-aldehyde SAE-C[4]P counterpart. The [1+1] cage features an endohedrally functionalized cavity slightly larger than the [4+2] octa-imine cage. The [1+1] tetra-imine cage features two chemically non-equivalent calix[4]pyrrole binding sites and guest-exchange portals with different dimensions at each hemisphere.

10) The [1+1] tetra-imine cage forms two isomeric 1:1 inclusion complexes with *para*-substituted pyridine *N*-oxide derivatives. Both complexes are thermodynamically and kinetically stable. The binding constants of the 1:1 complexes, ranging from 10^4 to 10^5 M^{-1} in a $CDCl_3$:CD_3CN 9:1 solvent mixture, are comparable to those of the octa-imine [4+2] analog.

11) Compared to the [4+2] octa-imine cage, the [1+1] tetra-imine produce an acceleration (EM) of the included 1,3-cycloaddition reaction of 4-azidomethyl pyridine *N*-oxide with 4-ethynyl pyridine *N*-oxide that is one order of magnitude lower. This difference is likely due to the larger cavity size of the [1+1] tetra-imine cage, which positions the reacting groups of the bound substrates slightly farther apart. The larger cavity of [1+1] tetra-imine cage is advantageous for achieving reaction turnover. The ditopic 1,4-isomer resulting from the included cycloaddition reaction is a loose fit for the cage's cavity and can be replaced by the monotopic reacting substrates.

12) The reaction of the longer 4-aminoethyl pyridine *N*-oxide with 4-ethynyl *N*-oxide included in the [1+1] tetra-imine cage exhibits an acceleration factor (EM) of approximately 10^4 M. This value is getting closer to the 10^7 M factor

estimated by Page and Jencks for the entropic contribution to rate acceleration in bimolecular enzymatic reactions. Our findings highlight the significance of shape, size, and length complementarity between substrates, products, and container cavities in achieving reactions' turnover and high acceleration factors for the reactions occurring in the cage's cavity.

List of abbreviations

ACN	-	Acetonitrile
AcOEt	-	Ethyl acetate
AE-C[4]P	-	Aryl Extended calix[4]pyrrole
APCI	-	Atmospheric Pressure Chemical Ionization
C[4]P	-	Calix[4]pyrrole
CB[*n*]	-	Cucurbit[*n*]urils
CIS	-	Complexation Induced Shifts
COSY	-	Correlated Spectroscopy
CPK	-	Corey-Pauling-Koltun model
CuAAC	-	Copper(I)-catalyzed alkyne-azide cycloaddition
DCM	-	Dichloromethane
DIPA	-	*N, N*-Diisopropylamine
DFT	-	Density Functional Theory
DMF	-	Dimethylformamide
DOSY	-	Diffusion Ordered Spectroscopy
EM	-	Effective Molarity
Equiv.	-	Equivalent
ESI	-	Electrospray Ionization
HPLC	-	High-performance Liquid Chromatography
HRMS	-	High-Resolution Mass Spectrometry
i.s.	-	Internal Standard
ITC	-	Isothermal Titration Calorimetry
MALDI	-	Matrix-Assisted Laser Desorption Ionization
MeOH	-	Methanol

MEP	-	Molecular electrostatic potential
MM3	-	Molecular Mechanics force field
$MTOA^+$	-	Methyltrioctylammonium
NCS	-	*N*-chlorosuccinimide
NMR	-	Nuclear Magnetic Resonance
nOe	-	Neclear Overhauser Effect
NOESY	-	Nuclear Overhauser Enhancement Spectroscopy
PC	-	Packing Coefficient
ROESY	-	Rotating-frame Enhancement Spectroscopy
r.t.	-	Room temperatre
SAE-C[4]P	-	Super Aryl-extended calix[4]pyrrole
SPS	-	Solvent Purification System
TBA^+	-	Tetrabutylammonium
TBTA	-	Tris(benzyltriazolylmethyl)amine
TFA	-	Trifluoroacetic Acid
THF	-	Tetrahydrofuran
TLC	-	Thin Layer Chromatography
TS	-	Transition State
VT	-	Variable Temperature
UV-Vis	-	Ultraviolet-Visible

UNIVERSITAT ROVIRA I VIRGILI
Receptors based on Aryl-extended Calix[4]pyrrole Scaffolds
Yifan Li

UNIVERSITAT
ROVIRA i VIRGILI

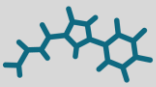

ICIQ

Institute
of Chemical
Research
of Catalonia